CHEMICAL REVIEWS

pubs.acs.org/CR Review

# Large-Area Epitaxial Growth of Transition Metal Dichalcogenides

*Published as part of Chemical Reviews virtual special issue "Two-Dimensional Layered Transition Metal Dichalcogenides".*

Guodong Xue,[#] Biao Qin,[#] Chaojie Ma,[#] Peng Yin,[#] Can Liu,* and Kaihui Liu*

Cite This: https://doi.org/10.1021/acs.chemrev.3c00851 Read Online

ACCESS | Metrics & More | Article Recommendations

**ABSTRACT:** Over the past decade, research on atomically thin two-dimensional (2D) transition metal dichalcogenides (TMDs) has expanded rapidly due to their unique properties such as high carrier mobility, significant excitonic effects, and strong spin−orbit couplings. Considerable attention from both scientific and industrial communities has fully fueled the exploration of TMDs toward practical applications. Proposed scenarios, such as ultrascaled transistors, on-chip photonics, flexible optoelectronics, and efficient electrocatalysis, critically depend on the scalable production of large-area TMD films. Correspondingly, substantial efforts have been devoted to refining the synthesizing methodology of 2D TMDs, which brought the field to a stage that necessitates a comprehensive summary. In this Review, we give a systematic overview of the basic designs and significant advancements in large-area epitaxial growth of TMDs. We first sketch out their fundamental structures and diverse properties. Subsequent discussion encompasses the state-of-the-art wafer-scale production designs, single-crystal epitaxial strategies, and techniques for structure modification and postprocessing. Additionally, we highlight the future directions for application-driven material fabrication and persistent challenges, aiming to inspire ongoing exploration along a revolution in the modern semiconductor industry.

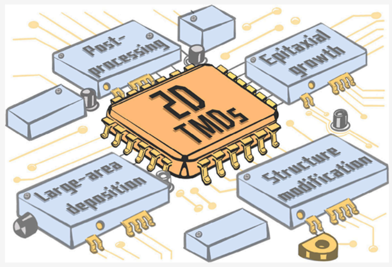


## CONTENTS



**Received:** November 19, 2023
**Revised:** July 14, 2024
**Accepted:** July 18, 2024

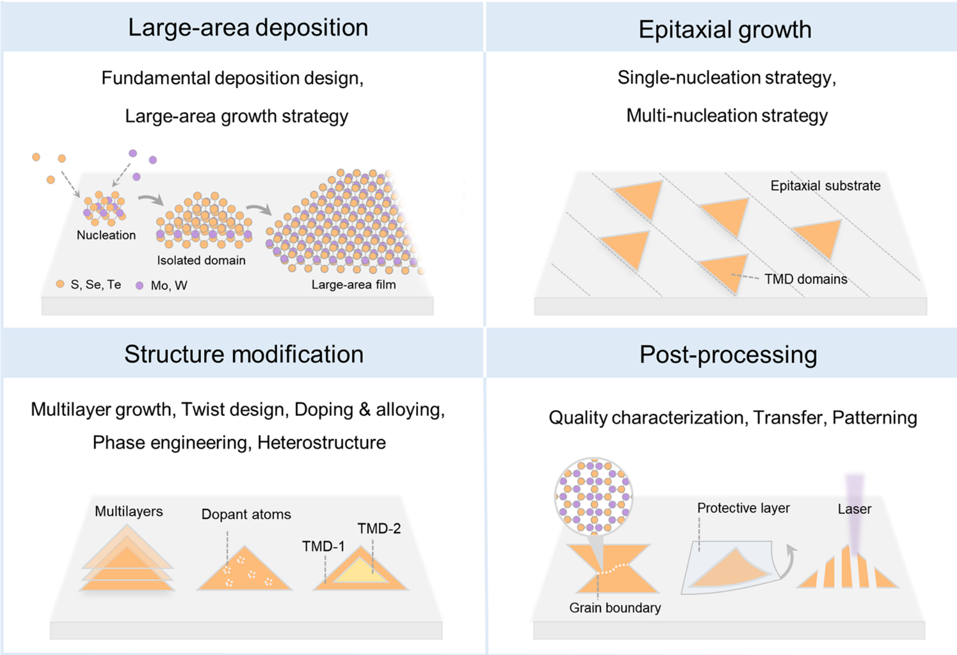


**Figure 1.** Overview of the four key aspects for large-area epitaxial growth of TMDs.



## 1. INTRODUCTION

Two-dimensional (2D) transition metal dichalcogenides (TMDs) are a class of materials with the formula of $MX_2$, where M denotes transition metal elements such as Mo, W or Nb, and X represents chalcogen elements such as S, Se or Te. Most TMDs are assembled as layered crystals via van der Waals (vdW) interactions, making them easily isolated into ultrathin layers, even down to a single layer with a thickness of only ∼0.7 nm. The different coordination environments of transition metal atoms lead to various structural phases such as trigonal prismatic and octahedral species. And this composition diversity and polymorphic nature of TMDs further provide a rich 2D material library for novel physics exploration.[1,2] For instance, fascinating properties including short-channel effect immunity in semiconducting 2H-$MoS_2$, topologically nontrivial phase in 1T′-$WTe_2$ and moiré exciton in $MoSe_2$/$WSe_2$ heterobilayers, have been gradually unveiled in laboratories in the past decade.[3−5] These progress have fully burned up the passion for pushing atomic TMD layers toward a promising future in electronics, optoelectronics, and spintronics.[6−9]

The evolution of 2D TMD devices is intrinsically necessitated on the advancements in material fabrication techniques. The preparation of extremely thin $MoS_2$ samples can be traced back to the 1960s, initially employing a stripping technique using adhesive tape to exfoliate $MoS_2$ down to near-monolayer levels.[10,11] Over subsequent decades, driven by the development of transmission electron imaging techniques and the growing demand to utilize TMDs in applications such as energy storage[12,13] and solid lubricants,[14−16] the investigation of TMDs has progressively shifted from 3D bulks toward lower dimensions. Around 2004, a pivotal moment in this journey occurred, inspired by the success in isolating monolayer graphene.[17] TMD monolayers of $MoS_2$ and $NbSe_2$ are consecutively obtained from their bulk counterparts.[18] This breakthrough not only represents a significant leap into the 2D era for TMDs, but also set the stage for a multitude of innovations in nanotechnology and material sciences.

Complementary to top-down mechanical exfoliation, bottom-up synthesis strategies were also employed to improve the accessibility of TMD materials around 2012. Techniques such as chemical vapor deposition (CVD), physical vapor deposition (PVD), metal−organic CVD (MOCVD), and molecular beam epitaxy (MBE) have been utilized and modified to meet the demand of large-area TMD films.[19−24] Technical aspects including crystallinity, uniformity, scalability, and integration compatibility have been steadily improved over the past decade.[25−30] To date, the film size of uniform monolayer $MoS_2$ polycrystals has already reached wafer scale up to 300 mm.[31,32] Besides that, high single crystallinity is another main pursuit to further improve the device performance and device-to-device consistency. By aligning multiple

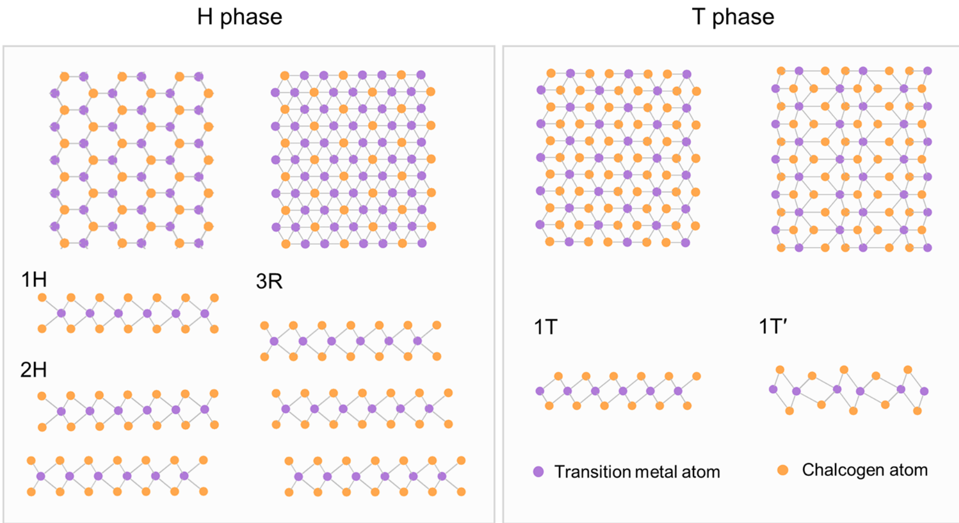


**Figure 2.** Schematics of the polymorphic structures for the TMDs.

TMD islands unidirectionally and stitching them into a large film, wafer-scale single crystals have become accessible in recent years.[33−39] The inherent epitaxial behavior of TMDs through substrate engineering is the theme of these routes, which has been systematically studied and driven forward wafer-scale chips with comparable performance to exfoliated crystal flakes.[36,40]

In addition to the pristine monolayers, a variety of structure modifications offer extra degree of freedom to tailor the functionalities of TMDs. Comprehensive techniques of external doping, stable alloying, and phase engineering are extensively supplemented for specific use including *p*-/*n*-type modulation, bandgap tuning, and semiconductor-metal transition.[41−44] Besides, there is plenty of room above the 2D basal plane, encouraging designs in homo- and heterointegration regarding layer numbers and twist angles. Moreover, corresponding wafer-scale transfer and patterning techniques are of great importance in bridging the synthesis of as-grown films to hybrid integration and device fabrication.[45]

This Review meticulously outlines the progress in the field of large-area TMDs over the past decade, encapsulating both fundamental designs and practical advancements. Here, we propose and primarily focus on four key aspects, i.e., large-area deposition, epitaxial growth, structure modification, and postprocessing (Figure 1). It begins with a brief introduction to the TMDs family, focusing on their crystal structures, elemental compositions and fascinating properties. Section 3 delves into the bottom-up synthesis designs for large-area TMD films. Advancements in epitaxial mechanisms and techniques aimed at producing single crystals are then discussed in Section 4. Sections 5 and 6 cover the strategies for structure modification and postprocessing, respectively. The Review reaches a crescendo in Section 7, highlighting some of the most promising scenarios and applications of 2D TMDs, effectively demonstrating their versatility and potential. The Review concludes in Section 8 with future perspectives and ongoing challenges, thereby encouraging in-depth exploration and technological innovation in large-area TMDs.

## 2. STRUCTURES, COMPOSITIONS AND PROPERTIES OF TMDs

As early as 1923, Linus Pauling investigated the crystalline structure of molybdenite (mineral $MoS_2$) by X-ray crystallography.[46] This layered crystal is held together by vdW forces, rendering it easily cleaved into nanometer-thick layers, even down to a monolayer, through techniques such as adhesive tape stripping or intercalation-assisted exfoliation.[47,48] The early stages of TMD research greatly benefited from these fabrication techniques, along with X-ray diffraction and nascent electron microscopy, which were instrumental in delineating the lattice arrangement and precise thickness of TMD layers. The exploration of TMDs at an atomic scale gained significant momentum with the advent of advanced imaging technologies such as scanning tunneling microscopy (STM), atomic force microscopy (AFM), and scanning transmission electron microscopy (STEM). A major breakthrough in the field was marked by the mechanical exfoliation of single-layer graphene by Geim et al. in 2004, paving the way for subsequent achievements in the fabrication and electrical measurements of monolayer TMDs, including $MoS_2$ and $NbS_2$.[18] In 2011, a series of pioneering studies concentrated for $MoS_2$. Heinz et al., Wang et al., and Kis et al., discovered the strong photoluminescence (PL) in monolayer $MoS_2$, as well as the impressive performance of $MoS_2$ transistors.[49−51] These findings fully fueled the exploration of the unique properties of 2D TMDs and sparked a rapid expansion in the field. This chapter is dedicated to providing a sketch of TMDs, including their crystal structure, chemical composition, physical properties, and potential applications. The aim of this section is to provide a comprehensive overview, that elucidates the fundamental physical concepts linking the basic structure and properties of TMDs, tailored especially for new audiences in this field.

### 2.1. Crystal Structures

For a typical monolayer TMD, two chalcogen atom layers and one metal layer are packaged together to form a sandwich structure, with a thickness of ∼6−7 Å. The exposed chalcogen-terminated surfaces are free of dangling bonds, which can prevent the absorption of external molecules, and thus lead to the ambient stability of TMDs. Considering the metal coordination in the fundamental building blocks (Figure 2),


https://doi.org/10.1021/acs.chemrev.3c00851
Chem. Rev. XXXX, XXX, XXX−XXX


**Figure 3.** Periodic table of known experimentally synthesized layered TMD materials (groups IV,[64−77] V,[78−99] VI,[2,100−102] VII,[59,60,103,104] and VIII[105−125]), summarizing their existing structural phases (H: trigonal prismatic, T: octahedral, T′: distorted octahedral, $T_d$: orthorhombic), typical band gaps (values at the bottom left corner of each grid, M: metallic), and observed electronic phases (superconducting, topological, and CDW).

monolayer TMDs can be broadly categorized into two configurations: trigonal prismatic ($D_{3h}$) and octahedral ($D_{3d}$), denoted as H and T phase, respectively. The octahedral coordination may evolve further variations, such as distorted octahedral T′ and orthorhombic $T_d$ structures. The phase structure evolution of TMDs is determined by thermodynamic preferences, which are primarily attributed to the *d*-electron count of the transition metal atom according to the crystal field theory.[44] Furthermore, taking monolayers as a fundamental building block, the stacking sequence of different monolayers gives rise to additional phase (or polytype) structures. These phases are described by a combination of digit and letter (such as 1T, 2H, and 3R), in which the digit (1, 2, and 3) indicates the number of stacking layers in a unit cell, and the letter (T, H, and R) denotes the trigonal, hexagonal and rhombohedral, respectively. For example, an inversion symmetric 2H phase (space group: $P6_3/mmc$) is constructed by stacking H-phase TMD monolayers in an "AA′AA′AA′..." sequence (A′ layers are 180° rotated from A layers). While it comes to the broken inversion symmetric 3R phase (space group: $R3m$) by aligning H-phase monolayers in an "ABCABC..." manner (here A, B, and C layers are orientated parallel to each other).[1]

The polymorphic nature of TMD materials enriches their electronic structures and physical properties. For example, the thermodynamic stable 2H-$MoS_2$ possesses a considerable bandgap of ~2 eV, rendering it an ideal semiconductor for high-performance electronic devices. In contrast, the high-symmetry 1T-$MoS_2$ phase exhibits metallic properties, with the capability to transition into the 1T′ phase through lattice distortion. Notably, the 1T′ variant exhibits a spin−orbit coupling induced bandgap, which is pursued as the 2D topological insulator candidate.[4] The 3R phase of TMDs, known for its broken inversion symmetry, shows promising applications in nonlinear optics and valleytronics.[52] Given these diverse phase-determined properties, numerous post-processing and synthetic strategies have been proposed to stabilize and purify some specific metastable phases. Transitions between these phases are also accessible by applying external chemical, thermal, or mechanical conditions. This versatility forms the basis for the intriguing field of phase engineering in TMD fabrication, which will be further discussed in Section 5.3.

### 2.2. Elemental Compositions

The TMD materials denoted by the general formula of $MX_2$ consist of a diverse category, where the M and X represent the transition metal and chalcogen atoms with the oxidation states of +4 and −2, respectively. From the aspect of elements, the metal atom M includes elements from group IVB to VIII, and the X is a chalcogen atom including S, Se, and Te. Compounds from groups IVB to VIIB typically crystalline in the layered structure, facilitating the synthesis of thin layers down to monolayers. Conversely, the compounds in group VIII dominantly are nonlayered in nature since they are more thermodynamically stable. A comprehensive first-principles study has predicted that up to 171 types of transition-metal oxides and dichalcogenides are calculated to be stable in monolayer.[53] Experimentally, over 40 types of these binary TMD materials have been successfully synthesized as monolayers or few-layer structures.

The TMD scope of the periodic table is shown in Figure 3. In general, the bandgap of TMDs decreases from sulfides, selenide, and even to a semimetal in tellurides. The *d*-electron counts of the coordinate metal atoms correlate with the material's electronic structure, phase structure, and the emergence of unique properties:

(a) The group IV ($d^0$: Ti, Zr, and Hf) TMDs are 1T phase favorable, and the Ti species are extensively investigated in the charge density wave (CDW) phenomenon, such as the $TiSe_2$ with a high transition temperature of around 200 K.[54] The Zr and Hf species are predicted as high-performance semiconductors with possible high


https://doi.org/10.1021/acs.chemrev.3c00851
Chem. Rev. XXXX, XXX, XXX−XXX

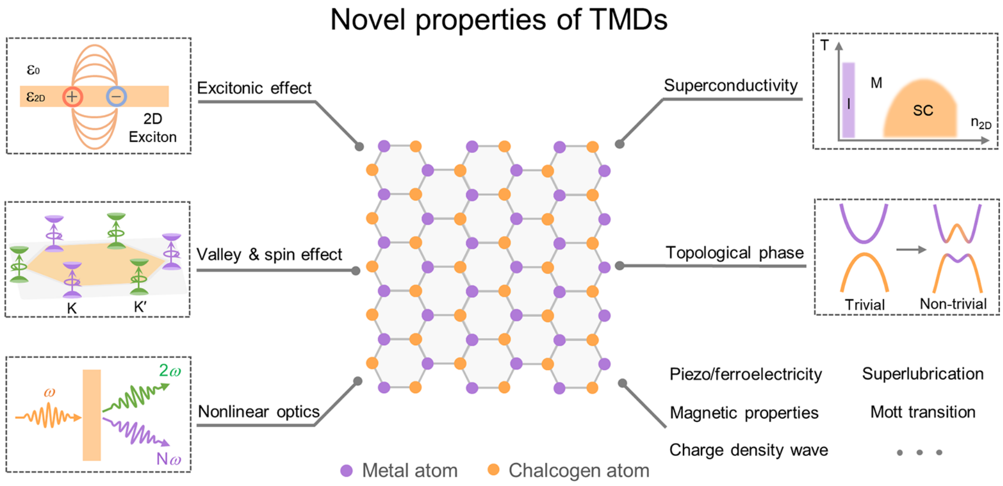


**Figure 4.** Schematic illustration of the novel properties of TMDs.

mobility (e.g., ~3500 $cm^2V^{-1}s^{-1}$ for $HfSe_2$) and could form a native high-$k$ layer by mild oxidation.[55,56]

(b) The group V ($d^1$: V, Nb, and Ta) TMDs are metallic in nature. The V-dichalcogenides have attracted much interest in room-temperature ferromagnetism.[57] The Nb and Ta species are the most studied TMD materials exhibiting superconductivity and CDW order at low temperatures.

(c) The group VI ($d^2$: Cr, Mo, and W) TMDs are polymorphic with the existence of multiple H, T, T′ phases, depending on the preparing conditions. The Cr-dichalcogenides exhibit novel thickness-dependent magnetic properties with promising applications in magneto-electronics.[58] The H-phase Mo and W species with sizable bandgap and excellent synthesizing convenience are considered as the most promising 2D semiconductors, and their 1T′ species (e.g., $WTe_2$ and $MoTe_2$) bring importance in exploring novel topological states.

(d) The group VII ($d^3$: Mn and Re) TMDs have attracted fewer investigations than the group VI. The Mn-dichalcogenides prefer nonlayered structures, and the layered species such as 1T-$MnSe_2$ demonstrated behavior in ferromagnetism at room temperature.[59] The Re species possess the strongly distorted T phase and serve as anisotropic semiconductors with potential applications in electronics and optoelectronics.[60]

(e) The group VIII (Fe, Co, Ni, Pd, and Pt) TMDs are mostly crystalline in nonlayered forms. Fe, Co, and Ni themselves are metallic elements with magnetic properties, and their dichalcogenides also have rich magnetic properties. For example, Fe-dichalcogenides exhibit a variety of magnetic behaviors, including ferromagnetism, ferrimagnetism, and antiferromagnetism. The Pd- and Pt-dichalcogenides show promise in applications such as polarized photodetectors and high-performance catalysts.[61]

The chemical richness and polymorphic structures suggest the TMD material family is a rich 2D material library for new physics exploration and on-demand concept device design.[62,63] Further composition engineering such as alloying, doping, and heterointegration can provide a huge number of combinations. To date, steady progress in the large-area fabrication of these materials fully fuels the field toward promising applications exceeding or complementary to existing technologies.

## 2.3. Novel Properties

2D TMDs exhibit distinct and extraordinary properties due to the reduced dimensionality.[126,127] The exceptional electronic structures, broken inversion symmetry, and enhanced Coulomb interaction within 2D TMDs give rise to numerous novel properties, including remarkable excitonic behaviors, giant optical nonlinearity, strong spin−orbit coupling effects, nontrivial topological physics, superconductivity, piezo-/ferroelectricity, and the formation of CDW, etc (Figure 4). In the following sections, we will proceed with a detailed introduction of these novel properties of TMDs, respectively.

**2.3.1. Excitonic Effects.** One of the remarkable features inherent to 2D TMDs is the pronounced influence of excitons, which govern their optical properties and phenomena.[127,128] Excitons are bound states formed by the attractive Coulomb force between a negatively charged electron and a positively charged hole.[129,130] Typically, excitons originate from the optical excitation in semiconductors, promising the efficient recombination and emission of light.[131,132] However, exciton binding energies are typically very weak (~10 meV) in conventional bulk materials, which exhibit negligible excitonic behavior.[133,134] In contrast, 2D TMDs possess tightly bound excitons with large exciton binding energies on the order of hundreds of meV, due to enhanced Coulomb interaction resulting from their reduced dimensionality.[135,136] Thus, diverse excitonic effects can be observed, such as enhanced photoluminescence emission, complex exciton fine structure and significant environmental sensitivity.[127,137−140]

Tightly bound excitons significantly influence the optical properties of monolayer TMDs. Thinning TMDs to monolayer limit not only facilitates the formation of tightly bound excitons, due to the quantum confinement and weakened dielectric screening effects, but also transitions them into direct bandgap semiconductors.[126,141,142] Consequently, a wealth of optical characteristics attributed to the strong excitonic effects have been observed in monolayer TMDs.[50,51,143,144] For example, monolayer TMDs can absorb light exceeding 15% at the resonance energy of exciton. Considering the atomic-scale thickness, they exhibit obviously stronger light-matter interaction than their bulk counterparts and the conventional semiconductors, such as GaAs and Si.[145] In addition, the


https://doi.org/10.1021/acs.chemrev.3c00851
Chem. Rev. XXXX, XXX, XXX−XXX

direct-bandgap characteristic leads to the emergence of robust PL in monolayer TMDs, where it is largely absent in the few-layer TMDs with indirect-bandgap.[50,51] Moreover, PL behaviors of monolayer TMDs exhibit the remarkable excitonic emission, including narrow spectra lines, wavelength-dependent emission efficiency, and temperature-dependent emission features.[146,147]

The weakened dielectric screening in 2D TMDs has also introduced exciting opportunities for modulating the excitonic behaviors using various external fields, such as electric fields, strain, and light.[148−154] Additionally, their weak interlayer vdW interactions facilitate the formation of new excitons by fabricating TMD homostructures or heterostructures through interlayer stacking.[155,156] This versatility provides a new degree of freedom to controlling the excitonic effects, enabling the exploration of unique exciton physics and applications.[157−161] Presently, the excitonic effects associated with high tunability and controllability have positioned 2D TMDs as promising candidates for advanced photonic and optoelectronic devices.[162−166]

**2.3.2. Nonlinear Optics.** Nonlinear optics is the cornerstone of coherent light generation and manipulation.[167,168] The emergence of 2D TMDs hold immense promise in this realm that becomes a highly sought-after area of research.[169−174] Direct-bandgap monolayer TMDs stand out in the nonlinear regimes, due to their large nonlinear susceptibility with the lack of inversion symmetry.[175−177] This feature facilitates the manifestation of various fascinating nonlinear optical phenomena,[146,178−182] such as even-order harmonic generations, exciton-resonance nonlinear enhancement, and valley-dependent nonlinear selection rules. In addition, the quantum confinement and atomically thin nature of 2D TMDs enable strong broadband nonlinear optical responses and phase-matching-free condition.[52,183]

Second harmonic generation (SHG), a well-studied nonlinear optical phenomenon, plays a crucial role in characterizing 2D TMDs. During this process, two incident photons with the same frequency $\omega$ create a single photon at the frequency $2\omega$ in noncentrosymmetric materials. For 2H phase TMDs belonging to $D_{6h}$ symmetry group, second-order nonlinear optical effects are forbidden (permitted) in their even layers (odd layers), due to the interlayer stacking with opposite dipole orientation.[169,170] As the thickness is reduced to monolayer, it changes to $D_{3h}$ symmetry group and breaks the inversion symmetry.[178] Nowadays, various SHG characterization techniques have been explored to fully understand the fundamental physics and properties of TMDs. For example, the layer number in 2H phase TMDs can be determined by the SHG response, which is only observed at odd layers and vanishes at even layers.[178,184,185] The excitonic effects of TMDs can also characterized through wavelength-dependent SHG responses, where the SHG intensity reveals a significant enhancement at both bright and dark exciton states.[146,186−188] Moreover, polarization-dependent SHG techniques have been developed to determine the lattice orientation, interlayer stacking angle, strain direction grain boundary, etc.[172,189−191]

In recent years, significant research has focused on the nonlinear optical behavior and properties of monolayer TMDs. Their large nonlinear susceptibility, combined with the capacity for seamless integration without lattice mismatch, makes them promising candidates for miniaturized and on-chip nonlinear photonics.[173,192−194] Nevertheless, the absolute energy conversion efficiency in monolayer TMDs is too weak for practical applications, due to the atomic thickness. To overcome these challenges, various strategies have been proposed to enhance the nonlinear optical response of 2D TMDs, such as excitons, electric field, element doping as well as hybridizing them with fibers, waveguides, quantum dots, and metamaterials.[146,150,195−201] Currently, a promising strategy is to increase the effective light propagation length in 2D materials, notably with multilayer rhombohedral TMDs with naturally broken inversion symmetry.[202,203] These intrinsic noncentrosymmetric thick 2D crystals allow simultaneously enhanced nonlinear efficiency and outpower, which has been exploited for the applications of compact nonlinear waveguide, ultrathin frequency-doubling crystal, and ultrathin quantum light source.[204−206] These advancements would open up exciting possibilities for 2D TMDs for developing compact and efficient nonlinear photonic devices.

**2.3.3. Valley Properties.** 2D TMDs with hexagonal lattices have two degenerate and inequivalent valleys located at K and K′ points of the Brillouin zone.[207,208] The valleys are largely separated in momentum space, where the electron intervalley scattering can be suppressed with a long lifetime in materials without obvious atomic-scale defects. As a result, the valley has been regarded as an internal degree of freedom (DOF) of an electron in addition to the spin and charge, where valley DOF has been used for information encoding and processing applications known as valleytronics.[208] The concept of valleytronics, which has been predicted for some time, now has been demonstrated in conventional bulk materials.[209−214] However, achieving precise control of the valley state has proven challenging due to the lack of strong coupling between an external field and valley index. The emergence of 2D TMDs have garnered significant attention in this field and offers new opportunities for exploring and controlling valley polarization, due to their capacity for manipulating of valley DOF using various fields.[215−217]

For 2D materials with the absence of inversion symmetry, they possess two nonzero physical quantities, Berry curvatures and orbital magnetic moments, which have the potential to control the valley DOF and distinguish between the two valleys.[218−221] By breaking the inversion symmetry of monolayer graphene, the emerging nonzero physical quantities have led to the observation of valley contrasting Hall transport.[218] In contrast, monolayer TMDs possess intrinsic inversion asymmetry, making them exceptionally suitable materials for exploring valley-dependent physics and phenomena.[221−225] For example, the strong spin−orbit coupling originated from the *d* orbitals of the heavy metal atom in TMDs enables the observation of spin-valley locked physics.[226,227] In addition, the exciton valley polarization can be easily tuned using external fields, including electrical and magnetism fields.[228−235] Furthermore, 2D TMD heterostructures have exhibited a much longer exciton valley lifetime than that of monolayer TMDs, which makes these interlayer excitons highly promising for valley-dependent applications.[236−245] These unique valley-dependent physics and phenomena in 2D TMDs and their heterostructures open up new opportunities to realize future spintronic and valleytronic devices.[246−248]

**2.3.4. Superconductivity.** The bulk Nb-dichalcogenides, previously studied as conventional low-temperature superconductors, could retain their intrinsic superconductivity even when exfoliated down to monolayer thickness.[249] The reduced dimensionality of 2D TMD superconductors generally lead to


https://doi.org/10.1021/acs.chemrev.3c00851
Chem. Rev. XXXX, XXX, XXX−XXX

a decrease in transition temperature ($T_c$).[250] For instance, the $T_c$ drops from ∼7 K for bulk $NbSe_2$ down to less than 3 K in its monolayer counterpart.[251] The advancement of the bottom-up synthesis methodology has significantly enhanced material accessibility for both fundamental research and promising applications of superconducting 2D TMDs.[252−254] In addition to intrinsic 2D superconductivity, chemical doping or electrostatic doping can bring the superconductivity in TMDs. For example, doping with alkali metals, such as $Cs_{0.3}MoS_2$ can lead to a $T_c$ around 6 K.[255] A qualitative and clean strategy involves field effect gating semiconducting TMDs by ionic liquids, which form an electrical double layer (EDL) and provide an ultradense sheet of carriers (>$10^{14}$ $cm^{-2}$) to modulate the superconducting behaviors. In 2012, Ye et al. achieved continuous gate tunning of the few-layered $MoS_2$, demonstrating the remarkable doping range appeared the superconducting dome in phase diagram.[256] This gate-induced superconductivity has been demonstrated a common behavior in series TMDs such as $MoSe_2$, $MoTe_2$ and CVD-growth $WS_2$.[257,258] Furthermore, these 2D TMD superconductors are identified as unconventional Ising superconductors with ultralarge in-plane critical field far beyond the Pauli paramagnetic limit.[251,259,260]

**2.3.5. Charge Density Wave.** When the temperature falls below a critical threshold, the stability of the Fermi surface in a system will be disrupted, leading to the redistribution of charge density and the formation of a periodic lattice space modulation known as a CDW.[261] This intriguing phenomenon is a collective excitation pattern involving phonons commonly observed in specific TMDs, including $NbSe_2$, $TaSe_2$, $TaS_2$, and $TiSe_2$.[54,262−268] According to the relationship between the wavelength and original lattice constant, the resulting periodic charge density wave can be categorized into two types: commensurate (CCDW, ratio is rational) and incommensurate (ICCDW, ratio is irrational) CDW. For 2D materials, owing to their intricate lattice and electronic structures, the origin of this temperature-dependent phase transition is still widely discussed, including Fermi surface nesting, electron−phonon coupling interaction, electron correlation interaction, etc. In short, as the temperature decreases, the electron ordering and lattice structure change, accompanied by the emergence of an energy gap at the Fermi surface, resulting in periodic lattice distortion and the opening of an energy gap. For instance, $VSe_2$ has near-linear Fermi surfaces in its band structure, facilitating perfect Fermi surface nesting and aligning with Peierls' theory.[269] However, experiments show that the formation of CDW in $NbSe_2$ is mainly due to strong electron−phonon coupling, rather than Peierls' theory.[270] The CDW state in TMDs can be modulated to a certain extent by temperature, stress, and local electric field, offering potential applications in nanodevices. For instance, leveraging the metal−insulator transition in 1T-$TaS_2$ at low temperatures enables the creation of FETs[271] with high switching ratios and nonvolatile memory.[272] Additionally, 1T-$TaS_2$ thin layers can rapidly and controllably transition between NCCDW and ICCDW states at room temperature, facilitating applications in electronic devices like voltage oscillators.[273] In some materials, CDWs have been found to be multiband,[263] offering exciting prospects for CDW-regulated quantum computing in the future.

**2.3.6. Magnetic Properties.** Ferromagnetism is defined by the alignment of magnetic moments (spins) within certain materials, resulting in a consistent and enduring magnetization.[274] In 3D systems, the realization of ferromagnetism requires the Curie temperature to significantly exceed room temperature. However, 2D materials face a distinctive challenge. In 1966, N. D. Mermin and H. Wagner demonstrated that the isotropic Heisenberg model with finite-range interactions at nonzero temperature cannot exhibit ferromagnetic or antiferromagnetic properties in 2D systems.[275] To overcome this constraint, the introduction of magnetic anisotropy becomes pivotal for 2D materials, enabling them to exhibit magnetism at specific temperatures. Magnetic anisotropy describes the relationship between magnetism and the relative orientation of the applied magnetic field concerning the lattice and stands as a fundamental requirement for the observation of ferromagnetism in 2D materials.[276,277] In 2017, researchers made a groundbreaking discovery of intrinsic long-range ferromagnetism in few-layer $Cr_2Ge_2Te_6$ and monolayer $CrI_3$. Both 2D materials rely on magnetic anisotropy to suppress thermal fluctuations inherent in 2D crystals.[278,279] Subsequently, Deng et al. discovered intrinsic ferromagnetism in 2D $Fe_3GeTe_2$ materials, which could further exhibit room-temperature ferromagnetism through doping.[280] The revelation of long-range magnetic ordering in these 2D crystals holds profound significance in understanding spin dynamics at the 2D level. Moreover, these findings possess the potential to unlock a multitude of applications, spanning from individual quantum devices to high-capacity data storage solutions.

Most 2D TMDs are inherently nonmagnetic, but local magnetic moments can be typically induced through the process of doping or adsorption of magnetic atoms.[281−284] In practice, these locally generated magnetic moments often suffer from the limited stability and controllability, making the establishment of the long-range magnetic order a huge challenge. Similarly, room-temperature ferromagnetism was also observed in 2D $MnSe_x$ layers grown on vdW substrates like GaSe and $SnSe_2$.[59] In recent years, ferromagnetic and antiferromagnetic properties have been unveiled in other 2D TMDs, specifically transition metal compounds such as Mn, Fe, and Cr, in combination with chalcogenide elements like S, Se, and Te.[285−294] In addition, Li et al. have reported the epitaxial growth of $CrSe_2$ nanosheets on $WSe_2$, revealing thickness-dependent ferromagnetism.[58] Theoretical investigations suggest that the magnetic ordering of $CrSe_2$ was significantly influenced by charge transfer from the $WSe_2$ substrate and interlayer coupling within $CrSe_2$. These groundbreaking discoveries are driving advancements in the fields of magnetoelectronics and spintronics.

**2.3.7. Piezoelectricity and Ferroelectricity.** 2D TMDs with inversion asymmetry serve as a kind of fascinating piezoelectric materials.[295] Piezoelectricity results from strain-induced electric polarization or electric-induced stain, allowing the efficient and reversible energy conversion between mechanical force and electricity.[296,297] The crucial indicator for multifunctional piezoelectric applications is the piezoelectric coefficient that characterizes the intercoupling efficiency between mechanical and electric energy.[297,298] Noncentrosymmetric 2D TMDs are of great interest in piezoelectricity due to their reduced dimensionality and large piezoelectric coefficient.[295,299,300] Monolayer $MoS_2$ was the first experimentally observed piezoelectricity in the family of 2D TMDs, which largely promoted the study of piezoelectricity in 2D materials.[301−303] Recently, various 2D TMDs, including monolayer or odd-layer 2H phase TMDs, 3R phase


https://doi.org/10.1021/acs.chemrev.3c00851
Chem. Rev. XXXX, XXX, XXX−XXX

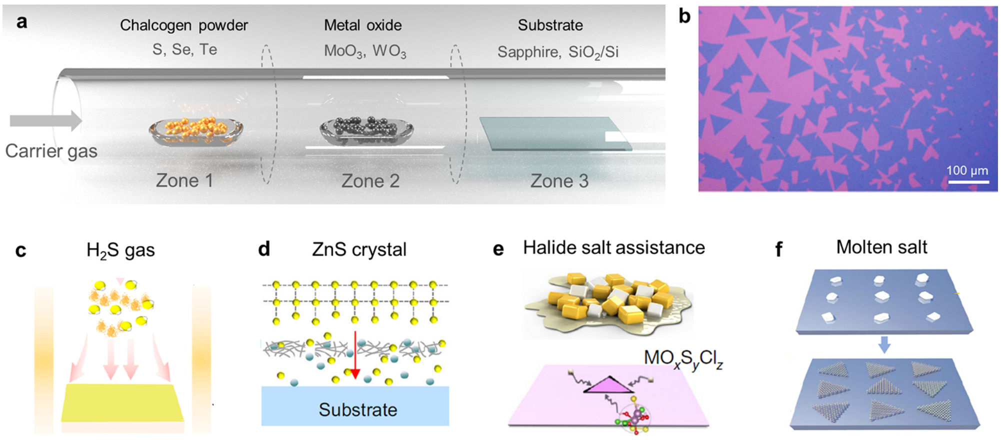


**Figure 5.** Feeding strategies of chalcogen and metal precursors for the vapor deposition of TMDs. (a) Schematic illustration of a typical configuration for the CVD growth of TMDs. (b) Optical image of the as-grown triangular monolayer $MoS_2$ islands. Reprinted with permission from ref 357. Copyright 2013 Springer Nature. (c) Vertical supply of gaseous $H_2S$ precursors for TMDs growth. Reprinted with permission from ref 362. Copyright 2020 American Chemical Society. (d) High-melting-point ZnS crystals supply S monomers for $MoS_2$ growth. Reprinted with permission from ref 366. Copyright 2022 Springer Nature. (e) Molten-salt-assisted CVD method for universal producing of TMD materials. Reprinted with permission from ref 368. Copyright 2018 Springer Nature. (f) Molten $Na_2MoO_4$ salt facilitates the patterned VLS growth of $MoS_2$ monolayers. Reprinted with permission from ref 379. Copyright 2019 Royal Society of Chemistry.

TMDs, and their heterostructures, have been demonstrated with strong piezoelectric effects.[304−306] In combination with the excellent piezoelectricity performance, 2D TMDs, and their heterostructures provide an ideal platform for novel piezoelectric applications in nanoelectromechanical systems and flexible electronic devices.[307−309]

Beyond the intrinsic piezoelectricity, ferroelectricity in 2D TMDs is also impressive with robust polarization down to atomic thicknesses.[307,310] Unlike conventional ferroelectrics, 2D TMDs, and other vdW ferroelectrics are robust against depolarization fields.[311] This is attributed to the efficient screening of the bound charges and lower polarization values of vdW systems. The ferroelectricity in the family of 2D TMDs is first demonstrated in topological semimetal few-layer $WTe_2$, where their spontaneous out-of-plane electric polarization could be switched using gate electrodes. However, ferroelectrics in native 2D TMDs are rare because they are centrosymmetric without spontaneous polarization for their bulk crystals.[312−314] Recently, 2D TMDs with stacking-engineered assemblies opened up a completely new field in 2D ferroelectrics.[315] When vdW materials are stacked to break the inversion symmetry, the interfacial charge transfer will lead to a reversal of the out-of-plane spontaneous polarization, enabling the sliding ferroelectricity.[316−318] This concept was experimentally demonstrated in artificially stacked 2D TMDs, where electrically switchable stacking configurations and ferroelectric domain wall evolution were investigated.[319,320] Meanwhile, the layer-dependent sliding ferroelectricity was also been demonstrated in the as-grown 3R $MoS_2$.[321] The studies on the field-effect transistors fabricated using 3R $MoS_2$ with different thicknesses revealed the critical roles layer in sliding ferroelectricity. The ferroelectricity in 2D TMDs offers new possibilities for creating 2D ferroelectrics and provides a new platform for investigating multiferroic phenomena.[311,314,322]

**2.3.8. Topological Properties.** The topological nature of materials has been a topic of interest since the discovery of the integral quantum Hall effect in 1980.[323,324] Topological materials, based on their band structures, are primarily categorized into two types: topological insulators (characterized by insulating inside the bulk while becoming conductive on the edge) and topological semimetals (characterized by the existence of pairs of Weyl points and Fermi arcs on the surface).[325,326] Recently, 1T′ phase TMDs have attracted great attention due to their nontrivial topological properties. Initial theoretical studies suggested that these materials exhibited significant band inversion around the Γ point, indicating their potential for achieving the quantum spin Hall effect.[4] This was later confirmed experimentally in monolayer 1T′-$WTe_2$, the first 2D material identified as a topological insulator, where the existence of edge states was demonstrated through Hall effect measurement and angle-resolved photoemission spectroscopy (ARPES).[327−329] Meanwhile, several kinds of multilayer 2D TMDs, including 1T′-$WTe_2$ and 1T′-$MoTe_2$, have been proved as topological semimetals,[330,331] where various Berry curvature effects are revealed, such as nonlinear Hall effect and circular photogalvanic effect.[332,333] These findings make 2D TMDs a new platform for exploring novel topological physics and quantum geometrical physics.

Recently, fancy topological states have also been unveiled in bilayer TMDs with a small twist angle, where a moiré superlattice and strong correlated electronic states are formed. In the moiré superlattice, electrons tend to fill in one specific valley rather than distributing equally between different valleys. This behavior leads to the formation of an orbital magnetic moment and breaks time-reversal symmetry, thereby facilitating the exploration of a novel type of topological insulator known as the "orbital Chern insulator".[334] For instance, in the $MoTe_2/WSe_2$ superlattice, the quantum anomalous Hall effect was observed clearly, which confirmed the formation of an orbital Chern insulator.[335] Furthermore, in twisted $MoTe_2$, fractional quantum anomalous Hall effect was observed through different experimental methods, signifying the presence of fractional Chern insulator in 2D TMD superlattices.[336−339] This groundbreaking discovery is considered a significant step toward the exploring of anyons.


https://doi.org/10.1021/acs.chemrev.3c00851
Chem. Rev. XXXX, XXX, XXX−XXX

## 3. VAPOR DEPOSITION OF LARGE-AREA TMD FILMS

The fascinating properties of TMDs have primarily been demonstrated involving micrometer-sized flakes obtained through top-down exfoliation from natural minerals or synthetic bulk crystals. However, this lab-scale approach is limited by its low yield and small sample size, which restricts the scalability and broader application of 2D TMDs. Therefore, the bottom-up growth of large-area TMDs emerges as a promising avenue, utilizing various thin-film fabrication techniques such as sputtering,[340] MBE,[341−343] pulsed laser deposition (PLD),[344−346] atomic layer deposition (ALD),[346−354] and vapor deposition methods (including CVD, PVD, and MOCVD). Considering factors such as scalability, crystallinity, uniformity, and fabrication cost, vapor deposition methods stand out as the most promising route toward large-area electronic 2D TMDs. In this section, we delve into a representative solid source CVD method, as shown in Figure 5a, offering a comprehensive entry point for a broad audience to grasp the fundamental concepts and understanding of TMD vapor deposition processes.[355] Section 3.1 guides readers through the fundamental designs in vapor deposition of TMDs, covering precursor feeding, surface nucleation, and growth promotion. Subsequently, in Section 3.2, we explore design strategies aimed at producing inch-sized TMD films—a challenging but crucial aspect facilitating the seamless transition of TMDs from laboratory research to practical applications.

### 3.1. Fundamental Designs in Vapor Deposition of TMDs

The vapor deposition process of large-area TMD materials can be broadly divided into three stages: (i) solid precursors vaporize at high temperatures (or using gaseous precursors) and create steady intermediate mass flows for reactions; (ii) these active intermediates aggerate into clusters at the high-surface-energy positions on the target substrate, serving as nuclei for TMD growth; (iii) the continued precursor feeding promotes the nuclei to grow into domains, eventually coalescing to form a large-area film. Successfully preparing a piece of TMD film necessitates carefully dealing with numerous parameters, including temperature, pressure, gas flow, substrates, precursors, and growth promotors.[356] Here we will introduce the fundamental designs in TMD vapor deposition, which are gradually forming a systematic methodology to advance the experimental production of large-area TMD films.

**3.1.1. Precursor Feeding.** The selection of appropriate precursors is the initial step in designing a vapor deposition reaction. More challenging than the synthesis of monoelemental 2D materials such as graphene, the vapor deposition of TMDs requires the efficient feeding of both chalcogen and metal precursors. A typical powder-based vapor deposition (or solid source CVD) of TMDs is illustrated in Figure 5a, where the multiheating-zone equipment is designed to simultaneously and independently evaporate the chalcogen and metal precursors. The generated mass flows at high temperatures are carried by inert gas and finally deposited onto the target substrate as monolayer TMD islands (Figure 5b).[357] For instance, in the case of $MoS_2$ vapor deposition using $MoO_3$ and sulfur powder as precursors, this solid phase chemical reaction can be described as

$$2MoO_3 + 7S \rightarrow 2MoS_2 + 3SO_2$$

The chalcogen source of sulfur melts at around 120 °C and creates an acceptable vapor pressure of ∼10 Pa.[358] In contrast, the vapor pressure is only $\sim 10^{-2}$ Pa for $MoO_3$ at 900 °C (note that $MoO_3$ is used as the metal source instead of pure Mo to increase the pressure of evaporated Mo precursor). This significant difference between chalcogen and transition metal precursors further complicates the synthesis process of $MoS_2$. Consequently, two critical aspects should be addressed for the precise synthesis of TMDs: (i) creating an active and steady mass flow to guarantee effective nucleation and uniform deposition, and (ii) tuning the concentration of as-fed chalcogen and metal precursors over a large range to modulate the TMD growth manner.

During the CVD growth process, upstream chalcogen powders or pellets can instantaneously generate sufficient gaseous sulfur molecules (mainly $S_8$ or smaller pyrolytic molecules) once the temperature is elevated. Therefore, the primary challenge for chalcogen precursors lies in improving their controllability to achieve a reliable and continuous feedstock flow. Wu et al. addressed this issue by premelting powder-form S precursors and subsequently resolidifying them into pellets to stabilize the sulfur concentrations during growth.[359,360] This approach notably suppressed defect densities (particularly chalcogen vacancies) to an ultralow level in both interior and edge regions of the TMD domains. In addition to the commonly used elemental chalcogen sources, diluted gaseous chalcogen hydride[361,362] ($H_2S$, $H_2Se$) and ethyl[26] ($(C_2H_5)_2S$, $(C_2H_5)_2Se$) are also widely utilized in CVD (Figure 5c) particularly MOCVD for synthesizing large-area TMD film due to their excellent diffusivity. The concentrations of these sources can be precisely modulated by controlling the partial pressure of reactants. Feng et al. bubbled liquid thiol ($C_{12}H_{25}SH$) into the CVD chamber, facilitating in situ healing of chalcogen defect and improving the crystalline quality.[363]

Furthermore, thermally stable chalcogen compounds offer an alternative avenue to match well with the vaporization of metal sources. Chalcogen salts like $Na_2SO_4$, $Na_2SeO_3$, and $Na_2TeO_3$, which melt around 700 °C, can effectively participate in synthesis while reducing the formation energies of TMDs.[364,365] Zuo et al. reported that high-melting-point metal sulfide crystals (ZnS, ZnSe, and ZnTe, Figure 5d) can release active chalcogen monomers by thermally breaking the dangling bonds on the bulk surface, significantly facilitating the robust growth of wafer-scale TMDs with excellent optical and electrical characteristics.[366] The slowly released chalcogen monomer is more active than dimers, making it more feasible to diffuse on the 2D surface and quickly heal the chalcogen vacancy, which accounts for the high crystallinity.

Distinguishing from the behavior of the chalcogen source, metal precursors often exhibit low volatility, and are difficult to support a sufficient mass flow. The commonly used metal oxides (such as $MoO_3$, $WO_3$ pellets, or mildly oxidized metal foil) undergo decomposition at significantly lower temperatures compared to pure metal precursors.[367] To further enable a robust and mild-condition synthesis, the halide salts (NaCl, KI) are frequently introduced to assist with the reaction. These molten salts react with metal oxides and form highly volatile metal oxychlorides, meanwhile yielding the active molten $Na_xMoO_y$ to further promote the reaction (Figure 5e). Benefiting from the assistance of halide salt, Zhou et al. have successfully synthesized up to 32 types of binary TMDs, notably expanding the library of 2D materials attainable via vapor phase deposition.[368] To access a controllable metal


https://doi.org/10.1021/acs.chemrev.3c00851
Chem. Rev. XXXX, XXX, XXX−XXX

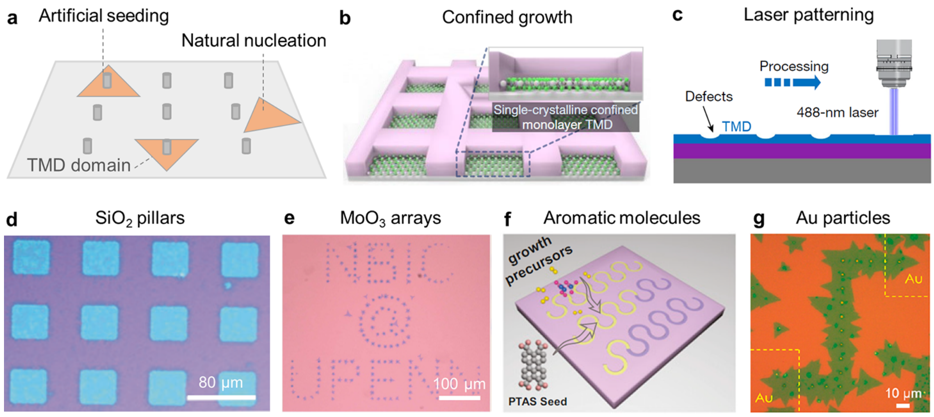


**Figure 6.** Surface nucleation control strategies for the vapor deposition of TMDs. (a) Schematic illustration of the natural and artificial seeding behaviors of TMDs. (b) Confined growth of single-crystalline TMDs by nucleating at selective areas via patterning $SiO_2$ masks. Reprinted with permission from ref 398. Copyright 2023 Springer Nature. (c) Laser-patterning of $WSe_2$ layers to create defect arrays for the selective growth of 2D $VSe_2$ crystals. Reprinted with permission from ref 399. Copyright 2020 Springer Nature. (d) Nucleation of $MoS_2$ facilitated by the patterned rectangular pillars on $SiO_2$/Si. Reprinted with permission from ref 395. Copyright 2013 Springer Nature. (e) Optical image of isolated $MoS_2$ flakes grown at specific locations by a patterned Mo source. Reprinted with permission from ref 404. Copyright 2015 Springer Nature. (f) Direct growth of $MoS_2$ nanostructures via seed-promoted growth and substrate engineering. Reprinted with permission from ref 409. Copyright 2019 National Academy of Sciences. (g) Optical image of Au-seeded growth of $MoS_2$ monolayers used as the transistor channel. Reprinted with permission from ref 410. Copyright 2018 American Chemical Society.

source feeding, a physical buffer layer can be placed between the precursor and substrate to stabilize the mass flow.[369−371] Another strategy is the dissolution of metal precursors in the target substrates such as Au and molten glass, and the source uniformly diffuses to the surface during high-temperature growth.[372−376]

To avoid complications arising from the sensitive precursor vaporizing process, Zhang et al. developed a flux-assisted growth strategy where precursors/cosolvents were eutectic and 2D growth within the confinement of mica.[377] This innovative approach led to the successful synthesis of 48 ternary or quaternary compounds and 23 nonlayered structures. Moreover, molten salts such as $Na_2MoO_4$[378] and $Na_2WO_4$ can be directly utilized as metal precursors for TMDs growth via a vapor−liquid−solid (VLS) mechanism[379] (Figure 5f). Gaseous metal carbonyls ($Mo(CO)_6$)[380] and volatile carbon-free halide compounds (e.g., $MoCl_5$,[381] $MoOCl_4$,[382] and $WF_6$[383]) are also suitable metal precursors to address the challenges in diffusivity while providing a controllable mass flow. However, it is essential to fully consider the toxicity and corrosivity aspects of these feedstock species.

The precursors both contain chalcogen and metal elementals, such as $MoS_2$ and $WS_2$ powders are commonly used in CVT and PVD experiments.[20,384−387] These thermally stable sources necessitate a considerably higher evaporation temperature, often requiring the addition of transport agents such as halide salt to address this problem. Moreover, these precursors enable the precisely controlled reverse flow strategies, contributing to the efficient fabrication of high-quality TMDs and their heterostructures.[388,389] Additionally, thermally decomposing salts such as $Na_2MoS_4$, $K_2MoS_4$, $K_2WS_4$, and $(NH_4)_2MoS_4$[390−393] can straightforwardly synthesize TMDs at a lower temperature and enable mass production, which will be further discussed in Section 3.2.1.

By now, a comprehensive precursor library and corresponding growth strategies have been developed to satisfy tailored TMDs synthesis requirements. Both chalcogen and metal precursors could be appropriately selected to strike a balance between crucial parameters like reactant concertation, diffusion uniformity, and operation convenience. This selection forms the foundation for designing subsequent kinetic and thermodynamic processes, encompassing surface nucleation, lateral growth, and more. Meanwhile, the quality of as-grown TMDs closely related to the purity, activity, and uniformity of precursors, constituting a key topic that should be further explored.

**3.1.2. Surface Nucleation.** Once the vaporized precursors diffuse to the deposition region, they are frequently absorbed onto the target substrate and aggregated into nuclei, acting as the "seeds" for the initial growth stage. Nucleation is well-known to occur naturally or artificially at sites with high surface energy, such as steps, kinks, defects, scratches, and nanoparticles on substrates (Figure 6a). This process is of great importance in controlling the uniformity, crystallinity, and grain size of the resulting TMD films. Besides, the controlled nucleation at selective locations leads to designed single-crystal TMD patterns without involving lithography and etching process, which facilitates the high-throughput device fabrications. In this section, we primarily focus on the basic concept and the control of the nucleation process during TMD deposition.

The edge formation energies of TMD materials are much lower than other 2D counterparts such as graphene and hBN, with even growth no catalysts. As a result, the random-orientated, small-sized, high-density, and discontinuous samples further complicated the surface nucleation engineering. During the vapor deposition of TMDs, the nucleation behaviors are sensitively related to metal source concentration and the diffusivity of Mo atoms on the edge site of $MoS_2$ being extremely slower than S atoms ($\sim 10^8$ times the difference in diffusion coefficients calculated at 1000 K).[394] Thus, growth parameters that affect the absorption, diffusion, and desorption of metal feedstocks can collectively influence the nucleation density of TMDs. For instance, to avoid the influence of Mo atoms diffusion caused by dust particles, Van der Zande et al. emphasized the importance of ultraclean substrates and fresh precursors, yielding low-density nucleation and large-area crystal growth.[357] As shown in Figure 6d, Najmaei et al.

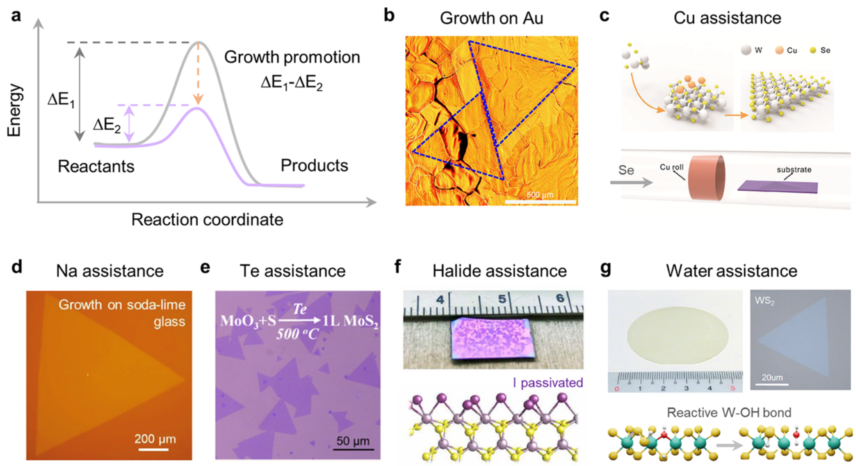


**Figure 7.** Growth promotion strategies for the vapor deposition of TMDs. (a) Schematic illustration of the energy profile for the lateral growth of TMDs. (b) As-grown millimeter-sized triangular monolayer $WS_2$ domains on the Au foil. Reprinted with permission from ref 417. Copyright 2015 Springer Nature. (c)Schematic illustration and setup of the Cu-assisted self-limited growth of monolayer $WSe_2$. Reprinted with permission from ref 421. Copyright 2016 Wiley-VCH GmbH. (d) Millimeter-size monolayer $MoSe_2$ single-crystal domain growth on Na-containing soda-lime glass substrate. Reprinted with permission from ref 430. Copyright 2021 Wiley-VCH GmbH. (e) Tellurium-assisted low-temperature synthesis of $MoS_2$ on $SiO_2$/Si substrate. Reprinted with permission from ref 439. Copyright 2015 American Chemical Society. (f) Halide-enabled growth of millimeter-sized $MoS_2$ domains on $SiO_2$/Si substrate (top panel) and schematic illustration of the Mo-zigzag edge passivated by iodine atoms (bottom panel). Reprinted with permission from ref 431. Copyright 2021 AAAS. (g) Hydroxide vapor phase deposition of low defect density $WS_2$ monolayers (top panel) and schematic illustration of the presence of W−OH bonds during the growth (bottom panel). Reprinted with permission from ref 437. Copyright 2022 Springer Nature.

designed rectangular ∼40 nm thick $SiO_2$ pillars to assist the self-seeding of $MoS_2$ and obtained large-area continuous films.[395] Generally, a lower metal mass flow could efficiently suppress the nucleation density and provide more leave space for large domain expansion. Besides, nucleation density decreases exponentially with substrate temperature due to thermally activated processes. The ultralow nucleation density (several per $mm^2$) provides a road toward large-area single crystals, which will be further discussed in Section 4.1.

For the nucleation morphology, the center of TMDs sometimes begins with the Mo-contained nanoparticles, referring to a "self-seeding" nucleus accommodating absorbed or diffused feedstocks. Cain et al. carefully explored the nucleus centers of CVD-$MoS_2$ samples and identified them as the suboxide $MoO_{3-x}$ with a fullerene-like core−shell structure.[396] In this regard, a lower reactant concentration on the substrate results in a planar nucleation and growth behavior without the central nanoparticle.[397]

The sensitive nature of TMDs nucleation provides opportunities for precise control of this process, including substrate modulation and introduction of foreign promoters. Recently, Kim et al. programmed the substrate into arrays with nucleation energy differences by patterning the $SiO_2$ mask and confined the single nucleus within the target region (Figure 6b), yielding single-domain arrays with high electrical performance and reliably avoiding dealing with undesired grain boundaries.[398] This nonepitaxial strategy is compatible with arbitrary substrates that can provide single-crystal channels in a large wafer size. As shown in Figure 6c, Li et al. created local defects at $WSe_2$ layers by focused laser irradiation, which served as a specific nucleation position for the deposition of periodic top-layer metallic TMDs (such as $VS_2$ and $VSe_2$).[399] The as-grown scalable heterostructure arrays exhibited excellent device performance and yield due to the atomically clean vdW contact. Furthermore, patterned dispersion of metal precursors ($MoO_3$ arrays,[400] $Na_2MoO_4$ particles,[379] $WO_3$/NaCl mixture,[401] W pads,[402,403] and so on) leads to localized high-concentration metal sources that encourage nucleation at these defined locations. Han et al. patterned Mo source using conventional lithographic methods and controlled prepared highly crystalline $MoS_2$ with predefined positions (Figure 6e).[404] Innovatively, source and drain metals based on tungsten could directly serve as seeds for the growth of channel TMDs, Cheng et al. demonstrated the selective growth of $WS_2$ that fills the 40 nm channel between patterned W electrode pads, which keep good short-channel characteristics with high on/off ratios.[405]

Additionally, seeding promoters can artificially facilitate the nucleation process to obtain high-quality crystal growth.[406,407] Substrate treatment with aromatic molecules such as perylene-3,4,9,10-tetracarboxylic acid tetrapotassium salt (PTAS), 3,4,9,10-perylene-tetracarboxylic acid dianhydride (PTCDA), or reduced graphene oxide (r-GO) significantly facilities the growth of large-area TMDs crystals at lower deposition temperature.[408] Notably, inorganic particles exhibit poor performance in nucleation promotion. The discovery of artificial nucleation behaviors then enables spatial-selective nucleation designing. Guo et al. enhanced hydrophilicity through the area-selectively plasma-treated substrate (Figure 6f), and then the hydrophilic PTAS promoted nucleation within the plasma-treated patterns.[409] Similarly, properly sized artificial metal structures (such as Au dots and Au rods) can govern nucleation due to favorable formation energy of $MoS_2$ on the Au surface, therefore the nucleus first occurred at metal structures before 2D growth commenced (Figure 6g).[410−413]

To summarize, as the initial stage of TMDs material growth, surface nucleation behavior has attracted extensive attention in mechanism exploration and material designing. Achieving robust nucleation with precise control over density, positions, and orientations is the prerequisite for further growth promotion toward high-quality TMDs film. More importantly, the nucleation process provides a window to regulate


https://doi.org/10.1021/acs.chemrev.3c00851
Chem. Rev. XXXX, XXX, XXX−XXX

crystalline orientations, which is the most critical topic in preparing wafer-scale single-crystal TMDs and will be systematically discussed in Section 4.2.

**3.1.3. Growth Promotion.** From the perspective of the kinetics in TMD growth, the reaction rate is determined by the transition state theory. As shown in Figure 7a, reactants must first overcome an energy barrier to reach an intermediate state at the peak of the energy profile, and finally convert to products. Therefore, it is essential to evaluate the energy barriers that govern serial critical steps during TMDs growth, including precursor decomposition, feedstock diffusion and adatom attachment. A relatively flat energy profile (illustrated by the violet line) is more favorable to promote the transitions through intermediate states and facilitate the growth process. To achieve this, various strategies such as utilizing specific substrates and introducing additives have been developed to substantially lower the energy barriers. By reducing the barrier from $\Delta E_1$ to $\Delta E_2$, the reaction rate can increase exponentially following the relation of $\exp(\Delta E_1 - \Delta E_2/k_B T)$, where $k_B$ denotes the Boltzmann constant and $T$ is the temperature. Such a fast growth rate enables the rapid and robust preparation of large-sized TMD domains or high-coverage film.

In general, appropriately elevating the growth temperature can improve the growth rate by ensuring sufficient precursor feeding and enhancing the surface migration rate, which is a customary and systematically studied parameter for tuning the growth manner.[414] Zhang et al. employed the reverse flow reactor and demonstrated the up to 45 $\mu$m/s growth rate of $WS_2$ reaching an ultrahigh growth temperature ($T$ = 1300 °C).[388] Benefiting from the advanced growth strategies and characterizations, the temperature-modulated ultrafast growth record has been updated from several micrometers per minute to exceeding 100 $\mu$m/s.[415] Substrate engineering can also reduce the surface diffusion barrier and improve the overall growth rate. For example, the molten glass substrate (melting above 750 °C), provides an atomically smooth surface and efficiently improves the feedstock migration coefficient and growth rate.[416]

Metal catalysts are widely employed in low-dimensional growth of materials such as graphene, hBN, and carbon nanotubes, which also work efficiently in the TMDs growth. Au substrates facilitate the self-limited catalytic surface growth and enable a millimeter-size $WS_2$ domain growth (Figure 7b).[417] It is also suggested that the low energy barriers and exothermic nature of W and Se diffusion and attachment on the edges of $WSe_2$ on the Au substrate contributed to the rapid growth process.[418] Besides, nickel particles show a powerful catalyzing effect that enables the rapid decomposition of intermediate $MoS_6$ to $MoS_2$, which is a critical step with a high energy barrier and limits the overall growth rate.[419,420] Liu et al. introduced Cu into the CVD growth system, where the Cu atoms could adsorb at the $WSe_2$ surface and facilitate the self-limited monolayer growth (Figure 7c).[421] Then the W atoms preferred to bond with active edges resulting in an ultrafast lateral growth rate.

Various salts have been harnessed to efficiently promote the synthesis process with their mechanisms broadly falling into two categories: (i) assisting the volatilization/diffusion of metal feedstocks and (ii) decreasing the reaction barrier through the catalytic effect. It is worth mentioning that these additives often perform a complex synergy of the above beneficial effects. For example, halide salts (such as NaCl, KI, and so on) are widely used in decreasing the melting point of metal precursors discussed above sections; meanwhile, the alkali component (Na, K) serves as an intermediate catalyst and reduces the reaction energy barrier.[422−429] Zhang et al. adopted Na-containing soda-lime glass as the substrate (Figure 7d) and revealed that the incorporation of Na decreased the highest nucleation energy barrier.[430] In addition, halide atoms (I, Cl, Br) also passivate the edges of the TMD domain and modify the growth dynamics (Figure 7f).[431] The reaction energy barriers are linearly correlated to the dissociation energies of Mo−halogen bonds, and the utilization of KI enables fast growth of ultralarge single crystal $MoS_2$ domain. Moreover, Wu et al. found that heated additive KI can release $I_2$ (widely used in CVT synthesis), acting as a transport agent and carrying metal feedstocks to the target substrate.[432] Similarly, fluorine released from a high-temperature $BaF_2$ plate efficiently facilitates the rapid vaporizing of metal precursor and spontaneously facilitates intermediate formation for large-area $WS_2$ growth.[433] Overall, the growth promotion benefiting from halide salts lies in a complex mechanism deserving detailed exploration.

Diluted hydrogen is a commonly used gaseous additive to create a reduced atmosphere during TMDs growth, especially selenide species sometimes definitely require the assistance of $H_2$.[434−436] As shown in Figure 7g, Wan et al. introduced the $H_2O$ vapor to the CVD chamber reacted with the high-purity metal tungsten foil, and generated the intermediate $WO_2(OH)_2$.[437] Simulations indicated the hydroxide W−OH bonds exhibited lower dissociation energy than the W−O bonds in conventionally used $WO_3$ precursor. Which facilitated the sulfidation process and enabled the preparation of wafer-scale low-defect-density $WS_2$. Similarly, Sassi et al. demonstrated that moisture promoted the defect formation in precursors and enabled a low-temperature growth of $WSe_2$.[438] Elemental additives such as tellurium powders, when mixed with metal precursors can produce a Te-containing intermediate phase and enable a low-temperature synthesis (Figure 7e).[439]

Benefiting from the efforts in exploring the growth promotion of TMDs, robust and fast lateral growth has been steadily realized while permitting synthesis under much milder conditions. This progress not only elucidates the intricate growth mechanism but also encourages the development of fabrication techniques better suited to market demands and industrialization.

## 3.2. Growth Strategies of Large-Area TMD Films

Drawing insights from the successes of commercially established semiconductors such as silicon, gallium arsenide (GaAs), and gallium nitride (GaN), the efficient production of large-area single-crystal stands as the cornerstone of the semiconductor industrial manufacturing processes. For the emergent 2D semiconductors, the uniform film size should be scaled up step by step from micrometer-sized isolated islands to inch-sized standard wafers. Because large-area TMDs wafers meet industry standards can facilitate seamless integration into full-scale manufacturing processes alongside silicon techniques. Furthermore, an expansive operational area within a single-piece TMDs wafer enables the incorporation of complex circuits and a significant increase in device yield per production cycle, leading to cost-saving production. Aiming toward this goal, a number of strategies have been developed to improve the uniform area of the prepared TMD films. In this section, the large-area TMD growth strategies are divided into four


https://doi.org/10.1021/acs.chemrev.3c00851
Chem. Rev. XXXX, XXX, XXX−XXX

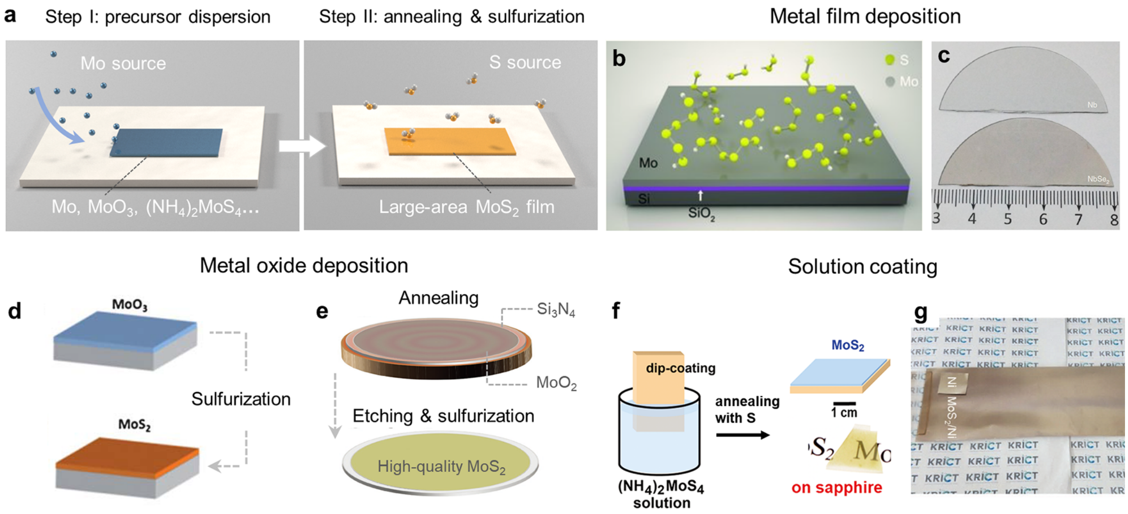


**Figure 8.** Two-step growth of large-area TMD films. (a) Schematic illustration of the two-step processes of fabrication TMD films. Step I: transition metal precursors such as Mo, $MoO_3$, or $(NH_4)_2MoS_4$ are dispersed on a large-area substrate. Step II: the predeposited precursors are annealed and sulfurized into large-area TMD films. (b) Large-area fabrication of $MoS_2$ by sulfurizing predeposited Mo thin film on the $SiO_2$/Si substrate. Reprinted with permission from ref 442. Copyright 2012 Wiley-VCH GmbH. (c) As-deposited Nb film and selenization-prepared $NbSe_2$ film on 2-in. sapphire substrates. Reprinted with permission from ref 253. Copyright 2019 Springer Nature. (d) Synthesis of $MoS_2$ layers by sulfurizing thermally evaporated $MoO_3$. Reprinted with permission from ref 443. Copyright 2012 Royal Society of Chemistry. (e) Synthesis of highly crystalline $MoS_2$ films converted from capping layer annealing process-treated $MoO_2$ films. Reprinted with permission from ref 456. Copyright 2020 Wiley-VCH GmbH. (f) Schematic illustration of the fabrication process of $MoS_2$ thin layers by thermolysis of $(NH_4)_2MoS_4$ precursor. Reprinted with permission from ref 390. Copyright 2012 American Chemical Society. (g) Roll-to-roll prepared $MoS_2$ film on the Ni substrate by thermal decomposition of $(NH_4)_2MoS_4$. Reprinted with permission from ref 391. Copyright 2018 Wiley-VCH GmbH.

types according to the supply manner of metal source, that is, two-step, "point-to-face", "face-to-face", and vapor phase strategies. Each of these strategies plays an important role in improving the size of TMD films satisfying industrial requirements.

**3.2.1. Two-Step Strategy.** As discussed previously, the key to synthesizing large-area TMD films lies in the homogeneous supply of metal precursors. A direct and effective strategy is depositing a uniform metal-containing precursor film via established techniques such as spin coating, sputtering, thermal/e-beam evaporating, PLD, and ALD.[440,441] Then followed by a high-temperature sulfurization process as illustrated in Figure 8a. This proposed two-step strategy clearly offers advantages in terms of robust and scalable fabrication of large-area TMDs films on a range of substrates, making it particularly favorable for cost-effective production. Nevertheless, the limited material quality restricted their potential for high-performance applications in electronics and optoelectronics. Therefore, the main challenges of the two-step strategy lie in two perspectives: (i) acquiring a continuous TMDs film with controlled thickness, especially monolayer and (ii) improving the crystallinity.

In 2012, Zhan et al. pioneered the scalable fabrication of TMDs by depositing a Mo thin layer on the Si/$SiO_2$ substrate and sulfurizing it into a large-area crystalline $MoS_2$ film.[442] It also resulted in introducing critical defects that decayed the mobility of the films (Figure 8b). At the same stage, Lin et al. alternatively thermally deposited $MoO_3$ and achieved a uniform 2-in. wafer-scale $MoS_2$ film through sulfurization (Figure 8d).[443] Subsequent studies have explored in improving the thickness control of $MoS_2$ layers by employing various deposition techniques. Lee et al. e-beam evaporated $MoO_3$ layer at a low rate of less than 0.1 Å/s, enabling the creation of controllably fabricating $MoS_2$ films ranging from 2 to 12 layers.[444] The ALD could efficiently govern the precursor thickness by adjusting the process cycles, yielding uniform $MoS_2$ films with the desired number of layers.[445] Moreover, the sulfurization process of $MoO_2$ microcrystals can be modulated to favor a layer-by-layer growth of $MoS_2$ films.[446] The addition of halide salts such as NaCl can further assist with the layer number control process in a two-step strategy. Versatile assembly of deposited metal precursors also provides freedom in patterned growth of diverse TMDs materials and corresponding heterostructures/alloys.[254,447−452]

The bottleneck of the two-step strategy lies in limited quality of the obtained TMD films. Generally, a high sulfurization temperature and a precisely controlled S vapor flow can lead to a high-quality $MoS_2$ film ensuring the sufficient reaction.[453,454] The presence of oxygen in the metal precursor is also crucial for the crystallinity of the TMD films. As shown in Figure 8c, Lin et al. prepared the Nb film in $H_2O$/$O_2$-free conditions and then converted it into high-quality $NbSe_2$ layers, which not only exhibited excellent superconductivity but also remained stable under harsh treatments.[253] Additionally, the pretreatment of precursor layers also can efficiently improve the quality of two-step grown film. For example, Tai et al. preannealed the Mo foil at 1400 °C to smooth the surface and enlarge the grain size, the finally obtained continuous $MoS_2$ film could be easily transferred by etching the Mo foil using $FeCl_3$ solution.[455] Besides, Xu et al. capped a $Si_3N_4$ layer on the deposited $MoO_2$ (>5 nm due to the thermal stability, Figure 8e) and preannealed the system at 900 °C.[456] This recrystallization process could efficiently improve the quality of precursors, therefore the sulfurized $MoS_2$ films exhibited improved electrical performance. The epitaxy $MoO_2$ with a defined crystalline orientation could show "heredity" in the converted $MoS_2$ film, suggesting the potential of synthesizing single-crystalline TMDs on various substrates.[457,458]

An alternative within the two-step strategy involves utilizing the liquid precursor solutions to fabricate large-area TMD

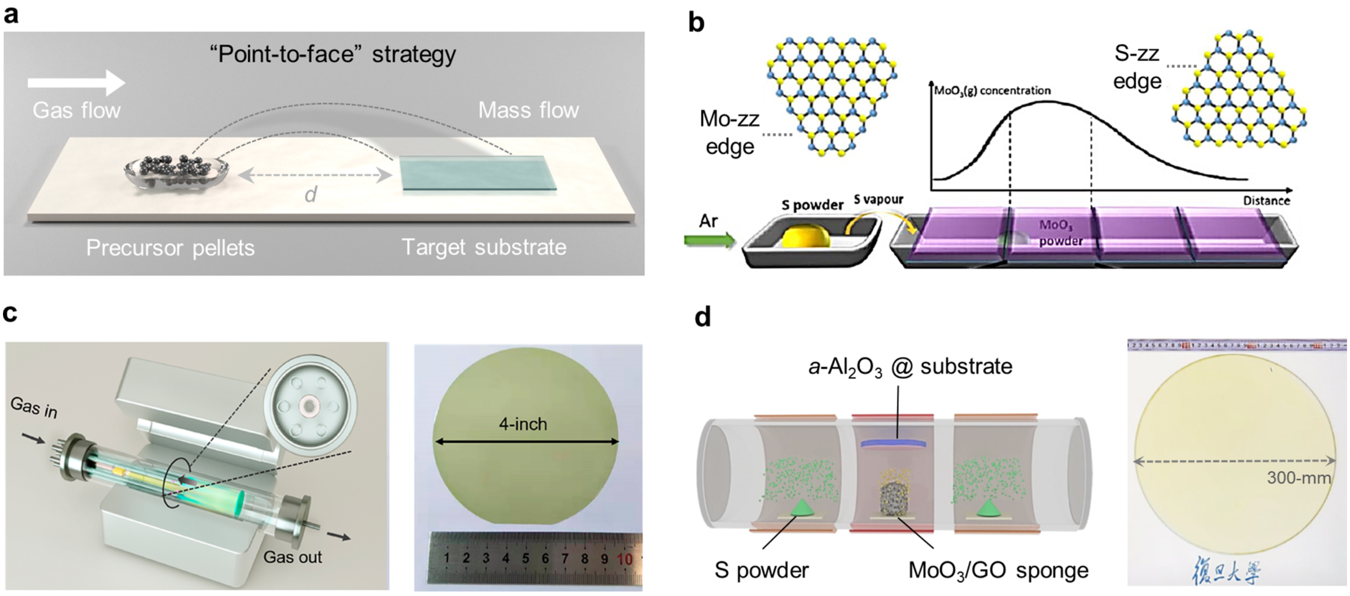


**Figure 9.** Point-to-face fabrication of large-area TMD films. (a) Schematic illustration of the precursor feeding configuration utilizing a "point-to-face" strategy. (b) Study of the shape evolution of monolayer $MoS_2$ crystals by the $MoO_3$ diffusion concentration gradient. Reprinted with permission from ref 478. Copyright 2014 American Chemical Society. (c) Multisource CVD setup and the 4-in. monolayer $MoS_2$ film prepared on a sapphire substrate. Reprinted with permission from ref 25. Copyright 2020 American Chemical Society. (d) Fabrication of 300 mm monolayer $MoS_2$ film on amorphous-$Al_2O_3$/Si substrate. Reprinted with permission from ref 32. Copyright 2023 Springer Nature.

materials.[459] Liu et al. dip-coated the substrate with a $(NH_4)MoS_4$ layer and annealing it at high-temperature.[390] The thermolysis of precursor yielded a crystalline $MoS_2$ film and the quality could be further improved with S vapor presence (Figure 8f). This mild thermolysis reaction avoids the high-temperature sulfurization processes and diversifies the available substrates such as plastic plates and metal foils.[460,461] For example, Lim et al. coated the $(NH_4)MoS_4$ solution on Ni foil and followed with a roll-to-roll thermal decomposition. This process produced a 50 cm length of $MoS_2$ layers that demonstrated applicable catalytic activity(Figure 8g).[391] Similarly, Baidoo et al. coated liquid transition metal precursors on rollable oxide Al foils and sulfurized them by ammonium sulfide, achieving a 14-in. sized $SnS_2/ReS_2/MoS_2$ heterostructure.[462] While the liquid precursor coating and converting process may limit the quality of TMD materials compared to vapor-deposited methods, its scalability and operation convenience makes it a promising option for direct patterning growth and mass production of TMDs.[464,465]

**3.2.2. "Point-to-face" Strategy.** The point-to-face strategy is the most used method in vapor depositing large-area TMD materials, which starts with solid metal and chalcogen precursors (either in powder or pellet form) positioned upstream or under the target substrates, as shown in Figure 9a. As previously discussed, in this strategy, metal and chalcogen precursors could be spatially separated, which are individually heated due to their differences in vaporizing temperature. Additionally, the substrate could also be ramped to a specific temperature to control the growth manner of TMDs. Consequently, the point-to-face strategy typically requires a multiheating-zone CVD furnace (sometimes using a heating belt to vaporize the sulfur source) to meet these varying temperature requirements. Independently control over each growth parameters allows for more freedom in tuning of crystalline orientation, domain size, crystal morphology, coverage ratio, defect density and so on. Owing to its superior controllability, this strategy is lab-preferred and efficiently advances the development of TMDs synthesized via bottom-up approaches. While the mechanism of the point-to-face strategy has been discussed above, this section will mainly focus on recent improvements aimed at synthesizing larger-area TMD films.

The operation convenience of the point-to-face strategy has made it a pioneering choice in vapor depositing large-area monolayer TMDs. In 2012, Lee et al. demonstrated the growth of $MoS_2$ by loading the $MoO_3$ powder in a ceramic boat and mounting it with $SiO_2$/Si substrates, where a separate sulfur powder served as the chalcogen source upstream.[19] This setup enabled the formation of star-shaped $MoS_2$ domains on the substrate, which eventually merged into a large-area monolayer film with sizes of several millimeters. This pioneering work established a framework for using CVD to prepare various large-area TMDs, including $MoS_2$, $MoSe_2$, $WS_2$, $WSe_2$, $MoTe_2$, $WTe_2$, and so on.[466−473] To further improve the controllability, the sulfur precursor, metal precursor, and substrate were decoupled to separate spatial positions.[474−476] Yu et al. further refined this method by employing independent carrier gas pathways for $MoO_3$ and S sources, including a small amount of oxygen into the $MoO_3$ pathway to prevent premature sulfurization during growth.[477] This improvement enabled the epitaxial growth of a 2-in. monolayer $MoS_2$ film on a c-plane sapphire substrate with highly orientated domain distribution. The limited diffusion ability of metal precursors leads to a sharp variation in feedstock concentration spatially, thus altering the precursor ratio with distance from the point-like sources. This feature has inspired a deeper understanding of TMD growth behaviors concerning precursor ratios. For instance, Wang et al. studied the shape evolution of monolayer $MoS_2$ with Mo/S ratio, observing a transition from S-zigzag to the Mo-zigzag termination while tuning the Mo/S ratio from 1:>2 to 1:<2, as illustrated in Figure 9b.[478,479] Nevertheless,

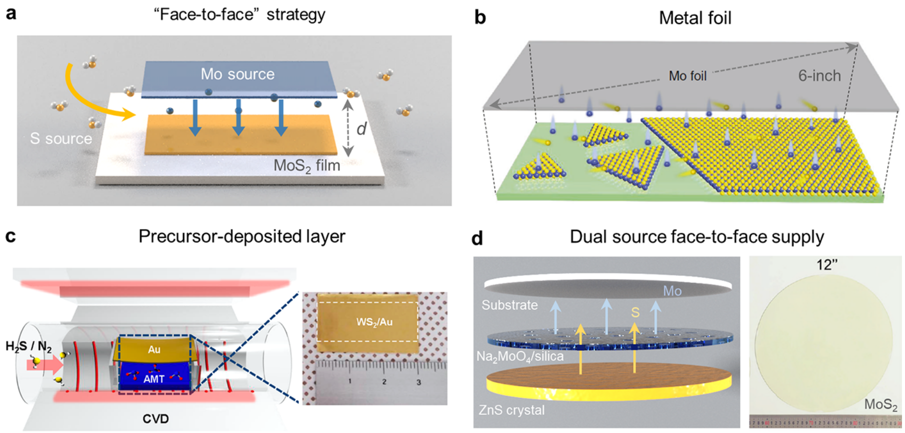


**Figure 10.** Fabrication of large-area TMD films by face-to-face strategy. (a) Schematic illustration of the face-to-face supplement of Mo source for the large-area growth of $MoS_2$ film. (b) Fabrication of the 6-in. $MoS_2$ film on soda-lime glass substrate by face-to-face precursor supply with metal foil. Reprinted with permission from ref 422. Copyright 2018 Springer Nature. (c) Growth of centimeter-scale monolayer $WS_2$ film on Au foil face down to a precursor plate with ammonium metatungstate (AMT). Reprinted with permission from ref 496. Copyright 2015 American Chemical Society. (d) Fabrication of 12-in. $MoS_2$ film by both face-to-face supplement of metal and chalcogen precursors. Reprinted with permission from ref 31. Copyright 2023 Elsevier.

supplying precursors in such a point-like manner presents a significant challenge in further enlarging TMD films.

To overcome the challenge related to material size, plenty of modified point-to-face methods have been developed to ensure a more uniform distribution of metal mass flow. One such modification involves placing the substrate vertically relative to the gas flow, which helps avoid the sharp concentration gradient typically seen in the horizontal direction.[480−482] As shown in Figure 9c, Wang et al. employed a multisource design in the traditional CVD setup.[25] This design featured six independent mini-tubes, each containing the same amount of $MoO_3$ precursors, to deliver feedstocks uniformly and establish a uniform Mo concentration across the cross-section of mass flow. A 4-in. sapphire substrate placed vertically and subjected to precisely controlled growth parameters facilitated the epitaxy of a high-uniform $MoS_2$ monolayer with superior electrical performance. Recently, Yu et al. optimized this configuration as a designed vertical CVD system, which enabled the epitaxial growth of 8-in. $MoS_2$ wafers with excellent uniformity.[483] This modified point-to-face method also demonstrates its versatility in preparing 4-in. monolayer $MoSe_2$ wafers.[484] Yang et al. also designed a showerhead configuration to facilitate the uniform supply of Mo precursors, which is similar to the face-to-face strategy discussed in the following section.[485] In addition to creating more "points" to guarantee large-area uniformity, He et al. introduced a localized supply of Mo precursor via a small-diameter nozzle, and moved the sapphire substrates under the downward-diffusing feedstock.[486] This technique enabled the fabrication of 2-in. continuous $MoS_2$ film, with thickness control achieved by adjusting the number of moving cycles. In another advancement shown in Figure 9d, Xia et al. improved the spatial homogeneity of both chalcogen and metal precursors, successfully fabricating a monolayer $MoS_2$ film up to 12 in. in diameter.[32] Wherein the Mo source was effectively controlled by encapsulating $MoO_3$ in the porous graphene oxide (GO) sponge, and two sulfur sources were arranged symmetrically at the center $MoO_3$ source. This setup ensured a uniform Mo and S precursor distribution across a 300 mm amorphous $Al_2O_3$/Si substrate.

In summary, the widely used point-to-face strategy produces electronics-grade large-area TMDs films due to their excellent controllability and equipment accessibility. Through innovative modifications to the growth system, the size of TMD wafers produced has expanded to inches. However, the efficiency of the point-to-face fabrication process still falls short of meeting the demands of TMD material industrialization. Therefore, enhancing the high-throughput capabilities of this method remains an area in need of further exploration.

#### 3.2.3. "Face-to-Face" Strategy.

To achieve a more uniform distribution of precursor concentrations, a face-to-face strategy has been developed for the fabrication of large-area TMDs. This growth system involves positioning a target substrate and a similarly sized source plate in a face-to-face arrangement as is illustrated in Figure 10a. This setup allows for a uniform mass transfer of precursors, especially nonvolatile metal feedstocks, providing a uniform concentration profile at the substrate surface. Due to the efficient precursor feeding capability, this face-to-face strategy is especially advantageous for preparing inch-sized TMD films. Moreover, this arrangement not only conserves space within the furnace but also significantly increases the yield of TMD materials per batch, thereby facilitating efficient mass production.[487] As a compromise, the bonded substrate and precursors have to be exposed to the same temperature, resulting in a loss of flexibility to independently modulate their heating profiles. As a complement to the point-to-point strategy, the face-to-face approach primarily concentrates on producing large-area TMD films by creating a uniform large-area source and optimizing the source−substrate configuration.

The homogeneous metal foils are naturally suited as an ideal source in face-to-face strategy.[488,489] As shown in Figure 10b, Yang et al. bridged a Mo foil above the soda-lime glass substrate in a parallel geometry, employing oxygen as a carrier gas to facilitate precursor volatilization.[422] This face-to-face approach enabled the rapid growth of uniform monolayer 6 in. $MoS_2$ films in just 8 min. For comparison, employing a point-to-face feeding route on a similar-sized substrate revealed a distinct precursor concentration gradient during $MoS_2$ growth. To introduce flexibility in thickness control, Yang et al. utilized a halide salt-coated Mo foil in face-to-face growth. This

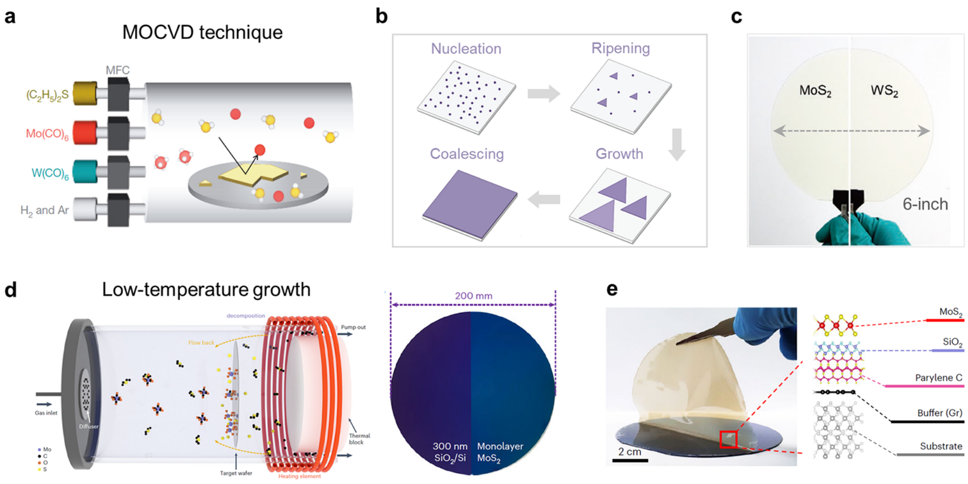


**Figure 11.** Fabrication of large-area TMDs based on vapor phase strategy. (a) Schematic illustration of a typical MOCVD setup. Reprinted with permission from ref 26. Copyright 2015 Springer Nature. (b) Diffusion-controlled MOCVD consists of controlled nucleation, ripening, and lateral growth processes. Reprinted with permission from ref 506. Copyright 2018 American Chemical Society. (c) Monolayer $MoS_2$ and $WS_2$ grown on 6-in. quartz substrates by pulsed MOCVD. Reprinted with permission from ref 507. Copyright 2020 Wiley-VCH GmbH. (d) Low-temperature MOCVD setup and the as-grown 300 mm $MoS_2$ monolayer on $SiO_2$/Si substrate. Reprinted with permission from ref 27. Copyright 2023 Springer Nature. (e) Low-temperature growth of a 4-in. $MoS_2$ film on the parylene C substrate. Reprinted with permission from ref 518. Copyright 2023 Springer Nature.

modification enabled the adjustment of the thickness of the 6-in. $MoS_2$ film from 1L to over 20L by changing NaCl promoter concentrations.[490] This face-to-face configuration requires close proximity between the source and substrate to ensure a uniform precursor concentration, often resulting in excessive feeding. This dilemma hinders the adjustment of the Mo/S ratio, which is known as a key parameter in TMDs epitaxy. An innovative solution involves inserting a carbon cloth as a buffer layer between the Mo foil and the target epitaxial sapphire substrate.[371] This design gently filtered the precursor and ensured a moderate concentration. Employing the face-to-face strategy, this setup facilitated the epitaxial growth of 7 pieces of uniform 2-in. single-crystal $MoS_2$ films on C/A sapphire in a single batch.

In addition to metal foils, predeposited precursor plates are also commonly used in the face-to-face strategy, allowing for finely controlled amounts of precursor.[491−495] In 2015, Yun et al. dropped the water-soluble ammonium metatungstate (AMT) on $Al_2O_3$ to serve as a large-area W source, facing an Au foil substrate.[496] The parallelly configurated system inserted with $H_2S$ gas reacted at high temperature to produce an over 6 $cm^2$ $WS_2$ film on the target Au substrate (Figure 10c). Such solution-processed precursors offer more freedom in source concentration design. Lee et al. dissolved $MoO_3$ powder in ammonium hydroxide and spin-coated the solution on $SiO_2$/Si for face-to-face $MoS_2$ synthesis.[497] They were able to precisely control low supersaturation levels by optimizing the solution concentration. As a result, parameters such as average nucleation density, crystal size, and $MoS_2$ coverage were systematically studied as a function of the amount of precursor. To further uniformly supply both chalcogen and metal sources, it is proposed to design a face-to-face supply of both chalcogen and metal precursors. Guo et al. employed $Na_2MoO_4$-containing perforated carbon nanotube film as a precursor plate, where Mo precursor was released from the solid part and S vapor passed through the hollow part, ensuring the uniform growth of $MoS_2$ monolayers.[498] Recently, Xue et al. developed an approach by packaging ZnS plate, $Na_2MoO_4$-coated perforated silica, and target substrate into a producing module.[31] These modules were then stacked as integrated arrays for batch production as shown in Figure 10d. The sufficient and uniform precursor feeding design enabled the fabrication of 3 pieces of 12-in. monolayer $MoS_2$ wafers in a single process cycle.

Overall, the face-to-face strategy developed from the point-to-face strategy has speeded up the transition of lab-scale sample preparation toward the downstream application of wafer-scale TMDs materials. The low-cost feature and acceptable material quality enable it as a candidate technique for 2D material manufacture. In the future, the expected fabrication based on the face-to-face strategy should balance the mass-producing capability and material crystallinity (lower vacancy density and grain-boundary density) to satisfy the high-end industrialization demand in next-generation electronics and optoelectronics.

#### 3.2.4. Vapor Phase Strategy.

The metal−organic compounds are widely known in the production of III−V semiconductor and oxide superconductor thin films. For the MOCVD growth of TMDs, volatile metal precursors efficiently address the issue of insufficient vapor pressure that is often occurred in metal oxide counterparts. For example, the hexacarbonyl compound $Mo(CO)_6$ can create a vapor pressure of 0.177 Torr at 25 °C, which is several orders of magnitude higher than $MoO_3$.[23] The excellent volatility of the precursors guarantees the high-throughput growth of TMD films with wafer-scale uniformity. The typical MOCVD setup as illustrated in Figure 11a includes $Mo(CO)_6$, $S(CH_2CH_3)_2$, accessory $H_2$, and inert carrier gas.[26] These components are injected into the growth chamber and modulated individually by mass flow controllers during the growth process. The partial pressure of every component can be precisely controlled and supply a wide chalcogen/metal ratio window up to $10^5$.[499] The TMD thin films prepared by the MOCVD technique were demonstrated earlier with limited control in crystallinity and thickness.[500] In 2015, Eichfeld et al. presented the fabrication of monolayer $WSe_2$ with precise control of growth parameters


https://doi.org/10.1021/acs.chemrev.3c00851
Chem. Rev. XXXX, XXX, XXX−XXX

in MOCVD.[22] Remarkably, Kang et al. successfully synthesized 4-in. $MoS_2$ and $WS_2$ films with excellent homogeneity and electrical performance.[26] The flexible control over precursor partial pressures facilitated a layer-by-layer growth model, ensuring complete coverage and uniform thickness. Recently, Kwon et al. fabricated the 200 mm polycrystalline $MoS_2$ wafer by MOCVD and demonstrated its compatibility with a commercial fabrication facility.[501] These milestones fully prove the vast potential for scalable 2D TMDs production via MOCVD. Meanwhile, several challenges have emerged as (i) the limited domain size requires further enlargement to improve the crystallinity and (ii) the carbon contamination that stems from precursors should be prevented or removed.

The typical grain size of TMD films prepared by MOCVD is ~100 nm, which is around two orders smaller than the power-based CVD counterparts. Parameters including optimizing growth temperature, metal/chalcogen ratio, $H_2$ concentration, chamber pressure, and the choice of substrate can tune the nucleation density and grain size in a large range.[502] Furthermore, the additives such as alkali-metal can be introduced to the MOCVD process to promote the lateral grain size.[503] Kim et al. demonstrated that pre-exposing the sapphire substrate to alkali metal halides (NaCl and KI) could suppress nucleation and dramatically increase the lateral island size to the order of 10 $\mu$m.[504] Although the alkali metal residuals were washed out after the transfer process, evidence suggests that the use of these additives disrupted the epitaxial relationship between the TMDs and sapphire due to interfacial alkali adatoms.[505] Benefiting from the excellent controllability of MOCVD, the nucleation and lateral growth stages can be decoupled, introducing a key ripening process to promote large grain formation. As shown in Figure 11b, Zhang et al. introduced a brief nucleation stage driven by a higher W flow rate, then turned off the W source and ripened the $WSe_2$ nucleus by annealing in the Se source, finally reintroduced a lower W flow to further promote the lateral growth.[506] The obtained fully covered $WSe_2$ film epitaxially oriented with respect to the sapphire substrate. Additionally, the pulsed injection of precursors with periodic interruption also drives a nucleation ripen process, which was employed for high-throughput production of $MoS_2$ and $WS_2$ wafers up to 6 in. (Figure 11c).[507] Further elevating the temperature during the ripening process can significantly increase the grain size to over 20 $\mu$m with high crystallinity.[508] Moreover, Cohen et al. designed a water vapor etching process during pulsed-MOCVD growth, which also suppressed the nucleation density and increased the average grain size.[509] These advancements in MOCVD fabrication of 2D TMDs preserve its advantages in terms of controllability and scalability while enhancing the quality of the prepared materials.

It is also suggested that an undesired carbon layer could be simultaneously formed at the interface of the substrate and as-grown TMDs during MOCVD.[510,511] This carbon contamination can limit the lateral growth of islands and hinder the coalescence process. In this regard, an appropriate concentration of $H_2$ or water flow can be employed to remove the carbonaceous species.[512] Alternatively, a carbon-free chalcogen precursor such as $H_2S$ also reduces the excessive carbon and elemental impurities and produces high-quality TMDs films.[499,513]

Importantly, the MOCVD techniques are suited for the low-temperature growth due to the utilized active and volatile reactants. Plenty of strategies have been developed to lower the MOCVD processing temperature to within the BEOL-compatible regime.[514−516] For instance, Park et al. preciously controlled the flow rate of organic precursors and synthesized high-quality $MoS_2$ crystals with domain sizes up the 120 $\mu$m at a temperature of 320 °C.[517] In recent studies, the precursor decomposition and target substrate regions have been decoupled, significantly reducing the growth temperature to much below the BEOL limit and enabling the use of various substrates (Figure 11d). Zhu et al. achieved the direct deposition of $MoS_2$ film on a 200 mm $SiO_2$/Si substrate at 275 °C with high electrical mobility ~35.9 $cm^2V^{-1}s^{-1}$.[27] This demonstrated the potential for integrating 2D semiconductors with advanced silicon CMOS circuits. Similarly, Hoang et al. synthesized $MoS_2$ monolayers on polymers and 30-$\mu$m-thickness glass substrate at an ultralow growth temperature of ~150 °C (Figure 11e).[518] The high-quality material further enables the fabrication of flexible logic circuits and transparent phototransistors.

## 4. EPITAXIAL GROWTH OF LARGE-AREA SINGLE CRYSTALS

In addition to the size requirements for TMD films, pristine single crystals are considered a promising industrial choice due to several superiorities. First, single-crystal TMD films circumvent the performance degradation associated with defective grain boundaries inherent in their polycrystalline counterparts, ensuring device-to-device consistency during integration. Second, the pristine lattice arrangement in a single-crystal TMD enhances the environmental tolerance of the prepared film, a crucial factor in postprocessing and device durability. Beyond that, the demand for single-crystal TMDs is particularly high in some symmetry-sensitive applications such as valleytronics, nonlinear optics, and polarization detection. Therefore, epitaxial growth of large-area single-crystal TMDs becomes a primary target in envisioning the future roadmap of 2D semiconductor technology. To date, two primary strategies are employed for the epitaxy of large-area single-crystal TMDs: (i) single nucleation growth, involving the evolution of an individual single nucleus into a large-size domain; (ii) multinucleation strategy, which seamlessly stitches together different unidirectionally aligned domains. In the following discussion, we will explore the efforts in single-crystal TMD epitaxy aligned with these two strategies.

### 4.1. Single-Nucleation Strategy

Similar to the preparation of single-crystal silicon ingots, the most straightforward approach to obtaining single-crystal TMDs involves initiating growth from a single nucleus and expanding it into a large-area film (Figure 12a). This strategy works efficiently in the synthesis of single-crystal graphene up to inch-size.[519] As for the fabrication of TMDs, this single-nucleation strategy is hampered by the multielement requirements and excess nuclei at active sites. The typical domain size is limited to hundreds of nanometers to tens of micrometers, and the stitched domains always lead to the formation of grain boundaries. To provide adequate space for nucleus expansion, the nucleation density should be efficiently suppressed, potentially limited to only one single nucleus during the growth process. Meanwhile, growth promotion should be addressed to guarantee efficient feeding for each nucleus, as discussed in the previous sections. Here, we mainly focus on the nucleation density control toward a pristine large-area TMD single crystal.

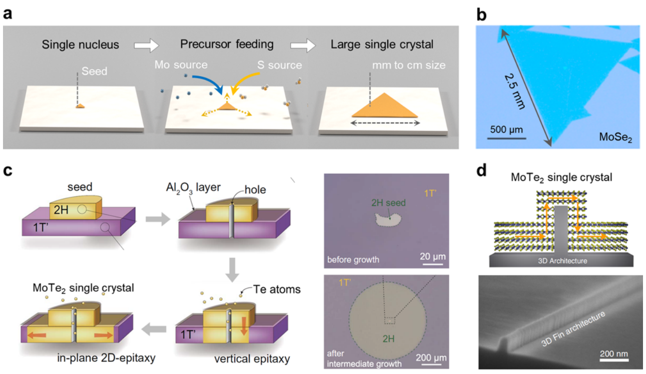


**Figure 12.** Large-area single-crystal TMDs prepared by a single-domain growth strategy. (a) Schematic illustration of the single-domain growth strategy starting from the feeding of a single nucleus to the eventual formation of a large-sized TMD crystal. (b) As-synthesized triangular monolayer $MoSe_2$ crystal on a molten glass substrate with size ∼2.5 mm. Reprinted with permission from ref 416. Copyright 2017 American Chemical Society. (c) Seeded 2D epitaxy growth of single-crystal 2H-$MoTe_2$ driven by phase transition. Reprinted with permission from ref 533. Copyright 2021 AAAS. (d) Heteroepitaxial growth of single-crystal 2H-$MoTe_2$ film on 3D fin architectures. Reprinted with permission from ref 536. Copyright 2022 Springer Nature.

By adjusting the basic parameters such as the amount of precursor, growth temperature, and flow rate, the nucleation density of TMD domains can be significantly suppressed.[467,520−523] Gong et al. fine-tuned the flow rate of carrier gas and reduced the nucleation density of $MoSe_2$ from $10^5$ to 25 nuclei per square centimeter.[524] The millimeter-scale $MoSe_2$ single crystals, visible to the naked eye, can be obtained on the $SiO_2$/Si substrate. Furthermore, the etching effect introduced by oxygen can reduce the nucleation density, leading to large-size single-crystal domains by etching away unstable nuclei from the substrate.[525] Xin et al. developed an alternate growth-etching method to obtain submillimeter-scale monolayer single-crystal $WS_2$.[526] Periodic etching stages were introduced during the growth, making the smaller domains etched away and therefore decreasing the nucleation density. Chang et al. proposed a novel self-capping vapor−solid reaction technique for the growth of large-area $MoS_2$ thin films. In this process, an intermediate liquid phase precursor is formed by the reaction of $MoO_3$ and NaF, and this precursor subsequently undergoes sulfurization to $MoS_2$ on the substrate.[527] The initially formed $MoS_2$ seeds acted as a capping layer that reduced the nucleation density and facilitated the lateral growth, leading to the formation of large single-crystal $MoS_2$ up to ∼1.1 mm. The VLS growth of TMDs in a confined space is also demonstrated to enhance the domain size up to millimeter size.[528] The mechanism lies in the reduced nucleation density by restricting the supply area of organosulfur to the metal salt source. Chen et al. reported the growth of triangular monolayer $MoSe_2$ domains with sizes up to ∼2.5 mm on the molten glass substrate (Figure 12b).[416] The glass melted above 750 °C allowed a quasi-atomic smooth liquid surface that suppressed the nucleation event, thereby facilitating the growth of ultralarge $MoSe_2$ crystals.

In a specific scenario, the phase transition from 1T′-$MoTe_2$ to 2H-$MoTe_2$ can drive the single-domain growth of a large-area single crystal.[529,530] The energy difference between 1T′-$MoTe_2$ and the stable 2H phase is relatively small, at approximately 40 meV/f.u.[531] In practice, a deficiency of Te atoms (>2%) asserts the stabilization of 1T′ phase, which can further recrystallize to 2H single crystal by feeding excessive Te source. Polycrystalline 1T′-$MoTe_2$ can be obtained via the tellurization of deposited Mo thin films, followed by annealing in a Te-rich atmosphere. This process induces the formation of a nucleus, which subsequently expands outward to create a large-sized single-crystal domain. Xu et al. modulated the kinetic rates of nucleation and crystal growth, and successfully synthesized a 2H-$MoTe_2$ single-crystal domain with a diameter as large as 2.34 mm.[532] Further stitching of multiple domains still remained grain boundaries in the full coverage film. Subsequently, as shown in Figure 12c, by dry transferring an exfoliated 2H-$MoTe_2$ flake on 1T film, which then serves as the "seed" to trigger the phase transition of 1T phase to 2H one, with a deposited $Al_2O_3$ layer preventing the natural nucleation. Te atoms were only introduced from the probe-punched hole at the seeded region and enabled the fabrication of 1-in. single crystal 2H-$MoTe_2$ from one nucleus.[533] This phase transition driven in-plane 2D epitaxy is substrate insensitive, which facilitates the homogeneous integration (rapid epitaxy in stacking direction or direct multitier growth[534]) and heterogeneous integrations.[535] In this regard, Pan et al. demonstrated the universal epitaxy of single crystal 2H-$MoTe_2$ on arbitrary substrates (silicon, GaN, 4H-SiC, sapphire) without considering their crystal symmetry, lattice mismatch, and even the surface geometry. As shown in Figure 12d, they realized the heteroepitaxy of the 2D single-crystal domain across the 3D fin architectures, which fully unveiled the integration capability of this phase transition method.[536]

To date, the lateral size of single TMD domain has reached a millimeter size or larger via various innovative designs.[537] Despite there is still a gap in single crystal size and fabrication scalability compared with the multinucleation strategy (as discussed in the subsequent section), the single domain strategy is still steadily pursued due to its superior crystallinity, which avoids any imperfectly stitching-induced grain boundaries.

### 4.2. Multinucleation Strategy

Another proposed strategy for single-crystal TMDs is stitching unidirectional islands into a large-area film. This efficient and scalable strategy relies on the epitaxial technique, that is, the deposited monolayer is well-aligned with the specific orientations on a crystalline substrate. It is well-known that traditional epitaxial growth of 3D film on a 3D substrate requires strict lattice matching (both in lattice constant and lattice symmetry), otherwise the interfacial misfit dislocations would hinder the high-quality epitaxy. Fortunately, as 2D materials are free of dangling bonds, TMDs allow for relaxed conditions concerning lattice constants due to the existence of a vdW gap at the interface during epitaxial growth. Surface symmetry has become the dominant factor in this growth system. The as-grown TMDs islands will be "pinned" and aligned with energetically preferred orientations, resembling the process of stacking a Lego brick onto the surface of another larger Lego brick. In this regard, Dong et al. proposed a theoretical guideline in the epitaxy of directional 2D materials on a crystalline substrate.[538] Specifically, the number of equivalent but different directions of a 2D material can be calculated as

$$N_1 = \frac{|G_{sub}|}{|G_{2D@sub}|}$$


https://doi.org/10.1021/acs.chemrev.3c00851
Chem. Rev. XXXX, XXX, XXX−XXX

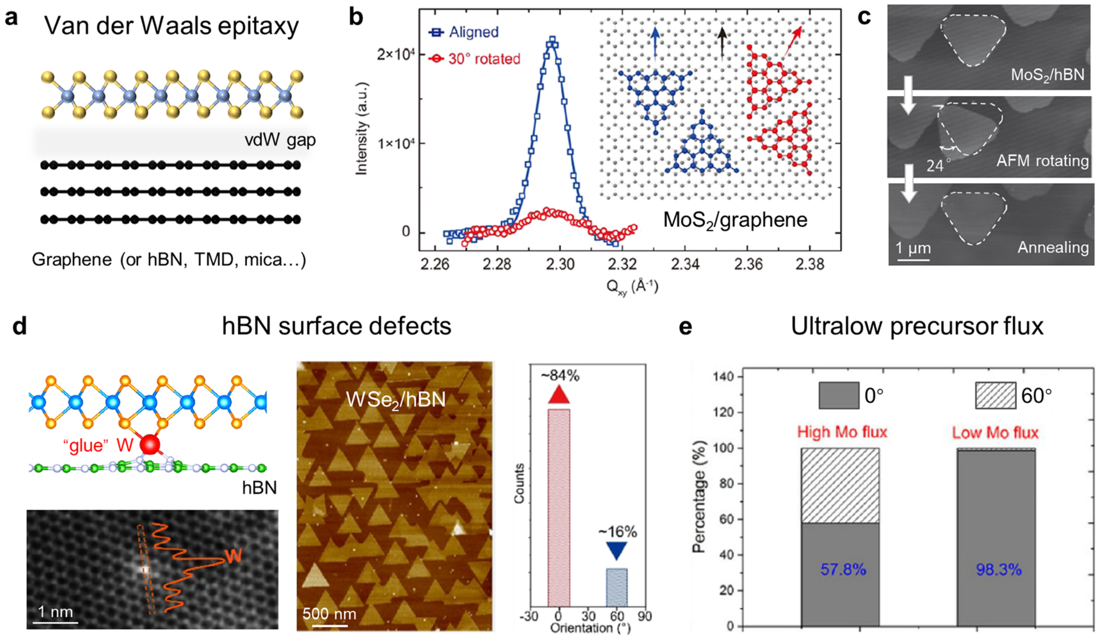


**Figure 13.** VdW epitaxy growth of TMDs on dangling-bond-free substrates. (a) Schematic illustration of the epitaxial growth of TMDs on vdW materials. (b) GIWAXS data of the $MoS_2(010)$ peak taken along the aligned growth (blue) and the 30° rotated growth (red), Inset, the schematic of the two growth orientations of $MoS_2$ on graphene. Reprinted with permission from ref 552. Copyright 2016 American Chemical Society. (c) The stable state of $MoS_2$ on hBN demonstrated by the AFM tip manipulation technique. Reprinted with permission from ref 564. Copyright 2017 Wiley-VCH Verlag GmbH & Co. KGaA, Weinheim. (d) Unidirectional growth of $WSe_2$ on defective hBN substrate. The single-atom vacancies on the hBN surface trap W atoms and break surface symmetry. Reprinted with permission from ref 567. Copyright 2019 American Chemical Society. (e) Histogram of the percentage of $MoS_2$ grains growth by MBE with various orientations under different Mo flux. Reprinted with permission from ref 569. Copyright 2017 American Chemical Society.

where $G_{sub}$ and $G_{2D@sub}$ are symmetry groups of the substrate and the 2D material-substrate system, respectively. For the epitaxial growth of TMDs with $D_{3h}$ symmetry, the $C_1$, $C_{2v}$, $C_{3v}$, and $C_{6v}$ symmetric substrates would lead to 1, 2, 1, and 2 types of equivalent directions, respectively. In other words, unidirectional TMD islands can be accessed via the substrates in the surface symmetry group is a subgroup of $D_{3h}$. Therefore, substrate engineering is the key to the epitaxial growth of large-area single-crystal TMDs. In this chapter, we will first review the epitaxial growth of TMDs on vdW substrate in Section 4.2.1, a "flatland" that dominates the island direction mainly by lattice symmetry. Then we turn to the 3D textured crystalline substrates with "terrace" reconstructed by metal (Section 4.2.2) and insulating substrates (Section 4.2.3).

**4.2.1. Epitaxy on vdW Materials.** VdW epitaxial growth was first achieved by Koma et al. via growing ultrathin selenium film on cleaved tellurium surfaces and ultrathin $NbSe_2$ film on cleaved $MoS_2$ surfaces.[539] Remarkably, an accommodatable lattice mismatch of even 50% for vdW epitaxy enables it a powerful technique in the field of film epitaxy.[540,541] When it comes to the epitaxy growth of large-area TMD materials, 2D vdW materials like graphene and hBN (Figure 13a) naturally appear as ideal substrates for several reasons: (i) The as-growth TMDs coupled with these dangling-bond-free substrates via the vdW force and additional growth-induced strain can be alleviated in the vdW gap.[542] (ii) The bottom-up synthesis of large-area single-crystal graphene and hBN have been realized earlier, offering a high-quality platform for TMDs epitaxial growth. (iii) The extensive 2D material family encompasses numerous categories together with rich surface symmetries and chemical properties. This diversity enables the selection of suitable substrates for the critical single-crystal TMDs epitaxy.

Chemical-inert epitaxial graphene layers have emerged as proper templates due to their scalable synthesis and transfer techniques. In 2012, Shi et al. directly prepared high-quality $MoS_2$ flakes on the CVD graphene/Cu substrate by thermally decomposing a low dose of $(NH_4)_2MoS_4$ precursor at 400 °C.[543] Besides, leaving the easily sulfurized Cu foil by transferring the graphene layer elsewhere or directly preparing the graphene/SiC substrate further enables high-temperature TMD growth strategies.[544−548] In general, during the vdW epitaxy, the TMD materials with $D_{3h}$ symmetry growth on $C_{6v}$ symmetry graphene (or the surface of graphite) would result in two preferred orientations.[549−551] As shown in Figure 13b, Liu et al. demonstrated the rotational commensurability in CVD-$MoS_2$ and epitaxial graphene, which was driven by the energetically favorable alignment in spite of the existence of ~28% lattice mismatch.[552] Besides, the epitaxy behavior of TMDs on graphene has been systemically studied, revealing that various factors including grain boundaries, dislocations, layer number, and stacking order of the graphene layers significantly affect TMD growth.[553−556] Although high-symmetric graphene seems not to be the optimal substrate for single-crystal TMDs growth, this direct synthesis route can produce heterostructures with a clean interface and some degree of lattice alignment.[557,558] Hoang et al. reported the low-temperature epitaxial growth of highly orientated $MoS_2$ on a 4-in. wafer-size graphene/sapphire substrate, leading to the construction of $MoS_2$/graphene heterostructures with ultra-high photoresponsivity.[559]

Electrically insulating hBN layers have proven to be a superior alternative for the epitaxy growth of TMDs. The


https://doi.org/10.1021/acs.chemrev.3c00851
Chem. Rev. XXXX, XXX, XXX−XXX

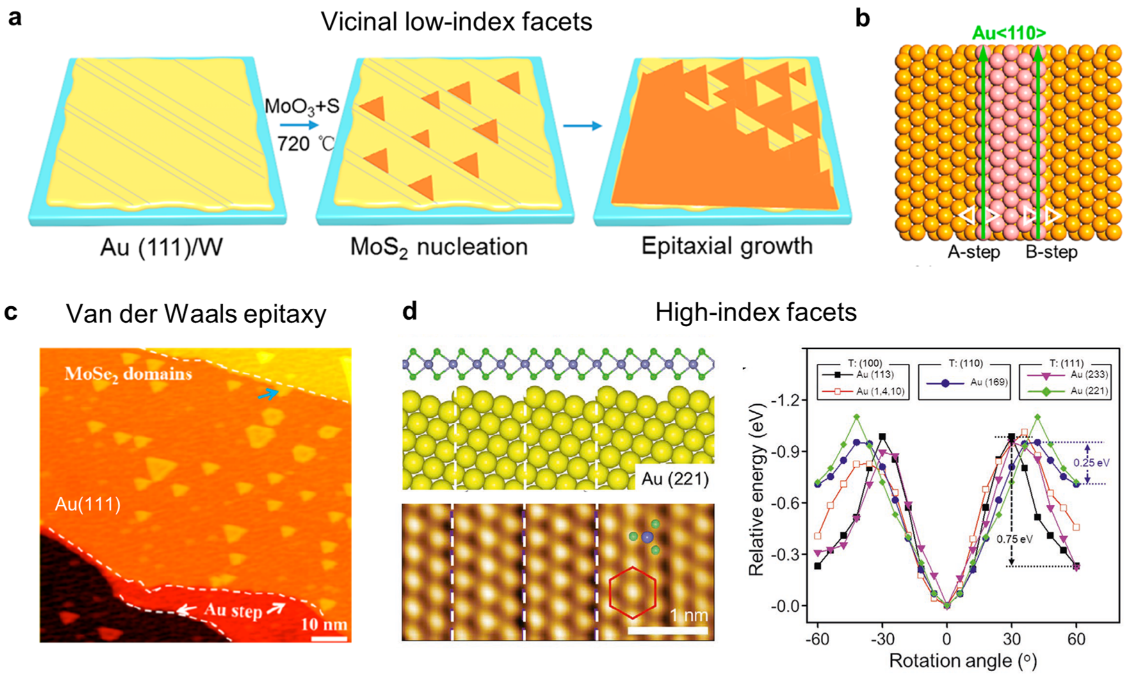


**Figure 14.** Large-area epitaxy growth of single-crystal TMDs on metal substrates. (a) Schematic illustration of epitaxy growth of centimeter-scale $MoS_2$ on vicinal low-index Au(111) substrate. (b) Two typical step edges (A-step and B-step) along the ⟨110⟩ direction of the vicinal Au(111) surface. (a,b) Reprinted with permission from ref 33. Copyright 2020 American Chemical Society. (c) STM image of $MoSe_2$ domains on the Au(111) grown by MBE. Reprinted with permission from ref 597. Copyright 2022 American Chemical Society. (d) Structural model and STM image of a $WS_2$ film grown on a high-index Au (221) substrate (left panel). Relative binding energies of a $W_3S_6$ cluster on different atomic sawtooth Au surfaces as a function of rotation angle (right panel). Reprinted with permission from ref 599. Copyright 2021 Wiley-VCH Verlag GmbH & Co. KGaA, Weinheim.

reasons lie in that (i) the atomically flat surface and outstanding dielectric properties of hBN make it efficiently suppress the extrinsic scattering from charged impurities compared with oxide substrates;[560,561] and (ii) in theory, the diatomic hBN with inversion symmetry broken naturally has the potential to relieve the energy degeneracy of the as-grown twinned TMD domains. In 2014, Okada et al. achieved the direct synthesis of $WS_2$ on exfoliated hBN flakes, the results indicated that the triangular $WS_2$ domains were crystalline into two dominant orientations.[562] Similar growth behavior has also been reported in subsequent studies. For instance, Yan et al. observed the aligned growth of $MoS_2$ on hBN with rotation angles of less than 5 degrees.[563] Yu et al. found the twinned CVD $MoS_2$ triangular (0° and 60°) epitaxy on hBN occurred with a ratio of nearly 1:1.[564] And the artificially rotated as-grown domains could rotate back to the initial states after annealing due to the superlubricating $MoS_2$-h-BN interface (Figure 13c).

Indeed, the orientational preference of twinned TMD structures is still nearly degeneracy although using the inversion asymmetric hBN substrate, and a more controllable epitaxy strategy is required for realizing the large-area single crystal growth.[565,566] In this regard, Zhang et al. identified the point defects (e.g., B vacancies) in the hBN substrate could enhance the orientational epitaxy of TMD materials and obtained ~90% $MoS_2$ flakes with the same orientation (Figure 13d). Moreover, Zhang et al. employed plasma treatment to introduce defects in hBN, and a 95% major $WSe_2$ orientation could achieved during the nucleation window of MOCVD growth.[567] The mechanism stemmed from the vacancies of hBN which traps the W atoms and further breaks the surface symmetry.[568] Besides, Fu et al. adopted a high growth temperature and ultralow precursor flux to reduce the twinned domains (only ~1.3% antialigned grains) during the MBE growth of $MoS_2$ on the hBN substrate (Figure 13e).[569] The success in synthesizing large-area hBN layers further fuels the epitaxial growth of large-area TMDs. Steady progress has been achieved by preparing the desired hBN substrate such as transferring it from the Cu foils or directly depositing it on sulfide-resistant surfaces such as Au foil,[570] Ni−Ga alloy,[571] and sapphire,[572,573] then follows the epitaxial growth of TMD materials. Lee et al. synthesized the large-area single-crystal $WS_2$ film (aligned orientations within ±1.33°) using the single crystalline hBN/Au substrate, where the hBN film was substituted or etched away during the growth of the $WS_2$ film.[574]

Obviously, the dangling-bond-free TMD material could also work as a vdW epitaxial substrate and form vertical or lateral heterostructures[575−578] (e.g., $MoS_2/WS_2$ and $MoS_2/WSe_2$). Surface-inert mica with an atomically flat surface such as fluorophlogopite mica ($KMg_3AlSi_3O_{10}F_2$) is also considered an excellent substrate for vdW epitaxy.[82,579−581] Its in-plane hexagonal lattice matches with TMD materials and can be cleaved into a transparent and flexible thin sheet for further device fabrication. Distinguished from the twinned growth manner of TMDs, Wang et al. realized the epitaxial growth of unidirectional transition-metal oxide nanosheets on mica,[582] which inspired the single crystal epitaxy of other similar materials on this substrate.

Nearly immune to the dangling bonds and textures of conventional 3D substrates, vdW epitaxy on atomically flat substrates could provide large-area TMDs with more uniform and intrinsic properties. Nevertheless, this also indicates there are still limited methods that can be introduced to break the energy degeneracy of antiparallel growth orientations. In the future, more universal, reliable and powerful growth strategies should be proposed in this attractive system to realize robust growth of large-area TMD single crystals.

**4.2.2. Epitaxy on Metal Substrates.** Singe-crystal metal foils with various facets provide rich surface structures and serve as a substrate library for the epitaxial growth of 2D materials. Notably, face-centered cubic (fcc) metals like Cu, Ni, and Au can be acquired as single crystals with large areas from centimeters to even meters.[583] This is achieved by thermodynamically transforming commercial polycrystalline foils into low-index facets ({100}, {110} and {111}) through an appropriate annealing process. Single-crystal graphene is already accessible through epitaxial growth on single-crystal Cu(111) foil with a size of up to 0.5 m.[584] However, when dealing with diatomic materials with broken inversion symmetry, such as hBN and TMDs (with $C_{3v}$ and $D_{3h}$ symmetry, respectively), the use of perfect high-symmetry facets (such as $C_{6v}$ for {111} surface) as templets is no longer suitable due to the formation of twinned crystals. This dilemma was previously addressed in the epitaxy of hBN by utilizing low-symmetry Cu(110) vicinal surface and direct lateral docking hBN to Cu(111) steps.[585,586] Although there is a similar symmetry between hBN and TMDs, the Cu foil is still not suitable for scalable TMD growth because it is susceptible to sulfurization.

Subsequently, the focus shifted toward employing the chemically inert Au substrates, which also possess an fcc structure, as the alternative epitaxial templates for TMD materials. At the early stage, noble single-crystal Au(111) substrate was unitized as an ideal templet for TMDs islands growth under ultrahigh vacuum conditions, primarily for STM research.[587,588] In practice, in 2014, Shi et al. selected polycrystalline Au foil as the substrate for large-area TMD growth.[589,590] This metallic substrate combined with as-grown nanosized $MoS_2$ flakes exhibited remarkable hydrogen evolution reaction (HER) activity. As discussed in the previous section, the catalytic effect from the Au surface also enhances the grain size and growth rate, through the commercial polycrystalline Au foil leading to the formation of a film composed of randomly oriented TMD domains.[591,592] In 2016, Zhang et al. demonstrated the twinned growth behavior of $ReS_2/WS_2$ vertical heterostructure on Au(111), which is indicative of epitaxial growth of large-area orientated TMDs on Au foil.[593] Similarly, Lu et al. achieved epitaxial growth of $MoSe_2$ on Au(111) by MBE, observing domain alignment along two preferred directions.[594]

While the epitaxy manner of TMDs on Au foil shed light on preparing large-area single crystal film by domain stitching, a critical scientific problem arose regarding how to break the energy degeneracy of two preferred orientations when using the Au(111) substrate with $C_{6v}$ symmetry of top layer atoms.[595] In 2020, Yang et al. realized the fabrication of ∼3×3 cm single-crystal $MoS_2$ film on vicinal Au(111) substrate (Figure 14a).[33] Insight STM characterizations and density functional theory (DFT) calculations suggested the presence of steps along the Au ⟨110⟩ direction played a crucial role in breaking the symmetry of the antiparallel orientations. The mechanism hinges on that, for both A- and B-steps (two types of steps along the Au ⟨110⟩, Figure 14b), the Mo-zz edge docking acts as the minimum energy configuration compared to other possibilities (such as S-zz or AC docking). In this regard, an energy difference of 0.16 eV/f.u. between Mo-zz/A-step and Mo-zz/B-step favored the latter, driving the epitaxial growth of $MoS_2$ domains in that direction. The single crystal substrate was prepared by melting and resolidifying commercial Au foils on W foils, which reduced the substrate cost and enabled the large-size film growth. Moreover, Li et al. sputtered a 600 nm-thick Au onto a 2-in. sapphire substrate and annealed it into the desired (111) facet.[596] This wafer-size flat substrate enabled the fabrication of the 2-in. $MoS_2$ film with over 99% unidirectional ratio by carefully controlling the growth temperature. Ding et al. investigated the epitaxial mechanism of TMD growth on Au(111) via cross-sectional STEM,[597] which revealed that ∼90% of TMDs seeds nucleated on the surface terraces rather than on surface steps, yet they still exhibited the unidirectional growth manner (Figure 14c). In other words, the Au(111) surface-guided vdW epitaxy could directly lead to the growth of single-crystal TMDs. The surface steps further determined the thickness and integrity of the TMDs film. Based on this mechanism, Xia et al. successfully prepared wafer-scale $MoSe_2$ and $WSe_2$ single-crystal on Au(111) substrate at low temperatures (200−400 °C) by the MBE method.[598]

The extensive library of high-index Au facets with low surface symmetry provides a versatile platform for the universal growth of single-crystal TMDs. Choi et al. demonstrated the resolidified Au foil could randomly produce high-index facets such as (5,7,11), (169), and (114).[599] These "sawtooth" surfaces as shown in Figure 14d (left panel) featured periodic step edges and low-index terraces including (111), (110), and (100). Remarkably, centimeter-sized single-crystal $WS_2$, $WSe_2$, $MoS_2$, $MoSe_2/WSe_2$ heterostructure and $W_{1-x}Mo_xS_2$ alloy were universally prepared on these sawtooth surfaces, regardless of specific Miller indices (Figure 14d, right panel). The underlying mechanism is explained as the presence of energetically favorable adsorption sites at periodic sawtooth gullet step edges, which guided the unidirectional growth of TMD domains. Additionally, some low-symmetry high-index facets vicinal to low-index surfaces also facilitate the robust growth of single-crystal TMDs. For instance, Hu et al. reported the epitaxial growth of single-crystal $MoS_2$ aligned with the high-symmetric directions of the 2-fold symmetry vicinal Au(101) surface (e.g., (627), (839), (10,1,12)).[600] Such a symmetry-mismatched epitaxy further supports the notion of a step-edge-guiding effect during the unidirectional TMD domain growth.

In addition to surface symmetry engineering, the growth parameters can also dominate the epitaxial growth of TMDs on metal substrates. First, a higher heating temperature favors the formation of unidirectional islands. This can be explained as that, although the designed surface structures break the energy degeneracy of two favorable twinned directions, an energy barrier still needs to be overcome to rotate one metastable direction into another. Therefore, sufficient thermal energy is required to facilitate this process during the nucleation stage. Second, the appropriate precursor flux ratio plays a vital role in the epitaxial growth of TMDs. In general, a higher chalcogen/metal ratio is more favorable for the preparation of single-crystal TMD films. For example, the proportion of 0 and 60° oriented $MoS_2$ domains on Au(111) was tuned from ∼49 to 98% by changing the $S/MoO_3$ ratio from ∼2:1 to 3:1. Besides, Yang et al. controlled a specific Mo/S ratio of 2:1 to design the morphology of $MoS_2$ into aligned ribbons on high-index Au facets vicinal to Au(111).[601] By extending the growth time,


https://doi.org/10.1021/acs.chemrev.3c00851
Chem. Rev. XXXX, XXX, XXX−XXX

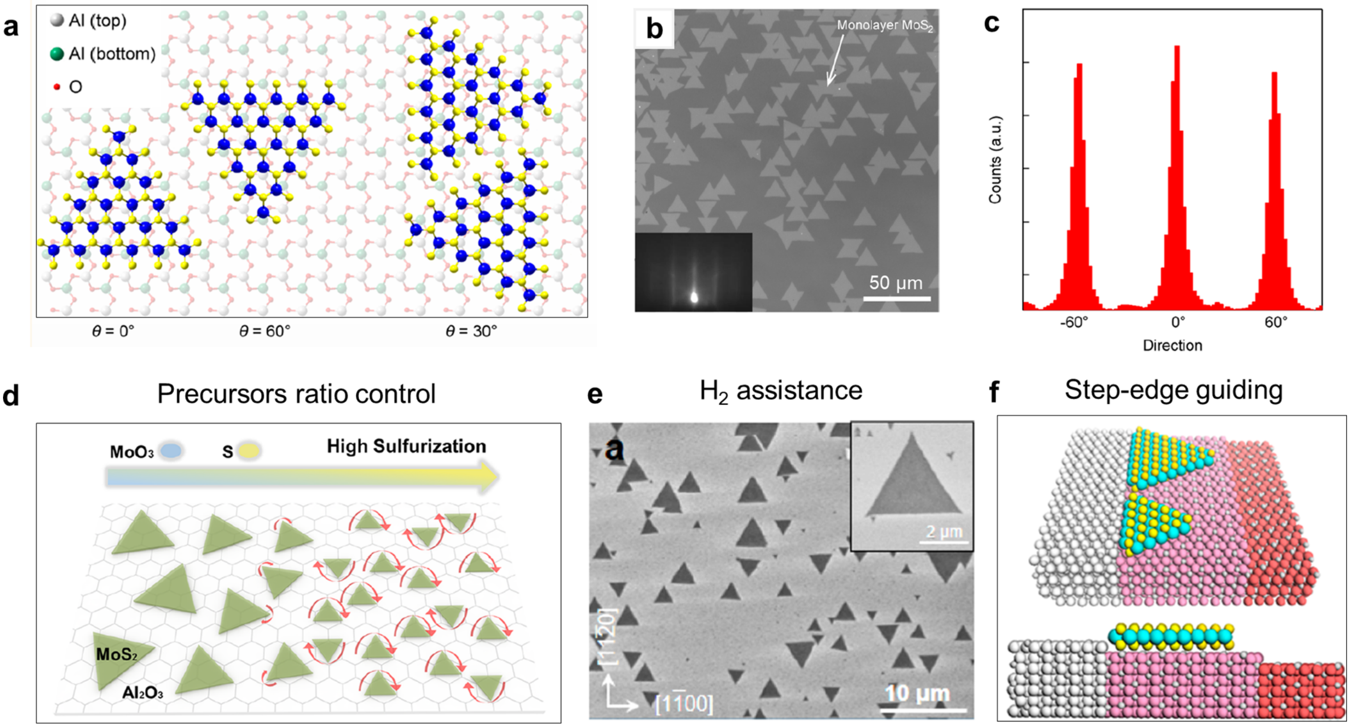


**Figure 15.** Large-area epitaxy growth of TMDs on sapphire substrates. (a) Schematic illustration of relative lattice orientations between monolayer $MoS_2$ and c-plane sapphire (b) Optical image of monolayer $MoS_2$ grains grown on atomically smooth annealed sapphire, inset, RHEED pattern acquired on the as-grown sample. (c) Orientation histogram based on the area shown in part (b) exhibits that the majority of $MoS_2$ grains are oriented along 0° and ±60°. (a−c) Reprinted with permission from ref 605. Copyright 2015 American Chemical Society. (d) Schematic illustration of the ratio between sulfur and molybdenum oxide controlling the orientation of $MoS_2$ islands on sapphire. Reprinted with permission from ref 606. Copyright 2017 American Chemical Society. (e) SEM images of as-grown aligned $WS_2$ islands on sapphire with the assistance of $H_2$. Reprinted with permission from ref 609. Copyright 2018 American Chemical Society. (f) Schematic illustration of the step-edge guided aligned nucleation of $WSe_2$ on c-plane sapphire. Reprinted with permission from ref 619. Copyright 2015 American Chemical Society.

these unidirectional monolayer TMD ribbons could be stitched together into an inch-sized continuous single crystal.

Overall, chemically inert metal with rich surface structures have demonstrated their excellent capability in producing inch-sized single-crystal monolayer TMDs. These metallic substrates also bring convenience in the electrochemical bubbling transferring of the film to arbitrary substrates. Meanwhile, versatile characterizations that require substrate conductivity such as LEED and STM, could be directly carried out to investigate the material quality and epitaxial behavior. However, this poses challenges for electronic device fabrication directly on the as-grown metal substrate without subsequent transfer. Looking ahead, several promising research directions include (i) the reliable and industry-compatible fabrication of large-area single-crystal substrates with specific facets and (ii) an in-depth understanding of the epitaxy mechanism, especially regarding the step- and surface-guided effect. These insights will not only advance our fundamental understanding but also enable the robust production of single-crystal TMDs.

**4.2.3. Epitaxy on Insulating Substrates.** Thermal stable sapphire ($\alpha$-$Al_2O_3$) substrate is commercially used in the III−V semiconductor epitaxy for light-emitting diodes (LEDs) manufacturing.[602] After decades of development, its low-cost production and mature processing techniques provide sufficient freedom in designing suitable surfaces for the oriented growth of nanomaterials. Sapphire is also considered an ideal mate with TMDs due to several reasons: (i) its insulating and transparent nature facilitates the further fabrication of electronics and optoelectronic devices; (ii) the negligible reaction with chalcogen atoms and the hexagonal symmetry of the sapphire substrate enables the high-temperature epitaxy growth of directional TMD islands; (iii) single-crystalline sapphire wafers sliced from an ingot provide rich choices in substrate sizes (ranging from 1 to 12 in.) and crystallographic planes (c, a, m, r, v planes along with desired miscut angles). Over the past decade, electronic-grade wafer-scale TMD single crystals have been successfully synthesized on designed sapphire substrates. Sapphire has become one of the most promising epitaxial substrates for TMD semiconductors toward industrialization. In this section, we will review the journey of the epitaxial growth of TMDs on sapphire from random orientation to bicrystalline structures, and further to single crystalline.

In practice, the TMD islands sometimes grow randomly (nonepitaxially) on the as-received sapphire substrate rather than aligning as desired.[603] Considerable efforts have been devoted to regularizing them into oriented epitaxial growth manner. In 2014, Ji et al. analyzed the orientation distribution of the $MoS_2$ domain growth on the commonly used c-plane (0001) sapphire, identifying there were two preferred directions along with misaligned species.[604] Subsequently, Dumcenco et al. indicated that a high-temperature (1000 °C) preannealing of the sapphire substrates could produce atomically smooth terraces, facilitating the oriented growth of $MoS_2$.[605] As shown in Figure 15a−c, 91.5% of domains aligned well with 0° and ±60°, while a small fraction (6%) exhibited orientations of ±30°. During the nucleation window, small clusters could rotate or slide along the surface until they


https://doi.org/10.1021/acs.chemrev.3c00851
Chem. Rev. XXXX, XXX, XXX−XXX

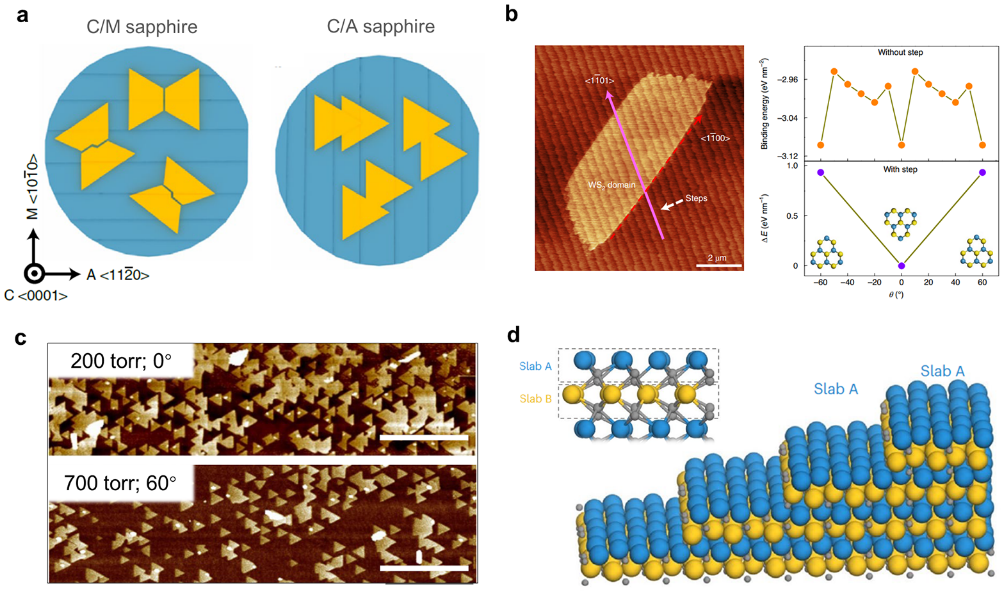


**Figure 16.** Large-area epitaxy growth of single-crystal TMDs on sapphire substrates. (a) Step orientations on C/M and C/A sapphire wafers and the corresponding epitaxial $MoS_2$ domain alignment. Reprinted with permission from ref 34. Copyright 2021 Springer Nature. (b) AFM image of a $WS_2$ island growth on a-plane sapphire (left panel) and DFT calculations of the binding energies of a $WS_2$ island with different rotation angles on the a-plane sapphire surface (right panel). Reprinted with permission from ref 35. Copyright 2021 Springer Nature. (c) AFM images $WSe_2$ domains grown on c-plane sapphire at 200 Torr (top panel) and 700 Torr (bottom panel), showing the preferred orientations of 0° and 60°, respectively. Reprinted with permission from ref 629. Copyright 2023 Springer Nature. (d) Atomic structure of c-plane sapphire with single-type terraces whose step height is equivalent to two slabs, insert, the A and B slab stack alternatingly exhibits a mirror-symmetric arrangement. Reprinted with permission from ref 632. Copyright 2023 Springer Nature.

are eventually anchored in the most stable orientation upon reaching a certain size. This substrate pretreatment technique has been widely adopted in subsequent studies. Furthermore, critical growth parameters such as temperature, the chalcogen-to-metal source ratio, and hydrogen flow have been systematically investigated to ensure the aligned arrangement of TMDs on sapphire substrates. Yu et al. employed a much higher growth temperature of 930 °C to obtain thermally stable 0° and 60° domains on annealed sapphire, which was finally stitched into 2-in. highly oriented $MoS_2$ film.[477] However, a lower growth temperature below 820 °C would result in misorientations due to insufficient thermal energy for TMD nuclei to rotate or slide into the most stable configurations. Aljarb et al. explored the impact of the S/Mo source ratio on the orientation control of $MoS_2$ on sapphire, indicating that the S-rich environment during nucleation would promote the 0°/60° oriented growth (Figure 15d).[606] Suenaga et al. further demonstrated the $MoS_2$ grain alignment could be tuned between 0°/60° (edge parallel to [1$\bar{1}$00]) and ±30° (edge normal to [1$\bar{1}$00]) by changing the sulfur supply.[607] A similar behavior was also observed by Lai et al. while introducing an appropriate oxygen flow.[608]

Surface structures of sapphire, such as termination type, passivating layer, reconstructed step, and crystalline plane, directly dominate the growth behavior of TMDs. Ji et al. introduced a high concentration (more than 40%) of $H_2$ gas during the growth process, leading to the formation of Al-rich sapphire surface.[609] This surface is more strongly coupled with $WS_2$ compared to the O-rich surface, and can effectively suppress the randomly oriented grains (Figure 15e). Similarly, Park et al. showed that a high growth temperature could convert the sapphire surface from OH-termination to half-Al termination, and further promoted the epitaxial growth of $MoS_2$.[610] A passivation layer between 3D sapphire and 2D TMDs is also observed during the oriented growth, which is considered as a "quasi" vdW epitaxy system proposed by Koma et al. in 1989.[611,612] For instance, Lin et al. revealed the existence of a Se-rich layer at the $WSe_2$/sapphire interface during the MOCVD epitaxial growth.[513] Cohen et al. found an ordered $WO_3$ interface layer at the sapphire surface, which played a key role in the oriented quasi-vdW epitaxial growth of $WS_2$.[613] In addition to the above widely used c-plane sapphire, Ma et al. carried out the epitaxial growth of $MoS_2$ on a-plane (11$\bar{2}$0) sapphire and obtained rectangle domains aligned to the [1$\bar{1}$00] direction.[614]

These explorations in reaction condition and substrate engineering have guaranteed the robust oriented epitaxial growth of TMDs on sapphire, and significantly inspired chemists and physicists to further pursue the breaking of the energy degeneracy toward single-crystal films. A key step in achieving large-area single-crystal is designing a lower symmetry sapphire template (such as $C_{3v}$, $C_1$, and $C_s$), which thermodynamically suppresses twined islands. The most proposed strategies involve utilizing atomic step and surface symmetry.

The atomic steps originate from the vicinal sapphire surface, a crystalline surface miscut slightly deviated from a low-index plane.[615] A proper annealing process could reconstruct this surface into the sawtoothed structure with periodical step edges and flat terraces. For example, commercial c-plane sapphire wafers are always prepared by miscutting ∼0.2° toward M-axis ⟨1$\bar{1}$00⟩ (defined as C/M)[616] after annealing at ∼1,000 °C, which always leads to the formation of terraces with ∼50−70 nm width and step height of 0.22 nm ($c$/6, $c$ is the lattice constant of $\alpha$-$Al_2O_3$) along the ⟨11$\bar{2}$0⟩ direction.[605] These periodical nanostructures on sapphire have been widely used in the anisotropic growth of 1D nanotubes and nanowires over the past decade.[617,618] As for the epitaxial growth of

**Table 1. Summary of Epitaxial Growth of Large-Area Single-Crystal TMDs**

| Substrate | Strategy | Growth technique | Materials | Size | Performance: Mobility ($cm^2\ V^{-1}\ s^{-1}$) | Performance: On/off ratio | Ref |
|---|---|---|---|---|---|---|---|
| hBN | Low precursor flux | MBE | $MoS_2$ | 2-in. | 23.2 ± 0.2 | ∼$10^6$ | 632 |
| hBN | Defects assistance | MOCVD | $WSe_2$ | – | 4.2 | – | 632 |
| Au(111) | Step-edge guiding | CVD | $MoS_2$ | 1-in. | 11.2 | 7.7 × $10^5$ | 33 |
| Sawtooth Au surface | Step-edge guiding | CVD | $WS_2$ ($WSe_2$, $MoS_2$, $MoSe_2/WSe_2$, $W_{1-x}Mo_xS_2$ alloy) | cm scale | ∼3 | ∼$10^8$ | 599 |
| Au(111) | Temperature guiding | CVD | $MoS_2$ | 2-in. | – | | 596 |
| Au(111) vicinal facets | Step-edge guiding | CVD | $MoS_2$ ($WS_2$, $MoSe_2$, $WSe_2$, $MoS_xSe_{2-x}$) | 1-in. | 7–11 | $10^5$–$10^6$ | 601 |
| Au(101), Au(001), Au(111) vicinal facets | Step-edge guiding | CVD | $MoS_2$ | mm scale | 6.6–11.7 | 1.0–3.7 × $10^7$ | 600 |
| Au(111) | Enhanced Au/TMD interaction | MBE | $MoSe_2$, $WSe_2$ | 2-in. | – | | 598 |
| c-plane sapphire | Step-edge guiding | MOCVD | $WS_2$ | 2-in. | 16 | ∼$10^7$ | 621 |
| a-plane sapphire | Dual-coupling guiding | CVD | $WS_2$ | 2-in. | 0.8–1.6 | – | 35 |
| a, c, m, n, r, and v-plane sapphire, MgO and $TiO_2$ | Time sequence control | CVD | $MoS_2$ ($WS_2$, $NbS_2$, $MoSe_2$, $WSe_2$, $NbSe_2$) | – | ∼38 | ∼$10^8$ | 627 |
| c/a-plane sapphire | Step-edge guiding | CVD | $MoS_2$ | 2-in. | 77.6 | ∼$10^9$ | 34 |
| c/a-plane sapphire | Step-edge guiding | CVD | $MoSe_2$ | 2-in. | – | | 625 |
| c-plane sapphire | Surface termination control | CVD | $MoS_2$ | cm scale | – | | 610 |
| c-plane sapphire | Step-edge guiding | CVD | Fe-doped $MoS_2$ | 2-in. | ∼54 | ∼$10^8$ | 622 |
| c-plane sapphire | Step-edge guiding | CVD | Fe-doped $MoS_2$ | 4-in. | ∼100 | ∼$10^9$ | 623 |
| c-plane sapphire | Decoration layer control | CVD | $MoS_2$ | 2 × 1 $cm^2$ | 12 | $10^7$–$10^8$ | 624 |
| c/a-plane sapphire | Step-edge guiding | CVD | $MoS_2$ | 2-in. × 7 | ∼44 | ∼$10^7$ | 371 |
| c-plane sapphire | Sapphire/TMD interaction | CVD | $MoS_2$ | 2-in. | 30.7 | 1–4 × $10^7$ | 632 |
| c-plane sapphire | Step-edge guiding | MOCVD | $WSe_2$ | 2-in. | ∼0.4 | ∼$10^6$ | 629 |
| c-plane sapphire | Buffer layer control | CVD | $MoS_2$ | 2-in. | ∼140 | $10^9$ | 631 |

TMDs, in 2015, Chen et al. employed the atomic steps on c-plane sapphire to guide the aligned nucleation and growth of $WSe_2$ (Figure 15f),[619] and Hwang et al. further suggested a controlled introduction of $H_2$ could promote the step-edge aligned nucleation of $MoSe_2$ on sapphire.[620] This step-guiding effect can directly facilitate the unidirectional growth of TMDs. Chubarov found that maintaining a suitable temperature (850 °C) during the nucleation stage led to aligned steps and corresponding unidirectional $WS_2$, otherwise, a higher temperature (1000 °C) would distort the steps and misorient TMD islands.[621] Li et al. reported that introducing Fe significantly reduced the formation energy of periodical steps on sapphire, successfully fabricating a 4-in. Fe-doping $MoS_2$ single crystal mainly relying on these steps.[622,623] Chang et al. reported the $Fe_2O_3$ decoration layers could boost the single-orientated growth of $MoS_2$ on c-plane sapphire.[624]

Designing step orientations with careful consideration of the epitaxial relationship between sapphire and TMDs has proven to be an efficient strategy for breaking the energy degeneracy of twined structures. In 2021, Li et al. suggested the R30° epitaxial relationship between c-plane sapphire and as-grown $MoS_2$, that is, the $MoS_2$ in-plane lattice vectors ($\langle 11\bar{2}0\rangle$ direction) have a 30° rotation from the A axis $\langle 11\bar{2}0\rangle$ of sapphire.[34] Consequently, the $\langle 11\bar{2}0\rangle$ steps on standard C/M sapphire just go along with the armchair direction of $MoS_2$ during the epitaxial process, which could not break the energy degeneracy in this configuration (Figure 16a). To address this, they innovatively customized the C/A sapphire substrate for the single crystal $MoS_2$ growth, wherein the ∼1° miscut toward the A-axis $\langle 11\bar{2}0\rangle$ could generate atomic steps along $\langle 1\bar{1}00\rangle$ direction. These steps paralleled the zigzag edge of $MoS_2$ islands further broke the energy degeneracy and led to a more than 99% unidirectional alignment. This miscut strategy has shown universality and Li et al. subsequently utilized the C/A sapphire to realize the fabrication of the 2-in. sized $MoSe_2$ single crystal.[625] Yang et al. combined the "face-to-face" strategy with C/A sapphire to batch-produce wafer-scale single crystal $MoS_2$ films.[371] Moreover, Liu et al. achieved aligned nucleation of bilayer $MoS_2$ on high-temperature annealed C/A sapphire with critical step height, which will be further discussed in Section 5.1.1.[626]

The synergy of epitaxial relationship and atomic steps was explained as a "dual-coupling effect" by Wang et al.[35] They employed the vicinal a-plane $(11\bar{2}0)$ sapphire as an epitaxial templet. Initially, the interaction between $C_2$ symmetry a-plane and $D_{3h}$ symmetry $WS_2$ resulted in two preferred antiparallel domains (zigzag edges along the $\langle 1\bar{1}00\rangle$ direction). The coupling between vicinal-cutting induced steps ($\langle 1\bar{1}01\rangle$ direction) and $WS_2$ islands further broke the energy degeneracy (Figure 16b), finally enabling the fabrication of 2-in. sized single crystal films. The proposed dual-coupling mechanism appears as a universal strategy for the epitaxy of single-crystal noncentrosymmetric TMDs ($MoS_2$, $WS_2$, $NbS_2$, $MoSe_2$, $WSe_2$, and $NbSe_2$).[627,628] By precisely controlling of simultaneous formation of grain nuclei and substrate steps, the growth of twined $MoS_2$ grains could be suppressed due to the existence of steps, regardless of step edge orientations. This unidirectional aligned behavior has been realized on textured insulating substrates including vicinal $a(11\bar{2}0)$, $c(0001)$,


https://doi.org/10.1021/acs.chemrev.3c00851
Chem. Rev. XXXX, XXX, XXX−XXX

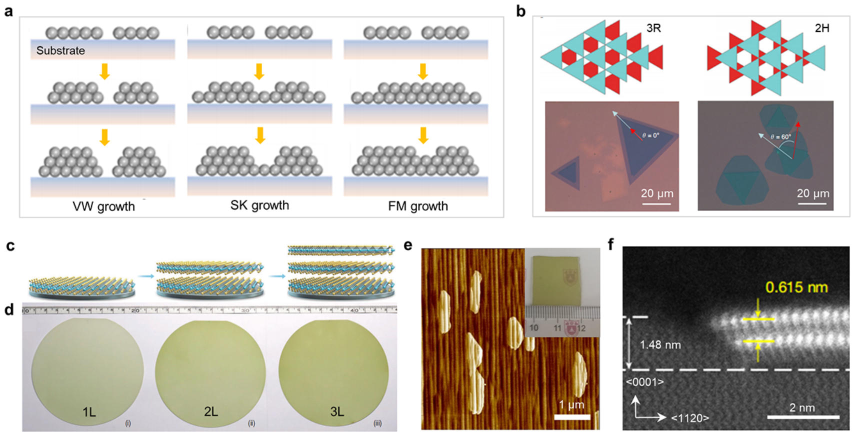


**Figure 17.** Strategies for the growth of multilayer TMDs. (a) Schematic for the three thin-film growth modes. Reprinted with permission from ref 653. Copyright 2021 American Chemical Society. (b) Reverse-flow CVD growth of AA and AB stacking bilayer $MoS_2$. Reprinted with permission from ref 656. Copyright 2019 Springer Nature. (c) Schematic diagram of the layer-by-layer epitaxy of wafer-scale multilayer $MoS_2$ film. (d) Optical images of the as-prepared 1L, 2L, and 3L $MoS_2$ wafers. (c,d) Reprinted with permission from ref 648. Copyright 2022 Oxford University Press. (e) AFM and Optical images of the uniform nucleation and epitaxy bilayer $MoS_2$. (f) HAADF-STEM cross-sectional image of bilayer $MoS_2$ nucleating at the sapphire step edge. (e,f) Reprinted with permission from ref 626. Copyright 2022 Springer Nature.

m($1\bar{1}00$), n($11\bar{2}3$), r($1\bar{1}02$), and v($22\bar{4}3$) plane sapphire as well as MgO(100) and $TiO_2$(110).

In addition to the step-guide effect, the reaction conditions could also dominate the unidirectional growth of TMDs on sapphire. Zhu et al. systematically studied the epitaxial behavior of $WSe_2$ on c-plane sapphire via MOCVD, focusing on precursor supplement and reactor pressure. Besides the step-assisted nucleation, the surface chemistry of the sapphire (terminal OH removal and Se passivation) could tune the nucleation orientations to either 0° or 60° (Figure 16c).[629] And the areal coverage of twin boundaries could be suppressed as <15% over wafer-scale substrates. The importance of surface reconstruction was also demonstrated in the epitaxial growth of $MoS_2$ on $\beta$-$Ga_2O_3$ (001) substrate, wherein the interfacial layer could be tuned between $Mo^{5+}$ and $Mo^{4+}$ by precursor concentration, then changed the atomic registry either 0° or 60°.[630] Recently, Li et al. reported that a suitable Mo/S precursor ratio led to the formation of a specific interfacial reconstructed layer, which enabled the epitaxial growth of ultrahigh-quality $MoS_2$ single-crystal on commercial sapphire substrates.[631]

In fact, the atom arrangement of an ideal c-plane sapphire (without steps) naturally possesses the $C_3$ symmetry that is suitable for single-crystal TMDs growth. Fu et al. suggested that the confusion of twined domains on c-plane sapphire originates from the exposed surface existing compositionally equivalent but symmetrically reflected crystal slabs A and B interfaced by steps (one slab thickness 2.17 Å).[632] A precise design of step height (even number of slab thicknesses, i.e., ~0.43 nm) by controlling the miscut angle and annealing temperature could lead to a single-type slab surface for the single crystal TMDs growth (Figure 16d). The universal growth of unidirectional $MoS_2$ domains on both stepped C/A and C/M sapphire further confirmed this claim. This result strongly demonstrated the critical role of surface atomic symmetry in the epitaxial growth of wafer-scale single-crystal TMDs.

These steady advancements in the epitaxial technique of TMDs on sapphire have efficiently improved their electrical performance due to the suppression of grain boundaries. For example, Wang et al. achieved a remarkable average room-temperature device mobility of ~70 $cm^2V^{-1}s^{-1}$ and an on/off ratio of ~$10^9$ based on the as-grown 4-in. highly oriented $MoS_2$ monolayer.[25] The single-crystal prepared by Li et al. exhibited a FET mobility of 102.6 $cm^2V^{-1}s^{-1}$ and a saturation current of 450 $\mu A\ \mu m^{-1}$, together with >94% device yield and a 15% variation in mobility at the centimeter scale.[34] More detailed results on epitaxial growth and the corresponding performance are summarized in Table 1. In this regard, the challenge in material quality has been addressed step by step on the eve of the application of 2D semiconductors. In addition to the sapphire, numerous sulfide-resistant 3D crystalline substrates have also been fully explored in the growth of TMDs, such as quartz,[633,634] $SrTiO_3$,[635−638] $LaAlO_3$,[639] $Ga_2O_3$,[630,640] ZnO,[641] $TiO_2$,[642,643] MgO,[627] SiC,[644] GaN,[645,646] and GaAs[21,647] substrates. The epitaxial TMD islands are also regulated into preferred orientations which can be explained similarly to the case of sapphire.

In summary, seamless stitching of the single orientational domains into a film seems to be the key to the industrial-scale production of large-area single-crystal TMD film. The puzzle of epitaxial growth of TMDs on sapphire has also been gradually unraveled thanks to the combination of experimental and theoretical efforts. Nevertheless, several challenges remain to be addressed, (i) the epitaxial mechanism should be more clarified. Indeed, the epitaxy of TMDs on sapphire is a "black box" coupled with growth dynamics, surface chemistry, step edge, and atomic symmetry. These factors collectively contribute to complex results in both epitaxial registry and dominating factors in unidirectional growth. (ii) the reproducibility should be improved. For instance, the widely adopted step-guiding strategy requires a precise miscut angle and annealing process, to form atomic steps with the desired height, density, and orientation. Otherwise, the misoriented or multilayered TMD domains would hinder the uniform single-crystal growth.

## 5. STRUCTURAL MODIFICATION OF LARGE-AREA TMDs

Structural modifications, such as altering the arrangement of atoms, introducing defects, or incorporating different elements, have been widely proven to be effective strategies to tune


https://doi.org/10.1021/acs.chemrev.3c00851
Chem. Rev. XXXX, XXX, XXX−XXX

electronic properties and customize functionalities in both the traditional bulk and 2D semiconductors. Furthermore, the diverse polymorphisms of 2D TMDs provide an additional platform to enrich electronic structures and explore related physics, such as novel topological state in 1T′ phase monolayer $MoS_2$ and superconducting state in $NbSe_2$. Moreover, the pristine vdW interface of TMDs enables property tailoring via interlayer stacking engineering. Structures with varied layer numbers and stacking orders have attracted extensive investigations in electrical performance, interlayer excitons, nonlinear optics and so on. In this section, we will primarily review the diverse modification techniques for TMD materials, which include (i) component engineering via doping and alloying; (ii) defect engineering, (iii) phase engineering, and (iv) stacking engineering. These flexible structural modifications significantly diversify the application scenarios of TMDs.

## 5.1. Stacking Engineering

**5.1.1. Multilayer Growth.** As investigations into TMD advance, there is an increasing recognition that thickness exerts on their electrical and optical performance. Typically, as the number of layers increases, TMDs (such as $MoS_2$ and $WSe_2$) exhibit enhanced current density and higher carrier mobility, making them more suitable for the channel materials of ideal transistors. This advantage stems from the intrinsic properties of few-layer TMDs, including a reduced band gap and an increased screening effect that mitigates electron/phonon scattering.[648,649] Meanwhile, the stability of few layers helps minimize defects-induced Fermi-level pinning during the fabrication, and hence the Schottky barrier and contact resistance.[650−652] These attributes render them well-suited for demanding applications, including advanced transistors and high-performance sensing devices, where robust current-driving capabilities are essential. Moreover, multilayer TMD materials possess high capacitance and conductivity, making them valuable for manufacturing energy storage devices such as supercapacitors and lithium-ion batteries.

To elucidate the epitaxial growth mode of multilayer TMDs, a qualitative analogy can be drawn with conventional film growth. Generally, the growth of multilayer films can be classified into three types, depending on the interplay between adsorbate−adsorbate and adsorbate−substrate interactions (Figure 17a).[653] The main growth modes are (i) Volmer−Weber (VW) growth (3D growth), which happens when the adsorbate−adsorbate interaction is stronger than the adsorbate−substrate interaction. In this case, adsorbate molecules tend to bond to each other rather than spread out on the substrate, leading to the formation of islands that may coalesce over time. (ii) Frank−van der Merwe (FM) growth (2D growth), characterized by stronger adsorbate−substrate interactions than adsorbate−adsorbate interactions. Adsorbate molecules on the film surface uniformly cover it, forming a continuous layer. This mode, also known as layer-to-layer growth, typically occurs during the initial stages of thin film deposition, with new layers forming only after the completion of the underlying layers. (iii) Stranski−Krastanov (SK) growth (from 2D to 3D growth), lies between the VW growth and FM growth modes, where a few initial layers form uniformly before transitioning to island growth, resulting in a nonuniform film. The ideal vapor-phase deposition of multilayer TMDs is expected to follow a layer-by-layer growth mode. However, during the vapor deposition, the 2D growth mode is always favorable for the first few layers and then evolves into 3D mode for thick layers.

To explore this growth behavior in-depth, Shang et al. developed an integrated DFT and phase diagram modeling approach that demonstrated the existence of a substrate-related critical size, influencing both in-plane lateral and out-of-plane vertical growth during the layer-by-layer growth process.[394] Beyond this critical size, the bilayer $MoS_2$ becomes stable. In addition, Ye et al. theoretically and experimentally proved that lateral and vertical growth is mainly determined by the domain size, temperature, and adatom flux from the vapor of the initial layer.[654] To date, several strategies have been employed to ensure consistent and controllable layer-by-layer growth during the vapor deposition. A notable example is presented by Zheng et al., who introduced a strategy for layer-by-layer growth of $MoS_2$ in a confined space, utilizing a gas-phase rapid sulfurization technique with Mo oxides.[655] The precursors oxidized by Mo foil exhibited varied oxidation states to provide a rapid and continuous source flow, which enabled fine-tuning of the thickness of the $MoS_2$ flakes ranging from monolayer to more than 20 layers. Moreover, temperature and gas fluctuations during TMD growth often result in uncontrolled and undesired thick nucleation on the initial monolayer, which hinders uniform multilayer epitaxial growth. Zhang et al. introduced a reverse-flow CVD approach through precise control of process temperature and airflow direction during the unstable growth stages.[656] Bilayer $MoS_2$ with controllable AA and AB stacking structures were successfully prepared as shown in Figure 17b. Notably, FET devices based on AA stacking bilayer $MoS_2$ samples demonstrated superior electronic performance than the AB stacking counterpart. Recent studies have further confirmed this electronic difference attributed to the stronger interlayer coupling in AA stacking layers and thus the enhanced electron transport performance in the vertical direction.[657,658] The growth of large-area stacking-controlled bilayer $WS_2$ was achieved by a high flux feeding of the W source at high-temperature a-plane sapphire substrates.[659] The prepared R-stacked bilayers exhibited excellent carrier mobility (~30 times greater than monolayer $WS_2$) and interfacial ferroelectricity. Recently, Qin et al. developed an interfacial epitaxy strategy by continuously delivering metals and chalcogens to the interface between single-crystal nickel substrates. This methodology formed a consistent 3R stacking sequence, enabling the growth of various TMD single crystals with thicknesses ranging from a few layers to 15,000 layers.[660]

Epitaxial growth of large-area multilayer TMD films is more challenging from a thermodynamic perspective, where the surface energy of $MoS_2$ increases with the number of layers, which is unfavorable for the epitaxy of multilayer uniform films.[394,652,661,662] Research indicates that engineering the surface energy of $MoS_2$ through the substrate proximity effect could potentially overcome this thermodynamic limitation. In this regard, Wang et al. reported a layer-by-layer epitaxial growth strategy to prepare high-quality 4-in. multilayer (1L to 3L) $MoS_2$ films on sapphire substrate, as illustrated in Figure 17c,d.[648] The FET arrays based on the multilayer $MoS_2$ showed excellent average field-effect mobility at room temperature of 110 and 145 $cm^2V^{-1}$ $s^{-1}$ for bi- and trilayers, respectively. To circumvent limitations from layer-by-layer growth, the direct stitching of aligned multilayer TMD islands is proposed as an alternative strategy. In theory, the free energy is relatively small when the multilayer $MoS_2$ domains are edge-aligned on the sapphire steps. Therefore, it is possible to grow

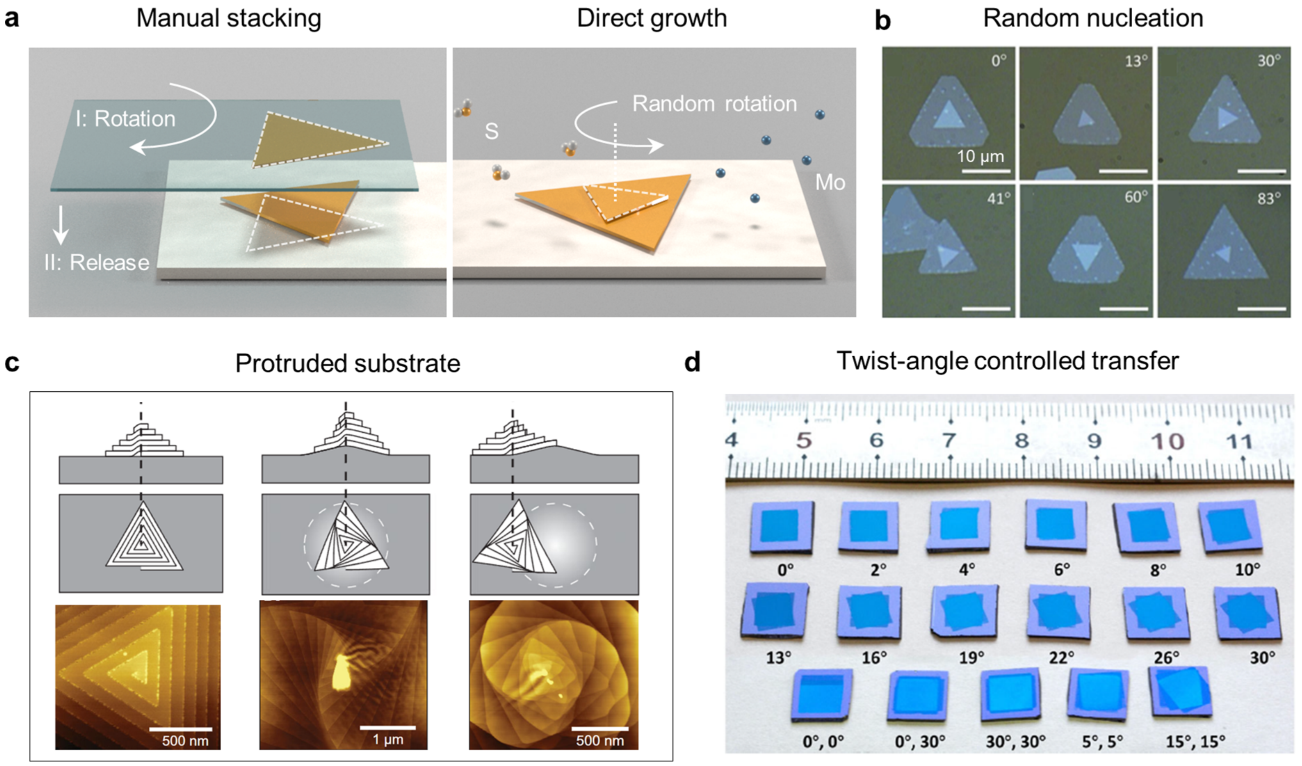


**Figure 18.** Fabrication strategies of large-area twist TMDs. (a) Schematic illustrations of manual stacking and direct growth of twist designing. (b) Optical images of CVD-grown bilayer $WS_2$ with twist angles 0°, 13°, 30°, 41°, 60°, and 83°, respectively. Reprinted with permission from ref 673. Copyright 2015 Wiley-VCH Verlag GmbH & Co. KGaA, Weinheim. (c) Controlled synthesis of supertwisted TMD spirals by introducing non-Euclidean curvatures. Reprinted with permission from ref 678. Copyright 2020 AAAS. (d) Optical images of centimeter-scale transferred $MoS_2$ bilayers with precisely controlled interlayer twist angles. Reprinted with permission from ref 679. Copyright 2020 Springer Nature.

multilayer islands with a controlled thickness on the surface with a certain step height and then stitch them together to obtain a uniform film.[663] Experimentally, Liu et al. successfully fabricated centimeter-scale bilayer $MoS_2$ films on sapphire substrates through edge nucleation and epitaxy.[626] C-plane sapphire substrates with a designed miscut angle allowed for the unidirectional alignment of $MoS_2$ domains. Furthermore, by carefully tuning the atomic terrace height, >99% of nucleations could be controlled as bilayer $MoS_2$ and finally coalesced into continuous film (Figure 17e and f).

Besides, strategies including ALD, MOCVD, and sulfuration of metal oxide precursors can realize the wafer-scale synthesis of multilayer TMDs.[26,664,443] In 2020, Liu et al. demonstrated the synthesis of wafer-scale, thickness-controllable $MoS_2$ films using ALD.[665] By utilizing $MoCl_5$ and hexamethyldisilathiane as precursors, and with the reaction temperature set at 350 °C under a pressure approaching 5 mbar, wafer-scale $MoS_2$ films were synthesized on wafer-scale sapphire and $SiO_2$ substrates. The thickness of $MoS_2$ layers was modulated by the ALD cycles. Furthermore, the experiment utilized these $MoS_2$ films to produce large-scale FET arrays and logic circuits, including inverters, NAND, AND, NOR, and OR gates, showcasing the potential for their scalable applications. In addition, Kalanyan et al. reported a pulsed MOCVD method to grow $MoS_2$ films with different thicknesses at the wafer scale.[664] Experimentally, they used metal−organic and organosulfur as precursors, and they deposited $MoS_2$ films with thickness from ~1 nm to ~25 nm with a growth rate of 0.12 nm/pulse. These methods provide new avenues for high-throughput production of wafer-scale multilayer TMDs, but the controllability and crystallinity required to be further improved.

The unique structure and properties of multilayer 2D TMDs offer new freedom for innovation in electronics and optoelectronics. However, the production of multilayer TMD materials poses practical challenges that necessitate careful consideration and resolution. (i) The precise stacking order (2H or 3R) between layers profoundly influences the performance of multilayer TMDs, which must be precisely controlled across the large-area multilayers. (ii) The thickness uniformity and single-crystallinity of the TMD multilayers are crucial to guarantee reproducibility and stability of corresponding devices. (iii) The synthesis of large-area uniform four or thicker TMD layers has not been validated on dielectric substrates.

**5.1.2. Twist Design.** Introducing arbitrary twist angle ($\theta$) between bilayer 2D layers provides the $\theta$-dependent moiré superlattice at the vdW interface. This distortion has attracted extensive attention in both TMD systems for exploring exotic phenomena such as strong correlation physics, moiré photonics, and optoelectronics. Experimentally, these artificial twisted crystals are mainly prepared by the "tear-and-stack" technique, where unavoidable contaminations, strains, and lattice reconstruction could limit the reproducibility and uniformity of the twisted samples.[666] Therefore, the direct synthesis of twist TMDs with a clean interface is promising for constructing ideal moiré materials (Figure 18a). However, the nontwisted AA and AB stacking are energetically favorable compared with arbitrary twisted structures. The main challenge lies in how to introduce perturbations to overcome this energy barrier and definitely design the interlayer twist angles.[667]

During the CVD growth of TMDs, twist bilayers could emerge randomly.[668−672] In 2015, Zheng et al. directly grew


https://doi.org/10.1021/acs.chemrev.3c00851
Chem. Rev. XXXX, XXX, XXX−XXX

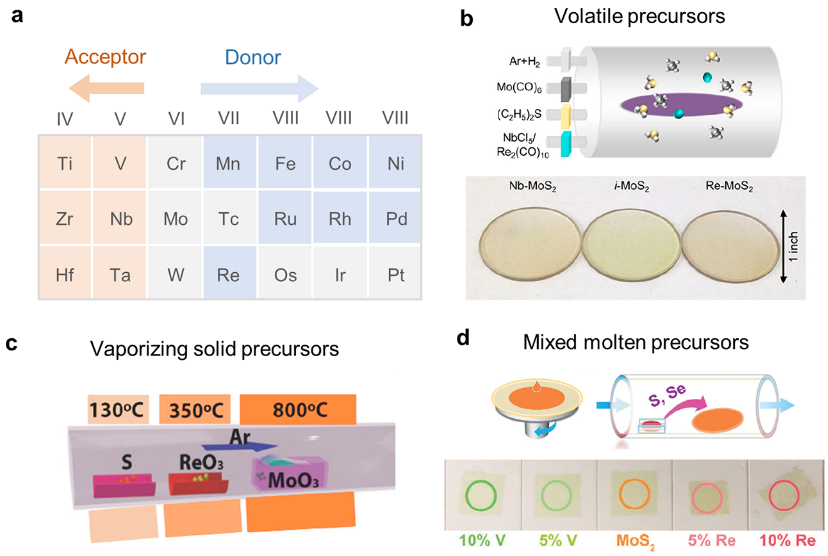


**Figure 19.** Donor/acceptor substitution of large-area TMDs. (a) Elements that can substitute the metal sites of Group VI TMDs, the orange and blue colors indicate their roles as either acceptors or donors, respectively. (b) Schematic illustrations of the MOCVD system for the growth of doped $MoS_2$ using volatile precursors (top panel) and the optical micrograph of intrinsic and doped $MoS_2$ grown on 1-in. fused silica (bottom panel). Reprinted with permission from ref 693. Copyright 2020 American Chemical Society. (c) Schematic for the synthesis of monolayer Re-$MoS_2$ using $ReO_3$ powder as the precursor. Reprinted with permission from ref 695. Copyright 2018 Wiley-VCH Verlag GmbH & Co. KGaA, Weinheim. (d) Schematic illustrations of the CVD growth of Re- and V-doped TMDs by mixed salt solution (top panel) and optical images of the transferred samples with different dopant concentrations (bottom panel). Reprinted with permission from ref 712. Copyright 2021 Wiley-VCH Verlag GmbH & Co. KGaA, Weinheim.

$WS_2$ bilayers with random twist angles of 0°, 13°, 30°, 41°, 60°, and 83° using the CVD method (Figure 18b).[673] Yu et al. found that the collision and coalescence of monolayer TMDs with different orientations led to twisted bilayers with high probability in a range of $20° < \theta < 55°$.[674] The mechanism was explained as the strain generated by coalescence induced the second-layer nucleation and preserved the original crystal misorientation angle. Recently, Xu et al. proposed a reconfiguring nucleation CVD strategy and synthesized a large number of TMD bilayers with random twist angles ranging from 0° to 120°.[675,676] Systematic examinations indicated that increasing the molar ratio of NaCl to $MoO_3$ or decreasing the gas flow rate could improve the yield (17.2%) and density (28.9 pieces/$mm^2$) of twisted $MoS_2$ samples. In addition, precise control of the interlayer twist in multilayer TMD spirals has been achieved through substrate engineering. These supertwist spiral structures are driven by screw dislocation, a typical line defect that enables the continuous growth of layered TMD in an out-of-plane direction.[677] Zhao et al. introduced the curved substrate surfaces and demonstrated the controlled growth of super-twisted spirals of $WS_2$ and $WSe_2$ materials (Figure 18c).[678] The success of this model can be attributed to its utilization of nanoparticles as protrusions on planar substrates, which introduces non-Euclidean curvature into the growth process. Experimental evidence provides further validation for the formation of moiré superlattices between atomic layers, emphasizing the potential for precise control of twist angles in TMD materials.

To date, the direct growth of twist TMDs is still limited by the small sample sizes and random twist angles. The production of large-area twist structures constitutes a pivotal step for applications in twistronics, which could be addressed by manually transferring large-area as-grown monolayers. In 2020, Liao et al. reported the centimeter-scale multilayer $MoS_2$ stacks with precisely controlled interlayer twist angles by water-assisted transfer of 2-in. highly oriented monolayer $MoS_2$ (Figure 18d).[679] Although this combination of epitaxial growth and transfer technique facilitates the realization of vdW stacked structures with precise twist angles over large areas, the interfacial imperfect still degenerates the quality of the prepared twisted crystals.

In summary, the emergence of as-grown twisted 2D TMDs offers an exciting avenue for exploring novel physics and enables promising electronic and optoelectronic applications. Nevertheless, the controlled and uniformly twist angles across the large-area synthesized multilayer TMDs are still challenging due to the competition with nontwist cases during the high-temperature growth process. New modulation mechanisms and growth strategies are requisite to satisfy the demands of high-quality moiré material in this field.

## 5.2. Component Engineering

### 5.2.1. Donor/acceptor Substitution.

Introducing impurity atoms into a perfect crystal lattice would lead to disturbances in period potential, allowing for the modulation of electronic structures. This component engineering is utilized as a powerful tool in bulk semiconductors for tuning the carrier types and concentrations. Selective n- and p-doping is crucial for constructing p−n junction in high-rectification diodes and high-response photodetectors. However, the ion implantation techniques, widely used in the silicon industry, can be challenging when applied to 2D materials due to the potential damage to their atomically thin structures. Alternatively, various strategies have been tailored for direct synthesizing doped 2D semiconductors such as MOCVD, vaporizing solid precursors, mixed dopant salts, and so on. For the functionalization of Group VI TMD materials (e.g., $MoS_2$ and $WSe_2$), Group V (e.g., V and Nb) and Group VII (e.g., Re and Mn) dopants work as acceptors and donors, resulting in p-


https://doi.org/10.1021/acs.chemrev.3c00851
Chem. Rev. XXXX, XXX, XXX−XXX

and n-type doping, respectively (Figure 19a). The isoelectronic doping (Mo and W) will be further discussed in Section 5.2.2. Besides electrical properties modulations, magnetic dopants such as Fe and Co elements could introduce fascinating magnetic properties to 2D semiconductors.[680−685]

To date, the main challenges of TMDs doping lie in the following respects: (i) diversity of doped elements. The range of dopants is limited due to concerns about lattice distortion extent and thermodynamic stability of impurity-doped structures. Precise tuning of doping conditions, selection of suitable precursors, and adoption of appropriate strategies are demanded to further reduce the formation energy and enable a flexible doping process.[686] (ii) fine-tuning doping concentration. Due to the quantum confinement and reduced screening in 2D materials, the ionization energy of dopants in TMDs is higher compared with the cases in bulk species. Consequently, a high doping concentration of up to several percent with excellent controllability is required for material performance modulation. (iii) spatial uniformity in doping. A steady precursor/dopant ratio during growth is the prerequisite for achieving large-area doped TMDs. Besides, numerous factors such as substrate surface, edge termination of TMDs, doping concentration, and annealing process can affect the uniformity of the prepared sample.[687−689]

The MOCVD technique using volatile metal precursors (e.g., heated $NbCl_5$, $Re_2(CO)_{10}$) works as a powerful tool for controlled doping of TMDs materials.[690−692] This method offers the advantage of fine-tuning the doping concentration over a wide range managed by a gas flow controller. Additionally, the use of active and volatile dopants facilitates large-area doping with excellent uniformity. As shown in Figure 19b, Gao et al. fabricated homogeneous 1-in. Nb-doped, intrinsic, and Redoped $MoS_2$ monolayer wafers using MOCVD.[693] The doping concentration can be reproducibly adjusted up to 20% and the electrical conductance of the Nb-doped $MoS_2$ was tuned over 7 orders of magnitude. Besides, benefiting from the precise control over precursor partial pressure in MOCVD, Kozhakhmetov et al. realized highly precise doping down to 0.0001% Re atoms in the $WSe_2$ lattice, and the growth and doping processes were carried out below the BEOL temperature limitation.[694] It is also suggested that the dilute Re doping (down to 500 ppm) could reduce the sulfur vacancy and improve the carrier transport.[691]

Solid dopant powders (e.g., $ReO_3$, $NbCl_5$, $FeCl_2$) are also widely employed in high-temperature CVD chambers to facilitate the doping process, which can be vaporized under similar conditions to those used for $MoO_3$ or $WO_3$ precursors. For instance, Zhang et al. utilized the "point-to-face" strategy to supply Re dopants by thermally evaporating $ReO_3$ powder at 350 °C (Figure 19c).[695] This process led to a Re doping concentration of 1 at% in $MoS_2$ crystal, which behaved as the n-type transport feature, and the defect-bound emission was significantly quenched. This is a universal technique benefiting from various available dopants and operation convenience, which has proven effective in preparing on-demand doped samples by introducing adequate Nb, Re, Fe, Co, Mn, V, Zn, Sn, Eu, and other impurities into TMD materials.[622,623,696−704] Similar to the challenge faced in power-based TMDs growth, as discussed in the previous sections, the diffusion-induced dopant concentration gradient should be carefully controlled to ensure large-area uniformity. To date, modified strategies such as halide salt assistance and molten salt mixing also have been developed for efficient doping.[705,706] Specifically, soluble precursors dispersed on the target substrate can provide a uniform dopant supplement for large-area sample growth.[707−711] Li et al. mixed the additive $NaVO_3/NaReO_3$ with $Na_2MoO_4/Na_2WO_4$ precursors, followed by sulfurization, which enabled the fabrication of high-crystallinity TMDs films with tunable doping concentrations (Figure 19d).[712]

In addition to the substitution of metal elements, the doping at chalcogen sites also facilitates property modifications. The Group XV (e.g., N and P) and Group XVII (e.g., F and Cl) atoms act as p- and n-dopants, respectively.[713−716] In-situ substitution with these nonmetal elements is challenging due to the high formation energy required in the vapor deposition conditions. Consequently, postprocessing of intrinsic TMDs provides an alternative way. The doping of corresponding nonmetal atoms has been realized by various methods, including plasma implanting, laser irradiation, solution soaking, and so on.[717−720] For example, Azcatl et al. exposed $MoS_2$ layers in $N_2$ plasma and realized the p-type covalent nitrogen doping together with a compressive strain.[721] Another strategy is predoping the target atoms into precursor films, Cao et al. prepared $WO_xN_y$ film using the ALD technique with controllable thickness, and the following sulfurization resulted in the N-doping $WS_2$ showing excellent p-type behavior.[722]

### 5.2.2. Isoelectronic Substitution.

When adequate amounts of impurity atoms are introduced into a host TMDs material, it can be regarded as the alloying of different components.[723] This allows for the continuous tuning of basic properties like lattice constants and band gaps over a wide range, depending on the concentration ratios. Isoelectronic atoms act as appropriate alloying pairs due to their similar lattice constants and M-X bond lengths, which are mixing-energy favorable and thermodynamic stable in structures. In 2013, Dumcenco et al. demonstrated the random alloying of metal elements (Mo or W) in monolayer $Mo_{1-x}W_xS_2$ as visualized using STEM.[724] To date, the disordered isoelectronic substitution of both chalcogen sites and metal sites has been realized experimentally (Figure 20a) to form a series of monolayer alloys including ternary[725−733] ($MoS_{2(1-x)}Se_{2x}$,

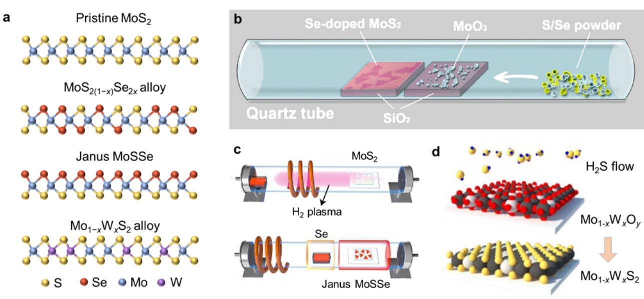


**Figure 20.** Isoelectronic substitution of large-area TMDs. (a) The atomic models of the isoelectronic substitutional monolayer $MoS_2$, from top to bottom, pristine $MoS_2$, $MoS_{2(1-x)}Se_{2x}$ alloy, Janus MoSSe, and $Mo_{1-x}W_xS_2$ alloy. (b) Controlled synthesis of large-area $MoS_{2(1-x)}Se_{2x}$ via CVD with S/Se powder positioned at low temperature zone. Reprinted with permission from ref 737. Copyright 2013 American Chemical Society. (c) Synthesis of the Janus MoSSe monolayer by striping the top-layer S via $H_2$ plasma and followed by thermal selenization. Reprinted with permission from ref 750. Copyright 2017 Springer Nature. (d) Controlled synthesis of $Mo_{1-x}W_xS_2$ alloys by sulfurizing supercycle ALD prepared $Mo_{1-x}W_xO_y$ layer. Reprinted with permission from ref 774. Copyright 2015 Springer Nature.


https://doi.org/10.1021/acs.chemrev.3c00851
Chem. Rev. XXXX, XXX, XXX−XXX

$WS_{2(1-x)}Se_{2x}$, $Mo_{1-x}W_xS_2$, and $Mo_{1-x}W_xSe_2$) and quaternary[366,734] ($Mo_{1-x}W_xSe_{2(1-y)}S_{2y}$ and $MoS_{2(1-x-y)}Se_{2x}Te_{2y}$) species. This flexible component design enables precise bandgap engineering, which is crucial for photon absorption/emission-related applications such as displays, sensors, and photodetectors. Specifically, the chalcogen site substitution selectively takes place at the top or bottom sublayers of TMDs resulting in structures known as Janus monolayers (e.g., MoSSe and WSSe).[735] Their intrinsic out-of-plane inversion asymmetry raises attractive properties such as out-of-plane SHG and piezoelectricity. In this section, we mainly focus on the preparation strategies for these disordered alloys and novel structures by isoelectronic substitution.

The isoelectronic substitution of chalcogen sites is feasible because these atoms are exposed at the surface of TMD materials and the structure is free to relax.[736] In 2013, Gong et al. utilized the mixed S and Se powders (Figure 20b) as the chalcogen precursors for vapor deposition of large-area $MoS_{2(1-x)}Se_{2x}$ monolayers on $SiO_2$/Si.[737] The band gap of the film could be arbitrarily tuned from 1.8 eV (pure $MoS_2$) to 1.5 eV (pure $MoSe_2$) by varying the S/Se atoms ratio. The detailed emission energies showed a bowing behavior while changing the composition. The operation convenience of this mixed chalcogen source has led to its widespread use in the one-pot deposition of random ternary alloys, with alloy content controlled by the source ratio.[488,738,739] For example, Fortin-Deschênes et al. employed a two-step strategy to construct the $WS_ySe_{2-y}/WS_xSe_{2-x}$ bilayer alloys with different chalcogen contents, achieving high-quality moirés with a tunable period from 10 to 45 nm, controlled by the lattice mismatch.[740] Moreover, Feng et al. simultaneously heated the $MoS_2$ and $MoSe_2$ powders and deposited them onto the target substrate to form $MoS_{2(1-x)}Se_{2x}$ ($x$ = 0−0.4) alloys.[741] Higher Se concentration ($x$ = 0.4−1.0) was also achieved by adding Se vapor in this PVD system.[742] Besides, the exposed chalcogen layers of TMDs can easily be decomposed and substituted by other chalcogen atoms at high temperatures.[743−745] Su et al. achieved fine-tuning of components by selenizing preprepared $MoS_2$ in selenium vapors, with substitution temperatures as a control factor.[746] Similarly, Taghinejad et al. exchanged the Se atoms of host $MoSe_2$ with S atoms and obtained $MoS_{2(1-x)}Se_{2x}$ structures, indicating that CVD-grown films with abundant vacancy defects are more easily alloyed.[747] This exchange strategy is also suitable in the tellurization process, Yun et al. converted $MoS_2$ and $WS_2$ into $MoS_{2-x}Te_x$ and $WS_{2-x}Te_x$ alloys with the assistance of sodium atoms.[748] Conversely, prepared 1T′-$MoTe_2$ could be alloyed with sulfur, triggering a phase transition to the 2H phase with varying alloy content.[749]

The postsubstitution of chalcogen layers indicates the novel Janus structure could be artificially designed by precisely controlling mild substituting conditions. In 2017, Lu et al. used $H_2$ plasma to strip the top S atom layer of monolayer $MoS_2$, forming the intermediate MoSH structure. This was then thermally selenized into a Janus MoSSe layer at 450 °C (Figure 20c).[750] The asymmetric structure was carefully examined by cross-section STEM, energy-dependent XPS, and out-of-plane SHG. Moreover, $H_2$ plasma-activated chalcogen powders could directly transform TMDs into Janus structures at room temperature, where active H radicals significantly reduce the reaction energy barriers.[751,752] This method has led to the creation of various Janus materials such as 2H-MoSSe, 1T′-MoSSe, WSSe, NbSSe, and their heterostructures.[753−755] Besides, low-energy Se implantation by PLD can kinetically convert $WS_2$ into desired Janus WSSe.[756,757] Alternatively, directly high-temperature substitution also gives similar results, Zhang et al. sulfurized the as-grown $MoSe_2$ monolayers at a specific temperature window of 750−850 °C, forming a Janus MoSSe structure.[758]

Oxygen atom substitution is a well-known isoelectronic dopant in TMDs, which always occurs during ambient condition oxidation or the introduction of oxygen during the growth process.[759−761] Pető et al. revealed that under ambient exposure, sulfur atoms in $MoS_2$ could be individually replaced by oxygen, ultimately leading to a $MoS_{2-x}O_x$ crystal.[762] The single-atom oxygen centers significantly improved the catalytic activity in electrochemical $H_2$ evolution. Besides the mild oxidation, the oxygen plasma treatment can quantitatively introduce O atoms into the TMD lattice and improve the electrical performance.[763,764] Jadwiszczak et al. applied $O_2$/Ar plasma to pristine $MoS_2$ layers and observed an initial deterioration in mobility, which then recovered to above-original levels after a critical 6-s treatment.[765] This phenomenon was attributed to the formation of a 2D $MoO_x$ layer that screened charges associated with sulfur vacancies.

The isoelectronic substitution at metal sites in TMDs needs to overcome the challenge of inhomogeneous mixing of metal atoms.[766−770] Their limited diffusion ability hinders the formation of large-area uniform alloys, leading to a gradient composition or even the formation of heterostructures. To bridge the growth temperature gap between $MoS_2$ and $WS_2$ when using oxide powders, Wang et al. replaced $WO_3$ with the more volatile $WCl_6$, successfully synthesizing large-area uniform $Mo_{1-x}W_xS_2$ alloy with tunable components.[771] Steady cofeeding of metals can also be achieved by uniformly dispersing precursors. For example, Lee et al. applied a solution processing method where $MoO_3$ and $WO_3$ were spin-coated onto the substrate and then heated to target temperature windows.[772] This approach enabled the controlled synthesis of a series of structures including $Mo_{1-x}W_xS_2$ alloy, $MoS_2$/alloy, alloy/$WS_2$, and $MoS_2/WS_2$ heterostructures. Similarly, Kim et al. dispersed $MoO_2$ and $W_{18}O_{49}$ nanoparticles across the substrate, adjusting the components by varying the Mo/W precursor ratio.[773] Additionally, the two-step strategy efficiently avoids the precursor diffusion issues by codepositing metal layers. Song et al. carried out the supercycle ALD process (consisting of $n$ cycles of ALD $MoO_x$ and $m$ cycles of ALD $WO_3$) to obtain a $Mo_{1-x}W_xO_y$ layer (Figure 20d).[774] This layer was then sulfurized into $Mo_{1-x}W_xS_2$ alloy by heating in $H_2S$ gas. The alloying Mo/W ratio corresponded to the $n/m$ ratio of the ALD supercycles. Park et al. cosputtered a $Mo_{1-x}W_x$ metal film and subsequently sulfurized it to form $Mo_{1-x}W_xS_2$ multilayers, where postlaser processing could thin the film into a monolayer alloy.[448] Zheng et al. used PLD to prepare centimeter-sized $Mo_{0.5}W_{0.5}Se_2$ alloying films. Their work demonstrated that alloying engineering in TMDs could significantly suppress the deep-level defect states and further improve the device performance.[775]

### 5.3. Phase Engineering

The polymorphic nature of TMDs and corresponding diverse electronic structures provide extra freedom for functionalization by phase engineering. For group VI TMDs, the access to metastable 1T/1T′ phase inspires fruitful explorations such as hydrogen evolution, contact optimization, and topological FETs.[776−778] Electrochemical ion intercalation-based exfoliation of TMD serves as a high-yield producing strategy for


https://doi.org/10.1021/acs.chemrev.3c00851
Chem. Rev. XXXX, XXX, XXX−XXX

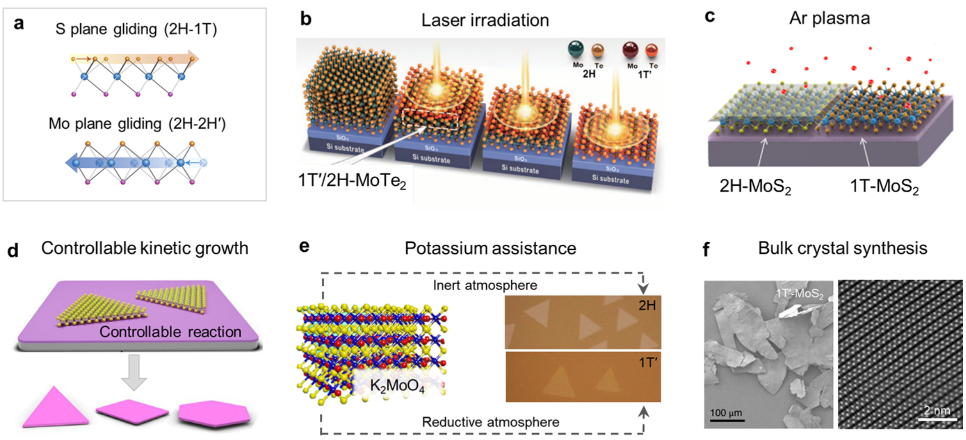


**Figure 21.** Phase engineering of large-area TMDs by phase transition and selective synthesis. (a) Atomic mechanism of the 2H/1T phase transition of $MoS_2$ by gliding atomic planes of S and Mo planes, which results in the 2H → 1T and 2H → 2H′ transition, respectively. Reprinted with permission from ref 786. Copyright 2014 Springer Nature. (b) Laser-driving 2H → 1T′ phase transition of $MoTe_2$. Reprinted with permission from ref 787. Copyright 2015 AAAS. (c) Formation of 1T phase $MoS_2$ by Ar plasma treatment. Reprinted with permission from ref 788. Copyright 2017 American Chemical Society. (d) Kinetic growth mode for the controllable synthesis of transition metal chalcogenides with different phases and compositions. Reprinted with permission from ref 804. Copyright 2023 Springer Nature. (e) K-assisted selective CVD growth of 1T′ and 2H phase $MoS_2$ monolayers. Reprinted with permission from ref 811. Copyright 2018 Springer Nature. (f) The SEM image of the prepared micrometer-sized 1T′-$MoS_2$ bulk crystals (left panel) and the STEM image of single-layer 1T′-$MoS_2$ nanosheet (right panel). Reprinted with permission from ref 812. Copyright 2018 Springer Nature.

preparing metallic 1T/1T′ nanosheets, but it potentially suffers from limited phase purity and lateral size.[779,780] Alternatively, the controllable phase transition and direct-growth approaches enabled the phase engineering of large-area TMDs. In theory, the energy barriers ($\Delta E$) between the 2H and 1T/1T′ species should be overcome to obtain metastable phases, which vary in TMDs with different chemical components. For example, in Mo-dichalcogenides, the $\Delta E$ are evaluated to be $\Delta E[MoS_2] > \Delta E[MoSe_2] > \Delta E[MoTe_2]$.[531] Specifically, $WTe_2$ inherently possesses the 1T′ ground-state structure. In this section, we mainly focus on various phase engineering strategies aimed at large-area phase transition and selective synthesis of metastable phase TMDs.

The phase transition of TMDs could be triggered via various modulations such as electron beam irradiation, laser irradiation, electrostatic doping, plasma bombardment, chemical treatment, strain engineering, and plasmon excitation.[781−785] As shown in Figure 21a, the atomic mechanism of the 2H/1T phase transition in $MoS_2$ lies in the gliding atomic planes of S and/or Mo, where an intermediate phase acts as an important precursor.[786] Chalcogen vacancies in TMDs can serve as electron donors and facilitate the phase transformation. For example, laser irradiation was employed to create irreversible Te vacancy and derive the phase transition of 2H-$MoTe_2$ to 1T′ species (Figure 21b).[787] The transistors based on the 2H/1T′ patterns exhibited excellent performance due to the ohmic contact. Similarly, the bombardment from gentle Ar plasma with certain kinetic energy also induced a phase transition from 2H to 1T in monolayer $MoS_2$ (Figure 21c).[788] Besides the defect induction, another commonly used phase transition strategy is the introduction of alkali ions by chemical treatment. The mechanism lies in the charge transfer from the alkali ions to the host 2H species leading to the change of electron counts in *d* orbitals of transition metal atoms, thereby stabilizing the metallic 1T phase.[789−792] For example, Kappera et al. immersed the poly(methyl methacrylate) (PMMA) masked 2H-$MoS_2$ sample in *n*-butyl lithium and realized the locally patterned transition to the 1T phase.[793] Moreover, this phase transition process is layer-dependent, where the phase stability for 2H-$MoS_2$ is demonstrated to decrease in thicker layers.[794]

Besides the phase transition strategy, phase selectable synthesis of large-area TMDs is also a favorable approach because of the high phase purity and crystallinity. The direct synthesis of metastable phases of TMDs can be achieved by techniques such as optimizing reaction kinetics, composition tuning, addictive assistance, interface engineering, and precursor design.[795−803] As shown in Figure 21d, Zhou et al. demonstrated a competitive-chemical-reaction-based growth mechanism and controllably synthesized 67 types of transition metal chalcogenides (TMCs) and transition metal phosphorus chalcogenides (TMPCs) with defined phase, controllable structure, and tunable component.[804] Low-concentration doping and wide-range alloying process facilitate the phase controlling between the H and T phases.[805−807] For example, the $WTe_{2x}S_{2(1-x)}$ alloys prepared via the one-step CVD method processed a phase transition from 1H to 1T′ while the Te concentration $x$ increasing.[808] Moreover, the interfacial interaction between as-grown material and substrate also provides the freedom for the phase-controlled growth of TMDs. The Se-pretreated Au(111) is more favorable for 1T′-$MoSe_2$ growth due to the Mo intercalation of the Au−Se interface stabilizing the 1T′ phase.[809] The in-plane compressive strain at the interface of $WSe_2$ and $SrTiO_3$ (100) substrate enabled the 100% pure 1T′ phase growth via MBE.[810]

Liu et al. demonstrated a K-enriched CVD growth of high-phase-purity 1T′-$MoS_2$ monolayers using $K_2MoS_4$ as the precursor (Figure 21e).[811] The 1T′ phase was calculated as more stable than the 2H phase while increasing K concentration exceeding 44%. Similarly, these K-contained precursors were also utilized to synthesize high-phase purity 1T′ TMDs bulk crystals. As shown in Figure 21f, by designing a two-step reaction between $K_2MoO_4$ and S powders, micrometer-sized metallic-phase 1T′-$MoS_2$ was robustly fabricated.[812] The as-prepared metastable structures were convertible to 2H species by thermal annealing or laser


https://doi.org/10.1021/acs.chemrev.3c00851
Chem. Rev. XXXX, XXX, XXX−XXX

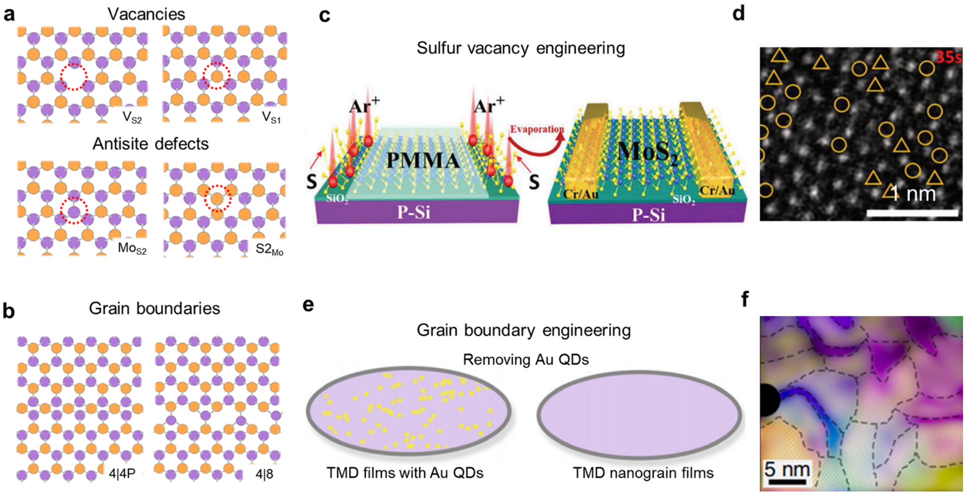


**Figure 22.** Defect structures and corresponding engineering in large-area TMDs. (a) Typical atomic structure diagram of point defects (vacancies and antisite defects). (b) Typical atomic structure diagram of line defect (grain boundaries). (c) Schematic for the monolayer $MoS_2$ FET with ohmic contact by sulfur-vacancy engineering. (d) HAADF-STEM image of monolayer $MoS_2$ after 35 s of argon plasma processing. (c,d) Reprinted with permission from ref 829. Copyright 2015 Wiley-VCH Verlag GmbH & Co. KGaA, Weinheim. (e) Growth of wafer-scale nanograin TMD films by the Au quantum dots assist CVD. (f) False-colored frequency filtered images of TMD films with ultrahigh grain boundary densities. (e,f) Reprinted with permission from ref 839. Copyright 2020 Springer Nature.

irradiation. Furthermore, this synthetic method appeared general for large-scale fabrication of metastable 1T′-phase TMDs including $WS_2$, $WSe_2$, $MoS_2$, $MoSe_2$, $WS_{2x}Se_{2(1-x)}$, and $MoS_{2x}Se_{2(1-x)}$.[813]

Despite significant advancements in the phase engineering of TMDs, the development of techniques for direct synthesizing large-area, thickness-controlled, and phase-pure metastable TMDs is still in its nascent stages due to the constraints imposed by formation energy. Their applications are also constrained by challenges in large-scale production and the limited thermal stability of metastable TMDs, which leads to phase transitions and the formation of mixed phases. Therefore, in-depth studies of the growth mechanisms and structural changes of metastable TMDs, utilizing advanced in situ techniques, may provide valuable insights for developing new synthesis strategies to produce metastable TMDs and promote their widespread application.

### 5.4. Defects Engineering

Atomically-thin TMDs typically possess a high defect density of $\sim 10^{13}$ $cm^{-2}$ that crucially modulates their electronic and optical properties. Defect engineering strategies involve the deliberate introduction, healing, or modification of defects within the crystal lattice that can tailor TMDs for diverse application scenarios. Suppressing the defect density toward the perfect single crystal is the ultimate goal of the TMD material synthesis, to take advantage of their fascinating intrinsic characteristics. An alternative proposal is employing the defects to functionalize TMDs. For example, defects can reduce the metal contact resistance, improving the device performance based on 2D TMDs.[814] In addition, the density of catalytic sites can be increased by introducing specific types of defects in the hydrogen evolution process, thus improving the reaction rate and efficiency.[815] In this section, we will briefly introduce the 0D and 1D defects in the vapor-deposited TMDs, and then discuss the potential applications based on these intrinsic or extrinsic defects.

In practice, owing to the ultrathin 2D nature and exceedingly high surface area of TMDs, the introduction of defects during sample synthesis remains inevitable regardless of the synthetic method employed. Defects within TMDs are disruptions in the orderly geometric arrangement of atoms in a crystalline solid, and the classification of defect structures can be divided into two categories, namely 0D point defects and 1D line defects. Point defects occur at specific locations within the TMD lattice as shown in Figure 22a, including the vacancies (monosulfur vacancy $V_S$, disulfur vacancy $V_{S2}$, vacancy complex of Mo and nearby three sulfur $V_{MoS3}$ and so on) and antisite defects (Mo atom substituting a S2 column $Mo_{S2}$ and a S2 column substituting a Mo atom $S2_{Mo}$).[816] The dominant category of point defects is different depending on the synthetic methods, for instance, the sulfur vacancies are frequently observed in the CVD and mechanical exfoliation sample, but Mo antisites are dominant in PVD samples.[817] Line defects involve atoms or lattice dislocations arranged linearly along distinct orientations, the dominant line defects in TMDs are the 1D grain boundaries. The complex dislocation cores compose various grain boundaries in vapor-deposited polycrystalline TMDs (such as 5|7, 4|4, 4|6, 4|8, and 6|8 fold rings).[816] For example, two 60° rotated grains could give different boundary structures (Figure 22b), 4-fold rings with point sharing at a common S2 site (4|4P structure), and 4-fold rings with edge-sharing (4|4P structure). These rich defect structures hold the potential to modulate the electronic structure of TMDs, and corresponding engineering has provided a range of opportunities in fields such as optics, electronics, and catalysis.[814,815,818−821]

The defects have a double-sided effect on the electrical performance of TMD-based devices. On the one hand, these defects can serve as localized scattering centers, degenerating the mobility of charge carriers. On the other hand, defect states provide extra freedom in functionalizing electronic and optoelectronic devices.[822] In 2016, Ly et al. demonstrated that grain boundaries in $MoS_2$ reduced its electrical properties, and the performance is misorientation-angle-dependent on the grain boundaries.[823] Therefore, how to reduce the defect density and access ultrapure TMDs has become a widely concerned topic. In recent years, numerous strategies such as poly(4-styrenesulfonate) processing, grain boundary sliding,


https://doi.org/10.1021/acs.chemrev.3c00851
Chem. Rev. XXXX, XXX, XXX−XXX

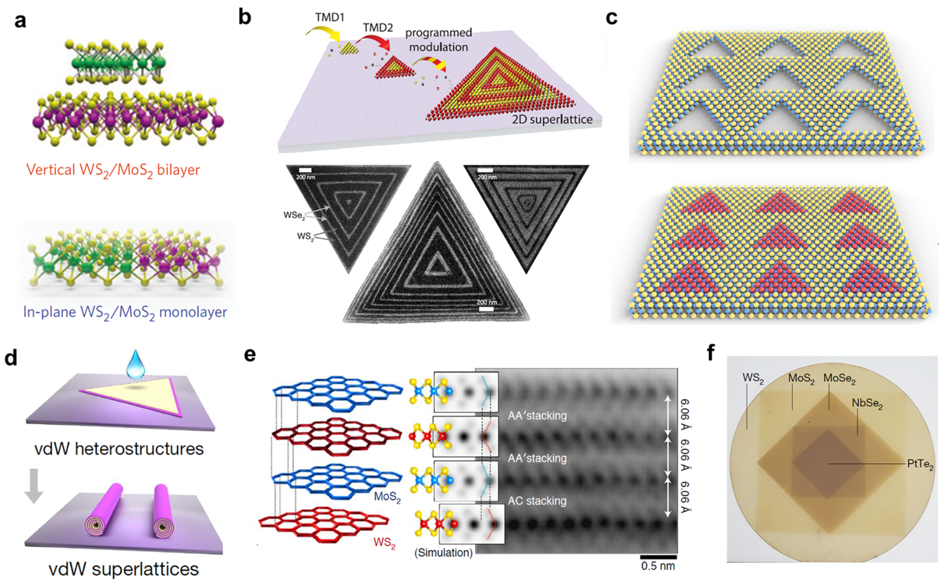


**Figure 23.** Preparation strategies of large-scale lateral and vertical TMD heterostructures. (a) Schematic of the vertically stacked $WS_2/MoS_2$ heterostructures synthesized at 850 °C and corresponding in-plane heterojunctions grown at 650 °C. Reprinted with permission from ref 843. Copyright 2014 Nature Materials. (b) Schematic of 2D superlattices based on monolayer TMDs and SEM images of three monolayer $WS_2/WSe_2$ superlattices. Reprinted with permission from ref 852. Copyright 2018 Science. (c) Schematic of a holey $WS_2$ structure featuring a periodic array of triangular holes (up) and the $WS_2$−$WSe_2$ monolayer mosaic heterostructures produced on the holey $WS_2$ templates (down). Reprinted with permission from ref 854. Copyright 2022 Nature Nanotechnology. (d) Schematic illustration of the fabrication process of roll-up vdW superlattices. Reprinted with permission from ref 380. Copyright 2021 Nature. (e) Schematics (left) and bright-field STEM images (right) with the corresponding atomic model simulations for coherent SL stacks. Reprinted with permission from ref 861. Copyright 2021 Nature Nanotechnology. (f) Optical image of wafer-scale multiblock vdW superconductor heterostructure films for a five-block heterostructure consisting of $WS_2$, $MoS_2$, $MoSe_2$, $NbSe_2$, and $PtTe_2$ (from bottom to top) grown on sapphire. Reprinted with permission from ref 452. Copyright 2023 Nature.

electrode-induced healing, and modulating precursor ratio have been carried out to obtain TMDs with ultralow defect density.[824−827] Reducing the line-defects by epitaxial techniques were systematically discussed in the previous chapter. In addition, studies have shown that chalcogen atom vacancies in TMDs at contact regions can significantly reduce contact resistance and improve device performance.[814,828] Xiao et al. reported the defect engineering to achieve ohmic contact (as low as 1.7 kΩ·$\mu$m) between the metal and CVD monolayer of $MoS_2$ with a large number of sulfur vacancies introduced by mild Ar plasma treatment (Figure 22c,d).[829] The prepared monolayer $MoS_2$ FETs behaved ultrahigh carrier mobility of 153 $cm^2\ V^{-1}\ s^{-1}$ and large on/off ratio of $4 \times 10^9$.

The defective sites of TMDs usually have high reactivity, which can adsorb and activate reaction substances and promote the catalytic reaction. In 2015, Deng et al. demonstrated for the first time that single-atomic Pt metal doping in HER can increase the catalytic activity of $MoS_2$.[830] Single-atomic doping including elements like Ru, Co, Au, Pd, and so on, has also demonstrated improved catalytic activity within TMDs.[831−834] In 2015, Li et al. reported optimizing HER performance by introducing S vacancies and strain in monolayer $MoS_2$.[835] Theoretical and experimental results show that the S vacancy serves as a catalytic site, and the gap states around the Fermi level allow hydrogen to directly bind with exposed Mo atoms and improves the catalytic activity. In recent years, improving the catalytic activity of TMDs by grain boundary engineering has attracted widespread attention.[815,836−838] For example, He et al. fabricated wafer-scale nanograin TMD films via Au quantum dot assisted CVD, with ultrahigh grain boundary densities up to $\sim 10^{12}$ $cm^{-2}$ (Figure 22e,f).[839] The excellent catalytic properties were examined by microelectrochemical measurements, characterized by onset potentials of −25 mV and Tafel slopes of 54 mV $dec^{-1}$, further demonstrating the high activation of the grain boundaries in TMDs.

Moreover, defect engineering based on TMDs also shows great promise in fields such as magnetism, piezoelectricity, and nonvolatile resistive switching.[819,840,841] From the aspect of material synthesis, achieving accurate location and density (from ultralow to ultrahigh) control of TMDs still remains a challenge. This also requires high-throughput and high-resolution characterization techniques to ensure the precise density and configuration of defects. Overall, defect engineering is a powerful tool that expected to modulate the performance of TMD materials and provide new designing freedom in multiple fields such as electronics, catalysis, and energy conversion.

### 5.5. Heteroepitaxial Growth

Flexible assembly of two or more different semiconductors produces artificial heterostructures, a fundamental archetype in solid-state physics, enlightening applications in LED, solar cells, and semiconductor lasers. Atomically-thin TMDs without interlayer dangling bonds serve as ideal "nanoLogo" building blocks to form desired heterostructures taking no account of lattice mismatching. In practice, proof-of-concept TMD heterostructures could be fabricated layer-by-layer restacking using a micromanipulator. However, the low throughput and unavoidable interfacial imperfections (such as bubbles and adsorbed hydrocarbons) block further exploration and application of these artificial structures. In this regard, bottom-up epitaxial synthesis acts as a clean and scalable method for producing TMD heterostructures, avoiding exposure to external contaminations and size limitations


https://doi.org/10.1021/acs.chemrev.3c00851
Chem. Rev. XXXX, XXX, XXX−XXX

during the transfer process, thereby facilitating the reliable production of heterostructure devices. Besides the vertical (out-of-plane) structures, seamless stitching of TMDs constructs the atomic lateral (in-plane) TMD heterostructures—the ultimate-thickness heterojunctions that are not achievable by transfer technique. The main challenge of heteroepitaxy lies in the controllable switching of metal or chalcogen sources. Therefore, vapor-based techniques (CVD or MOCVD) with flexibly modulated precursors have developed as the most common method to access high-quality heterostructures. In this section, we mainly focus on the vapor-based synthesis for large-scale TMD heterostructures, including lateral/vertical species and corresponding superlattices.

Inspired by the access of pure monolayer TMDs via vapor deposition, in 2014, three independent groups reported the direct synthesis of both vertical and lateral TMD heterostructures. Huang et al. employed the PVD strategy with a combination of $WSe_2$ and $MoSe_2$ powder as sources, and successfully obtained the monolayer $WSe_2/MoSe_2$ lateral heterostructure.[842] Gong et al. demonstrated a one-step CVD approach to selectively produce vertically stacked or lateral heterostructures of $WS_2/MoS_2$ by controlling the growth temperature.[843] At high growth temperatures (850 °C), the $WS_2$ epitaxially grew over $MoS_2$ monolayers and formed vertically heterostructure bilayers with a preferred stacking order. Besides, the low-temperature growth process (650 °C) resulted in lateral epitaxy of $WS_2$ at $MoS_2$ edges, forming seamless in-plane heterostructures with the atomically sharp interface (Figure 23a). The underlying mechanism of this selective growth behavior was further explored later by the nucleation kinetics model.[844] Duan et al. reported a precise design enabling in situ switching of vapor-phase precursors, facilitating lateral epitaxial growth of single- or few-layer TMD lateral heterostructures (including $WS_2/WSe_2$ and $MoS_2/MoSe_2$).[845] These advancements demonstrated the flexibility and efficiency of constructing large-scale TMD lateral/vertical heterostructures via vapor-based growth techniques, which also underscore the importance of precise control of precursors over source versatility and timing.

As for the controlled synthesis of lateral TMD heterostructures, the aforementioned one-step strategy leads to a clean heterointerface and is relatively limited in versatility due to the unavoidable alloying during the high-temperature process.[846,847] In this regard, the two-step synthesis of lateral TMD heterostructures serves as the complementary design. For instance, Li et al. fabricated $WSe_2/MoS_2$ lateral heterostructures by following the epitaxial growth of $MoS_2$ along the edges and on the top surface of as-synthesized $WSe_2$. The interfacial alloying was prevented by precisely controlling the relative vapor amounts of $MoO_3$ and sulfur during the subsequent $MoS_2$ growth.[848] Moreover, lateral heterostructures such as $MoS_2/WS_2$, $WSe_2/MoSe_2$, $WS_2/WSe_2$, $MoS_2/MoSe_2$ and $WS_2/ReS_2$ can also be obtained based on similar processes.[844,849−851]

Furthermore, the direct fabrication of more complex lateral heterostructures/superlattices is the ultimate goal in lateral epitaxy. Significant efforts have been dedicated to precisely tuning various precursors during synthesis toward desired superlattices. In 2018, Xie et al. synthesized lateral $WS_2/WSe_2$ superlattices using a modulated MOCVD process (Figure 23b). This setup possesses two distinctive features: first, it enables individual and precise control over the concentration of each precursor, facilitating direct tuning of the supercell dimensions. Second, it allows for the rapid switching of TMD composition, such as from $WS_2$ to $WSe_2$ and vice versa, with the width of each component determined by controlling the timing of the switch.[852] During the sequential growth process, the main challenge lies in managing excessive thermal degradation or uncontrolled nucleation during temperature fluctuations between growth steps, which limits the reliable formation of monolayer heterostructures. Zhang et al. developed the step-by-step CVD process by introducing a reverse flow during the sequential vapor deposition growth process. This innovation facilitated the cooling of existing 2D crystals and effectively prevented undesired thermal degradation and uncontrolled homogeneous nucleation.[389] Furthermore, Sahoo et al. achieved controlled growth of lateral TMD heterostructures simply by altering the carrier gas. Specifically, they found that a combination of $N_2$ and $H_2O$ facilitated the growth of $MoX_2$, while Ar and $H_2$ halted the growth of $MoX_2$ and instead promoted the growth of $WX_2$.[853] A similar setup can also be utilized to prepare heterophase structures such as 2H-1T′ $WS_2-ReS_2$.[851]

In addition to the step-by-step vapor-phase methods discussed above, a thermal etching process is introduced to create precise heterostructure arrays on as-prepared TMD films. In 2022, Zhang et al. introduced an ingenious synthetic strategy for producing mosaic heterostructure arrays in monolayer 2D atomic crystals. This method involves creating periodic triangular hole arrays in 2D crystals with precisely controlled sizes and atomically clean edges through laser patterning and an anisotropic thermal etching process. These arrays then serve as templates for the endoepitaxial growth of another 2D crystal, resulting in monolayer mosaic heterostructures with atomically sharp heterojunction interfaces (Figure 23c). They further improved the thermal etching process by combining it with laser irradiation, resulting in more controllable etched hole arrays on 2D-TMDs with clear atomic terminations and atomic sharp edges.[854] These methods can be extensively applied to the synthesis of various TMD heterostructures, including $WS_2/WSe_2$, $WS_2/MoS_2$, and $WSe_2/MoS_2$, thereby aiding in the establishment of a customizable material platform for 2D heterostructures.[855]

The layer-by-layer synthesis of vertical TMD heterostructures follows the growth behavior introduced in the vdW epitaxy introduced in Section 4.2.1. The precise control over their epitaxial registry, layer number, and stacking order have been systematically explored, enabling the fabrication of diverse vertical heterostructures such as $NbS_2/MoS_2$, $NbSe_2/WSe_2$, $CdI_2/WS_2$, $CdI_2/WSe_2$, $CdI_2/MoS_2$, $PbI_2/WS_2$, $PbI_2/WSe_2$, and $PbI_2/MoS_2$.[58,856−860] In 2022, Wu et al. employed a CVD approach to fabricate bilayer $WSe_2$ transistors with synthetic $VSe_2$ vdW contacts by inducing controlled crack formation. Width-controllable nanogaps emerged between the connected $VSe_2$ domains during the cooling process, enabling the fabrication of transistors with atomically clean interfaces and minimal damage to the underlying $WSe_2$.[649] Zhao et al. introduced a novel capillary-force-driven rolling-up process that could effectively delaminate synthesized $SnS_2/WSe_2$ vdW heterostructures from the growth substrate. This process resulted in the formation of $SnS_2/WSe_2$ roll-ups with alternating monolayers of $WSe_2$ and $SnS_2$, thereby creating high-order $SnS_2/WSe_2$ vdW superlattices (Figure 23d). This rolling-up strategy can be extended to create diverse 2D/2D vdW superlattices and complex three-component 2D/2D/2D vdW superlattices ($SnS_2/MoS_2/WS_2$), as well as structures beyond 2D materials, including 3D or 1D materials.[380]

The direct synthesis of complex vertical heterostructures or superlattices requires a more precise modulation of precursor feeding, nucleation position, and deposition sequence. In 2021, Jin et al. utilized kinetics-controlled vdW epitaxy near the equilibrium limit via MOCVD to achieve precise layer-by-layer stacking growth.[861] In this method, TMD monolayers exhibiting preferred in-plane crystal orientations are initially epitaxially grown and transferred onto $SiO_2/Si$ substrates to serve as templates. Subsequently, TMD superlattices with programmable stacking periodicities can be controllably synthesized by fine-tuning the feeding circles of metal−organic precursors. The heteroepitaxial vertical superlattices comprised more than two types of different TMD monolayers, such as $MoS_2$, $WS_2$, and $WSe_2$, and were free of interlayer atomic mixing (Figure 23e). Li et al. selectively patterned nucleation sites on monolayer or bilayer semiconducting TMD, allowing for precise control over the nucleation and growth of various metallic TMD with designable periodic arrangements and tunable lateral dimensions at predetermined spatial locations. This process resulted in the fabrication of a series of vdW heterostructure arrays, including $VSe_2/WSe_2$, $NiTe_2/WSe_2$, $CoTe_2/WSe_2$, $NbTe_2/WSe_2$, $VS_2/WSe_2$, $VSe_2/MoS_2$, and $VSe_2/WS_2$.[399]

Complementary to the layer-by-layer heteroepitaxial growth, the two-step chalcogenization of deposited metals facilitates the fabrication of large-area vertical heterostructures with diverse TMDs.[846] Recently, Zhou et al. introduced a multicycle vapor-deposition process employing a high-to-low temperature strategy for growing wafer-scale vertical TMD superconductor heterostructures.[452] The diverse TMD blocks were grown by chalcogenization of corresponding sputtered metal films with controlled thickness. During the stacking process, the material with the highest growth temperature typically serves as the bottom layer, with other TMD layers sequentially grown based on chalcogenization temperature from high to low. As shown in Figure 23f, this general strategy enabled the flexible fabrication of inch-sized multiblock TMD heterostructures, which feature a scalable pathway for constructing complex vertical heterostructure arrays.

In summary, the heteroepitaxial growth of TMDs demonstrates excellent freedom in synthesizing artificial structures with vdW materials as “nanoLogos”. Most developed methodologies and growth mechanisms including both lateral edge-epitaxy and vertical vdW-epitaxy are based on the concepts in fabricating pure TMDs. Specifically, there are still several challenges that require to be addressed. (i) Most synthetic strategies involve prolonged or multicycle high-temperature processes for the sequential fabrication of TMD blocks, which may lead to decomposition, etching, or alloying of the as-grown 2D layers. (ii) The heterostructure scalability including their thickness, stacking order, twist angle, and material universality should be further improved to satisfy customized demands. (iii) From aspects of high-end electronics and optoelectronics, efficient production of wafer-scale single-crystalline TMD heterostructures still serves as a critical topic in this field.

## 6. POSTPROCESSING OF LARGE-AREA TMDs

As previously discussed, significant advancements have been achieved in the large-area epitaxial growth and property tailoring of TMDs. On this basis, postprocessing techniques aimed at future industrialization have emerged as a key research focus at the current technological stage. As an emerging channel material, TMDs necessitate techniques for high-throughput and precise quality characterization. On the other hand, hybrid integration with well-developed silicon circuits will be a key node for the industrialization of TMD materials. In this section, we will mainly focus on the developments in characterization techniques for TMDs, followed by a systematic review of the large-area transfer techniques and advanced patterning strategies. These studies are essential for optimizing material fabrication and establishing unified technological standards, and will further boost the compatibility of 2D TMDs with well-developed silicon industry.

### 6.1. Quality Characterization

Comprehensively evaluating the synthesized TMD materials helps to establish a standard grading system like traditional semiconductors with different levels, which is essential for finding their specific application scenarios. For example, the electronic-grade wafer-scale TMDs with ultralow defect density hold the potential in fabricating high-end integrated circuits. Meanwhile, TMD films with high-density point defects or grain boundaries are more suitable for catalytic applications due to the increased active sites. Therefore, reliably characterizing the quality of the as-prepared TMD material acts as a key “bridge” that connects the material synthesis and related applications. Benefiting from pivotal advancements in both scientific instruments (e.g., electron microscopes, scanning probe microscopes, and X-ray diffractometers) and intrinsic physical mechanisms (e.g., exciton physics and nonlinear optics in TMDs), diverse characterization methods have been proposed and applied in publications of TMDs from material synthesis, high-performance devices, and new physics explorations. In this section, we provide a brief overview of the key evaluation criteria for large-area TMD materials. And then introduce some detailed characterization techniques for both 0D and 1D defects in TMDs. In particular, we will further discuss characterizing the single crystallinity of large-area epitaxial TMD films.

**6.1.1. Determinants of Quality.** Different generations of semiconductor materials have varied standards for evaluating their crystal quality based on their elemental composition, preparation method, and technical maturity. For instance, the single-element silicon materials typically sliced from single-crystal ingots exhibiting ultralow impurity densities of $\sim 10^{-11}$. III−V gallium nitride films epitaxially grown by MOCVD primarily contain dislocation defects ranging from $10^4$−$10^6$ $cm^{-2}$. For the large-area 2D TMD, the key points in evaluating their intrinsic crystal quality are concluded as follows:

(i) Defect density: The vapor-deposited TMDs always possess high-density point defects, typically in the range of $10^{12}$ to above $10^{13}$ $cm^{-2}$, and the sulfur vacancies are dominant in the CVD and mechanical exfoliated samples. This value is orders greater than that in 2D elemental graphene.[823] These defects can significantly impact the optical and electrical performance of monolayer TMDs that act as centers for strong carriers scattering and nonradiative recombination.[862,863] As discussed in previous sections, to date, the point defect density of the vapor-deposited TMD monolayers could be suppressed in the order of $10^{12}$ $cm^{-2}$ by optimizing the precursors and growth parameters. Liu et

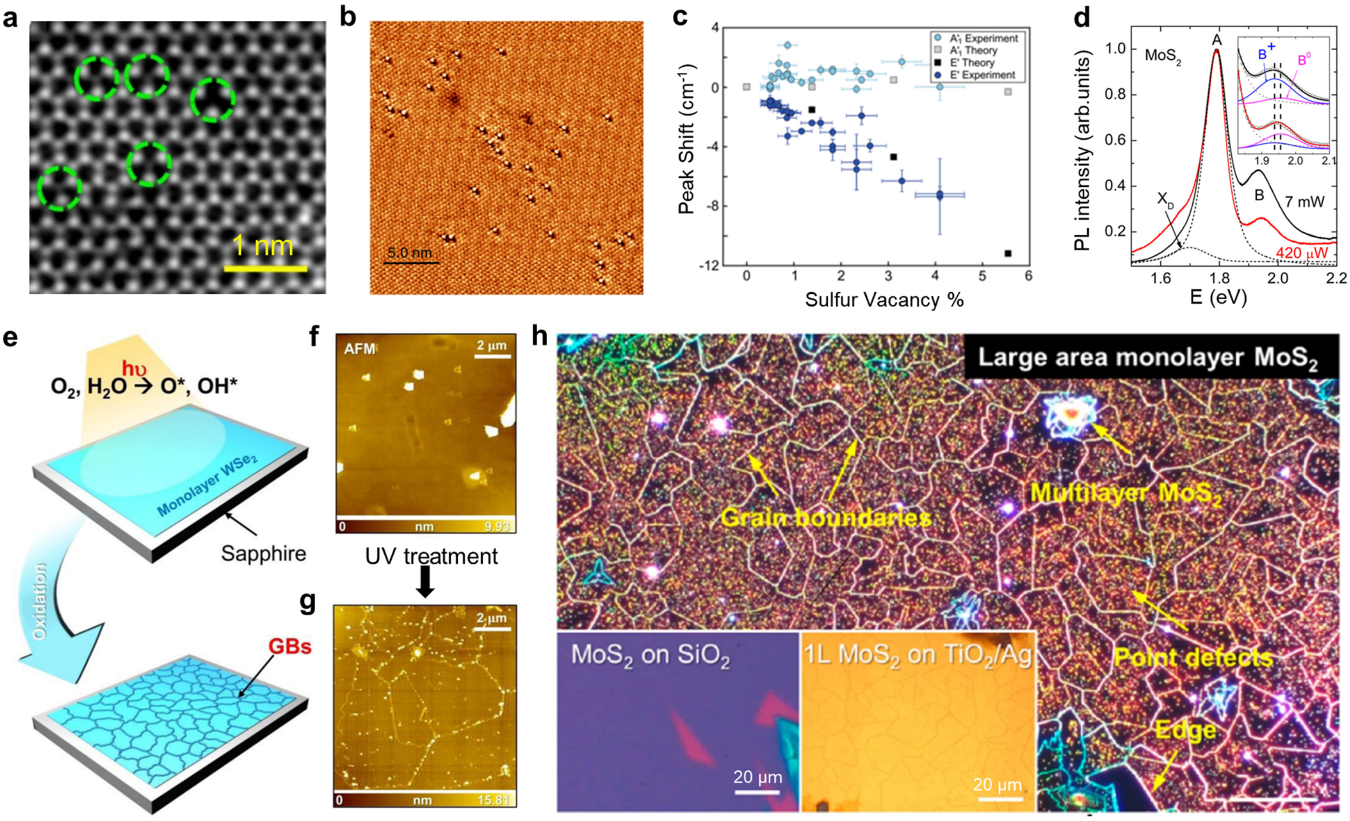


**Figure 24.** Characterizations of the defect distribution in large-area TMDs. (a) STEM characterization of $V_S$ and $V_{S2}$ vacancies in monolayer $MoS_2$. Reprinted with permission from ref 817. Copyright 2015 Springer Nature. (b) Atomic resolution STM image of oxidized monolayer $MoS_2$. Reprinted with permission from ref 762. Copyright 2018 Springer Nature. (c) Experimental and theoretical Raman peak shifts versus sulfur vacancies in $MoS_2$. Reprinted with permission from ref 872. Copyright 2016 American Chemical Society. (d) Normalized room temperature PL spectra of $MoS_2$ monolayer measured at different laser powers. Reprinted with permission from ref 875. Copyright 2018 Wiley-VCH Verlag GmbH & Co. KGaA, Weinheim. (e−g) Schematic for the visualization of grain boundaries by UV treatment. (e−g) Reprinted with permission from ref 878. Copyright 2014 American Chemical Society. (h) Visualization of the defects in CVD-grown $MoS_2$ by dark-field optical images, including grain boundaries, point defects, and edges. Reprinted with permission from ref 879. Copyright 2015 American Chemical Society.

al. demonstrated a two-step flux method to fabricate ultrapure $WSe_2$ bulk crystals with $\sim 10^9$ cm$^{-2}$ for charged defects and $\sim 10^{11}$ cm$^{-2}$ for isovalent defects.[827] The exfoliated monolayer exhibited ultrahigh room-temperature hole mobility above 840 cm$^2$ V$^{-1}$ s$^{-1}$. These results indicate it is still a valuable synthetic topic in pursuing the direct synthesis of an ideal large-area TMD monolayer.

(ii) Single crystallinity: Stitching of TMD domains with random orientations forms 1D grain boundaries in large-area films. The FETs with interdomain channels show much degeneration in carrier mobility compared with intradomain devices. And the interdomain mobility varied with the misorientation angles nonlinearly.[823] Therefore, the single-crystal TMD film is desired to ensure consistent electronic properties and minimize device-to-device variations. Grain boundaries should be efficiently avoided to guarantee the repeatability and reliability of the integrated device arrays. Numerous epitaxial growth strategies have been developed to address these line defects and to date, the wafer-scale single crystal TMDs are accessible toward high-performance electronics.

(iii) Uniformity: The concept of uniformity in large-area TMDs includes lots of factors such as defect density, coverage rate, multilayer nucleations, growth-induced strain, adsorption of hydrocarbons, and so on. The spatial distribution of these intrinsic or extrinsic imperfections is always nonuniform in experiments. For instance, the varied precursor concentrations across inch-sized substrates result in different coverage rates and defect densities at different regions. The uniformity serves as an important standard in evaluating the applicational capabilities of large-area TMD films. However, this parameter is sometimes ignored in publications and leads to an overstate of the material quality.

In summary, accurately evaluating the quality of a piece of as-synthesized large-area TMDs should take multiple aforementioned structural parameters into account. Certainly, these results are also influenced by synthetic strategies, growth parameters, characterization methods, and other factors. In the future, more detailed technological standards and characterization processes are required to be unified collaboratively by the research and industrial community.

**6.1.2. Defects Distribution.** Precise defect information on TMDs including the locations, densities, and atomic configurations is the key parameter of the quality of TMDs, which could further guide the optimization of the material growth and device fabrication process. In general, researchers should find the appropriate defect characterization techniques by balancing the resolution, efficiency, cost, and damage to samples. Here we mainly introduce several frequently used characterization techniques including electron microscopes, scanning probe microscopes, spectral measurement, electrical measurement, and direct visualization.

The development of aberration correction technology has further improved the spatial resolution of transmission electron microscopy (TEM), enabling the atomic-scale imaging of TMD materials.[864] To date, high-resolution transmission electron microscopy (HRTEM) and STEM serve as the routine methods used to characterize the crystal structure of TMDs at the microscopic scale. HRTEM is a phase contrast-based imaging technique that can directly observe the atomic configuration of a sample and clearly distinguish defects by comparing the intensity distribution in the image. HRTEM techniques typically provide lattice images rather than actual atomic images. In contrast, STEM techniques can provide images of atoms whose intensity is proportional to the atomic number (Z-contrast), and atoms can be distinguished by brightness (Figure 24a).[817] For example, the contrast of point defects (such as vacancies) is significantly different from the intrinsic atomic columns, while dislocations can cause distortions in atomic arrangements, presenting irregular contrast patterns. Both approaches can provide microscopic information about a sample at atomic spatial resolution, including layered structures, lattice defects, grain boundaries, and electronic structures. In addition, samples need to be transferred to specific microgrids before characterization, which is a complex process that is not compatible with large-area characterization.

Scanning tunneling microscopy (STM) is also a significant method for high-resolution defect characterization.[865] When characterizing oxygen atoms on the surface of TMDs, STEM technology faces challenges due to the low contrast and variability of oxygen atoms. In contrast, STM measurements can reveal the structure of these oxygen defects thanks to their atomic resolution and low-energy tunneling electrons (Figure 24b).[762] At the same time, STM has the advantage of revealing electronic properties affected by point defects. However, STM is limited by the sample environment and is not suitable for samples directly grown on an insulating substrate. Moreover, for defect detection, STM technology can only handle weakly adsorbed atoms (~1 eV).[866] Detecting mobile defects, doping, and their corresponding structural evolution requires much higher energies (~10 eV), presenting a challenge for STM technology.[867]

The comprehensive characterization of large-area TMDs often employs fast optical spectroscopic techniques such as Raman, PL, and SHG. These methods facilitate nondestructive material characterization and do not depend on substrate species. Raman spectroscopy, for instance, features molecular vibrations and lattice modes by analyzing the frequency shifts of scattered light in the sample. This technique offers a unique advantage in structurally characterizing materials, as factors like layer number, doping, alloy composition, and stress-induced effects are all manifest within the Raman scattering (peak positions, intensities, and peak widths).[648,695,868−871]

Defects, in particular, can induce alterations in lattice vibrations, resulting in shifts or the appearance of characteristic peaks in the Raman spectra. Taking $MoS_2$ as an example, both experimental and theoretical investigations demonstrate that the typical in-plane vibration mode $E_{2g}$ (~384 $cm^{-1}$) and out-of-plane vibration mode $A_{1g}$ (~405 $cm^{-1}$) shift with increasing sulfur vacancy concentration (Figure 24c), and the difference between these two peaks exhibits a linear correlation.[872] Moreover, Mignuzzi et al. have explored defect-induced new Raman scattering peaks resulting from $Mn^+$ ion bombardment in monolayer $MoS_2$ flakes.[873] The Raman spectra of $MoS_2$ with different line defect densities show that as line defect decreases (indicating increased defect density), the $E_{2g}$ peak shifts to lower wavenumbers, while the $A_{1g}$ peak shifts to higher wavenumbers. DFT calculations suggest that these shifts are attributed to phonon localization. Moreover, the new Raman peak appears at about 227 $cm^{-1}$, and its strength is proportional to the defect density.

Furthermore, defects in monolayer TMDs with direct band gaps can be detected using PL spectroscopy. PL spectra typically encompass fluorescence peaks arising from free carriers and excitons.[874] Excitons are bound states of electrons and holes, and their formation and recombination are influenced by material defects. Certain defects can provide trap levels, capturing free carriers and forming excitons. For electronic states, the appearance of defects brings about defect states between the conduction and valence band, and causes PL peak position deviation and intensity attenuation. Hence, by analyzing the intensity and position of excitonic peaks in PL spectra, information about relevant defects within the material can be inferred. For example, typical room-temperature PL spectra of $MoS_2$ exhibit distinct A and B excitonic bands at around 1.79 and 1.95 eV, respectively (Figure 24d).[875] Additionally, a weak $X_D$ peak can be observed at 1.69 eV, which is associated with defect-bound excitons. In higher-quality samples, the defect-related $X_D$ peak may not be observable at room temperature. To attain more precise characterization of sample quality, techniques such as BN encapsulation and low-temperature testing are often employed.[876,877] These methods effectively reduce the spectral broadening caused by phonons and the influence of the substrate. However, these strategies can sometimes increase the complexity of defect analysis. Moreover, PL mapping is an approach to detect the presence of defects, which can identify the grain boundary and show differences in quantum yield, peak location, and peak width of PL.[878] However, the PL spectrum itself has drawbacks, which are susceptible to other factors such as strain, electron doping, and substrate. In addition, PL spectroscopy is not effective for nonluminous metal materials and semiconductors.

With the continuous expansion of the production scale of TMD materials, the need for high-throughput characterization methods is becoming increasingly urgent. Currently, for the comprehensive characterization of large-area 2D TMDs, two strategies have been prominently employed. One approach involves defect visualization techniques. It is challenging to recognize ambiguous grain boundaries due to their weak optical contrast. By selective etching and controlled adsorption, the optical contrast of defects can be greatly improved, thus realizing defect visualization of large-area TMD.[879−881] These methods have the advantages of convenience and fast defect imaging in a large range. For instance, Ly et al. introduced a method utilizing ultraviolet irradiation and selective oxidation to characterize defects (grain boundaries) on large-area monolayer $WSe_2$ (Figure 24e).[878] Atomic force microscopy (AFM) was utilized to contrast the distribution of grain boundaries before and after ultraviolet exposure (Figures 24f, g), revealing distinct grain boundaries. This grain boundary visualization method can also be achieved through wet-etching techniques using water, $H_2O_2$


https://doi.org/10.1021/acs.chemrev.3c00851
Chem. Rev. XXXX, XXX, XXX−XXX

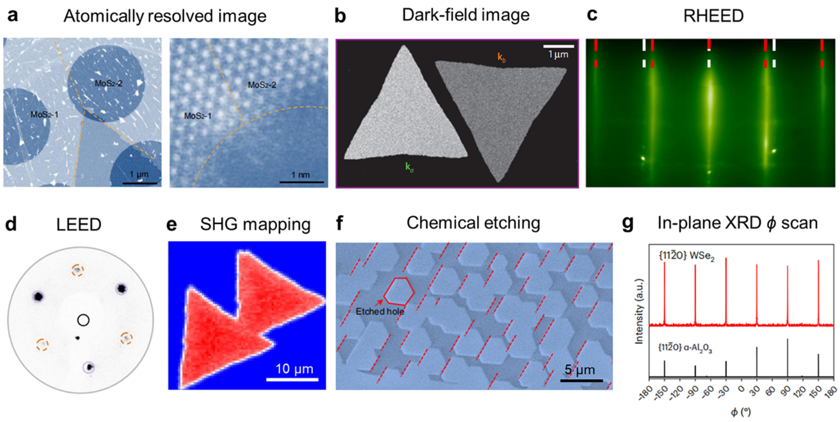


**Figure 25.** Characterizations of the single crystallinity in large-area TMDs (a) STEM image of the stitching position of two $MoS_2$ crystal domains. Reprinted with permission from ref 627. Copyright 2023 Springer Nature. (b) Dark-field image of $MoS_2$ crystals as the triangles are rotated 180° from one another. Reprinted with permission from ref 357. Copyright 2013 Springer Nature. (c) RHEED pattern of the $MoS_2$/sapphire along the $Al_2O_3$ $\langle 10\bar{1}0\rangle$ direction. Reprinted with permission from ref 34. Copyright 2021 Springer Nature. (d) Typical LEED pattern for the single-crystalline monolayer $WS_2$ film. Reprinted with permission from ref 35. Copyright 2021 Springer Nature. (e) Polarized SHG mapping of two unidirectional $MoS_2$ domains. Reprinted with permission from ref 34. Copyright 2021 Springer Nature. (f) False color SEM image of single-crystalline $WS_2$ film after $O_2$ etching. Reprinted with permission from ref 35. Copyright 2021 Springer Nature. (g) In-plane XRD azimuthal angle ($\phi$) scans of planes of $WSe_2$ and $\alpha$-$Al_2O_3$ confirming the 6-fold $[11\bar{2}0]$ $WSe_2(0001)//[11\bar{2}0]$ $\alpha$-$Al_2O_3(0001)$ epitaxial relationship. Reprinted with permission from ref 629. Copyright 2023 Springer Nature.

solution, and calcium hypochlorite solutions.[880−882] Additionally, surface adsorption serves as another means of defect visualization. Jeong et al. directed Ag nanoparticles generated from annealed $TiO_2$/Ag thin films to aggregate at defect sites on TMDs under white light irradiation, effectively anchoring them to those positions, thereby visualizing large-area $MoS_2$ defects (Figures 24h).[879] Notably, while most etching techniques can merely identify the position of grain boundaries, surface adsorption allows precise anchoring of point defects. However, both adsorption and etching will damage TMD films in different degrees. Another strategy involves the utilization of extensive electrical performance statistics. This requires fabricating a large number of devices and subjecting them to electrical testing, thereby obtaining statistical data to assess overall material performance and defect status. For instance, Liu et al. calculated mobility data for 150 bilayer $MoS_2$ film FETs.[626] The results indicated an average mobility of 107.0 ± 7.8 $cm^2$/V·s, with the optimum mobility being 122.6 $cm^2$/V·s, and a mobility variation of 7.3% achieved through Gaussian fitting. These outcomes underscored the high quality and uniformity of $MoS_2$ films.

In-depth investigation of defects provides a unique opportunity to unveil the properties of materials, facilitating the design and optimization of materials to meet the diverse requirements of various applications. However, the diversity of defect types and the nanoscale nature of these materials pose challenges to accurate defect quantification. Moreover, with the gradual expansion of the production scale of TMD materials, there are technical obstacles to achieving high-throughput defect characterizations.[883]

**6.1.3. Single Crystallinity.** Driving by the great demands of wafer-scale TMD single crystals to eliminate the influence from grain boundaries, substantial progress has been achieved in the production of single-crystal TMDs, such as wafer-scale single-crystal $MoS_2$, $WS_2$, $MoSe_2$, and so on. However, the comprehensive examination of the single crystallinity across the inch-sized TMD films is still challenging. In this section, we will provide a detailed discussion of the methods associated with characterizing single-crystallinity of TMDs.

Similar to the previous section on point defect characterization, atomic-resolution techniques including TEM and STEM are also employed as the most powerful tools to characterize the single-crystallinity in TMDs. When two unidirectional TMD domains are stitched seamlessly, they appear as an ordered and consistent arrangement of atoms in STEM (Figure 25a).[627] Besides, dark-field TEM producing by selecting the scattered electrons was first utilized by van der Zande et al. to identify the single crystallinity of monolayer $MoS_2$.[357] Unlike the 6-fold symmetric graphene, the monolayer $MoS_2$ lattice is divided into molybdenum sublattices and sulfur sublattices, resulting in a 3-fold symmetric selected area electron diffraction (SAED) pattern. The six $[\bar{1}100]$ diffraction points are divided into two families, $\mathbf{k}_a$ and $\mathbf{k}_b = -\mathbf{k}_a$. The experimental and simulated results indicate that the $\mathbf{k}_a$ spots are ∼10% higher in intensity for an 80 kV electron beam, which points toward the molybdenum sublattice. Therefore, this asymmetry in diffraction intensity enables the characterization of TMD domain orientations using dark-field images formed by positing an aperture at specific diffraction spots (Figure 25b). Similarly, dark-field low-energy electron microscopy (DF-LEEM) can also verify the unidirectional arrangement between crystal domains.[590] Although high-resolution electron microscopes could give an atomic insight into single-crystallinity and corresponding growth mechanism, their limited characterizing efficiency and complex sample preparation hinder comprehensively evaluating large-area TMD films.

Low-energy electron diffraction (LEED) serves as a critical technique for analyzing the single-crystal characteristics of 2D materials. Due to the low energy of the electron beam, the incident electrons can only enter the depth of a few atomic layers on the surface, so the obtained information is the crystal surface structure. It is employed to characterize the periodic structure of the sample surface over a large area, and is an effective method to study the atomic arrangement of the surface layer of the single crystal. Compared with the real image obtained by TEM, the data obtained by LEED is the result of computational transformation. The electron beam


https://doi.org/10.1021/acs.chemrev.3c00851
Chem. Rev. XXXX, XXX, XXX−XXX

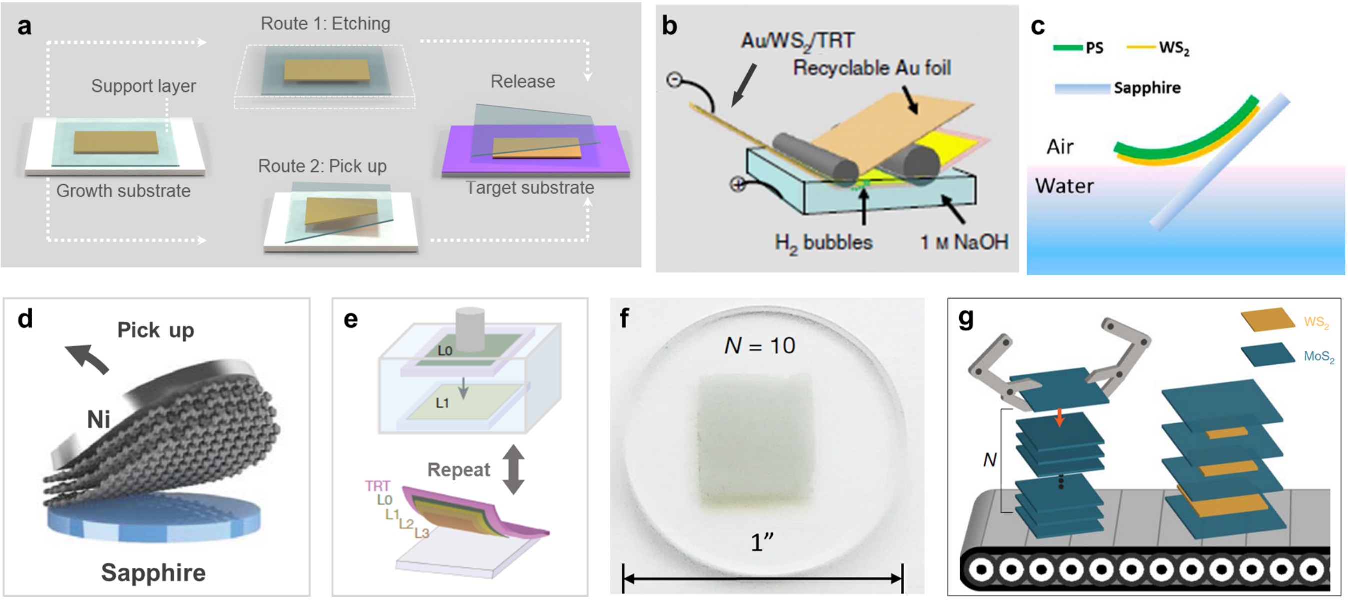


Figure 26. Transfer techniques of large-area TMDs. (a) Schematic of techniques for transfer techniques of TMDs. (b) Schematic of the roll-to-roll/bubbling process. Reprinted with permission from ref 417. Copyright 2015 Springer Nature. (c) Schematic of the water-assisted direct pick-up transfer. Reprinted with permission from ref 916. Copyright 2015 American Chemical Society. (d) Schematic of the metal-assisted direct pick-up transfer. Reprinted with permission from ref 920. Copyright 2018 AAAS. (e) Schematic of the vdW force assisted direct pick-up transfer. Reprinted with permission from ref 925. Copyright 2017 Springer Nature. (f) Photograph of large-area $MoS_2$ films transferred onto 1-in. wafer-scale fused silica substrates. Reprinted with permission from ref 926. Copyright 2021 Springer Nature. (g) Schematic of automated transfer by a robotic instrument. Reprinted with permission from ref 927. Copyright 2022 Springer Nature.

utilized in LEED can cover an area of up to 1 mm$^2$, demanding high uniformity of the sample over extensive areas.[596,601] The principle of diffraction dictates that the LEED pattern should represent the reciprocal lattice of the sample's 2D surface lattice. For most TMD materials with a hexagonal lattice on the surface, the reciprocal lattice remains a hexagonal lattice. However, due to symmetry breaking, under certain electron energies, the LEED pattern will appear alternately between light and dark (Figure 25d).[35] This phenomenon is usually considered a characteristic of TMD materials with highly aligned orientation. However, LEED measurement can be challenging for samples on insulating substrates due to potential charge accumulation, often requiring additional steps to enhance sample conductivity.

Reflection high-energy electron diffraction (RHEED) is also a surface characterization technique that depends on electron diffraction.[884,885] Unlike LEED (20−300 eV), the electron beam energy used in RHEED is usually higher (30−100 keV), and the high-energy electron beam is guided to the sample surface at a grazing angle. Due to the incident angle, the RHEED result obtained from a single-crystal sample is streaky patterns formed along a certain direction by the reciprocal lattice of the sample's 2D surface lattice (Figure 25c).[34] For instruments capable of rotating the sample, reciprocal lattice rods in more directions can be obtained, and the lattice information on the sample can be calculated through the streak spacing and instrument parameters. However, the high cost of the instrument, strict vacuum requirements, and possible electron beam damage to the sample are also significant disadvantages in the application of RHEED.

The sensitive optical spectroscopic strategies are in great demand to visualize the grain boundaries quickly and noninvasively.[883] The PL intensity and peak position mappings could recognize the stitched twin grains attributed to the defects and strains at the grain boundaries.[886] Besides, inversion asymmetric monolayer TMDs with strong second-order nonlinear response enabled the probe of the crystal orientations with polarization-dependent SHG detection. The grain boundary region can also be clearly revealed by SHG mapping, where the SHG signals generated from the neighboring grains with different orientations are canceled.[178,818,887] Experimental results demonstrated destructive SHG signals at the grain boundaries when there is a misoriented angle. On the contrary, the SHG signal shows consistent intensity across the domain and stitching region of two unidirectional TMD domains as shown in Figure 25e.[34] Furthermore, Karvonen et al. reported using multiphoton (SHG and THG) microscopy to detect grain boundaries between crystalline domains regardless of the degree of crystal axis rotation.[888]

Chemical etching is also a high-throughput method to examine the single crystallinity of TMDs over a large scale using an optical microscope. For example, when the TMD film is placed in an oxidative environment or thermal annealing for etching, the etched holes on the single-crystalline region have similar shapes and the same orientation (Figure 25f).[35,854] Besides, as discussed above, the etching will first occur at the defective grain boundaries if there are any twist angles between different domains. Compared with other methods, these etching strategies are effective, low-cost, and operation-convenient for visualizing the single crystallinity of large-area TMD films. However, the etching effect is invasive to the crystal lattice, and the accuracy required to be further improved.

The X-ray diffraction (XRD) measurements also work as a nondestructive and rapid characterizing technique in analyzing the large-area crystalline orientation of TMDs and their epitaxial relationship with growth substrate. Due to the lack of periodicity along the {000*l*} direction of the as-grown 2D TMDs, only {*hki*0} planes could be studied by the in-plane XRD.[889] In which the X-ray incidence plane (defined by the incident and diffracted wave vectors) should nearly coincide with the 2D basal plane. A typical characterization result is shown in Figure 25g, in which initial alignment is performed on the $\{11\bar{2}0\}$ planes of the c-sapphire substrate, then setting $2\theta$ at $\{11\bar{2}0\}$ planes of 2D $WSe_2$ and azimuthal angle ($\phi$) scan provided six sharp peaks.[629] Which indicated the 6-fold $[11\bar{2}0]$ $WSe_2$//$[11\bar{2}0]$ $\alpha$-$Al_2O_3$ (0001) epitaxial relationship, and full-width and half-maximum (fwhm) of the narrow $\phi$-scan peaks demonstrated there were few twisted $WSe_2$ domains in-plane. Synchrotron grazing-incidence wide-angle X-ray scattering (GIWAXS) with a high-intensity beam is also utilized to study the epitaxial relationship of TMDs with low electron density substrates such as graphene/SiC.[552] Furthermore, X-ray photoelectron diffraction (XPD) could probe the orientation information on TMDs mirror domains due to different core-level photoemission intensities from the different atom layers.[890]

## 6.2. Transfer Techniques

The vdW integration enables damage-free integration of 2D TMDs, producing nearly ideal atomically smooth surfaces that enable the efficient interface control and multifunctional heterojunctions, thereby significantly enhancing the performance and integration density of electronic devices. The vdW integration via transfer techniques is a crucial step in advancing TMD materials from laboratory to industrial fabrication (from “lab” to “fab”), as it is compatible with various device types and complex surface morphologies. Essential in the gate-first process of TMD IC, transfer techniques effectively prevent the degradation of component formed during the front-end-of-line process in IC fabrication. This is because the preprepared electrode and gate dielectric cannot withstand the high temperature during the growth of TMDs, which can reach temperatures as high as 800 °C or higher. Transfer techniques help maintain a reasonable thermal budget for IC fabrication and ensure compatibility with existing industrial fabrication methods. Typically, the flat 2D TMDs without dangling bonds couple with the substrate via weak vdW force. Moreover, the unique mechanical properties of TMDs, including low surface energy (e.g., $MoS_2$, 35−48.3 mJ·m$^{-2}$)[891,892] and high Young’s modulus (e.g., $MoS_2$, 270 GPa),[893] lend these materials the requisite stability and resilience throughout the transfer process. These characterizations enable the seamless dissociation and subsequent transfer of uniform, atomically thin films onto various substrates, granting TMDs an advantage over conventional non-vdW materials.

In this section, we mainly focus on the large-area transfer of the as-grown TMDs. Two primary transfer techniques have been developed: chemical etching transfer and direct pick-up transfer (Figure 26a). The former is typically employed when TMDs are grown on substrates with strong adhesion, like certain metals, necessitating chemical reactions to sever these interactions. Conversely, when the coupling between TMD and the substrate (such as sapphire or $SiO_2$/Si) is comparatively weak, a physical lift-off facilitates a direct pick-up by manipulating surface energy without resorting to chemical etching. These methods have successfully transferred a range of large-area TMD films, up to inch-scale dimensions, which have found applications in fundamental physical property exploration,[894,895] electronic devices[896,897] and optoelectronic devices.[898,899]

Nonetheless, the uniformity and quality of the transferred TMD films are of great importance in preserving their intrinsic properties. In practice, many transfer methods suffer from imperfections, which may arise due to several factors: (i) Wrinkles and cracks would be introduced because of thermal and mechanical perturbations during the transfer process, surface energy differences between the supporting layer and TMDs, capillary forces in the solution evaporation, and other processes. (ii) Bubbles at the interface are usually introduced because of trapped air pockets, residual water or reagents during the transfer process, which lead to poorer contact, proximity effects and varying stress effects on interlayer excitons. (iii) Polymer residues are unavoidable during the chemical transfer process, which reduce device conductivity. In response to these issues (wrinkles, cracks, bubbles, and polymer residues), concerted efforts are being made to enhance the standard transfer methodologies, with a focus on minimizing contamination and maintaining film integrity.

**6.2.1. Chemical Etching Transfer.** With the increase of applications demanding large-scale TMD films for devices such as integrated circuits, the development of scalable, non-destructive transfer techniques became necessary. Consequently, many methods initially devised for transferring graphene were adapted for TMD films. One of the most widely employed techniques is the polymer-assisted chemical etching method (Figure 26a).[496] This transfer process involves several steps: (i) Polymer is initially uniformly spin-coated onto the TMD/growth substrate, serving as a supporting layer. (ii) The polymer/TMD/growth substrate assembly is then carefully floated on the surface of an etching solution, facilitating complete and clean chemical etching of the growth substrate. (iii) After thorough cleaning with deionized water, the polymer/TMD structure is transferred onto the target substrate. The polymer supporting layer is subsequently removed, either by dissolution in acetone or through annealing, ultimately yielding the TMD/target substrate configuration.

Scaling this process up to larger dimensions without compromising the TMD film’s structural integrity is crucial. The suitability of the support layer plays a crucial role in the transfer process. The PMMA with suitable flexibility, robustness, and compatible thermal expansion coefficient makes it a preferred choice for a supporting layer.[900,901] However, its tendency to crack, wrinkle, or leave residues has driven researchers to explore alternatives.[902] In a recent development, Mondal et al. successfully demonstrated a residue-free transfer technique for CVD-grown TMD samples employing polypropylene carbonate (PPC) as the supporting layer instead of PMMA.[903] The experimental results indicate that PPC leaves significantly less (almost negligible) chemical residue compared to PMMA and exhibits better adhesion to TMD. More polymers, such as PC,[904,905] PVA,[906] PLA,[905] and others,[902,907] are utilized to support the layers, effectively addressing the issues of chemical residue and folding during the transfer process.

The conventional method of chemical etching substrate transfer typically necessitates the use of harsh chemical corrosion agents, such as KOH, which inevitably leads to damage to the TMD materials. Furthermore, employing aggressive chemical reagents for etching the growth substrate renders it nonreusable, resulting in a relatively costly production process and hindering its industrial application. Consequently, an alternative transfer technique known as bubble transfer has emerged for transferring CVD-grown TMD films on metal substrates.[908] In contrast, the bubble transfer method employs an electrical current to generate bubbles between the substrate and TMD, weakening their adhesion and enabling separation without substrate etching. For instance, Yun et al. utilized the bubble method to successfully transfer cm-scale, CVD-grown $WS_2$ films from gold foil onto $SiO_2$/Si substrates for electrical studies.[496] Gao et al. extended the bubble method to incorporate a roll-to-roll structure for the production of large-area flexible films (Figure 26b).[417] These films included homogeneous single and double layer $WS_2$, as well as $WS_2$/graphene heterostructures. The weak interaction between $WS_2$ and Au enables the mass production of large-area, flexible monolayer $WS_2$ thin film transistor arrays using the electrochemical bubble method. Moreover, seeking to avoid introducing unnecessary impurities due to chemical reactions, Ma et al. pioneered an ultrasonic bubbling technique in which microbubbles, are induced by ultrasound instead of electrochemical reaction.[909] Notably, this method ensures a straightforward transfer process without the need for any detrimental etching agents or chemical reactions, but inevitably some cracks will be introduced.

Chemical etching transfer technologies, including chemical etching and bubble methods, offer easy operation, industrial compatibility, and the ability to transfer large areas, making them cater to the necessity for large-area films in high-end applications. Meanwhile, addressing the challenges of sample degradation and substrate damage remains critical, especially since chemical etching methods often involve potentially damaging chemical reagents and are prone to impurity contamination from polymer residues. Additionally, the use of volatile, toxic solvents like acetone for polymer layer removal requires special handling and disposal procedures. While the bubbling method mitigates the need for substrate etching, it introduces risks of rupture and folding in the TMD films during bubble generation. Future developments must focus on optimizing these processes to further minimize defects and impurities. Finding solutions that can achieve the balance of material quality, size, cost, and efficiency is vital and urgent, ensuring the broad scalability and integration of TMDs into next-generation electronic devices. At the same time, people are pursuing a complete dry transfer without chemical reagents to deal with these issues and realize this vision.

**6.2.2. Direct Pick-up Transfer.** To address the limitations associated with chemical etching, such as potential sample degradation and polymer contamination, the surface energy assisted direct pick-up transfer method has been adopted, offering a nondestructive alternative. In this transfer process, a supporting layer initially adheres to the TMD films, forming a stack of supporting layer/TMD/growth substrate. The transfer occurs when the adhesive force between the supportive layer and the TMD supersedes that between the TMD and its growth substrate, allowing the composite to be picked up and placed onto the target substrate. By contrast, if the TMD adheres more strongly to the target substrate, the supporting layer can be removed separately, leaving the TMD on the target substrate. Surface energy assisted direct pick-up methods facilitate ultraclean transfer without the need for chemical etching, dissolution reactions, and sometimes even liquid involvement in order to achieve complete dry transfer.

Initially, laboratories utilize polymers like PDMS to create stamps for supporting layers.[894,895,910,911] By adjusting the polymer's surface energy through temperature manipulation, they could modulate the energy relationships among the stamps, TMDs, and substrate for successful TMD transfer. However, stamp-based transfer methods, similar to mechanical exfoliation, are limited by the size of the material being transferred. Therefore, researchers have developed various methods for surface energy adjustment via water, metal, and vdW forces to enable direct pick-up transfers.

Water serves as an efficient medium to control surface energy dynamics, simplifying the lifting of TMD films from substrates by modifying the surface energy balance.[912−914] Introducing a water layer between a hydrophilic substrate and a hydrophobic supportive layer allows the transfer of the TMD/supportive layer stack.[915] Upon water evaporation, the TMD adheres to the target substrate, facilitating the supportive layer's removal through thermal adjustment. For instance, Xu et al. demonstrated a polystyrene (PS) supporting layer-based transfer process using water-assisted transfer. They leveraged capillary forces in water to alter the surface energy relationship between TMDs and the growth substrate, facilitating their transfer to the target substrate (Figure 26c).[916] Using water, inch-scale TMD films can be transferred losslessly to flexible substrates,[477] even abandoning the supporting layer to complete the transfer. Hong et al. demonstrated the transfer of a single layer of $MoS_2$ from glass to a graphite substrate using solely ultrapure water, completely eliminating the need for polymer support.[917] In addition, ice has also been used as a supporting layer for ultraclean transfers.[918]

Metal-assisted transfer techniques have exhibited efficacy in facilitating clean transfers of TMD films.[919] The interaction between metals and TMDs is marked by a high surface energy, which simplifies the pick-up process. As a result, metal-assisted transfer methods have shown feasibility in achieving clean TMD transfers. The greater mechanical stiffness of metal films also enhances stability during the transfer process, preserving the structural integrity of the transferred film. For example, Jaewoo et al. used a 600-nanometer-thick Ni film as an atomic-scale adhesive supporting layer, enabling high-throughput production of multiple single-layer wafer-scale 2D materials, with a notable achievement of 5 cm diameter films (Figure 26d).[920] Huang et al. demonstrated a gold-assisted mechanical stripping method for the separation of 40 types of single-crystal monolayers.[921] Liu et al. evaporated a thin gold film onto the meticulously polished surface of a silicon wafer, then stripped the gold film from the substrate using a heat release band and a polyvinylpyrrolidone (PVP) interface layer.[922] The ultraflat gold strip enables a tight and uniform vdW contact between gold and the two-dimensional vdW crystal surface, aiding material transfer. Similarly, bismuth has been identified as a viable support for transferring TMDs, underscoring the diversity of metals applicable in this context.

The vdW force assisted direct pick-up transfer offers a chemical-free and solvent-free approach to efficiently strip TMD layers from their growth substrate, eliminating the need for etchants or solvents.[923,924] Materials with intrinsic vdW forces and surface energies compatible with TMDs act as natural support layers, permitting unblemished transfers. This method allows for precise layer stacking, aiding in the construction of heterostructures and devices, making it invaluable for controlled material integration. Its versatility spans large-area material transfer, from micrometers to


https://doi.org/10.1021/acs.chemrev.3c00851
Chem. Rev. XXXX, XXX, XXX−XXX

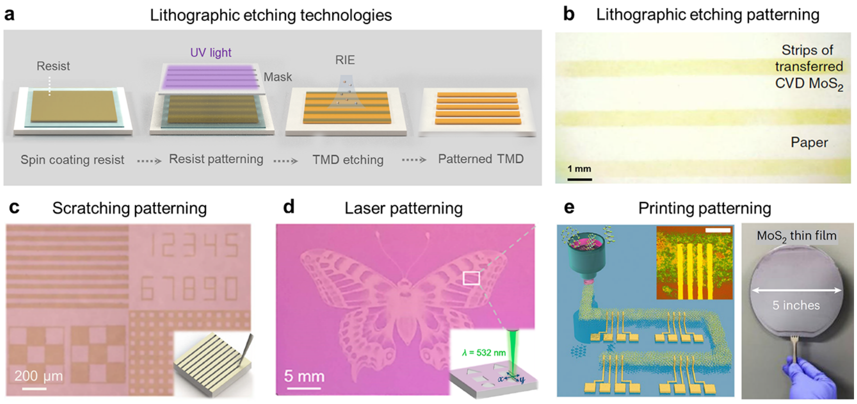


**Figure 27.** Patterning techniques for large-area TMDs. (a) Schematic illustration of lithographic etching technologies for TMDs. (b) Optical micrograph showing the patterned $MoS_2$ strips on paper by lithographic etching technologies. Reprinted with permission from ref 931. Copyright 2020 Springer Nature. (c) Optical images of patterned $MoS_2$ films by scratching patterning. Inset: illustration of the scratching-lithography process. Reprinted with permission from ref 939. Copyright 2020 IOP Publishing Ltd. (d) Photograph of patterned $MoS_2$ films by laser patterning. Inset: illustration of the laser patterning. Reprinted with permission from ref 944. Copyright 2022 American Chemical Society. (e) Schematic illustration (inset: optical microscopic image) of an inkjet-printed large-area superconducting $NbSe_2$ wire (left panel) and image of slot-die-coated SEA and $MoS_2$ on a 5-in. silicon wafer (right panel). Reprinted with permission from ref 950. Copyright 2021 Springer Nature (left panel). Reprinted with permission from ref 951. Copyright 2023 Springer Nature (right panel).

centimeters, applicable in research and industrial settings. Kang et al. successfully employed the vdW force assisted direct pick-up transfer to transfer and stack TMD layers in a vacuum environment, facilitating the creation of CVD-grown TMD heterostructures with pristine interfaces (Figure 26e).[925] Kim et al. reported the development of an extremely anisotropic thermal conductor based on large-area vdW films with random interlayer rotation, achieved through the vdW force assisted direct pick-up transfer. This innovation yielded a room-temperature thermal anisotropy ratio of nearly 900 in $MoS_2$, one of the highest thermal anisotropy ratios ever recorded (Figure 26f).[926] Furthermore, the vdW force assisted direct pick-up transfer can be seamlessly integrated into automated transfer instrument for TMDs, leveraging van der Waals forces between the materials. Mannix et al. introduced a robotic four-dimensional pixel assembly method that utilizes the vdW force assisted direct pick-up transfer to fabricate vdW solids with unprecedented speed, meticulous design, large surface areas, and precise angle control (Figure 26g).[927]

With the rapid advancement of the electronics industry, TMDs are emerging as a critical element in the next generation of semiconductor materials. Serving as the bridge in the application of TMD materials, transfer technology offers a clean, nondestructive, smooth, straightforward, and environmentally friendly method. This opens up limitless possibilities for the potential applications of 2D materials. To align with the demands of the electronics industry, there is a more pressing need to develop TMD transfer technology that can accommodate large areas and achieve mechanical automation.

### 6.3. Patterning Techniques

Patterning techniques possessing TMDs as specific morphology at the nanoscale represent an enabling technology for further boosting the pristine material properties. Nanopatterning plays a crucial role in shaping TMDs into arbitrarily complex geometries in order to meet the specific requirements of the desired target application. For instance, the realization of TMD-based optical metasurfaces needs morphology control on the subwavelength scale thus producing spatially varying optical constants which are able to induce nonconventional light-matter interaction.[928,929] In the field of electronics, pattern engineering is an effective route toward the fabrication and miniaturization of integrated circuits. In addition to traditional lithography, some approaches designed specifically for TMDs, such as utilizing specialized probes, have dramatically shrunk feature sizes from microns to nanometers, achieving resolutions below 20 nm and enabling wafer-scale production capabilities.[930] In this section, we mainly focus on the patterning techniques of the as-grown TMDs: lithographic etching technology, direct writing technology, and inkjet printing technology.

As an important part of the traditional semiconductor micromachining process, well-established lithographic etching technologies, including UV lithography, electron beam lithography (EBL), reactive ion etching (RIE), etc., are widely used for patterning TMD devices. Figure 27a illustrates the typical process flow for the lithography and etching processes. A resist layer is first spin-coated onto a target TMD film, followed by the baking process to remove the solution and eliminate the strain built-in after spin-coating. The mask featuring the desired nanopattern is then aligned and exposed to ultraviolet light to pattern the photoresist (or scanning to expose the preset pattern by high energy electron beam). Following this, the development process removes the photoresist from the exposed area and leaves the specific patterned photoresist covering the TMD target pattern, which serves as a mask for the TMD during the subsequent etching process. Followed by the etching process, the patterned TMD film was successfully fabricated.

According to the etching mediums, the etching process can be categorized into dry etching and wet etching, with typical dry etching involving a chemical reaction activated by plasma or high-energy beam bombardment, without the use of a solution. In addition to oxygen plasma, reactive ion etching (RIE), a mature commercial dry etching method, is commonly used for fabricating specific TMD structures in integrated circuit manufacturing. In RIE chambers, high-pressure ionization of plasma generated by corrosive gases (e.g., $CHF_3$, $CF_4$, and $SF_6$) that exhibit strong chemical reactivity. These gases react with the atoms of the etched sample, producing volatile substances that corrode the sample's surface.


https://doi.org/10.1021/acs.chemrev.3c00851
Chem. Rev. XXXX, XXX, XXX−XXX

Precise control over etching parameters allows the fabrication of two-dimensional nanopatterns of varying thickness. In 2013, Chen et al. reported the etching of bulk $MoS_2$ by $SF_6$ to achieve the controlled fabrication of large-area patterned arrays.[716] Following this, Conti et al. achieved specific $MoS_2$ patterns by etching $MoS_2$ on sapphire with $SF_6$ and transferred the patterns to paper, resulting in $MoS_2$ array devices with impressive on/off ratios and mobility (Figure 27b).[931] Furthermore, Meng et al. utilized $CF_4$ RIE etching to fabricate $MoS_2$ TFTs based on 2-in.-$MoS_2$ on sapphire with Au Film laminated on the fresh as-grown $MoS_2$.[932] The Au Film acted as protection layer from ambient absorption, dry etching mask and electrical contacts, achieving transistors with median mobility of 54 $cm^2$ $V^{-1}$ $s^{-1}$, drive current of 210 $\mu$A $\mu m^{-1}$, and excellent uniformity, leading to the realization of high-resolution displays.

Although wet etching is another universal nanopatterning method, its development has been slow due to the limitations of immersion solutions. In 2020, Munkhbat et al. introduced a wet etching approach that achieves anisotropic TMD etching with atomic precision.[933] They formed circular holes on TMD surfaces through EBL and RIE, followed by anisotropic etching in an aqueous solution of $H_2O_2$ and $NH_4OH$ to create hexagonal hole arrays. They showed that TMDs can etched along certain crystallographic axes, such that the obtained edges are nearly atomically sharp and exclusively zigzag-terminated. To address the limitations of solution-based wet etching, Liu et al. expanded this method to thermal etching. They annealed TMDs after laser irradiation to enable anisotropic thermal etching.[934] This approach allowed for controlled hole sizes and densities in bilayer $WS_2$ with different arrangements, achieving precise patterning in this two-dimensional material.

In summary, the etching process is particularly suitable for large-area processing, making it of great promise for batch production.[935] The minimal feature size is close to sub-10 nm. In addition, etching technologies are compatible with modern semiconductor integration process, which possibly makes TMDs easy to be integrated on silicon-based substrates.[936] Etching technologies are suitable for batch production which has been widely employed in the silicon-based industry. Still, the photoresist residues will hinder the application of 2D materials.[937] And TMD's atomic thinness makes it susceptible to damage. Ultraviolet exposure and direct metal electrode evaporation potentially cause edge defects and morphological inconsistencies, reducing device performance.

To prevent unintended material modifications and eliminate the impact of residuals and laser exposure, direct writing technology primarily utilizes two key tools: probes and lasers. For instance, scanning probe lithography has been employed to directly fabricate single-layer TMD patterns without relying on sacrificial resist materials.[938] In 2020, Wei et al. introduced scratch lithography, where metal tungsten tips mechanically scrape the surface of two-dimensional materials to achieve patterned processing at a wafer scale, with an accuracy of approximately 1 $\mu$m, similar to UV lithography (Figure 27c).[939] Moreover, Zhao et al. utilized tip-induced oxidation to achieve controlled oxidation at resolutions below 100 nm,[940] effectively producing controllable-sized two-dimensional graphical materials by manipulating tip bias, amplitude set point, and humidity. Laser processing has emerged as another crucial direct-write technique for patterning 2D nanopatterns.[941,942] In 2018, Lin et al. presented photothermal plasma nanolithography,[943] an all-optical lithography technique enabling high-throughput, versatile, and mask-free patterning of various atomic layers. More recently, Poddar et al. developed a resistless lithography method based on direct laser patterning (Figure 27d),[944] successfully fabricating FET arrays using monolayer $MoS_2$ and $WSe_2$. However, direct writing technology typically requires more time to achieve high-resolution results at atomic or molecular scales, resulting in higher costs and increased energy consumption compared to lithography. Consequently, it is challenging to apply direct writing technology for wafer-scale imaging tasks.

Inkjet printing technology, developed over a decade, is an efficient patterning method employing solution intercalation.[945,946] It involves dispersing TMD in solution to create ink[947,948] and employs controlled programming to quickly and precisely print TMD in situ.[463,949] This approach is particularly valuable for producing large-area patterns with relatively low resolution, typically exceeding 1 $\mu$m. In 2021, Li et al. used an electrochemical stripping method to produce high-yield, large-size single crystal monolayers of up to 300 $\mu$m, using $NbSe_2$ serving as a model system (Figure 27e, left panel).[950] The resulting twisted $NbSe_2$ vdW heterojunction exhibited remarkable stability, excellent interface properties, and critical current modulation in response to a magnetic field flux quantum suitable for integer molar lattice. More recently, Kwon et al. employed a commercial slot printing process to manufacture wafer-scale transistor arrays based on $MoS_2$. At room temperature, the average carrier mobility of the FET reached 80.0 $cm^2$ $V^{-1}$ $s^{-1}$, with Hall's measurement indicating 132.9 $cm^2$ $V^{-1}$ $s^{-1}$ (Figure 27e, right panel).[951]

Achieving high-quality and controllable two-dimensional material nanopatterns is paramount in transitioning from laboratory-scale research to practical applications. Traditional lithography technology remains widely used in TMD patterning due to its maturity, compatibility with modern industry, and mass manufacturing capabilities. However, its complex steps introduce unknown modulations, hindering the assurance of controlled TMD device performance. Consequently, there is a pressing need to explore novel patterning methods for 2D TMDs, aiming to fabricate devices while minimizing thermal, mechanical, and chemical damage, as well as avoiding unnecessary modulations.

## 7. APPLICATIONS OF LARGE-AREA TMDs

In the past decade, the unique properties of 2D TMDs have sparked numerous application-driven explorations in fields such as electronics, optoelectronics, and photonics. Proof-of-concept devices such as ultrascaled transistors, flexible displays, and wearable electronics have appeared as promising "killer applications" for large-area TMD materials. The device performance, integration density and reliability are steadily advanced as the evolution of synthesis methodology of TMDs. These rapid developments significantly fueled the efforts for pushing the lab-to-fab transition of TMDs by worldwide scientists and companies like TSMC, Samsung, and Intel.[952] In this section, we mainly focus on the diverse application scenarios of large-area synthesized TMDs, including electronics, photonics, sensors, catalysis and other potential fields.

### 7.1. Electronics

In response to the increasing demand for high integration density of transistors guided by Moore's law, CMOS device sizes have been steadily decreasing in recent decades. However,


https://doi.org/10.1021/acs.chemrev.3c00851
Chem. Rev. XXXX, XXX, XXX−XXX

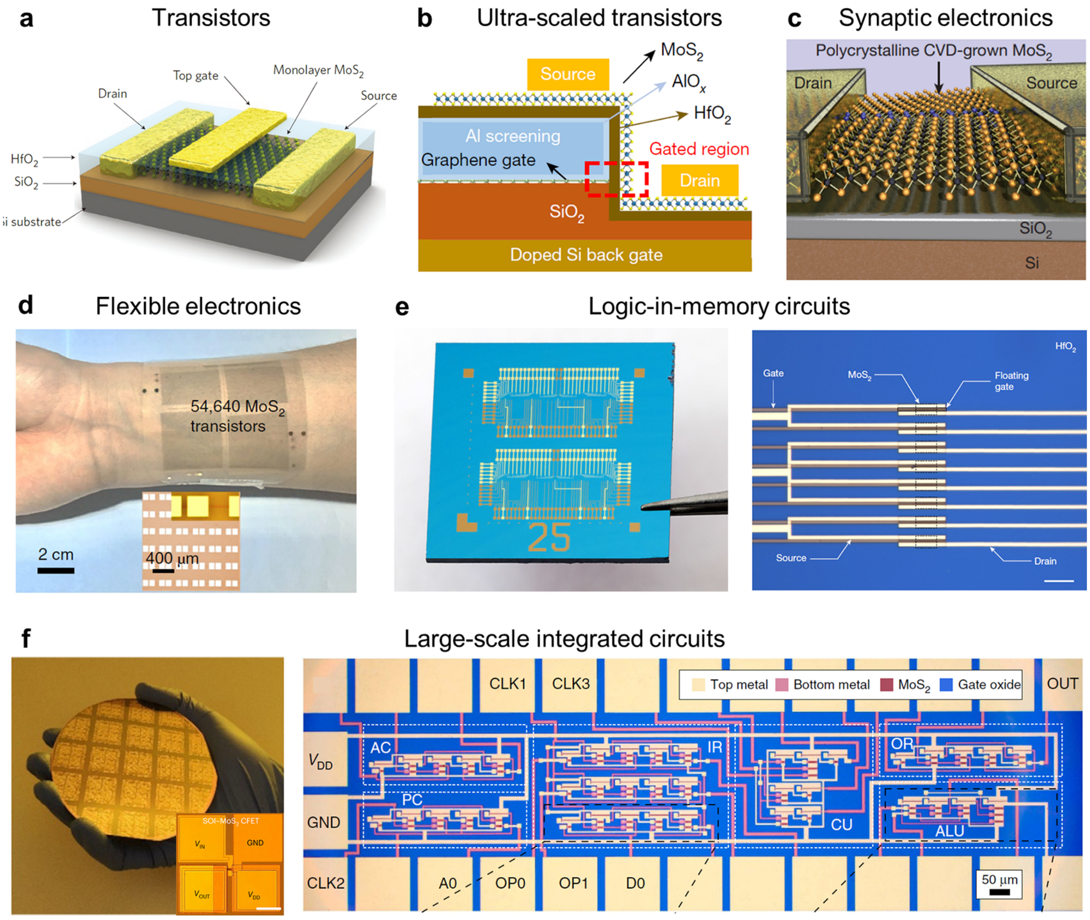


**Figure 28.** Applications of TMDs for electronics. (a)Schematic illustration of transistors based on TMDs. Reprinted with permission from ref 49. Copyright 2011 Springer Nature. (b) Schematic of ultrathin edge gate monolayer $MoS_2$ side-wall transistor. Reprinted with permission from ref 955. Copyright 2022 Springer Nature. (c) Schematic of a $MoS_2$ memtransistor device for synaptic electronics. Reprinted with permission from ref 980. Copyright 2018 Springer Nature. (d) Photograph of very large-scale flexible $MoS_2$ transistor arrays. Inset: magnified image of FET arrays. Reprinted with permission from ref 984. Copyright 2020 Springer Nature. (e) The logic-in-memory circuits based on TMDs. Left, photograph of a fabricated 12 mm × 12 mm die with logic-in-memory cell arrays. Right, optical image of the fabricated floating-gate memory array. Reprinted with permission from ref 992. Copyright 2020 Springer Nature. (f) Large-scale integrated circuits based on TMDs. Optical image of the 3D-stacked CFET wafer after $MoS_2$ transfer (left panel). Inset: the zoom-in image of the CFET device. Reprinted with permission from ref 935. Copyright 2023 Springer Nature. Microscope image of the microprocessor (right panel). Reprinted with permission from ref 999. Copyright 2017 Springer Nature.

as the transistor channel length and thickness reduce and approach the physical limits, the influence of scattering mechanism, dangling bond, and short-channel effects will inevitably be introduced, which will cause a decrease in device mobility and drift in threshold voltage, lending to Moore's Law failure. Sustaining Moore's Law and unlocking the potential of the next generation of computers will necessitate entirely new materials and devices.[953] Monolayer TMDs, with subnanometer (<1 nm) thickness, emerge as prime candidates for pushing the boundaries beyond the ultimate scaling limits of conventional silicon (<5 nm). Atomic layer thickness and no dangling bonds position TMDs as a potentially superior supplement for advanced silicon-based processes. Consequently, extensive research has been conducted on TMD-based FETs. A critical moment occurred in 2011 when Radisavljevic et al. unveiled a monolayer $MoS_2$-based FET that operated at room temperature with a remarkable current on/off ratio of $10^8$ and exhibited ultralow standby power dissipation—powered by a single-layer $MoS_2$ with a mobility of at least 200 $cm^2\ V^{-1}\ s^{-1}$ (Figure. 28a).[49] Subsequently, TMD-based transistors have been the subject of extensive research and have seen periods of sustainable development.

On account of their intrinsic immunity to short-channel effects and advancements in structure fabrication have unlocked even more promising avenues for short-channel transistors. Xie et al. developed a grain boundary widening technique with graphene electrodes for contacting monolayer $MoS_2$ and fabricated FETs with channel lengths scaling down to ≈4 nm.[954] The practicality of $MoS_2$ transistors with a 1 nm physical gate length using a single-walled carbon nanotube as the gate electrode has also been validated.[3] Further pioneering in 2022, Wu et al. demonstrated side-wall $MoS_2$ transistors with an atomically thin channel and a physical gate length of sub-1 nm using the edge of monolayer graphene as the gate electrode. (Figure 28b).[955] Transistor architectures play a role in the performance since structural variations can affect the gate's ability to modify the electric field applied to the channel. Thanks to their layered nature, 2D semiconductors are also adapted to various transistor architectures, from planar to three-dimensional (3D), illustrating compatibility with advanced Si technology. The 3D structure allows for better gate control and higher current for a given footprint of the transistor. Recently, fin field-effect-transistors (FinFETs),[956] multibridge-channel field effect transistors (MBCFETs),[957] and CFETs[958,959] based on TMDs have been developed. Gate-all-around (GAA) devices are considered to be promising devices because of their excellent electrostatic control properties and area efficiency.[960] Additionally, low-temperature monolithic three-dimensional integration (M3D) of TMDs has been realized by vdW lamination of entire prefabricated circuit tiers. By further repeating the vdW lamination process tier by tier, an M3D integrated system is achieved with 10 circuit tiers in the vertical direction, where the processing temperature is controlled to 120 °C. Furthermore, by vertically connecting devices within different tiers through vdW intertier vias, various logic, and heterogeneous structures are realized with desired system functions.[961] The ability to shrink transistors to such diminutive sizes reveals electrical performance possibilities that surpass those of silicon-based technologies, signaling a new era where the physical constraints of silicon are no longer a boundary to the progress of ultrascaled electronics.

As the device size continues to miniaturize, the metal and dielectric layers deposited on the TMDs are a major limitation to increasing the performance of transistors. During deposition of metal and dielectric layers, the evaporated atoms destroy the TMDs atomic lattice generating defects that result in the Fermi level being pinned by the interfacial state, and the potential barrier height is independent of Schottky-Mott limit.[962] For TMDs-based FET applications, the core of tuning the FETs transport characteristics is to modulate the 2D semiconductor-metal contact barrier by the gate voltage. Addressing this, a series of inventive strategies have been designed to decrease the contact resistance, including improvement of metal-TMD contact, vdW contact, and adding an extra tunneling layer. Shen et al. reported ohmic contact with zero Schottky barrier height between semimetallic bismuth and semiconducting monolayer TMDs.[963] Recently, Jiang et al. reported a yttrium-doping approach to convert semiconducting $MoS_2$ into metallic $MoS_2$, which improves the band alignment and provides ohmic device contacts. The yttrium-doped $MoS_2$ acts as a metallic buffer that improves charge carrier transfer from the metal electrode to semiconducting $MoS_2$.[964] Analogously, Pt,[965] Au,[966] In,[967,968] and Sb[969] have also been demonstrated a substantial reduction in contact resistance when interfaced with TMDs. In contrast to contacts formed by deposited metals, vdW contacts via transfer not only prevent damage to the TMD but also reduce contact resistance, making them a proven and effective contact method.[970−973] Liu et al. defined a highly efficient and damage-free strategy for metal integration by transferring metal films (silver or platinum) with a work function that matches the conduction band or valence band edges of molybdenum sulfide.[974] Another important aspect is the deposition of superior gate dielectrics atop TMD films. These dielectrics not only regulate the current via gate capacitance but also insulate the gate from the channel, mitigating leakage currents. Advanced deposition techniques have been showcased, including the introduction of a seeding layer, remote plasma treatments, and ultraviolet-ozone exposure to attain homogeneous high-*k* dielectrics. Xu et al. reported a high-quality dielectric film $Sb_2O_3$ with sub-1 nm equivalent oxide thickness and fabricated monolayer $MoS_2$-based FETs with the thinnest equivalent oxide thickness (0.67 nm).[975] The transistors exhibited an on/off ratio of over $10^6$ using an ultralow operating voltage of 0.4 V, achieving unprecedently high gating efficiency. Other than conventional high-*k* dielectrics such as $Al_2O_3$ or $HfO_2$,[976] electrolytes such as ionic liquid,[977] ion gel[978] or polymer electrolyte,[979] are emerging as alternative dielectrics for gating TMD FETs.

With continuous advances in transistor processing technology, the electrical performance of TMDs materials at the ultimate size based on atomic layer thickness has been proved, and device processes compatible with 2D materials such as contact and dielectric layers are being optimized, propelling their adoption across the electronics field. Their expanding importance in synaptic electronics, flexible electronics, logic-in-memory circuits, and integrated circuits is unmistakable. As one of the pivotal elements in extending Moore's Law, TMD-based transistors are progressively cementing their role as a cornerstone technology for future electronics.

The integration of TMDs into the domain of synaptic electronics is attracting substantial attention due to their biocompatibility, enhanced carrier dynamics, and adaptability for implementation in both two and three-terminal device architectures. TMDs-based memristors are suitable for emulating the biological synapses of the human brain's neural network, which possess the capability to regulate resistance across multiple states by recording the history of electrical stimulation. A landmark study by Sangwan et al. in 2018 introduced a memtransistor employing polycrystalline monolayer $MoS_2$ as the channel. This memtransistor combines the functionalities of a memristor and a transistor, exhibiting reversible stepwise resistance changes as well as long-term potentiation (LTP) and long-term depression (LTD) behaviors in response to sequential voltage pulses (Figure 28c).[980] The 2D planar geometry of this device enables the integration of multiple terminals, enriching channel connectivity. This design not only improves heterosynaptic plasticity but also reflects the complex synaptic connections found in biological neural networks. These artificial synapses are instrumental in simulating neural transmission and the physical sensing of information, potentially constructing computing systems that rival the robustness and efficiency of the human brain. Furthermore, the synergy of artificial synapses with various nanomaterial-based active channels opens doors to applications such as visual recognition,[981,982] and hardware neural networks,[983] underscoring their practicality.

The application of TMDs in the realm of flexible electronics, sensors, and display technologies is rapidly expanding, fueled by their outstanding properties such as flexibility, transparency, and biocompatibility.[984−987] These characteristics render TMDs particularly suitable for cutting-edge applications in the ever-evolving field of flexible technology. A notable advancement in this area was reported by Li et al., who successfully fabricated transparent $MoS_2$-based transistors and logic circuits on flexible substrates. Utilizing 4-in. wafer-scale $MoS_2$ monolayers (Figure 28d),[984] these FETs achieved impressive device density (1518 transistors per $cm^2$), high yield (97%), and exhibited remarkable performance metrics including on/off ratios of $10^{10}$, current densities of about 35 $\mu A\ \mu m^{-1}$, and mobilities of approximately 55 $cm^2\ V^{-1}\ s^{-1}$. Further enhancing the $MoS_2$ monolayers, encapsulation with hydrophobic fluoropolymer combined with chemical treatment using TSFI not only augmented their environmental stability but also remarkably improved the quantum yield, approaching unity in monolayer $MoS_2$.[988] This breakthrough has paved the way for the development of flexible high-speed organic light emitting diode (OLED) displays from atomic layers of


https://doi.org/10.1021/acs.chemrev.3c00851
Chem. Rev. XXXX, XXX, XXX−XXX

$MoS_2$.[989] The resulting flexible and bendable active-matrix OLED displays, incorporating $MoS_2$ transistors, are particularly promising for wearable display technologies. Moreover, flexible $MoS_2$ phototransistors have shown remarkable durability, maintaining their mobility even after 1,000 bending cycles, indicative of their excellent mechanical stability. Additionally, $MoS_2$ FET-based strain sensors[990] capable of detecting human body motions and biosensors[991] for identifying cancer biomarkers have been developed, leveraging the unique properties of $MoS_2$. These advancements underscore the significant potential of TMDs in creating flexible, high-performance devices that could revolutionize various aspects of technology, from wearable electronics to advanced sensing and diagnostic tools.

In the realm of computing, traditional Von Neumann architectures, characterized by their distinct processing and storage units, face limitations in power and memory, particularly in the context of expanding data-intensive applications. TMDs emerge as a compelling solution possessing the functionalities of both logic and storage, with their significant direct bandgap and high switching ratios. This integration positions TMDs as a promising candidate for pioneering the next generation of logic-in-memory architectures. In 2020, Marega et al. reported a logic-in-memory devices and circuits based on floating-gate field-effect transistors (FGFETs) utilizing large-area $MoS_2$ as the active channel material (Figure 28e).[992] These FGFETs exhibit a conductance that can be precisely and continuously adjusted, making them ideal as the foundational elements for reconfigurable logic circuits. In these circuits, logic operations are executed directly using the memory elements, enhancing both efficiency and speed. Moreover, in 2021, Wang et al. developed a TMD-based dynamic random-access memory (DRAM) cell with a 2T1C (two-transistor, one-capacitor) structure.[993] This design not only retains data for over 10 s but also supports 3-bit memory storage. Moreover, Ning et al. introduced a novel duplex device structure.[994] This design combines a ferroelectric field-effect transistor with an atomically thin $MoS_2$ channel, realizing a universal in-memory computing architecture conducive to in situ learning. Leveraging the tunable ferroelectric energy landscape, the duplex device demonstrates exceptional performance across various parameters, including endurance (over $10^{13}$ cycles), retention (exceeding 10 years), speed (4.8 ns), and energy efficiency (22.7 fJ $bit^{-1}$ $\mu m^{-2}$). Additionally, this technology facilitated the implementation of a hardware neural network, which achieved a remarkable 99.86% accuracy in a nonlinear localization task using in situ trained weights. More recently, Marega et al. reported an integrated 32 × 32 vector-matrix multiplier with 1024 floating-gate field-effect transistors with a high yield and low device-to-device variability, using monolayer $MoS_2$ as the channel material.[995] Logic-in-memory architecture, with its capacity to blend storage and processing, stands as a potent alternative to conventional Von Neumann computers.[481] This architecture is particularly well-suited to meet the escalating computational demands in fields like artificial intelligence, where speed and efficiency are paramount. The advancements in TMD-based devices and circuits herald a new era in computing, where the seamless integration of logic and memory functions can significantly enhance computational capabilities and efficiency.

The situation of TMDs-based device research is currently undergoing a critical transformation, as the focus shifts from laboratory settings to industrial fabrication and applications via developing large-scale integrated functional circuits using 2D TMDs. This shift holds the promise of integrating TMDs into the modern integrated circuit industry, encompassing applications in sensors, optoelectronic units, and basic logic modules.[896,897,951,972,996,997] For example, Tong et al. demonstrated the potential of TMDs in heterogeneous complementary FETs on a 4-in. wafer. This innovation combined p-type FETs fabricated using silicon-on-insulator technology with n-type FETs made from $MoS_2$ (Figure 28f, left panel).[935] By effectively matching the mobility and employing multiple-gate modulation of the $MoS_2$, they addressed the mobility mismatch issue prevalent in fully silicon-based systems. Additionally, there has been progress in the integration of 8-in. NMOS using TMDs,[27] further underscoring the scalability of these materials in advanced semiconductor applications. Based on existing growth and device integration technologies, scaled manufacturing sizes[31,32] have been achieved and various logic gate functions have been implemented as analog electronics.[897,998] To construct digital integrated circuits capable of complex functions, multiple digital circuit modules such as logic gates, registers, and counters are intricately combined. These circuits form the backbone of modern electronics, including central processing units (CPUs). In a groundbreaking development, Wachter et al. integrated 115 CVD-grown $MoS_2$ FETs to build a microprocessor capable of processing one bit (Figure 28f, right panel).[999] These pioneering efforts in wafer-level integration highlight the vast potential for very-large-scale integration (VLSI) of 2D materials. Currently, low-integration-density ICs exploiting TMDs' advanced properties have become a reality, with some companies already commercializing them. The demand is particularly high for sensors and high-power transistors made from TMDs. However, utilizing TMDs to construct high-integration-density ICs presents a more complex challenge. Intrinsic defects in these materials can significantly impact the yield, variability, reliability, and stability of devices.

Additionally, emerging TMDs have attracted tremendous research attention for the future application in optoelectronics for the past decade. Most TMDs possess a direct band gap, which shows higher efficiency of charge-to-photon conversion, compared with that of an indirect band gap. In the recent years, LEDs, photodiodes, photodetectors, and solar cells have been intensively investigated based on mechanical exfoliated TMD sheets.[898,1000,1001] For wafer-scale TMD films, the optoelectronic study mainly focused on photodetectors.[447,460,1002]

Photodetectors based on 2D TMD operate mostly on the basis of the photovoltaic effect and exhibit lower dark currents and higher responsivity. In 2013, Lopez-Sanchez et al. demonstrated ultrasensitive monolayer $MoS_2$ phototransistors with improved device mobility and ON current. Phototransistors show a maximum external photoresponsivity of 880 A $W^{-1}$ at a wavelength of 561 nm and a photo response in the 400−680 nm range.[898] Subsequently, Chang et al. reported a phototransistor based on $MoSe_2$, which presents a much faster response time (<25 ms) than the corresponding 30 s for the CVD $MoS_2$ monolayer at room temperature in ambient conditions.[1002] Recently, Huo et al. designed ultrasensitive two-dimensional photodetectors, which use an in-plane phototransistor with an out-of-plane vertical $MoS_2$ p−n junction as a sensitizing scheme.[1000] The vertical built-in field separates the photoexcited carriers efficiently and


https://doi.org/10.1021/acs.chemrev.3c00851
Chem. Rev. XXXX, XXX, XXX−XXX

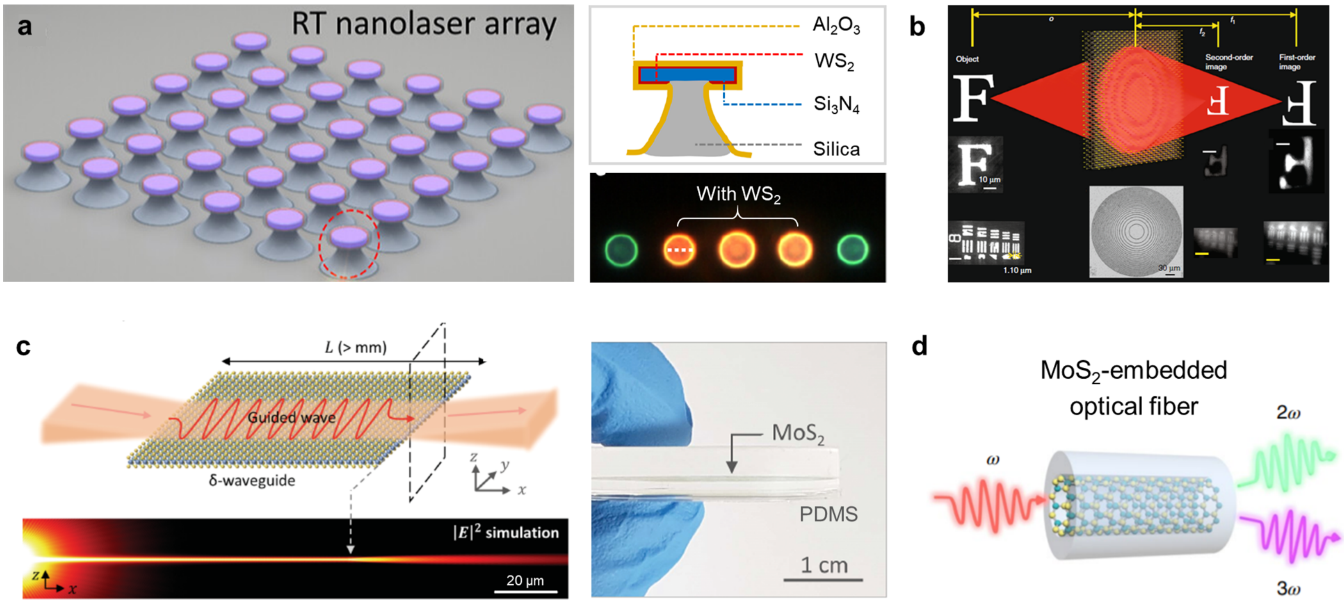


**Figure 29.** Application in optics and photonics for large-area 2D TMDs. (a) Excitonic laser arrays with directly grown $WS_2$ between $Si_3N_4$ microdisks and $Al_2O_3$ at room temperature. Reprinted with permission from ref 1019. Copyright 2022 American Chemical Society. (b) A large-scale flat lens based on monolayer TMDs with high performance for diffraction-limited wide imaging. Reprinted with permission from ref 942. Copyright 2020 Springer Nature. (c) δ waveguides based on wafer-scale monolayer $MoS_2$. Reprinted with permission from ref 1025. Copyright 2023 AAAS. (d) Monolayer $MoS_2$ embedded optical fiber for ultrahigh nonlinearity. Reprinted with permission from ref 199. Copyright 2020 Springer Nature.

produces a photoconductive gain of $>10^5$ electrons per photon, external quantum efficiency greater than 10%, responsivity of 7 $\times$ $10^4$A $W^{-1}$, and a time response on the order of tens of ms.

As a promising beyond CMOS technology, transitioning from laboratory research to industrial production of 2D TMD-based ICs poses significant challenges. These are not confined to material synthesis, process integration, and device performance evaluation but also extend to circuit design issues. Addressing these challenges will be crucial for realizing the full potential of TMDs in the semiconductor industry, particularly as we approach the physical limits of traditional silicon-based technologies. The successful integration of TMDs into large-scale functional circuits could mark a new era in electronics, offering enhanced performance and new capabilities in a wide range of applications.

## 7.2. Photonics

2D TMDs have garnered significant attention in the realm of optics and photonics due to their rich optical properties, including strong interaction with light, significant exciton effects, and substantial optical nonlinearity.[126−128,162,170] TMD monolayers are particularly intriguing with the remarkable optical characteristics and phenomena, which arises from an indirect-to-direct bandgap transition and breaking inversion symmetry when their thickness decreases to the monolayer limit.[177,221,1003] Compared to 2D TMDs of microscale dimensions obtained by the mechanical exfoliation method, the successful fabrication and transfer of large-area and high-quality TMDs promise superior reproducibility and controllability for scalable manufacturing and integrated photonics.[1004] This significant advancement could open up new avenues for advanced optical applications that fully leverage the capabilities of 2D TMDs. In the following, we will explore the various potential optical applications in 2D TMDs and emphasize the unique advantages offered by their large scales.

The unique excitonic effects observed in 2D TMDs have shown tremendous potential for applications in ultracompact coherent light lasers.[1005−1007] For 2D TMDs, the excitons are tightly bound, duo to the enhanced Coulomb interaction between electrons and holes. Monolayer TMDs, with a direct semiconductor bandgap and large exciton binding energy, exhibit strong excitonic emission, making them promising gain media.[1005] Their ultrathin nature and interfaces without dangling bonds allow for seamless integration of 2D TMDs onto any cavity, facilitating the achievement of ultralow-threshold nanolasers. In 2015, Wu et al. realized a significant milestone by demonstrating light lasing by integrating monolayer $WSe_2$ onto a photonic crystal cavity.[1008] In the meantime, Ye et al. reported the excitonic lasing using monolayer $WS_2$ in a microdisk resonator at cryogenic temperatures.[1009] Through the optimization of optical microcavities, researchers have achieved 2D TMDs-based light lasing at room temperature. This has been demonstrated not only in monolayer TMDs but also few-layer TMDs and their heterostructures.[1010−1017] Furthermore, large-area TMDs were in situ grown onto microcavity, which greatly overcame the difficulties and problems during the transfer processes, such as impurity introduction and operation complexity.[1018] Liu et al. demonstrated the excitonic laser arrays with directly grown $WS_2$ between $Si_3N_4$ microdisks and $Al_2O_3$ at room temperature (Figure 29a).[1019] The integration of large-area TMDs and innovative microcavity would provide exciting opportunities for TMD-based nanolasers across a spectrum of optical applications.

In addition to their excitonic properties for lasing, the high refractive index for 2D TMDs can significantly enhance light modulation interaction for ultrathin optical applications. In 2016, Yang et al. reported the thinnest optical lens consisting of few-layer $MoS_2$ (~6.3 nm) at the time.[1020] They utilized the high refractive index of 2D $MoS_2$ to facilitate strong light

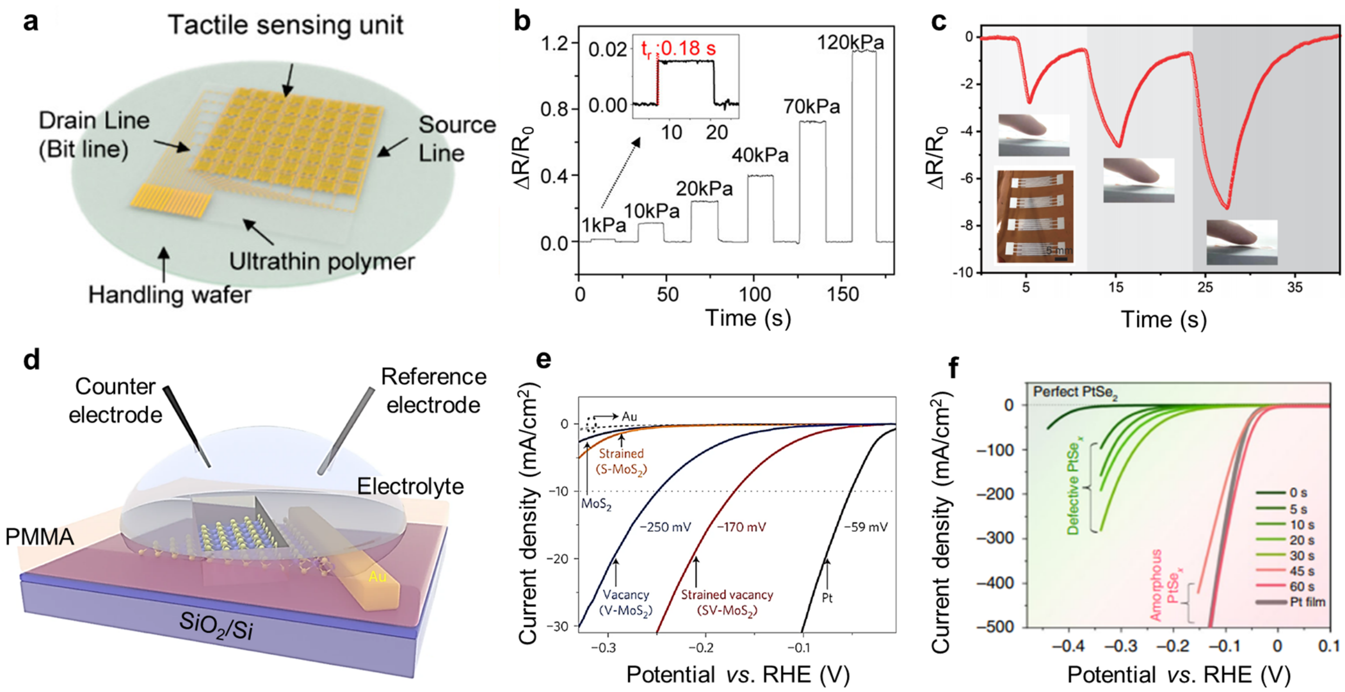


**Figure 30.** Application in sensors and catalysis for large-area 2D TMDs. (a) Schematic diagram of a large-area active matrix $MoS_2$ tactile sensor. (b) Relative resistance changes with time of $MoS_2$ film transistors under different pressures (1 to 120 kPa). The inset illustration shows the response characteristics at 1 kPa, and the response time is 0.18 s. (a,b) Reprinted with permission from ref 1032. Copyright 2019 American Chemical Society. (c) Electrical response of temperature sensor when a finger approaches the sensor. Reprinted with permission from ref 461. Copyright 2022 Wiley-VCH Verlag GmbH & Co. KGaA, Weinheim. (d) Typical schematic diagram of a three-electrode catalytic device. Reprinted with permission from ref 1050. Copyright 2023 Springer Nature. (e) Linear scan voltammograms of monolayer $MoS_2$ for different tensile strains and S-vacancies. Reprinted with permission from ref 835. Copyright 2015 Springer Nature. (f) Polarization curve of $PtSe_x$ material with a treatment duration of 0−60 s. Reprinted with permission from ref 838. Copyright 2022 Springer Nature.

modulation, thereby enabling a giant optical path difference across different layers of $MoS_2$ for precise light beam focusing. In 2020, Lin et al. achieved even thinner flat lenses by using monolayer TMDs.[942] They employed a femtosecond laser direct writing system to create local scattering media within the monolayer TMDs, overcoming the challenge of insufficient light modulation of atomically thin 2D materials. Leveraging large-area monolayer TMDs, they demonstrated a large-scale flat lens with high performance for diffraction-limited wide imaging (Figure 29b).[942] Subsequently, Teng and Li's two groups employed the supercritical principle to design ultrathin lenses to achieve subdiffraction limited focusing and imaging.[1021,1022] Furthermore, Van de Groep et al. demonstrated the electrical tunability of a millimeter-scale zone plate lens to improve focusing properties based on large-area monolayer $WS_2$ in the visible range.[1023] While the focusing efficiency of ultrathin TMD lenses is far below that of conventional bulky optical lenses, their compact-volume, high-tunability, and easy-integration create new novel possibilities for miniaturized and integrated optical systems.[1024]

The availability of large-area and high-quality TMDs has also paved the way for the development of innovative optical waveguides.[199,1025−1027] Lee et al. recently introduced the concept of $\delta$ waveguides based on wafer-scale monolayer $MoS_2$, where the ultrathin waveguide thickness $t$ and refractive index $n$ at the working wavelength $\lambda$ satisfy $nt/\lambda \ll 1$ (Figure 29c).[1025] These $\delta$ waveguides are capable of operating in the visible and near-infrared ranges, efficiently coupling and guiding light over millimeter-scale distances with minimal loss. Furthermore, they expanded the capabilities of $\delta$ waveguides to encompass functions such as refraction, focusing, grating, and interconnection. Beyond applications in the linear optical regime, large-area 2D TMDs also play a crucial role in nonlinear optics.[199,1026,1027] For example, Zuo et al. demonstrated that the direct growth of $MoS_2$ onto the fiber internal walls promised the optical fibers with ultrahigh nonlinearity (Figure 29d).[199] Compared to monolayer $MoS_2$/silica, a 25 cm-long fiber completely embedded monolayer $MoS_2$ showed a 300-fold enhancement in both SHG and THG. They also showed that the $MoS_2$-embedded PCF can serve as a saturable absorber for the all-fiber mode-locked laser. So far, large-area TMDs have provided a valuable material platform for creating ultrathin, compact, and miniaturized optical components and devices,[31,32] which is expected to drive the development of on-chip photonic circuitry and quantum photonics.

### 7.3. Sensors

Due to their atomically-thin layered structures, unique electrical properties, and large specific surface areas, 2D TMD materials offer unparalleled advantages in the realm of sensors. Over the past decade, sensors based on TMDs have found widespread applications in various fields, including gas detection, biosensing, environmental monitoring, electronic skin, and electronic devices. The TMD-based sensors can be categorized into three main types: physical sensors (e.g., mechanics, environmental factors), chemical sensors (e.g., gases, organic compounds, inorganic ions), and biosensors (e.g., biomolecules, antibiotics).[1028]


https://doi.org/10.1021/acs.chemrev.3c00851
Chem. Rev. XXXX, XXX, XXX−XXX

Physical sensors rely on physical reactions, including pressure sensors, strain sensors and temperature sensors.[1029−1031] Among them, pressure sensors primarily operated based on the piezoelectric and piezoresistive effects. The potential for piezoelectricity in TMDs was initially predicted in the theoretical calculation,[295] and in 2014, Wu et al. demonstrated a pressure sensor based on monolayer $MoS_2$.[301] However, the piezoelectric effect imposes strict requirements on materials, necessitating an inversion symmetry-breaking structure. In the case of common 2H-phase TMDs, only odd-numbered layers meet this requirement, posing challenges for implementing piezoelectric-based sensing devices with multilayer TMDs. In 2022, Hallil et al. reported the strong piezoelectricity of multilayer 3R-$MoS_2$ flakes, which possess an inversion symmetry-breaking structure.[306] Moreover, by introducing defects and altering the distribution of free carriers in $MoS_2$, additional polarization effects can arise due to the asymmetry of charge distribution, leading to enhanced piezoelectricity. In 2021, Choi et al. used hot solvent etching to fabricate large-scale $WS_2$ film piezoelectric sensors, demonstrating a 3-fold increase in the piezoelectric response voltage (96.74 mV) under 3 kPa compression compared to the original $WS_2$.[841] Pressure sensors using piezoresistive effect mechanisms have attracted extensive attention and reports. In 2015, Manzeli et al. conducted a study measuring the bandgap tuning in $MoS_2$ due to strain with different layer numbers, demonstrating the emergence of piezoresistive effects.[303] Following this, flexible tactile sensors have gained a great deal of attention. Park et al. engineered a $MoS_2$ haptic sensor array measuring 2.2 cm × 2.2 cm in area.[990] They integrated the sensor with a graphene electrode to achieve excellent mechanical flexibility, optical transmittance, and a high gauge factor within the visible color range. In 2019, Park et al. developed a large-area active-matrix $MoS_2$ tactile sensor (Figure 30a).[1032] In experiments, the resistance of sensor linearly increased with applied external pressure, exhibiting a sensitivity of $\Delta R/R_0 \approx 0.011$ kPa$^{-1}$ and a response time of ∼180 ms at high external pressure (Figure 30b). While carbon-based materials like graphene and carbon nanotubes have gained popularity for temperature sensors in recent years, the potential of TMD materials in this field has been relatively unexplored. In 2022, Daus et al. introduced a flexible monolayer $MoS_2$ temperature sensor array capable of detecting temperature changes in a few microseconds, a significant speed improvement over film metal sensors.[1033] Additionally, Li et al. recently reported a novel method combining inkjet printing and thermal annealing techniques for synthesizing large-area $MoS_2$ patterns.[461] In their study, the resistance of the temperature sensor decreased as the distance between the finger and the sensor decreased (Figure 30c).

Chemical sensors play a vital role in converting chemical information into readable signals, usually electrical signals, including gas sensing, organic compound detection, and ion sensing. Gas sensors, for instance, are instrumental in detecting and quantifying specific gas components in the atmosphere, with applications spanning environmental monitoring, industrial safety, and smart cities. The mechanism involves a redox reaction between the target gas and the surface of the TMD material, inducing alterations in the internal charge transfer process. When placed in an inert gas environment, the target gas molecules desorb, restoring the conductivity to its initial value. In 2012, Li et al. developed a NO gas sensor based on few-layer $MoS_2$.[650] While 1L $MoS_2$ exhibited unstable current, 2L, 3L, and 4L $MoS_2$ FET devices demonstrated stable and sensitive responses (with a minimum response of 0.8 ppm). Likewise, Liu et al. reported that sensors relying on $MoS_2$ epitaxially grown via CVD technology could effectively detect $NO_2$ and $NH_3$, reaching levels as low as 20 ppb and 1 ppm, respectively.[1034] In 2015, Cho et al. introduced a highly sensitive $MoS_2$ gas sensor and employed in situ luminescence characterization to elucidate the interaction between gas molecules and the charge transfer mechanism within $MoS_2$.[1035] Furthermore, gas sensors using TMD materials for gases such as CO and $CO_2$ have also been successfully demonstrated.[1036,1037] In addition, TMDs can also be used as sensitive materials for detecting organic compounds (acetone, ethanol, and methanol) and ion detection sensors.[1038−1040]

Biosensors that harness the unique properties of TMD materials for the detection of biomolecules have garnered significant interest. The atomic thickness and biocompatibility of TMDs plays a pivotal role in adsorbing biological analytes onto their surfaces, generating a sensing response. Biosensors can be categorized into three main types based on their working mechanisms: electrical, electrochemical, and optical.[1041] Electrical signal sensors utilizing TMD materials have demonstrated their prowess in detecting various biomolecules, including prostate cancer antigens, miRNA-155, SARS-CoV-2 and DNA.[991,1042−1044] For instance, Wang et al. pioneered the use of multilayer $MoS_2$ FET devices for the detection of the cancer marker protein prostate-specific antigen, achieving high sensitivity.[1045] Park et al. introduced an ultrasensitive biological FET (with a detection limit of 1 ag/mL) constructed from $MoS_2$ nanopores stimulated by nuclear pore complexes.[1046] This result was achieved by effectively coupling the aptamer to the nanoring at the edge of the $MoS_2$ nanopore. Moreover, electrochemical and optical signal sensors based on TMD materials also offer valuable avenues for detecting biomolecules.[1047−1049]

### 7.4. Catalysis

Clean and sustainable energy conversion technologies are pivotal in reducing reliance on fossil fuels. Catalytic processes play a vital role in the energy conversion journey and constitute a significant component of sustainable energy development. 2D TMD materials have garnered substantial research attention in catalytic reactions, owing to their distinctive electronic structure and surface properties, such as high specific surface area, abundant defect sites, and tunable coordination environment. In recent years, significant strides have been achieved in the field of electrocatalysis utilizing 2D TMDs, including the HER, carbon dioxide reduction reaction ($CO_2$RR), oxygen reduction reaction (ORR), oxygen evolution reaction (OER), etc.

The HER stands as one of the most prominent catalytic reactions. Extensive research has demonstrated that TMD materials, including $MoS_2$, $MoSe_2$, $WS_2$, $WSe_2$, $NbS_2$, exhibit exceptional electrocatalytic performance for HER, and the typical catalytic devices are shown in Figure 30d.[1050−1054] Enhancing HER involves several key regulatory strategies, including heteroatom doping, active site creation, phase control, and heterostructure construction.[777,839,1055−1057] Among these strategies, heteroatom doping emerges as a highly effective means of altering the electronic structure of TMD materials and reducing the Gibbs free energy of the electrocatalyst, thus facilitating the HER process.[1055] For instance, Xiong et al. employed Co doping to effectively modulate the electronic structure of $MoS_2$.[1058] As a result, the intrinsic conductivity is increased, the hydrogen adsorption free energy of $MoS_2$ is decreased under high HER conditions, and the catalytic active site is provided for OER. In 2016, Li et al. reported an effective approach for tuning the HER activity by introducing sulfur vacancies into monolayer 2H-$MoS_2$, effectively creating catalytic sites (Figure 30e).[835] By carefully combining the appropriate S vacancy and strain, they achieved an optimal hydrogen adsorption free energy, resulting in high intrinsic HER activity in the 2H-$MoS_2$ catalyst. Furthermore, metal-phase TMD materials have demonstrated superior performance in electrocatalysis compared to their semiconductor counterparts. Yu et al. successfully synthesized micron-sized metallic phase 1T′-$MoX_2$ (X = S, Se) materials at a large scale.[812] Electrochemical experiments revealed that the basal surface of 1T′-$MoS_2$ exhibited higher activity than that of 2H-$MoS_2$ in an acidic medium. Recently, Shi et al. demonstrated that 2H-$MoS_2$ facilitate the epitaxial of Pt nanoparticles, while the 1T′ phase supports single-atomically dispersed Pt atoms (s-Pt) with Pt loads up to 10 wt %. The experiment measures for s-Pt/1T′-$MoS_2$ a mass activity of 85 ± 23 A $mg_{pt}^{-1}$ at an overpotential of −50 mV.[1059] Heterostructure catalysts based on TMD materials have shown great promise for HER.[1060,1061] In 2015, Gao et al. constructed a heterogeneous $MoS_2/CoSe_2$ catalyst for highly active HER.[1052] In an acidic condition, $MoS_2/CoSe_2$ heterostructure catalysts exhibited remarkably fast HER rates, approaching those of commercial platinum/carbon catalysts. This performance likely arises from the catalytic synergy between the two materials, both possessing hydrogen evolution activity, and an increase in catalytic sites. Recently, He et al. prepared wafer-scale amorphous $PtSe_x$ ($1.2 < x < 1.3$) membranes, which acted as catalysts for achieving high-throughput hydrogen production (Figure 30f).[838] This innovative approach can be extended to other precious metals, including Pd, Ir, Os, Rh, and Ru elements. In addition, catalytic reactions such as $CO_2$RR and ORR based on TMD materials have also been confirmed.[1062−1066]

Based on the rich structural and electrical properties of 2D TMDs and regulatory strategies (heteroatom doping, active site creation, phase control, and heterostructure construction), the improvement of catalytic activity and stability provide opportunities for applications in catalysis. Furthermore, it may be possible to create efficient catalytic properties, promising unique functions, and application-specific customization by designing special materials and building creative structures. However, several key challenges remain for TMD catalysts such as understanding the role of defects and enhancing their stability.

### 7.5. Other Potential Applications

Beyond the aforementioned contents, diverse TMDs are progressively demonstrating potential applicability in various fields such as energy, mechanics, acoustics, environmental sciences, biology, and corresponding interdisciplinary research. For example, owing to their layered structure, high surface area, and excellent electrochemical performance, 2D TMDs have garnered extensive attention as electrode materials for energy storage devices like supercapacitors and lithium-ion batteries.[1067,1068] Tunable electronic properties and high thermoelectric figure of merit endow TMDs with substantial potential in the field of thermoelectric materials research, particularly in energy harvesting and thermoelectric heat energy conversion.[1069,1070] TMDs possess a unique layered structure, resulting in anisotropic thermal conductivity, with varying heat conduction rates in different directions.[926] Coupled with their high thermal stability and a favorable ratio of thermal to electrical conductivity, TMDs present significant potential in the development and application of high-performance thermal conductive materials. This is particularly relevant in areas requiring precise thermal management and stability at high temperatures, such as in cooling electronic devices, energy conversion systems, and aerospace applications.[1071] In recent years, TMDs have demonstrated considerable potential in biomedical applications. The high surface area and functionalization capabilities enable effective drug loading and targeted release in drug delivery systems. In cancer therapy, TMDs are being explored as potential materials for photothermal and photodynamic treatments.[1072] Moreover, the unique optical properties of TMDs render them valuable tools in biological imaging, particularly in fluorescence and photothermal imaging.[1073−1075] The excellent tunability of interlayer stacking, high mechanical properties, and atomic-level thickness also indicate TMDs with unique advantages in acoustic devices.[1076] Numerous application scenarios gradually emerge along with the in-depth exploration of the properties of TMDs, which also drive the advancement of the “on-demand” synthetic methodology of these materials.

## 8. SMMUARY AND PERSPECTIVES

After more than a decade of efforts, significant progress has been made in the large-area production of TMD materials. To date, over 40 types of 2D TMDs are accessible in the laboratory,[368,377] with some achieving standard wafer sizes up to 300 mm.[31,32,1077,1078] As for the crystallinity, the density of zero-dimensional defects has been successfully suppressed to $\sim 10^{12}$ $cm^{-2}$, a level comparable to that of exfoliated samples.[360,366,437,827] Meanwhile, one-dimensional defects, especially grain boundaries, have been effectively eliminated through the epitaxial growth of single-crystal films. To enrich the application scenarios beyond pristine monolayer TMDs, material modification techniques have been significantly advanced. For example, precise control of thickness, ranging from 1 to 3 layers over wafer scale, has facilitated the improvement of their intrinsic electrical performance.[626,648] Stable p/n type doping, continuous component alloying and semiconducting/metallic phase transition have offered much freedom in TMD property modification. The roadmap for TMD-based electronics is becoming increasingly clear, leading the way toward standard semiconductor technology.[208,1079−1083]

Even though significant progress has been made in the wafer-scale production of TMDs, several technique challenges remain to be addressed before the transition from fundamental research to industrial manufacturing. Specifically, numerous parameters within the growth dynamics, surface chemistry, step edges, and atomic symmetry and so on, would synergistically affect the epitaxial behavior and film uniformity. Therefore, these parameters all require in-depth investigation to ensure the reproducibility of TMD products. Besides clarifying the microscopic mechanisms, it is essential to focus on advancing high-throughput, low-cost and environmentally friendly production, as well as keeping a balance between production capacity and material quality. While the TMD wafer sizes have reached 300 mm, aligning with the mainstream of silicon, their


https://doi.org/10.1021/acs.chemrev.3c00851
Chem. Rev. XXXX, XXX, XXX−XXX

production capacity (dozens of pieces per batch) is still far behind the requirement promised as a mature semiconductor (annual demand for millions of wafers). On the other hand, a more immediate concern is that the excess defect density of as-synthesized TMDs (typically $\sim 10^{12}-10^{14}$ $cm^{-2}$) is even 2 to 4 orders of magnitude higher than that of the III−V compound semiconductors. In addition, alternative approaches like nonepitaxial patterned growth[398,1084,1085] or BEOL-compatible (<450 °C) direct growth[27,1086] should also be developed in parallel to advance industrialization.

Broaden the selection of material species is another key step toward diversifying the functionality of TMD wafers. To date, the majority of reported TMD materials have been primarily centered on $MoS_2$, owing to its well-balanced performance and synthesis flexibility. In fact, the diverse catalog of TMDs offers a valuable resource for advancing function/device innovation in the long term. For instance, among the tungsten family, monolayer $WS_2$ is predicted to an outstanding channel material with an ultrahigh phonon-limited mobility (>1100 $cm^2V^{-1}$ $s^{-1}$) and saturation velocity.[55,1087] In the context of constructing CMOS circuits, $WSe_2$ deserves attentions since it appears as a superior member among scarce p-type TMD semiconductors.[1088] For TMDs beyond Group VI like metallic $NbS_2$ and $VSe_2$ and those beyond thermally stable phases, the basic topics of epitaxial mechanism, wafer-scale synthesis, quality improvement and structure modification are still in a relatively early stage.[1089] Further refining of corresponding epitaxial techniques may inspire an in-depth exploration in physics.

As a rapidly rising material, TMDs still lack for unified technological standards concerning detailed quality information, such as defect density, layer number, crystalline orientation, coverage rate and domain size. Establishing these standards is a critical cornerstone for ensuring material quality and reliability when it serves as an option in further semiconductor industry. This is an important issue that should be addressed collaboratively by research and industrial community. Earlier on, 2D graphene took this essential step and established the joint terminology standard, which set a promising precedent for TMDs.[1090] Meanwhile, the reported devices based on TMDs should be clearly benchmarked in consideration of performance such as mobilities, saturation current, on/off ratio, subthreshold swing (SS) and drain-induced barrier lowering (DIBL). Such guidelines have been proposed previously to facilitate the effective comparison and evaluation of device performance reported by different institutions.[1091] Researchers are encouraged to adopt these standards to support long-term innovations in TMD technology.

Considering the current stage of technical route, the present commercialization of TMDs should start from seeking featured applications in some low-integration and cost-insensitive scenarios. As for the adoption of TMDs in electronics, due to the enormous investment of industrial upgrading, a more sensible option at this stage is complementary to the highly developed silicon techniques by hybrid integration. The International Roadmap for Devices and Systems (IRDS) has identified 2D materials as a prospective candidate for new-generation channel material, which is expected to complement mainstream CMOS technology by 2028.[1092] In the foreseeable future, we believe atomic TMD layers will break through the bottleneck of scaling down to sub-10 nm physical gate lengths in the post-Moore era. Furthermore, advancing application scenarios of TMDs such as beyond von Neumann computing, on-chip photonics, flexible optoelectronics, ferroelectrics and spintronics, all hold the potential to fuel revolutionary technologies brought by the 2D era.

## AUTHOR INFORMATION

### Corresponding Authors

**Can Liu** − *Key Laboratory of Quantum State Construction and Manipulation (Ministry of Education), Department of Physics, Renmin University of China, Beijing 100872, China*; Email: canliu@ruc.edu.cn

**Kaihui Liu** − *State Key Laboratory for Mesoscopic Physics, Frontiers Science Center for Nano-optoelectronics, School of Physics and International Centre for Quantum Materials, Collaborative Innovation Centre of Quantum Matter, Peking University, Beijing 100871, China; Songshan Lake Materials Laboratory, Dongguan 523808, China*; orcid.org/0000-0002-8781-2495; Email: khliu@pku.edu.cn

### Authors

**Guodong Xue** − *State Key Laboratory for Mesoscopic Physics, Frontiers Science Center for Nano-optoelectronics, School of Physics and Academy for Advanced Interdisciplinary Studies, Peking University, Beijing 100871, China*

**Biao Qin** − *State Key Laboratory for Mesoscopic Physics, Frontiers Science Center for Nano-optoelectronics, School of Physics, Peking University, Beijing 100871, China*

**Chaojie Ma** − *State Key Laboratory for Mesoscopic Physics, Frontiers Science Center for Nano-optoelectronics, School of Physics, Peking University, Beijing 100871, China*; orcid.org/0000-0003-3649-5220

**Peng Yin** − *Key Laboratory of Quantum State Construction and Manipulation (Ministry of Education), Department of Physics, Renmin University of China, Beijing 100872, China*

Complete contact information is available at: https://pubs.acs.org/10.1021/acs.chemrev.3c00851

### Author Contributions

#G.X., B.Q., C.M., and P.Y. contributed equally to this work.

### Notes

The authors declare no competing financial interest.

### Biographies

Guodong Xue is currently a doctoral candidate at Peking University. He received his B.S. degree from the University of Electronic Science and Technology of China in 2021. His research interests mainly focus on the growth, characterization, and application of 2D TMDs.

Biao Qin is currently a doctoral candidate at Peking University. He received his master degree from Hunan University in 2021. His research interests mainly focus on the growth, characterization, and applications of single-crystal 2D materials.

Chaojie Ma is currently a postdoctoral researcher at Peking University. He received his B.S. degree in 2014 and Ph.D. degree in 2019 from Northwestern Polytechnical University. His current research interests mainly focus on the optical characterization and application of 2D materials.

Peng Yin is currently a master candidate at Renmin University of China. He received his B.S. degree from University of Science and Technology Beijing in 2022. His research interests mainly focus on the design growth and modulation of 2D van der Waals materials.


https://doi.org/10.1021/acs.chemrev.3c00851
Chem. Rev. XXXX, XXX, XXX−XXX

Can Liu is currently a principal investigator at Renmin University of China. She received her B.S. degree from Northwestern Polytechnical University in 2014 and her Ph.D. degree from Peking University in 2019. From 2019 to 2021, she worked as a Postdoctoral Fellow at Peking University. Her research interests mainly focus on 2D material interfacial growth and spectral physics.

Kaihui Liu is currently a Boya Distinguished Professor at the State Key Laboratory for Mesoscopic Physics, School of Physics, Peking University. He received his B.S. degree from Beijing Normal University and his Ph.D. degree from the Institute of Physics, Chinese Academy of Sciences in 2009. Afterward he worked as a postdoctoral fellow at UC Berkeley, USA, until 2014. His current research interest is the growth and device physics of 2D single crystals.

## ACKNOWLEDGMENTS

This work was supported by the National Natural Science Foundation of China (52025023, 52322205, 51991342, 52250398, 52021006, 92163206, 12274456, 11888101, T2188101, 62305003), National Key R&D Program of China (2022YFA1403500 and 2022YFA1405600), Guangdong Major Project of Basic and Applied Basic Research (2021B0301030002), Beijing Municipal Science and Technology Project (Z221100005822003), and the Strategic Priority Research Program of Chinese Academy of Sciences (XDB33000000). This work has been supported by the New Cornerstone Science Foundation through the XPLORER PRIZE.

## REFERENCES

(1) Chhowalla, M.; Shin, H. S.; Eda, G.; Li, L. J.; Loh, K. P.; Zhang, H. The chemistry of two-dimensional layered transition metal dichalcogenide nanosheets. *Nat. Chem.* **2013**, *5*, 263−275.

(2) Manzeli, S.; Ovchinnikov, D.; Pasquier, D.; Yazyev, O. V.; Kis, A. 2D transition metal dichalcogenides. *Nat. Rev. Mater.* **2017**, *2*, 17033.

(3) Desai, S. B.; Madhvapathy, S. R.; Sachid, A. B.; Llinas, J. P.; Wang, Q.; Ahn, G. H.; Pitner, G.; Kim, M. J.; Bokor, J.; Hu, C.; et al. $MoS_2$ transistors with 1-nanometer gate lengths. *Science* **2016**, *354*, 99−102.

(4) Qian, X.; Liu, J.; Fu, L.; Li, J. Quantum spin Hall effect in two-dimensional transition metal dichalcogenides. *Science* **2014**, *346*, 1344−1347.

(5) Tran, K.; Moody, G.; Wu, F.; Lu, X.; Choi, J.; Kim, K.; Rai, A.; Sanchez, D. A.; Quan, J.; Singh, A.; et al. Evidence for moiré excitons in van der Waals heterostructures. *Nature* **2019**, *567*, 71−75.

(6) Cao, W.; Bu, H.; Vinet, M.; Cao, M.; Takagi, S.; Hwang, S.; Ghani, T.; Banerjee, K. The future transistors. *Nature* **2023**, *620*, 501−515.

(7) Liu, C.; Chen, H.; Wang, S.; Liu, Q.; Jiang, Y. G.; Zhang, D. W.; Liu, M.; Zhou, P. Two-dimensional materials for next-generation computing technologies. *Nat. Nanotechnol.* **2020**, *15*, 545−557.

(8) Wang, Q. H.; Kalantar-Zadeh, K.; Kis, A.; Coleman, J. N.; Strano, M. S. Electronics and optoelectronics of two-dimensional transition metal dichalcogenides. *Nat. Nanotechnol.* **2012**, *7*, 699−712.

(9) Du, L.; Molas, M. R.; Huang, Z.; Zhang, G.; Wang, F.; Sun, Z. Moiré photonics and optoelectronics. *Science* **2023**, *379*, eadg0014.

(10) Frindt, R. F.; Yoffe, A. D. Physical properties of layer structures - optical properties and photoconductivity of thin crystals of molybdenum disulphide. *J. Vac. Sci. Technol., A* **1963**, 273, 69−83.

(11) Frindt, R. F. Single crystals of $MoS_2$ several molecular layers thick. *J. Appl. Phys.* **1966**, *37*, 1928−1929.

(12) Du, G.; Guo, Z.; Wang, S.; Zeng, R.; Chen, Z.; Liu, H. Superior stability and high capacity of restacked molybdenum disulfide as anode material for lithium ion batteries. *Chem. Commun.* **2010**, *46*, 1106−1108.

(13) Yang, Y.; Fei, H.; Ruan, G.; Xiang, C.; Tour, J. M. Edge-oriented $MoS_2$ nanoporous films as flexible electrodes for hydrogen evolution reactions and supercapacitor devices. *Adv. Mater.* **2014**, *26*, 8163−8168.

(14) Spalvins, T. A review of recent advances in solid film lubrication. *J. Vac. Sci. Technol., A* **1987**, *5*, 212−219.

(15) Rapoport, L.; Bilik, Y.; Feldman, Y.; Homyonfer, M.; Cohen, S. R.; Tenne, R. Hollow nanoparticles of $WS_2$ as potential solid-state lubricants. *Nature* **1997**, *387*, 791−793.

(16) Chhowalla, M.; Amaratunga, G. A. Thin films of fullerene-like $MoS_2$ nanoparticles with ultra-low friction and wear. *Nature* **2000**, *407*, 164−167.

(17) Novoselov, K. S.; Geim, A. K.; Morozov, S. V.; Jiang, D.; Zhang, Y.; Dubonos, S. V.; Grigorieva, I. V.; Firsov, A. A. Electric field effect in atomically thin carbon films. *Science* **2004**, *306*, 666−669.

(18) Novoselov, K. S.; Jiang, D.; Schedin, F.; Booth, T. J.; Khotkevich, V. V.; Morozov, S. V.; Geim, A. K. Two-dimensional atomic crystals. *Proc. Natl. Acad. Sci. U. S. A.* **2005**, *102*, 10451−10453.

(19) Lee, Y. H.; Zhang, X. Q.; Zhang, W.; Chang, M. T.; Lin, C. T.; Chang, K. D.; Yu, Y. C.; Wang, J. T.; Chang, C. S.; Li, L. J.; et al. Synthesis of large-area $MoS_2$ atomic layers with chemical vapor deposition. *Adv. Mater.* **2012**, *24*, 2320−2325.

(20) Wu, S.; Huang, C.; Aivazian, G.; Ross, J. S.; Cobden, D. H.; Xu, X. Vapor-solid growth of high optical quality $MoS_2$ monolayers with near-unity valley polarization. *ACS Nano* **2013**, *7*, 2768−2772.

(21) Chen, M. W.; Ovchinnikov, D.; Lazar, S.; Pizzochero, M.; Whitwick, M. B.; Surrente, A.; Baranowski, M.; Sanchez, O. L.; Gillet, P.; Plochocka, P.; et al. Highly oriented atomically thin ambipolar $MoSe_2$ grown by molecular beam epitaxy. *ACS Nano* **2017**, *11*, 6355−6361.

(22) Eichfeld, S. M.; Hossain, L.; Lin, Y. C.; Piasecki, A. F.; Kupp, B.; Birdwell, A. G.; Burke, R. A.; Lu, N.; Peng, X.; Li, J.; et al. Highly scalable, atomically thin $WSe_2$ grown via metal-organic chemical vapor deposition. *ACS Nano* **2015**, *9*, 2080−2087.

(23) Choudhury, T. H.; Zhang, X.; Al Balushi, Z. Y.; Chubarov, M.; Redwing, J. M. Epitaxial growth of two-dimensional layered transition metal dichalcogenides. *Annu. Rev. Mater. Res.* **2020**, *50*, 155−177.

(24) Zhang, Y.; Yao, Y.; Sendeku, M. G.; Yin, L.; Zhan, X.; Wang, F.; Wang, Z.; He, J. Recent progress in CVD growth of 2D transition metal dichalcogenides and related heterostructures. *Adv. Mater.* **2019**, *31*, 1901694.

(25) Wang, Q.; Li, N.; Tang, J.; Zhu, J.; Zhang, Q.; Jia, Q.; Lu, Y.; Wei, Z.; Yu, H.; Zhao, Y.; et al. Wafer-scale highly oriented monolayer $MoS_2$ with large domain sizes. *Nano Lett.* **2020**, *20*, 7193−7199.

(26) Kang, K.; Xie, S.; Huang, L.; Han, Y.; Huang, P. Y.; Mak, K. F.; Kim, C. J.; Muller, D.; Park, J. High-mobility three-atom-thick semiconducting films with wafer-scale homogeneity. *Nature* **2015**, *520*, 656−660.

(27) Zhu, J.; Park, J. H.; Vitale, S. A.; Ge, W.; Jung, G. S.; Wang, J.; Mohamed, M.; Zhang, T.; Ashok, M.; Xue, M.; et al. Low-thermal-budget synthesis of monolayer molybdenum disulfide for silicon back-end-of-line integration on a 200 mm platform. *Nat. Nanotechnol.* **2023**, *18*, 456−463.

(28) Zhang, T.; Wang, J.; Wu, P.; Lu, A.-Y.; Kong, J. Vapour-phase deposition of two-dimensional layered chalcogenides. *Nat. Rev. Mater.* **2023**, *8*, 799−821.

(29) Li, H.; Li, Y.; Aljarb, A.; Shi, Y.; Li, L. J. Epitaxial growth of two-dimensional layered transition-metal dichalcogenides: Growth mechanism, controllability, and scalability. *Chem. Rev.* **2018**, *118*, 6134−6150.

(30) Qin, B.; Saeed, M. Z.; Li, Q.; Zhu, M.; Feng, Y.; Zhou, Z.; Fang, J.; Hossain, M.; Zhang, Z.; Zhou, Y.; et al. General low-temperature growth of two-dimensional nanosheets from layered and nonlayered materials. *Nat. Commun.* **2023**, *14*, 304.

(31) Xue, G.; Sui, X.; Yin, P.; Zhou, Z.; Li, X.; Cheng, Y.; Guo, Q.; Zhang, S.; Wen, Y.; Zuo, Y.; et al. Modularized batch production of 12-in. transition metal dichalcogenides by local element supply. *Sci. Bull.* **2023**, *68*, 1514−1521.

(32) Xia, Y.; Chen, X.; Wei, J.; Wang, S.; Chen, S.; Wu, S.; Ji, M.; Sun, Z.; Xu, Z.; Bao, W.; et al. 12-in. growth of uniform $MoS_2$ monolayer for integrated circuit manufacture. *Nat. Mater.* **2023**, *22*, 1324−1331.

(33) Yang, P.; Zhang, S.; Pan, S.; Tang, B.; Liang, Y.; Zhao, X.; Zhang, Z.; Shi, J.; Huan, Y.; Shi, Y.; et al. Epitaxial growth of centimeter-scale single-crystal $MoS_2$ monolayer on Au(111). *ACS Nano* **2020**, *14*, 5036−5045.

(34) Li, T.; Guo, W.; Ma, L.; Li, W.; Yu, Z.; Han, Z.; Gao, S.; Liu, L.; Fan, D.; Wang, Z.; et al. Epitaxial growth of wafer-scale molybdenum disulfide semiconductor single crystals on sapphire. *Nat. Nanotechnol.* **2021**, *16*, 1201−1207.

(35) Wang, J.; Xu, X.; Cheng, T.; Gu, L.; Qiao, R.; Liang, Z.; Ding, D.; Hong, H.; Zheng, P.; Zhang, Z.; et al. Dual-coupling-guided epitaxial growth of wafer-scale single-crystal $WS_2$ monolayer on vicinal a-plane sapphire. *Nat. Nanotechnol.* **2022**, *17*, 33−38.

(36) Zhao, T.; Guo, J.; Li, T.; Wang, Z.; Peng, M.; Zhong, F.; Chen, Y.; Yu, Y.; Xu, T.; Xie, R.; et al. Substrate engineering for wafer-scale two-dimensional material growth: Strategies, mechanisms, and perspectives. *Chem. Soc. Rev.* **2023**, *52*, 1650−1671.

(37) Zhang, Z.; Forti, S.; Meng, W.; Pezzini, S.; Hu, Z.; Coletti, C.; Wang, X.; Liu, K. Growth and applications of two-dimensional single crystals. *2D Mater.* **2023**, *10*, No. 032001.

(38) Liu, C.; Wang, L.; Qi, J.; Liu, K. Designed growth of large-size 2D single crystals. *Adv. Mater.* **2020**, *32*, 2000046.

(39) Zhang, Z.; Yang, X.; Liu, K.; Wang, R. Epitaxy of 2D materials toward single crystals. *Adv. Sci.* **2022**, *9*, 2105201.

(40) Wan, Y.; Fu, J. H.; Chuu, C. P.; Tung, V.; Shi, Y.; Li, L. J. Wafer-scale single-orientation 2D layers by atomic edge-guided epitaxial growth. *Chem. Soc. Rev.* **2022**, *51*, 803−811.

(41) Loh, L.; Zhang, Z.; Bosman, M.; Eda, G. Substitutional doping in 2D transition metal dichalcogenides. *Nano Res.* **2021**, *14*, 1668−1681.

(42) Xie, L. M. Two-dimensional transition metal dichalcogenide alloys: Preparation, characterization and applications. *Nanoscale* **2015**, *7*, 18392−18401.

(43) Kim, D.; Pandey, J.; Jeong, J.; Cho, W.; Lee, S.; Cho, S.; Yang, H. Phase engineering of 2D materials. *Chem. Rev.* **2023**, *123*, 11230−11268.

(44) Yang, H.; Kim, S. W.; Chhowalla, M.; Lee, Y. H. Structural and quantum-state phase transitions in van der Waals layered materials. *Nat. Phys.* **2017**, *13*, 931−937.

(45) Liu, Y.; Huang, Y.; Duan, X. Van der Waals integration before and beyond two-dimensional materials. *Nature* **2019**, *567*, 323−333.

(46) Dickinson, R. G.; Pauling, L. The crystal structure of molybdenite. *J. Am. Chem. Soc.* **1923**, *45*, 1466−1471.

(47) Murphy, D. W.; Hull, G. W. Monodispersed tantalum disulfide and adsorption complexes with cations. *J. Chem. Phys.* **1975**, *62*, 973−978.

(48) Joensen, P.; Frindt, R. F.; Morrison, S. R. Single-layer $MoS_2$. *Mater. Res. Bull.* **1986**, *21*, 457−461.

(49) Radisavljevic, B.; Radenovic, A.; Brivio, J.; Giacometti, V.; Kis, A. Single-layer $MoS_2$ transistors. *Nat. Nanotechnol.* **2011**, *6*, 147−150.

(50) Mak, K. F.; Lee, C.; Hone, J.; Shan, J.; Heinz, T. F. Atomically thin $MoS_2$: A new direct-gap semiconductor. *Phys. Rev. Lett.* **2010**, *105*, 136805.

(51) Splendiani, A.; Sun, L.; Zhang, Y.; Li, T.; Kim, J.; Chim, C. Y.; Galli, G.; Wang, F. Emerging photoluminescence in monolayer $MoS_2$. *Nano Lett.* **2010**, *10*, 1271−1275.

(52) Zhao, M.; Ye, Z.; Suzuki, R.; Ye, Y.; Zhu, H.; Xiao, J.; Wang, Y.; Iwasa, Y.; Zhang, X. Atomically phase-matched second-harmonic generation in a 2D crystal. *Light Sci. Appl.* **2016**, *5*, e16131.

(53) Rasmussen, F. A.; Thygesen, K. S. Computational 2D materials database: Electronic structure of transition-metal dichalcogenides and oxides. *J. Phys. Chem. C* **2015**, *119*, 13169−13183.

(54) Hildebrand, B.; Jaouen, T.; Mottas, M. L.; Monney, G.; Barreteau, C.; Giannini, E.; Bowler, D. R.; Aebi, P. Local real-space view of the achiral 1T-$TiSe_2$ $2 \times 2 \times 2$ charge density wave. *Phys. Rev. Lett.* **2018**, *120*, 136404.

(55) Zhang, W.; Huang, Z.; Zhang, W.; Li, Y. Two-dimensional semiconductors with possible high room temperature mobility. *Nano Res.* **2014**, *7*, 1731−1737.

(56) Yan, C.; Gong, C.; Wangyang, P.; Chu, J.; Hu, K.; Li, C.; Wang, X.; Du, X.; Zhai, T.; Li, Y.; Xiong, J. 2D group IVB transition metal dichalcogenides. *Adv. Funct. Mater.* **2018**, *28*, 1803305.

(57) Bonilla, M.; Kolekar, S.; Ma, Y.; Diaz, H. C.; Kalappattil, V.; Das, R.; Eggers, T.; Gutierrez, H. R.; Phan, M. H.; Batzill, M. Strong room-temperature ferromagnetism in $VSe_2$ monolayers on van der Waals substrates. *Nat. Nanotechnol.* **2018**, *13*, 289−293.

(58) Li, B.; Wan, Z.; Wang, C.; Chen, P.; Huang, B.; Cheng, X.; Qian, Q.; Li, J.; Zhang, Z.; Sun, G.; et al. Van der Waals epitaxial growth of air-stable $CrSe_2$ nanosheets with thickness-tunable magnetic order. *Nat. Mater.* **2021**, *20*, 818−825.

(59) O'Hara, D. J.; Zhu, T. C.; Trout, A. H.; Ahmed, A. S.; Luo, Y. K.; Lee, C. H.; Brenner, M. R.; Rajan, S.; Gupta, J. A.; McComb, D. W.; et al. Room temperature intrinsic ferromagnetism in epitaxial manganese selenide films in the monolayer limit. *Nano Lett.* **2018**, *18*, 3125−3131.

(60) Cui, F.; Li, X.; Feng, Q.; Yin, J.; Zhou, L.; Liu, D.; Liu, K.; He, X.; Liang, X.; Liu, S.; et al. Epitaxial growth of large-area and highly crystalline anisotropic $ReSe_2$ atomic layer. *Nano Research* **2017**, *10*, 2732−2742.

(61) Wang, Y.; Zhou, L.; Zhong, M.; Liu, Y.; Xiao, S.; He, J. Two-dimensional noble transition-metal dichalcogenides for nanophotonics and optoelectronics: Status and prospects. *Nano Res.* **2022**, *15*, 3675−3694.

(62) Lasek, K.; Li, J.; Kolekar, S.; Coelho, P. M.; Guo, L. a.; Zhang, M.; Wang, Z.; Batzill, M. Synthesis and characterization of 2D transition metal dichalcogenides: Recent progress from a vacuum surface science perspective. *Surf. Sci. Rep.* **2021**, *76*, 100523.

(63) Lu, T.; Wang, Y.; Cai, G.; Jia, H.; Liu, X.; Zhang, C.; Meng, S.; Liu, M. Synthesizability of transition-metal dichalcogenides: A systematic first-principles evaluation. *Mater. Futures* **2023**, *2*, No. 015001.

(64) Varma, S. J.; Kumar, J.; Liu, Y.; Layne, K.; Wu, J.; Liang, C.; Nakanishi, Y.; Aliyan, A.; Yang, W.; Ajayan, P. M.; Thomas, J. 2D $TiS_2$ layers: A superior nonlinear optical limiting material. *Adv. Opt. Mater.* **2017**, *5*, 1700713.

(65) Liu, Y.-H.; Porter, S. H.; Goldberger, J. E. Dimensional reduction of a layered metal chalcogenide into a 1D near-IR direct band gap semiconductor. *J. Am. Chem. Soc.* **2012**, *134*, 5044−5047.

(66) May, M. M.; Brabetz, C.; Janowitz, C.; Manzke, R. Charge-density-wave phase of 1T-$TiSe_2$: The influence of conduction band population. *Phys. Rev. Lett.* **2011**, *107*, 176405.

(67) Song, Z.; Lei, B.; Cao, Y.; Qi, J.; Peng, H.; Wang, Q.; Huang, L.; Lu, H.; Lin, X.; Wang, Y.-L.; et al. Epitaxial fabrication of two-dimensional $TiTe_2$ monolayer on Au(111) substrate with te as buffer layer. *Chin. Phys. B* **2019**, *28*, No. 056801.

(68) Chen, P.; Pai, W. W.; Chan, Y.-H.; Takayama, A.; Xu, C.-Z.; Karn, A.; Hasegawa, S.; Chou, M. Y.; Mo, S.-K.; Fedorov, A.-V.; Chiang, T.-C. Emergence of charge density waves and a pseudogap in single-layer $TiTe_2$. *Nat. Commun.* **2017**, *8*, 516.

(69) Zhang, M.; Zhu, Y.; Wang, X.; Feng, Q.; Qiao, S.; Wen, W.; Chen, Y.; Cui, M.; Zhang, J.; Cai, C.; et al. Controlled synthesis of $ZrS_2$ monolayer and few layers on hexagonal boron nitride. *J. Am. Chem. Soc.* **2015**, *137*, 7051−7054.

(70) Tenorio, G.; Bucio, L.; Escudero, R. Filamentary superconductivity in semiconducting policrystalline $ZrSe_2$ compound with zr vacancies. *J. Supercond. Novel Magn.* **2017**, *30*, 2381−2386.

(71) Song, Y.; Jia, C.; Xiong, H.; Wang, B.; Jiang, Z.; Huang, K.; Hwang, J.; Li, Z.; Hwang, C.; Liu, Z.; et al. Signatures of the exciton gas phase and its condensation in monolayer 1T-$ZrTe_2$. *Nat. Commun.* **2023**, *14*, 1116.

(72) Tsipas, P.; Tsoutsou, D.; Fragkos, S.; Sant, R.; Alvarez, C.; Okuno, H.; Renaud, G.; Alcotte, R.; Baron, T.; Dimoulas, A. Massless dirac fermions in $ZrTe_2$ semimetal grown on InAs(111) by van der Waals epitaxy. *ACS Nano* **2018**, *12*, 1696−1703.

(73) Wang, D.; Zhang, X.; Liu, H.; Meng, J.; Xia, J.; Yin, Z.; Wang, Y.; You, J.; Meng, X.-M. Epitaxial growth of $HfS_2$ on sapphire by chemical vapor deposition and application for photodetectors. *2D Mater.* **2017**, *4*, No. 031012.
(74) Gaiser, C.; Zandt, T.; Krapf, A.; Serverin, R.; Janowitz, C.; Manzke, R. Band-gap engineering with $HfS_xSe_{2-x}$. *Phys. Rev. B* **2004**, *69*, No. 075205.
(75) Rahman, S.; Saqib, H.; Liang, X.; Errandonea, D.; Resta, A. S.; Molina-Sanchez, A.; Gao, G.; Wang, L.; Tian, Y.; Mao, H. K. Pressure-induced metallization and robust superconductivity in pristine 1T-$HfSe_2$. *Mater. Today Phys.* **2022**, *25*, 100698.
(76) Aminalragia-Giamini, S.; Marquez-Velasco, J.; Tsipas, P.; Tsoutsou, D.; Renaud, G.; Dimoulas, A. Molecular beam epitaxy of thin $hfte_2$ semimetal films. *2D Mater.* **2017**, *4*, No. 015001.
(77) Mleczko, M. J.; Zhang, C.; Lee, H. R.; Kuo, H. H.; Magyari-Kope, B.; Moore, R. G.; Shen, Z. X.; Fisher, I. R.; Nishi, Y.; Pop, E. $HfSe_2$ and $ZrSe_2$: Two-dimensional semiconductors with native high-kappa oxides. *Sci. Adv.* **2017**, *3*, e1700481.
(78) Arnold, F.; Stan, R.-M.; Mahatha, S. K.; Lund, H. E.; Curcio, D.; Dendzik, M.; Bana, H.; Travaglia, E.; Bignardi, L.; Lacovig, P.; et al. Novel single-layer vanadium sulphide phases. *2D Mater.* **2018**, *5*, No. 045009.
(79) Ji, Q.; Li, C.; Wang, J.; Niu, J.; Gong, Y.; Zhang, Z.; Fang, Q.; Zhang, Y.; Shi, J.; Liao, L.; et al. Metallic vanadium disulfide nanosheets as a platform material for multifunctional electrode applications. *Nano Lett.* **2017**, *17*, 4908−4916.
(80) Yuan, J.; Wu, J.; Hardy, W. J.; Loya, P.; Lou, M.; Yang, Y.; Najmaei, S.; Jiang, M.; Qin, F.; Keyshar, K.; et al. Facile synthesis of single crystal vanadium disulfide nanosheets by chemical vapor deposition for efficient hydrogen evolution reaction. *Adv. Mater.* **2015**, *27*, 5605−5609.
(81) Duvjir, G.; Choi, B. K.; Ly, T. T.; Lam, N. H.; Chun, S.-H.; Jang, K.; Soon, A.; Chang, Y. J.; Kim, J. Novel polymorphic phase of two-dimensional $VSe_2$: The 1T' structure and its lattice dynamics. *Nanoscale* **2019**, *11*, 20096−20101.
(82) Zhang, Z.; Niu, J.; Yang, P.; Gong, Y.; Ji, Q.; Shi, J.; Fang, Q.; Jiang, S.; Li, H.; Zhou, X.; et al. Van der Waals epitaxial growth of 2D metallic vanadium diselenide single crystals and their extra-high electrical conductivity. *Adv. Mater.* **2017**, *29*, 1702359.
(83) Yilmaz, T.; Vescovo, E.; Sadowski, J. T.; Sinkovic, B. Spectroscopic evidence of highly correlated electrons in $VSe_2$. *Phys. Rev. B* **2022**, *105*, 245114.
(84) Shi, J.; Huan, Y.; Zhao, X.; Yang, P.; Hong, M.; Xie, C.; Pennycook, S.; Zhang, Y. Two-dimensional metallic vanadium ditelluride as a high-performance electrode material. *ACS Nano* **2021**, *15*, 1858−1868.
(85) Coelho, P. M.; Lasek, K.; Nguyen Cong, K.; Li, J.; Niu, W.; Liu, W.; Oleynik, I. I.; Batzill, M. Monolayer modification of $VTe_2$ and its charge density wave. *J. Phys. Chem. lett.* **2019**, *10*, 4987−4993.
(86) Leroux, M.; Cario, L.; Bosak, A.; Rodière, P. Traces of charge density waves in $NbS_2$. *Phys. Rev. B* **2018**, *97*, 195140.
(87) Stan, R.-M.; Mahatha, S. K.; Bianchi, M.; Sanders, C. E.; Curcio, D.; Hofmann, P.; Miwa, J. A. Epitaxial single-layer $NbS_2$ on Au(111): Synthesis, structure, and electronic properties. *Physl Rev. Mater.* **2019**, *3*, No. 044003.
(88) Yan, R.; Khalsa, G.; Schaefer, B. T.; Jarjour, A.; Rouvimov, S.; Nowack, K. C.; Xing, H. G.; Jena, D. Thickness dependence of superconductivity in ultrathin $NbS_2$. *Applied Physics Express* **2019**, *12*, No. 023008.
(89) Nakata, Y.; Sugawara, K.; Ichinokura, S.; Okada, Y.; Hitosugi, T.; Koretsune, T.; Ueno, K.; Hasegawa, S.; Takahashi, T.; Sato, T. Anisotropic band splitting in monolayer $NbSe_2$: Implications for superconductivity and charge density wave. *npj 2D Mater. Appl.* **2018**, *2*, 12.
(90) Xi, X.; Zhao, L.; Wang, Z.; Berger, H.; Forró, L.; Shan, J.; Mak, K. F. Strongly enhanced charge-density-wave order in monolayer $NbSe_2$. *Nat. Nanotechnol.* **2015**, *10*, 765−769.
(91) Nagata, S.; Abe, T.; Ebisu, S.; Ishihara, Y.; Tsutsumi, K. Superconductivity in the metallic layered compound $NbTe_2$. *J. Phys. Chem. Solids* **1993**, *54*, 895−899.
(92) Li, J.; Zhao, B.; Chen, P.; Wu, R.; Li, B.; Xia, Q.; Guo, G.; Luo, J.; Zang, K.; Zhang, Z.; et al. Synthesis of ultrathin metallic $MTe_2$ (M = V, Nb, Ta) single-crystalline nanoplates. *Adv. Mater.* **2018**, *30*, 1801043.
(93) Bai, Y.; Jian, T.; Pan, Z.; Deng, J.; Lin, X.; Zhu, C.; Huo, D.; Cheng, Z.; Liu, Y.; Cui, P.; et al. Realization of multiple charge-density waves in $NbTe_2$ at the monolayer limit. *Nano Lett.* **2023**, *23*, 2107−2113.
(94) Wang, Z.; Sun, Y.-Y.; Abdelwahab, I.; Cao, L.; Yu, W.; Ju, H.; Zhu, J.; Fu, W.; Chu, L.; Xu, H.; et al. Surface-limited superconducting phase transition on 1T-$TaS_2$. *ACS Nano* **2018**, *12*, 12619−12628.
(95) Kumakura, T.; Tan, H.; Handa, T.; Morishita, M.; Fukuyama, H. Charge density waves and superconductivity in 2H-$TaSe_2$. *Czech. J. Phys.* **1996**, *46*, 2611−2612.
(96) Feng, R.; Wang, W.; Bao, C.; Zhang, Z.; Wang, F.; Zhang, H.; Yao, J.; Xu, Y.; Yu, P.; Ji, S.-H.; et al. Selective control of phases and electronic structures of monolayer $TaTe_2$. *Adv. Mater.* **2024**, *36*, 2302297.
(97) Guo, J.; Huang, C.; Luo, H.; Yang, H.; Wei, L.; Cai, S.; Zhou, Y.; Zhao, H.; Li, X.; Li, Y.; et al. Observation of three superconducting transitions in the pressurized cdw-bearing compound $TaTe_2$. *Physl Rev. Mater.* **2022**, *6*, L051801.
(98) Fu, W.; Chen, Y.; Lin, J.; Wang, X.; Zeng, Q.; Zhou, J.; Zheng, L.; Wang, H.; He, Y.; He, H.; et al. Controlled synthesis of atomically thin 1T-$TaS_2$ for tunable charge density wave phase transitions. *Chem. Mater.* **2016**, *28*, 7613−7618.
(99) Nakata, Y.; Yoshizawa, T.; Sugawara, K.; Umemoto, Y.; Takahashi, T.; Sato, T. Selective fabrication of mott-insulating and metallic monolayer $TaSe_2$. *ACS Appl. Nano Mater.* **2018**, *1*, 1456−1460.
(100) Habib, M. R.; Wang, S.; Wang, W.; Xiao, H.; Obaidulla, S. M.; Gayen, A.; Khan, Y.; Chen, H.; Xu, M. Electronic properties of polymorphic two-dimensional layered chromium disulphide. *Nanoscale* **2019**, *11*, 20123−20132.
(101) van Bruggen, C. F.; Haange, R. J.; Wiegers, G. A.; de Boer, D. K. G. $CrSe_2$, a new layered dichalcogenide. *Physica B+C* **1980**, *99*, 166−172.
(102) Meng, L.; Zhou, Z.; Xu, M.; Yang, S.; Si, K.; Liu, L.; Wang, X.; Jiang, H.; Li, B.; Qin, P.; et al. Anomalous thickness dependence of curie temperature in air-stable two-dimensional ferromagnetic 1T-$CrTe_2$ grown by chemical vapor deposition. *Nat. Commun.* **2021**, *12*, 809.
(103) Keyshar, K.; Gong, Y.; Ye, G.; Brunetto, G.; Zhou, W.; Cole, D. P.; Hackenberg, K.; He, Y.; Machado, L.; Kabbani, M.; et al. Chemical vapor deposition of monolayer rhenium disulfide ($ReS_2$). *Adv. Mater.* **2015**, *27*, 4640−4648.
(104) Lu, S.; Peng, K.; Wang, P. D.; Chen, A. X.; Ren, W.; Fang, X. W.; Wu, Y.; Li, Z. Y.; Li, H. F.; Cheng, F. Y.; et al. Molecular beam epitaxy growth of monolayer hexagonal $MnTe_2$ on Si(111) substrate. *Chin. Phys. B* **2021**, *30*, 126804.
(105) Zhang, H.; Dai, Y.-M.; Liu, L.-M. Novel monolayer pyrite $FeS_2$ with atomic-thickness for magnetic devices. *Comput. Mater. Sci.* **2015**, *101*, 255−259.
(106) Liu, H.; Xue, Y. Van der waals epitaxial growth and phase transition of layered $FeSe_2$ nanocrystals. *Adv. Mater.* **2021**, *33*, 2008456.
(107) Chen, S.; Liu, H.; Chen, F.; Zhou, K.; Xue, Y. Synthesis, transfer, and properties of layered $FeTe_2$ nanocrystals. *ACS Nano* **2020**, *14*, 11473−11481.
(108) Zhao, Y.; Cong, H.; Li, P.; Wu, D.; Chen, S.; Luo, W. Hexagonal $ruse_2$ nanosheets for highly efficient hydrogen evolution electrocatalysis. *Angew. Chem., Int. Ed.* **2021**, *60*, 7013−7017.
(109) Wang, Y.; Liu, C.; Duan, H.; Li, Z.; Wang, C.; Tan, H.; Feng, S.; Liu, R.; Li, P.; Yan, W. Controlled synthesis of van der Waals $CoS_2$

for improved p-type transistor contact. *Nanotechnology* **2024**, *35*, No. 025601.
(110) Hu, Z.; Zhang, L.; Chakraborty, A.; D'Olimpio, G.; Fujii, J.; Ge, A.; Zhou, Y.; Liu, C.; Agarwal, A.; Vobornik, I.; et al. Terahertz nonlinear Hall rectifiers based on spin-polarized topological electronic states in 1T-cote$_2$. *Adv. Mater.* **2023**, *35*, 2209557.
(111) Hwang, J.; Kim, K.; Zhang, C.; Zhu, T.; Herbig, C.; Kim, S.; Kim, B.; Zhong, Y.; Salah, M.; El-Desoky, M. M.; et al. Large-gap insulating dimer ground state in monolayer IrTe$_2$. *Nat. Commun.* **2022**, *13*, 906.
(112) Kim, H. S.; Kim, S.; Kim, K.; Min, B. I.; Cho, Y.-H.; Wang, L.; Cheong, S.-W.; Yeom, H. W. Nanoscale superconducting honeycomb charge order in IrTe$_2$. *Nano Lett.* **2016**, *16*, 4260−4265.
(113) Nicholson, C. W.; Rumo, M.; Pulkkinen, A.; Kremer, G.; Salzmann, B.; Mottas, M.-L.; Hildebrand, B.; Jaouen, T.; Kim, T. K.; Mukherjee, S.; et al. Uniaxial strain-induced phase transition in the 2D topological semimetal IrTe$_2$. *Commun. Mater.* **2021**, *2*, 25.
(114) Shao, Y.; Song, S.; Wu, X.; Qi, J.; Lu, H.; Liu, C.; Zhu, S.; Liu, Z.; Wang, J.; Shi, D.; et al. Epitaxial fabrication of two-dimensional NiSe$_2$ on Ni(111) substrate. *Appl. Phys. Lett.* **2017**, *111*, 113107.
(115) Zhao, B.; Dang, W.; Liu, Y.; Li, B.; Li, J.; Luo, J.; Zhang, Z.; Wu, R.; Ma, H.; Sun, G.; et al. Synthetic control of two-dimensional NiTe$_2$ single crystals with highly uniform thickness distributions. *J. Am. Chem. Soc.* **2018**, *140*, 14217−14223.
(116) Oyedele, A. D.; Yang, S.; Liang, L.; Puretzky, A. A.; Wang, K.; Zhang, J.; Yu, P.; Pudasaini, P. R.; Ghosh, A. W.; Liu, Z.; et al. PdSe$_2$: Pentagonal two-dimensional layers with high air stability for electronics. *J. Am. Chem. Soc.* **2017**, *139*, 14090−14097.
(117) ElGhazali, M. A.; Naumov, P. G.; Mirhosseini, H.; Süß, V.; Müchler, L.; Schnelle, W.; Felser, C.; Medvedev, S. A. Pressure-induced superconductivity up to 13.1 K in the pyrite phase of palladium diselenide PdS$_2$. *Phys. Rev. B* **2017**, *96*, No. 060509.
(118) Liu, C.; Lian, C.-S.; Liao, M.-H.; Wang, Y.; Zhong, Y.; Ding, C.; Li, W.; Song, C.-L.; He, K.; Ma, X.-C.; et al. Two-dimensional superconductivity and topological states in PdTe$_2$ thin films. *Physl Rev. Mater.* **2018**, *2*, No. 094001.
(119) Zhao, Y.; Qiao, J.; Yu, P.; Hu, Z.; Lin, Z.; Lau, S. P.; Liu, Z.; Ji, W.; Chai, Y. Extraordinarily strong interlayer interaction in 2D layered PtS$_2$. *Adv. Mater.* **2016**, *28*, 2399−2407.
(120) Shi, J.; Huan, Y.; Hong, M.; Xu, R.; Yang, P.; Zhang, Z.; Zou, X.; Zhang, Y. Chemical vapor deposition grown large-scale atomically thin platinum diselenide with semimetal−semiconductor transition. *ACS Nano* **2019**, *13*, 8442−8451.
(121) Wang, Y.; Li, L.; Yao, W.; Song, S.; Sun, J. T.; Pan, J.; Ren, X.; Li, C.; Okunishi, E.; Wang, Y.-Q.; et al. Monolayer PtSe$_2$, a new semiconducting transition-metal-dichalcogenide, epitaxially grown by direct selenization of Pt. *Nano Lett.* **2015**, *15*, 4013−4018.
(122) Fu, L.; Hu, D.; Mendes, R. G.; Rümmeli, M. H.; Dai, Q.; Wu, B.; Fu, L.; Liu, Y. Highly organized epitaxy of dirac semimetallic PtTe$_2$ crystals with extrahigh conductivity and visible surface plasmons at edges. *ACS Nano* **2018**, *12*, 9405−9411.
(123) Wang, X.; Zhou, Z.; Zhang, P.; Zhang, S.; Ma, Y.; Yang, W.; Wang, H.; Li, B.; Meng, L.; Jiang, H.; et al. Thickness-controlled synthesis of CoX$_2$ (X = S, Se, and Te) single crystalline 2D layers with linear magnetoresistance and high conductivity. *Chem. Mater.* **2020**, *32*, 2321−2329.
(124) Dai, C.; Li, B.; Li, J.; Zhao, B.; Wu, R.; Ma, H.; Duan, X. Controllable synthesis of nis and NiS$_2$ nanoplates by chemical vapor deposition. *Nano Res.* **2020**, *13*, 2506−2511.
(125) Xu, C.; Li, B.; Jiao, W.; Zhou, W.; Qian, B.; Sankar, R.; Zhigadlo, N. D.; Qi, Y.; Qian, D.; Chou, F.-C.; et al. Topological type-II dirac fermions approaching the fermi level in a transition metal dichalcogenide NiTe$_2$. *Chem. Mater.* **2018**, *30*, 4823−4830.
(126) Mak, K. F.; Shan, J. Photonics and optoelectronics of 2D semiconductor transition metal dichalcogenides. *Nat. Photonics* **2016**, *10*, 216−226.
(127) Wang, G.; Chernikov, A.; Glazov, M. M.; Heinz, T. F.; Marie, X.; Amand, T.; Urbaszek, B. Colloquium: Excitons in atomically thin transition metal dichalcogenides. *Rev. Mod. Phys.* **2018**, *90*, No. 021001.
(128) Xiao, J.; Zhao, M.; Wang, Y.; Zhang, X. Excitons in atomically thin 2D semiconductors and their applications. *Nanophotonics* **2017**, *6*, 1309−1328.
(129) Elliott, R. J. Intensity of optical absorption by excitons. *Phys. Rev.* **1957**, *108*, 1384.
(130) Knox, R. S. *Theory of excitons*; Academic Press, 1963.
(131) Feldmann, J.; Peter, G.; Gobel, E. O.; Dawson, P.; Moore, K.; Foxon, C.; Elliott, R. J. Linewidth dependence of radiative exciton lifetimes in quantum wells. *Phys. Rev. Lett.* **1987**, *59*, 2337−2340.
(132) Scholes, G. D.; Rumbles, G. Excitons in nanoscale systems. *Nat. Mater.* **2006**, *5*, 683−696.
(133) Pelekanos, N. T.; Ding, J.; Hagerott, M.; Nurmikko, A. V.; Luo, H.; Samarth, N.; Furdyna, J. K. Quasi-two-dimensional excitons in (Zn,Cd)Se/ZnSe quantum wells: Reduced exciton-lo-phonon coupling due to confinement effects. *Phys. Rev. B Condens Matter* **1992**, *45*, 6037−6042.
(134) Dvorak, M.; Wei, S. H.; Wu, Z. Origin of the variation of exciton binding energy in semiconductors. *Phys. Rev. Lett.* **2013**, *110*, No. 016402.
(135) Chernikov, A.; Berkelbach, T. C.; Hill, H. M.; Rigosi, A.; Li, Y.; Aslan, O. B.; Reichman, D. R.; Hybertsen, M. S.; Heinz, T. F. Exciton binding energy and nonhydrogenic rydberg series in monolayer WS$_2$. *Phys. Rev. Lett.* **2014**, *113*, No. 076802.
(136) He, K.; Kumar, N.; Zhao, L.; Wang, Z.; Mak, K. F.; Zhao, H.; Shan, J. Tightly bound excitons in monolayer WSe$_2$. *Phys. Rev. Lett.* **2014**, *113*, No. 026803.
(137) Mak, K. F.; He, K.; Lee, C.; Lee, G. H.; Hone, J.; Heinz, T. F.; Shan, J. Tightly bound trions in monolayer MoS$_2$. *Nat. Mater.* **2013**, *12*, 207−211.
(138) Ye, Z.; Cao, T.; O'Brien, K.; Zhu, H.; Yin, X.; Wang, Y.; Louie, S. G.; Zhang, X. Probing excitonic dark states in single-layer tungsten disulphide. *Nature* **2014**, *513*, 214−218.
(139) You, Y.; Zhang, X.-X.; Berkelbach, T. C.; Hybertsen, M. S.; Reichman, D. R.; Heinz, T. F. Observation of biexcitons in monolayer WSe$_2$. *Nat. Phys.* **2015**, *11*, 477−481.
(140) Komsa, H.-P.; Krasheninnikov, A. V. Effects of confinement and environment on the electronic structure and exciton binding energy of MoS$_2$ from first principles. *Phys. Rev. B* **2012**, *86*, 241201.
(141) Koperski, M.; Molas, M. R.; Arora, A.; Nogajewski, K.; Slobodeniuk, A. O.; Faugeras, C.; Potemski, M. Optical properties of atomically thin transition metal dichalcogenides: Observations and puzzles. *Nanophotonics* **2017**, *6*, 1289−1308.
(142) Mueller, T.; Malic, E. Exciton physics and device application of two-dimensional transition metal dichalcogenide semiconductors. *npj 2D Mater. Appl.* **2018**, *2*, 29.
(143) Li, Y.; Chernikov, A.; Zhang, X.; Rigosi, A.; Hill, H. M.; van der Zande, A. M.; Chenet, D. A.; Shih, E.-M.; Hone, J.; Heinz, T. F. Measurement of the optical dielectric function of monolayer transition-metal dichalcogenides: MoS$_2$, MoSe$_2$, WS$_2$, and WSe$_2$. *Phys. Rev. B* **2014**, *90*, 205422.
(144) Tonndorf, P.; Schmidt, R.; Bottger, P.; Zhang, X.; Borner, J.; Liebig, A.; Albrecht, M.; Kloc, C.; Gordan, O.; Zahn, D. R.; et al. Photoluminescence emission and Raman response of monolayer MoS$_2$, MoSe$_2$, and WSe$_2$. *Opt. Express* **2013**, *21*, 4908−4916.
(145) Bernardi, M.; Palummo, M.; Grossman, J. C. Extraordinary sunlight absorption and one nanometer thick photovoltaics using two-dimensional monolayer materials. *Nano Lett.* **2013**, *13*, 3664−3670.
(146) Wang, G.; Marie, X.; Gerber, I.; Amand, T.; Lagarde, D.; Bouet, L.; Vidal, M.; Balocchi, A.; Urbaszek, B. Giant enhancement of the optical second-harmonic emission of WSe$_2$ monolayers by laser excitation at exciton resonances. *Phys. Rev. Lett.* **2015**, *114*, No. 097403.
(147) Selig, M.; Berghauser, G.; Raja, A.; Nagler, P.; Schuller, C.; Heinz, T. F.; Korn, T.; Chernikov, A.; Malic, E.; Knorr, A. Excitonic linewidth and coherence lifetime in monolayer transition metal dichalcogenides. *Nat. Commun.* **2016**, *7*, 13279.

(148) Conley, H. J.; Wang, B.; Ziegler, J. I.; Haglund, R. F., Jr.; Pantelides, S. T.; Bolotin, K. I. Bandgap engineering of strained monolayer and bilayer $MoS_2$. *Nano Lett.* **2013**, *13*, 3626−3630.

(149) Chernikov, A.; van der Zande, A. M.; Hill, H. M.; Rigosi, A. F.; Velauthapillai, A.; Hone, J.; Heinz, T. F. Electrical tuning of exciton binding energies in monolayer $WS_2$. *Phys. Rev. Lett.* **2015**, *115*, 126802.

(150) Seyler, K. L.; Schaibley, J. R.; Gong, P.; Rivera, P.; Jones, A. M.; Wu, S.; Yan, J.; Mandrus, D. G.; Yao, W.; Xu, X. Electrical control of second-harmonic generation in a $WSe_2$ monolayer transistor. *Nat. Nanotechnol.* **2015**, *10*, 407−411.

(151) Ross, J. S.; Wu, S.; Yu, H.; Ghimire, N. J.; Jones, A. M.; Aivazian, G.; Yan, J.; Mandrus, D. G.; Xiao, D.; Yao, W.; Xu, X. Electrical control of neutral and charged excitons in a monolayer semiconductor. *Nat. Commun.* **2013**, *4*, 1474.

(152) Chernikov, A.; Ruppert, C.; Hill, H. M.; Rigosi, A. F.; Heinz, T. F. Population inversion and giant bandgap renormalization in atomically thin $WS_2$ layers. *Nat. Photonics* **2015**, *9*, 466−470.

(153) Raja, A.; Chaves, A.; Yu, J.; Arefe, G.; Hill, H. M.; Rigosi, A. F.; Berkelbach, T. C.; Nagler, P.; Schuller, C.; Korn, T.; et al. Coulomb engineering of the bandgap and excitons in two-dimensional materials. *Nat. Commun.* **2017**, *8*, 15251.

(154) Leisgang, N.; Shree, S.; Paradisanos, I.; Sponfeldner, L.; Robert, C.; Lagarde, D.; Balocchi, A.; Watanabe, K.; Taniguchi, T.; Marie, X.; et al. Giant stark splitting of an exciton in bilayer $MoS_2$. *Nat. Nanotechnol.* **2020**, *15*, 901−907.

(155) Novoselov, K. S.; Mishchenko, A.; Carvalho, A.; Castro Neto, A. H. 2D materials and van der Waals heterostructures. *Science* **2016**, *353*, aac9439.

(156) Castellanos-Gomez, A.; Duan, X.; Fei, Z.; Gutierrez, H. R.; Huang, Y.; Huang, X.; Quereda, J.; Qian, Q.; Sutter, E.; Sutter, P. Van der Waals heterostructures. *Nat. Rev. Methods Primers* **2022**, *2*, 58.

(157) Shimazaki, Y.; Schwartz, I.; Watanabe, K.; Taniguchi, T.; Kroner, M.; Imamoglu, A. Strongly correlated electrons and hybrid excitons in a moiré heterostructure. *Nature* **2020**, *580*, 472−477.

(158) Andersen, T. I.; Scuri, G.; Sushko, A.; De Greve, K.; Sung, J.; Zhou, Y.; Wild, D. S.; Gelly, R. J.; Heo, H.; Berube, D.; et al. Excitons in a reconstructed moiré potential in twisted $WSe_2/WSe_2$ homobilayers. *Nat. Mater.* **2021**, *20*, 480−487.

(159) Wilson, N. P.; Yao, W.; Shan, J.; Xu, X. Excitons and emergent quantum phenomena in stacked 2D semiconductors. *Nature* **2021**, *599*, 383−392.

(160) Huang, D.; Choi, J.; Shih, C. K.; Li, X. Excitons in semiconductor moiré superlattices. *Nat. Nanotechnol.* **2022**, *17*, 227−238.

(161) Jin, C.; Regan, E. C.; Yan, A.; Iqbal Bakti Utama, M.; Wang, D.; Zhao, S.; Qin, Y.; Yang, S.; Zheng, Z.; Shi, S.; et al. Observation of moiré excitons in $WSe_2/WS_2$ heterostructure superlattices. *Nature* **2019**, *567*, 76−80.

(162) Huang, L.; Krasnok, A.; Alu, A.; Yu, Y.; Neshev, D.; Miroshnichenko, A. E. Enhanced light-matter interaction in two-dimensional transition metal dichalcogenides. *Rep. Prog. Phys.* **2022**, *85*, No. 046401.

(163) Pham, P. V.; Bodepudi, S. C.; Shehzad, K.; Liu, Y.; Xu, Y.; Yu, B.; Duan, X. 2D heterostructures for ubiquitous electronics and optoelectronics: Principles, opportunities, and challenges. *Chem. Rev.* **2022**, *122*, 6514−6613.

(164) Regan, E. C.; Wang, D.; Paik, E. Y.; Zeng, Y.; Zhang, L.; Zhu, J.; MacDonald, A. H.; Deng, H.; Wang, F. Emerging exciton physics in transition metal dichalcogenide heterobilayers. *Nat. Rev. Mater.* **2022**, *7*, 778−795.

(165) Koppens, F. H.; Mueller, T.; Avouris, P.; Ferrari, A. C.; Vitiello, M. S.; Polini, M. Photodetectors based on graphene, other two-dimensional materials and hybrid systems. *Nat. Nanotechnol.* **2014**, *9*, 780−793.

(166) Ross, J. S.; Klement, P.; Jones, A. M.; Ghimire, N. J.; Yan, J.; Mandrus, D. G.; Taniguchi, T.; Watanabe, K.; Kitamura, K.; Yao, W.; et al. Electrically tunable excitonic light-emitting diodes based on monolayer $WSe_2$ p−n junctions. *Nat. Nanotechnol.* **2014**, *9*, 268−272.

(167) Shen, Y. R. *The principles of nonlinear optics*; Wiley, 1984.

(168) Boyd, R. W. *Nonlinear optics*; Academic Press, 2008.

(169) Autere, A.; Jussila, H.; Dai, Y.; Wang, Y.; Lipsanen, H.; Sun, Z. Nonlinear optics with 2D layered materials. *Adv. Mater.* **2018**, *30*, 1705963.

(170) Wen, X.; Gong, Z.; Li, D. Nonlinear optics of two-dimensional transition metal dichalcogenides. *InfoMat* **2019**, *1*, 317−337.

(171) Zhang, J.; Zhao, W.; Yu, P.; Yang, G.; Liu, Z. Second harmonic generation in 2D layered materials. *2D Mater.* **2020**, *7*, No. 042002.

(172) Khan, A. R.; Zhang, L.; Ishfaq, K.; Ikram, A.; Yildrim, T.; Liu, B.; Rahman, S.; Lu, Y. Optical harmonic generation in 2D materials. *Adv. Funct. Mater.* **2022**, *32*, 2105259.

(173) Dogadov, O.; Trovatello, C.; Yao, B.; Soavi, G.; Cerullo, G. Parametric nonlinear optics with layered materials and related heterostructures. *Laser Photonics Rev.* **2022**, *16*, 2100726.

(174) Ullah, K.; Meng, Y.; Shi, Y.; Wang, F. Harmonic generation in low-dimensional materials. *Adv. Opt. Mater.* **2022**, *10*, 2101860.

(175) Janisch, C.; Wang, Y.; Ma, D.; Mehta, N.; Elías, A. L.; Perea-López, N.; Terrones, M.; Crespi, V.; Liu, Z. Extraordinary second harmonic generation in tungsten disulfide monolayers. *Sci. Rep.* **2014**, *4*, 5530.

(176) Autere, A.; Jussila, H.; Marini, A.; Saavedra, J. R. M.; Dai, Y.; Säynätjoki, A.; Karvonen, L.; Yang, H.; Amirsolaimani, B.; Norwood, R. A.; et al. Optical harmonic generation in monolayer group-VI transition metal dichalcogenides. *Phys. Rev. B* **2018**, *98*, 115426.

(177) Du, L.; Hasan, T.; Castellanos-Gomez, A.; Liu, G.-B.; Yao, Y.; Lau, C. N.; Sun, Z. Engineering symmetry breaking in 2D layered materials. *Nat. Rev. Phys.* **2021**, *3*, 193−206.

(178) Li, Y. L.; Rao, Y.; Mak, K. F.; You, Y. M.; Wang, S. Y.; Dean, C. R.; Heinz, T. F. Probing symmetry properties of few-layer $MoS_2$ and h-BN by optical second-harmonic generation. *Nano Lett.* **2013**, *13*, 3329−3333.

(179) Malard, L. M.; Alencar, T. V.; Barboza, A. P. M.; Mak, K. F.; de Paula, A. M. Observation of intense second harmonic generation from $MoS_2$ atomic crystals. *Phys. Rev. B* **2013**, *87*, 201401.

(180) Kumar, N.; Najmaei, S.; Cui, Q.; Ceballos, F.; Ajayan, P. M.; Lou, J.; Zhao, H. Second harmonic microscopy of monolayer $MoS_2$. *Phys. Rev. B* **2013**, *87*, 161403.

(181) Liu, H.; Li, Y.; You, Y. S.; Ghimire, S.; Heinz, T. F.; Reis, D. A. High-harmonic generation from an atomically thin semiconductor. *Nat. Phys.* **2017**, *13*, 262−265.

(182) Xiao, J.; Ye, Z.; Wang, Y.; Zhu, H.; Wang, Y.; Zhang, X. Nonlinear optical selection rule based on valley-exciton locking in monolayer $WS_2$. *Light Sci. Appl.* **2015**, *4*, e366−e366.

(183) Ciattoni, A.; Marini, A.; Rizza, C.; Conti, C. Phase-matching-free parametric oscillators based on two-dimensional semiconductors. *Light Sci. Appl.* **2018**, *7*, 5.

(184) Shinde, S. M.; Dhakal, K. P.; Chen, X.; Yun, W. S.; Lee, J.; Kim, H.; Ahn, J.-H. Stacking-controllable interlayer coupling and symmetric configuration of multilayered $MoS_2$. *NPG Asia Mater.* **2018**, *10*, e468.

(185) Säynätjoki, A.; Karvonen, L.; Rostami, H.; Autere, A.; Mehravar, S.; Lombardo, A.; Norwood, R. A.; Hasan, T.; Peyghambarian, N.; Lipsanen, H.; et al. Ultra-strong nonlinear optical processes and trigonal warping in $MoS_2$ layers. *Nat. Commun.* **2017**, *8*, 893.

(186) Lin, K.-Q.; Bange, S.; Lupton, J. M. Quantum interference in second-harmonic generation from monolayer $WSe_2$. *Nat. Phys.* **2019**, *15*, 242−246.

(187) Wang, Y.; Das, S.; Iyikanat, F.; Dai, Y.; Li, S.; Guo, X.; Yang, X.; Cheng, J.; Hu, X.; Ghotbi, M.; et al. Giant all-optical modulation of second-harmonic generation mediated by dark excitons. *ACS Photonics* **2021**, *8*, 2320−2328.

(188) Clark, D. J.; Senthilkumar, V.; Le, C. T.; Weerawarne, D. L.; Shim, B.; Jang, J. I.; Shim, J. H.; Cho, J.; Sim, Y.; Seong, M. J.; et al. Strong optical nonlinearity of CVD-grown $MoS_2$ monolayer as probed by wavelength-dependent second-harmonic generation. *Phys. Rev. B* **2014**, *90*, 121409.

(189) Hsu, W. T.; Zhao, Z. A.; Li, L. J.; Chen, C. H.; Chiu, M. H.; Chang, P. S.; Chou, Y. C.; Chang, W. H. Second harmonic generation from artificially stacked transition metal dichalcogenide twisted bilayers. *ACS Nano* **2014**, *8*, 2951−2958.

(190) Liang, J.; Zhang, J.; Li, Z.; Hong, H.; Wang, J.; Zhang, Z.; Zhou, X.; Qiao, R.; Xu, J.; Gao, P.; et al. Monitoring local strain vector in atomic-layered $MoSe_2$ by second-harmonic generation. *Nano Lett.* **2017**, *17*, 7539−7543.

(191) Yin, X. B.; Ye, Z. L.; Chenet, D. A.; Ye, Y.; O'Brien, K.; Hone, J. C.; Zhang, X. Edge nonlinear optics on a $MoS_2$ atomic monolayer. *Science* **2014**, *344*, 488−490.

(192) Trovatello, C.; Marini, A.; Xu, X.; Lee, C.; Liu, F.; Curreli, N.; Manzoni, C.; Dal Conte, S.; Yao, K.; Ciattoni, A.; et al. Optical parametric amplification by monolayer transition metal dichalcogenides. *Nat. Photonics* **2021**, *15*, 6−10.

(193) Zhang, Y.; Bai, X.; Arias Muñoz, J.; Dai, Y.; Das, S.; Wang, Y.; Sun, Z. Coherent modulation of chiral nonlinear optics with crystal symmetry. *Light Sci. Appl.* **2022**, *11*, 216.

(194) Klimmer, S.; Ghaebi, O.; Gan, Z.; George, A.; Turchanin, A.; Cerullo, G.; Soavi, G. All-optical polarization and amplitude modulation of second-harmonic generation in atomically thin semiconductors. *Nat. Photonics* **2021**, *15*, 837−842.

(195) Le, C. T.; Clark, D. J.; Ullah, F.; Jang, J. I.; Senthilkumar, V.; Sim, Y.; Seong, M.-J.; Chung, K.-H.; Kim, J. W.; Park, S.; et al. Impact of selenium doping on resonant second-harmonic generation in monolayer $MoS_2$. *ACS Photonics* **2017**, *4*, 38−44.

(196) Fryett, T.; Zhan, A.; Majumdar, A. Cavity nonlinear optics with layered materials. *Nanophotonics* **2017**, *7*, 355−370.

(197) Fryett, T. K.; Seyler, K. L.; Zheng, J.; Liu, C.-H.; Xu, X.; Majumdar, A. Silicon photonic crystal cavity enhanced second-harmonic generation from monolayer $WSe_2$. *2D Mater.* **2017**, *4*, No. 015031.

(198) Kim, Y.; Kim, H.; Jang, H.; Ahn, J.-H.; Lee, J. D. Dual resonant sum frequency generations from two-dimensional materials. *Nano Lett.* **2020**, *20*, 4530−4536.

(199) Zuo, Y.; Yu, W.; Liu, C.; Cheng, X.; Qiao, R.; Liang, J.; Zhou, X.; Wang, J.; Wu, M.; Zhao, Y.; et al. Optical fibres with embedded two-dimensional materials for ultrahigh nonlinearity. *Nat. Nanotechnol.* **2020**, *15*, 987−991.

(200) Hong, H.; Wu, C.; Zhao, Z.; Zuo, Y.; Wang, J.; Liu, C.; Zhang, J.; Wang, F.; Feng, J.; Shen, H.; et al. Giant enhancement of optical nonlinearity in two-dimensional materials by multiphoton-excitation resonance energy transfer from quantum dots. *Nat. Photonics* **2021**, *15*, 510−515.

(201) Chen, H.; Corboliou, V.; Solntsev, A. S.; Choi, D.-Y.; Vincenti, M. A.; de Ceglia, D.; de Angelis, C.; Lu, Y.; Neshev, D. N. Enhanced second-harmonic generation from two-dimensional $MoSe_2$ on a silicon waveguide. *Light Sci. Appl.* **2017**, *6*, e17060.

(202) Shi, J.; Yu, P.; Liu, F.; He, P.; Wang, R.; Qin, L.; Zhou, J.; Li, X.; Zhou, J.; Sui, X.; et al. 3R $MoS_2$ with broken inversion symmetry: A promising ultrathin nonlinear optical device. *Adv. Mater.* **2017**, *29*, 1701486.

(203) Abdelwahab, I.; Tilmann, B.; Wu, Y.; Giovanni, D.; Verzhbitskiy, I.; Zhu, M.; Berté, R.; Xuan, F.; Menezes, L. d. S.; Eda, G.; et al. Giant second-harmonic generation in ferroelectric $NbOI_2$. *Nat. Photonics* **2022**, *16*, 644−650.

(204) Xu, X. Y.; Trovatello, C.; Mooshammer, F.; Shao, Y. M.; Zhang, S.; Yao, K. Y.; Basov, D. N.; Cerullo, G.; Schuck, P. J. Towards compact phase-matched and waveguided nonlinear optics in atomically layered semiconductors. *Nat. Photonics* **2022**, *16*, 698−706.

(205) Guo, Q.; Qi, X.-Z.; Zhang, L.; Gao, M.; Hu, S.; Zhou, W.; Zang, W.; Zhao, X.; Wang, J.; Yan, B.; et al. Ultrathin quantum light source with van der Waals $NbOCl_2$ crystal. *Nature* **2023**, *613*, 53−59.

(206) Qi, J.; Ma, C.; Guo, Q.; Ma, C.; Zhang, Z.; Liu, F.; Shi, X.; Wang, L.; Xue, M.; Wu, M.; et al. Stacking-controlled growth of rBN crystalline films with high nonlinear optical conversion efficiency up to 1%. *Adv. Mater.* **2024**, *36*, 2303122.

(207) Yu, H.; Cui, X.; Xu, X.; Yao, W. Valley excitons in two-dimensional semiconductors. *Natl. Sci. Rev.* **2015**, *2*, 57−70.

(208) Schaibley, J. R.; Yu, H.; Clark, G.; Rivera, P.; Ross, J. S.; Seyler, K. L.; Yao, W.; Xu, X. Valleytronics in 2D materials. *Nat. Rev. Mater.* **2016**, *1*, 16055.

(209) Sham, L. J.; Allen, S. J.; Kamgar, A.; Tsui, D. C. Valley-valley splitting in inversion layers on a high-index surface of silicon. *Phys. Rev. Lett.* **1978**, *40*, 472−475.

(210) Gunawan, O.; Shkolnikov, Y. P.; Vakili, K.; Gokmen, T.; De Poortere, E. P.; Shayegan, M. Valley susceptibility of an interacting two-dimensional electron system. *Phys. Rev. Lett.* **2006**, *97*, 186404.

(211) Takashina, K.; Ono, Y.; Fujiwara, A.; Takahashi, Y.; Hirayama, Y. Valley polarization in Si(100) at zero magnetic field. *Phys. Rev. Lett.* **2006**, *96*, 236801.

(212) Zhu, Z.; Collaudin, A.; Fauqué, B.; Kang, W.; Behnia, K. Field-induced polarization of dirac valleys in bismuth. *Nat. Phys.* **2012**, *8*, 89−94.

(213) Isberg, J.; Gabrysch, M.; Hammersberg, J.; Majdi, S.; Kovi, K. K.; Twitchen, D. J. Generation, transport and detection of valley-polarized electrons in diamond. *Nat. Mater.* **2013**, *12*, 760−764.

(214) Goswami, S.; Slinker, K. A.; Friesen, M.; McGuire, L. M.; Truitt, J. L.; Tahan, C.; Klein, L. J.; Chu, J. O.; Mooney, P. M.; van der Weide, D. W.; et al. Controllable valley splitting in silicon quantum devices. *Nat. Phys.* **2007**, *3*, 41−45.

(215) Mak, K. F.; Xiao, D.; Shan, J. Light-valley interactions in 2D semiconductors. *Nat. Photonics* **2018**, *12*, 451−460.

(216) Zhao, S.; Li, X.; Dong, B.; Wang, H.; Wang, H.; Zhang, Y.; Han, Z.; Zhang, H. Valley manipulation in monolayer transition metal dichalcogenides and their hybrid systems: Status and challenges. *Rep. Prog. Phys.* **2021**, *84*, No. 026401.

(217) Rycerz, A.; Tworzydło, J.; Beenakker, C. W. J. Valley filter and valley valve in graphene. *Nat. Phys.* **2007**, *3*, 172−175.

(218) Xiao, D.; Yao, W.; Niu, Q. Valley-contrasting physics in graphene: Magnetic moment and topological transport. *Phys. Rev. Lett.* **2007**, *99*, 236809.

(219) Yao, W.; Xiao, D.; Niu, Q. Valley-dependent optoelectronics from inversion symmetry breaking. *Phys. Rev. B* **2008**, *77*, 235406.

(220) Xiao, D.; Chang, M.-C.; Niu, Q. Berry phase effects on electronic properties. *Rev. Mod. Phys.* **2010**, *82*, 1959−2007.

(221) Xu, X.; Yao, W.; Xiao, D.; Heinz, T. F. Spin and pseudospins in layered transition metal dichalcogenides. *Nat. Phys.* **2014**, *10*, 343−350.

(222) Behnia, K. Polarized light boosts valleytronics. *Nat. Nanotechnol.* **2012**, *7*, 488−489.

(223) Cao, T.; Wang, G.; Han, W.; Ye, H.; Zhu, C.; Shi, J.; Niu, Q.; Tan, P.; Wang, E.; Liu, B.; Feng, J. Valley-selective circular dichroism of monolayer molybdenum disulphide. *Nat. Commun.* **2012**, *3*, 887.

(224) Mak, K. F.; He, K.; Shan, J.; Heinz, T. F. Control of valley polarization in monolayer $MoS_2$ by optical helicity. *Nat. Nanotechnol.* **2012**, *7*, 494−498.

(225) Zeng, H.; Dai, J.; Yao, W.; Xiao, D.; Cui, X. Valley polarization in $MoS_2$ monolayers by optical pumping. *Nat. Nanotechnol.* **2012**, *7*, 490−493.

(226) Xiao, D.; Liu, G.-B.; Feng, W.; Xu, X.; Yao, W. Coupled spin and valley physics in monolayers of $MoS_2$ and other group-VI dichalcogenides. *Phys. Rev. Lett.* **2012**, *108*, 196802.

(227) Kormányos, A.; Burkard, G.; Gmitra, M.; Fabian, J.; Zólyomi, V.; Drummond, N. D.; Fal'ko, V. **k·p** theory for two-dimensional transition metal dichalcogenide semiconductors. *2D Mater.* **2015**, *2*, No. 022001.

(228) Jones, A. M.; Yu, H.; Ghimire, N. J.; Wu, S.; Aivazian, G.; Ross, J. S.; Zhao, B.; Yan, J.; Mandrus, D. G.; Xiao, D.; et al. Optical generation of excitonic valley coherence in monolayer $WSe_2$. *Nat. Nanotechnol.* **2013**, *8*, 634−638.

(229) Kim, J.; Hong, X. P.; Jin, C. H.; Shi, S. F.; Chang, C. Y. S.; Chiu, M. H.; Li, L. J.; Wang, F. Ultrafast generation of pseudo-magnetic field for valley excitons in $WSe_2$ monolayers. *Science* **2014**, *346*, 1205−1208.

(230) Sie, E. J.; McIver, J. W.; Lee, Y.-H.; Fu, L.; Kong, J.; Gedik, N. Valley-selective optical stark effect in monolayer $WS_2$. *Nat. Mater.* **2015**, *14*, 290−294.

(231) Wang, G.; Marie, X.; Liu, B. L.; Amand, T.; Robert, C.; Cadiz, F.; Renucci, P.; Urbaszek, B. Control of exciton valley coherence in transition metal dichalcogenide monolayers. *Phys. Rev. Lett.* **2016**, *117*, 187401.
(232) Ye, Y.; Xiao, J.; Wang, H.; Ye, Z.; Zhu, H.; Zhao, M.; Wang, Y.; Zhao, J.; Yin, X.; Zhang, X. Electrical generation and control of the valley carriers in a monolayer transition metal dichalcogenide. *Nat. Nanotechnol.* **2016**, *11*, 598−602.
(233) Ye, Z.; Sun, D.; Heinz, T. F. Optical manipulation of valley pseudospin. *Nat. Phys.* **2017**, *13*, 26−29.
(234) Zhang, X.-X.; Cao, T.; Lu, Z.; Lin, Y.-C.; Zhang, F.; Wang, Y.; Li, Z.; Hone, J. C.; Robinson, J. A.; Smirnov, D.; et al. Magnetic brightening and control of dark excitons in monolayer $WSe_2$. *Nat. Nanotechnol.* **2017**, *12*, 883−888.
(235) Lee, J.; Wang, Z.; Xie, H.; Mak, K. F.; Shan, J. Valley magnetoelectricity in single-layer $MoS_2$. *Nat. Mater.* **2017**, *16*, 887−891.
(236) Hao, K.; Moody, G.; Wu, F.; Dass, C. K.; Xu, L.; Chen, C.-H.; Sun, L.; Li, M.-Y.; Li, L.-J.; MacDonald, A. H.; et al. Direct measurement of exciton valley coherence in monolayer $WSe_2$. *Nat. Phys.* **2016**, *12*, 677−682.
(237) Lee, J.; Mak, K. F.; Shan, J. Electrical control of the valley Hall effect in bilayer $MoS_2$ transistors. *Nat. Nanotechnol.* **2016**, *11*, 421−425.
(238) Rivera, P.; Seyler, K. L.; Yu, H. Y.; Schaibley, J. R.; Yan, J. Q.; Mandrus, D. G.; Yao, W.; Xu, X. D. Valley-polarized exciton dynamics in a 2D semiconductor heterostructure. *Science* **2016**, *351*, 688−691.
(239) Kim, J.; Jin, C. H.; Chen, B.; Cai, H.; Zhao, T.; Lee, P.; Kahn, S.; Watanabe, K.; Taniguchi, T.; Tongay, S.; et al. Observation of ultralong valley lifetime in $WSe_2/MoS_2$ heterostructures. *Sci. Adv.* **2017**, *3*, 1700518.
(240) Wang, Z.; Chiu, Y.-H.; Honz, K.; Mak, K. F.; Shan, J. Electrical tuning of interlayer exciton gases in $WSe_2$ bilayers. *Nano Lett.* **2018**, *18*, 137−143.
(241) Jiang, C.; Xu, W.; Rasmita, A.; Huang, Z.; Li, K.; Xiong, Q.; Gao, W.-b. Microsecond dark-exciton valley polarization memory in two-dimensional heterostructures. *Nat. Commun.* **2018**, *9*, 753.
(242) Jin, C. H.; Kim, J.; Utama, M. I. B.; Regan, E. C.; Kleemann, H.; Cai, H.; Shen, Y. X.; Shinner, M. J.; Sengupta, A.; Watanabe, K.; et al. Imaging of pure spin-valley diffusion current in $WS_2$-$WSe_2$ heterostructures. *Science* **2018**, *360*, 893−896.
(243) Scuri, G.; Andersen, T. I.; Zhou, Y.; Wild, D. S.; Sung, J.; Gelly, R. J.; Bérubé, D.; Heo, H.; Shao, L.; Joe, A. Y.; et al. Electrically tunable valley dynamics in twisted $WSe_2/WSe_2$ bilayers. *Phys. Rev. Lett.* **2020**, *124*, 217403.
(244) Huang, Z. M.; Liu, Y. D.; Dini, K.; Tan, Q. H.; Liu, Z. J.; Fang, H. L.; Liu, J.; Liew, T.; Gao, W. B. Robust room temperature valley Hall effect of interlayer excitons. *Nano Lett.* **2020**, *20*, 1345−1351.
(245) Tang, Y. H.; Mak, K. F.; Shan, J. Long valley lifetime of dark excitons in single-layer $WSe_2$. *Nat. Commun.* **2019**, *10*, 4047.
(246) Wu, S.; Ross, J. S.; Liu, G.-B.; Aivazian, G.; Jones, A.; Fei, Z.; Zhu, W.; Xiao, D.; Yao, W.; Cobden, D.; et al. Electrical tuning of valley magnetic moment through symmetry control in bilayer $MoS_2$. *Nat. Phys.* **2013**, *9*, 149−153.
(247) Mak, K. F.; McGill, K. L.; Park, J.; McEuen, P. L. The valley Hall effect in $MoS_2$ transistors. *Science* **2014**, *344*, 1489−1492.
(248) Ciarrocchi, A.; Tagarelli, F.; Avsar, A.; Kis, A. Excitonic devices with van der Waals heterostructures: Valleytronics meets twistronics. *Nat. Rev. Mater.* **2022**, *7*, 449−464.
(249) Frindt, R. F. Superconductivity in ultrathin $NbSe_2$ layers. *Phys. Rev. Lett.* **1972**, *28*, 299−301.
(250) Qiu, D.; Gong, C.; Wang, S.; Zhang, M.; Yang, C.; Wang, X.; Xiong, J. Recent advances in 2D superconductors. *Adv. Mater.* **2021**, *33*, 2006124.
(251) Xi, X.; Wang, Z.; Zhao, W.; Park, J.-H.; Law, K. T.; Berger, H.; Forró, L.; Shan, J.; Mak, K. F. Ising pairing in superconducting $NbSe_2$ atomic layers. *Nat. Phys.* **2016**, *12*, 139−143.
(252) Wang, H.; Huang, X.; Lin, J.; Cui, J.; Chen, Y.; Zhu, C.; Liu, F.; Zeng, Q.; Zhou, J.; Yu, P.; et al. High-quality monolayer superconductor $NbSe_2$ grown by chemical vapour deposition. *Nat. Commun.* **2017**, *8*, 394.
(253) Lin, H.; Zhu, Q.; Shu, D.; Lin, D.; Xu, J.; Huang, X.; Shi, W.; Xi, X.; Wang, J.; Gao, L. Growth of environmentally stable transition metal selenide films. *Nat. Mater.* **2019**, *18*, 602−607.
(254) Ma, L.; Wang, X.; Wang, H.; Wang, X.; Zou, G.; Guan, Y.; Guo, S.; Li, H.; Chen, Q.; Kang, L.; et al. Van der Waals self-epitaxial growth of inch-sized superconducting niobium diselenide films. *Nano Lett.* **2023**, *23*, 6892−6899.
(255) Somoano, R. B.; Hadek, V.; Rembaum, A. Alkali metal intercalates of molybdenum disulfide. *J. Chem. Phys.* **1973**, *58*, 697−701.
(256) Ye, J. T.; Zhang, Y. J.; Akashi, R.; Bahramy, M. S.; Arita, R.; Iwasa, Y. Superconducting dome in a gate-tuned band insulator. *Science* **2012**, *338*, 1193−1196.
(257) Lu, J.; Zheliuk, O.; Chen, Q.; Leermakers, I.; Hussey, N. E.; Zeitler, U.; Ye, J. Full superconducting dome of strong ising protection in gated monolayer $WS_2$. *Proc. Natl. Acad. Sci. U. S. A.* **2018**, *115*, 3551−3556.
(258) Shi, W.; Ye, J.; Zhang, Y.; Suzuki, R.; Yoshida, M.; Miyazaki, J.; Inoue, N.; Saito, Y.; Iwasa, Y. Superconductivity series in transition metal dichalcogenides by ionic gating. *Sci. Rep.* **2015**, *5*, 12534.
(259) Lu, J. M.; Zheliuk, O.; Leermakers, I.; Yuan, N. F.; Zeitler, U.; Law, K. T.; Ye, J. T. Evidence for two-dimensional ising superconductivity in gated $MoS_2$. *Science* **2015**, *350*, 1353−1357.
(260) Saito, Y.; Nakamura, Y.; Bahramy, M. S.; Kohama, Y.; Ye, J.; Kasahara, Y.; Nakagawa, Y.; Onga, M.; Tokunaga, M.; Nojima, T.; et al. Superconductivity protected by spin-valley locking in ion-gated $MoS_2$. *Nat. Phys.* **2016**, *12*, 144−149.
(261) G, G. *Density waves in solids*; CRC press, 2018.
(262) Wang, Y. D.; Yao, W. L.; Xin, Z. M.; Han, T. T.; Wang, Z. G.; Chen, L.; Cai, C.; Li, Y.; Zhang, Y. Band insulator to mott insulator transition in 1T-$TaS_2$. *Nat. Commun.* **2020**, *11*, 4215.
(263) Pasztor, A.; Scarfato, A.; Spera, M.; Flicker, F.; Barreteau, C.; Giannini, E.; Wezel, J. V.; Renner, C. Multiband charge density wave exposed in a transition metal dichalcogenide. *Nat. Commun.* **2021**, *12*, 6037.
(264) Song, X.; Liu, L.; Chen, Y.; Yang, H.; Huang, Z.; Hou, B.; Hou, Y.; Han, X.; Yang, H.; Zhang, Q.; et al. Atomic-scale visualization of chiral charge density wave superlattices and their reversible switching. *Nat. Commun.* **2022**, *13*, 1843.
(265) Chatterjee, U.; Zhao, J.; Iavarone, M.; Di Capua, R.; Castellan, J. P.; Karapetrov, G.; Malliakas, C. D.; Kanatzidis, M. G.; Claus, H.; Ruff, J. P.; et al. Emergence of coherence in the charge-density wave state of 2H-$NbSe_2$. *Nat. Commun.* **2015**, *6*, 6313.
(266) Ugeda, M. M.; Bradley, A. J.; Zhang, Y.; Onishi, S.; Chen, Y.; Ruan, W.; Ojeda-Aristizabal, C.; Ryu, H.; Edmonds, M. T.; Tsai, H.-Z.; et al. Characterization of collective ground states in single-layer $NbSe_2$. *Nat. Phys.* **2016**, *12*, 92−97.
(267) Cho, D.; Cheon, S.; Kim, K. S.; Lee, S. H.; Cho, Y. H.; Cheong, S. W.; Yeom, H. W. Nanoscale manipulation of the mott insulating state coupled to charge order in 1T-$TaS_2$. *Nat. Commun.* **2016**, *7*, 10453.
(268) Yang, H. F.; He, K. Y.; Koo, J.; Shen, S. W.; Zhang, S. H.; Liu, G.; Liu, Y. Z.; Chen, C.; Liang, A. J.; Huang, K.; et al. Visualization of chiral electronic structure and anomalous optical response in a material with chiral charge density waves. *Phys. Rev. Lett.* **2022**, *129*, 156401.
(269) Chen, P.; Pai, W. W.; Chan, Y. H.; Madhavan, V.; Chou, M. Y.; Mo, S. K.; Fedorov, A. V.; Chiang, T. C. Unique gap structure and symmetry of the charge density wave in single-layer $VSe_2$. *Phys. Rev. Lett.* **2018**, *121*, 196402.
(270) Arguello, C. J.; Chockalingam, S. P.; Rosenthal, E. P.; Zhao, L.; Gutiérrez, C.; Kang, J. H.; Chung, W. C.; Fernandes, R. M.; Jia, S.; Millis, A. J.; et al. Visualizing the charge density wave transition in 2H-$NbSe_2$ in real space. *Phys. Rev. B* **2014**, *89*, 235115.
(271) Yu, Y.; Yang, F.; Lu, X. F.; Yan, Y. J.; Cho, Y. H.; Ma, L.; Niu, X.; Kim, S.; Son, Y. W.; Feng, D.; et al. Gate-tunable phase transitions in thin flakes of 1T-$TaS_2$. *Nat. Nanotechnol.* **2015**, *10*, 270−276.

(272) Mraz, A.; Vaskivskyi, I.; Venturini, R.; Svetin, D.; Chernolevska, Y.; Mihailovic, D. Charge configuration memory (CCM) device − a novel approach to memory. *Informacije MIDEM* **2021**, *51*, 167.
(273) Liu, G.; Debnath, B.; Pope, T. R.; Salguero, T. T.; Lake, R. K.; Balandin, A. A. A charge-density-wave oscillator based on an integrated tantalum disulfide-boron nitride-graphene device operating at room temperature. *Nat. Nanotechnol.* **2016**, *11*, 845−850.
(274) Samarth, N. Magnetism in flatland. *Nature* **2017**, *546*, 216−218.
(275) Mermin, N. D.; Wagner, H. Absence of ferromagnetism or antiferromagnetism in one- or two-dimensional isotropic heisenberg models. *Phys. Rev. Lett.* **1966**, *17*, 1133−1136.
(276) Shabbir, B.; Nadeem, M.; Dai, Z. G.; Fuhrer, M. S.; Xue, Q. K.; Wang, X. L.; Bao, Q. L. Long range intrinsic ferromagnetism in two dimensional materials and dissipationless future technologies. *Appl. Phys. Rev.* **2018**, *5*, No. 041105.
(277) Hossain, M.; Qin, B.; Li, B.; Duan, X. D. Synthesis, characterization, properties and applications of two-dimensional magnetic materials. *Nano Today* **2022**, *42*, 101338.
(278) Gong, C.; Li, L.; Li, Z. L.; Ji, H. W.; Stern, A.; Xia, Y.; Cao, T.; Bao, W.; Wang, C. Z.; Wang, Y. A.; et al. Discovery of intrinsic ferromagnetism in two-dimensional van der Waals crystals. *Nature* **2017**, *546*, 265−269.
(279) Huang, B.; Clark, G.; Navarro-Moratalla, E.; Klein, D. R.; Cheng, R.; Seyler, K. L.; Zhong, D.; Schmidgall, E.; McGuire, M. A.; Cobden, D. H.; et al. Layer-dependent ferromagnetism in a van der Waals crystal down to the monolayer limit. *Nature* **2017**, *546*, 270−273.
(280) Deng, Y. J.; Yu, Y. J.; Song, Y. C.; Zhang, J. Z.; Wang, N. Z.; Sun, Z. Y.; Yi, Y. F.; Wu, Y. Z.; Wu, S. W.; Zhu, J. Y.; et al. Gate-tunable room-temperature ferromagnetism in two-dimensional $Fe_3GeTe_2$. *Nature* **2018**, *563*, 94−99.
(281) Kaloni, T. P. Tuning the structural, electronic, and magnetic properties of germanene by the adsorption of 3d transition metal atoms. *J. Phys. Chem. C* **2014**, *118*, 25200−25208.
(282) Fan, X. L.; An, Y. R.; Guo, W. J. Ferromagnetism in transitional metal-doped $MoS_2$ monolayer. *Nanoscale Res. Lett.* **2016**, *11*, 154.
(283) Li, Q. Q.; Li, S.; Wu, D.; Ding, Z. K.; Cao, X. H.; Huang, L.; Pan, H.; Li, B.; Chen, K. Q.; Duan, X. D. Magnetic properties manipulation of $CrTe_2$ bilayer through strain and self-intercalation. *Appl. Phys. Lett.* **2021**, *119*, 162402.
(284) Zhou, X. Y.; Liu, C.; Song, L. T.; Zhang, H. M.; Huang, Z. W.; He, C. L.; Li, B. L.; Lin, X. H.; Zhang, Z. C.; Shi, S.; et al. Promoting the optoelectronic and ferromagnetic properties of $Cr_2S_3$ nanosheets via Se doping. *Sci. China Phys. Mech.* **2022**, *65*, 276811.
(285) Kriegner, D.; Vyborny, K.; Olejník, K.; Reichlová, H.; Novák, V.; Marti, X.; Gazquez, J.; Saidl, V.; Nemec, P.; Volobuev, V. V.; et al. Multiple-stable anisotropic magnetoresistance memory in antiferromagnetic MnTe. *Nat. Commun.* **2016**, *7*, 11623.
(286) Zhang, Y.; Chu, J.; Yin, L.; Shifa, T. A.; Cheng, Z.; Cheng, R.; Wang, F.; Wen, Y.; Zhan, X.; Wang, Z.; He, J. Ultrathin magnetic 2D single-crystal CrSe. *Adv. Mater.* **2019**, *31*, 1900056.
(287) Kang, L. X.; Ye, C.; Zhao, X. X.; Zhou, X. Y.; Hu, J. X.; Li, Q.; Liu, D.; Das, C. M.; Yang, J. F.; Hu, D. Y.; et al. Phase-controllable growth of ultrathin 2D magnetic FeTe crystals. *Nat. Commun.* **2020**, *11*, 3729.
(288) Wen, Y.; Liu, Z. H.; Zhang, Y.; Xia, C. X.; Zhai, B. X.; Zhang, X. H.; Zhai, G. H.; Shen, C.; He, P.; Cheng, R. Q.; et al. Tunable room-temperature ferromagnetism in two-dimensional $Cr_2Te_3$. *Nano Lett.* **2020**, *20*, 3130−3139.
(289) Chua, R.; Zhou, J.; Yu, X. J.; Yu, W.; Gou, J.; Zhu, R.; Zhang, L.; Liu, M. Z.; Breese, M. B. H.; Chen, W.; et al. Room temperature ferromagnetism of monolayer chromium telluride with perpendicular magnetic anisotropy. *Adv. Mater.* **2021**, *33*, 2103360.
(290) Li, N. N.; Zhu, L. L.; Shang, H. H.; Wang, F.; Zhang, Y.; Yao, Y. Y.; Wang, J. J.; Zhan, X. Y.; Wang, F. M.; He, J.; et al. Controlled synthesis and Raman study of a 2D antiferromagnetic p-type semiconductor: $\alpha$-MnSe. *Nanoscale* **2021**, *13*, 6953−6964.
(291) Zhu, X. K.; Liu, H.; Liu, L.; Ren, L. Z.; Li, W. Y.; Fang, L. M.; Chen, X. P.; Xie, L.; Jing, Y. M.; Chen, J. S.; et al. Spin glass state in chemical vapor-deposited crystalline $Cr_2Se_3$ nanosheets. *Chem. Mater.* **2021**, *33*, 3851−3858.
(292) Li, B. L.; Deng, X.; Shu, W. N.; Cheng, X.; Qian, Q.; Wan, Z.; Zhao, B.; Shen, X. H.; Wu, R. X.; Shi, S.; et al. Air-stable ultrathin $Cr_3Te_4$ nanosheets with thickness-dependent magnetic biskyrmions. *Mater. Today* **2022**, *57*, 66−74.
(293) Xiao, H.; Zhuang, W. Z.; Loh, L.; Liang, T.; Gayen, A.; Ye, P.; Bosman, M.; Eda, G.; Wang, X. F.; Xu, M. S. Van der Waals epitaxial growth of 2D layered room-temperature ferromagnetic $CrS_2$. *Adv. Mater. Interfaces* **2022**, *9*, 2201353.
(294) Zou, J. Y.; Yang, Y. M.; Hu, D. A. Y.; Kang, L. X.; Zhu, C.; Tian, D.; Lv, X. D.; Kutty, G.; Guo, Y. X.; Xu, M. Z.; et al. Controlled growth of ultrathin ferromagnetic $\beta$-MnSe semiconductor. *Smartmat* **2022**, *3*, 482−490.
(295) Duerloo, K. A. N.; Ong, M. T.; Reed, E. J. Intrinsic piezoelectricity in two-dimensional materials. *J. Phys. Chem. Lett.* **2012**, *3*, 2871−2876.
(296) Tressler, J. F.; Alkoy, S.; Newnham, R. E. Piezoelectric sensors and sensor materials. *J. Electroceram.* **1998**, *2*, 257−272.
(297) Sekhar, M. C.; Veena, E.; Kumar, N. S.; Naidu, K. C. B.; Mallikarjuna, A.; Basha, D. B. A review on piezoelectric materials and their applications. *Cryst. Res. Technol.* **2023**, *58*, 2200130.
(298) Jin, C. C.; Liu, D. M.; Zhang, L. X. An emerging family of piezocatalysts: 2D piezoelectric materials. *Small* **2023**, *19*, 2303586.
(299) Alyörük, M. M.; Aierken, Y.; Çakır, D.; Peeters, F. M.; Sevik, C. Promising piezoelectric performance of single layer transition-metal dichalcogenides and dioxides. *J. Phys. Chem. C* **2015**, *119*, 23231−23237.
(300) Blonsky, M. N.; Zhuang, H. L.; Singh, A. K.; Hennig, R. G. Ab initio prediction of piezoelectricity in two-dimensional materials. *ACS Nano* **2015**, *9*, 9885−9891.
(301) Wu, W. Z.; Wang, L.; Li, Y. L.; Zhang, F.; Lin, L.; Niu, S. M.; Chenet, D.; Zhang, X.; Hao, Y. F.; Heinz, T. F.; et al. Piezoelectricity of single-atomic-layer $MoS_2$ for energy conversion and piezotronics. *Nature* **2014**, *514*, 470−474.
(302) Zhu, H.; Wang, Y.; Xiao, J.; Liu, M.; Xiong, S.; Wong, Z. J.; Ye, Z.; Ye, Y.; Yin, X.; Zhang, X. Observation of piezoelectricity in free-standing monolayer $MoS_2$. *Nat. Nanotechnol.* **2015**, *10*, 151−155.
(303) Manzeli, S.; Allain, A.; Ghadimi, A.; Kis, A. Piezoresistivity and strain-induced band gap tuning in atomically thin $MoS_2$. *Nano Lett.* **2015**, *15*, 5330−5335.
(304) Lee, J. H.; Park, J. Y.; Cho, E. B.; Kim, T. Y.; Han, S. A.; Kim, T. H.; Liu, Y.; Kim, S. K.; Roh, C. J.; Yoon, H. J.; et al. Reliable piezoelectricity in bilayer $WSe_2$ for piezoelectric nanogenerators. *Adv. Mater.* **2017**, *29*, 1606667.
(305) Li, S.; Zhao, Z.; Yu, D.; Zhao, J.-Z.; Su, Y.; Liu, Y.; Lin, Y.; Liu, W.; Xu, H.; Zhang, Z. Few-layer transition metal dichalcogenides ($MoS_2$, $WS_2$, and $WSe_2$) for water splitting and degradation of organic pollutants: Understanding the piezocatalytic effect. *Nano Energy* **2019**, *66*, 104083.
(306) Hallil, H.; Cai, W.; Zhang, K.; Yu, P.; Liu, S.; Xu, R.; Zhu, C.; Xiong, Q.; Liu, Z.; Zhang, Q. Strong piezoelectricity in 3R-$MoS_2$ flakes. *Adv. Electron. Mater.* **2022**, *8*, 2101131.
(307) Cui, C.; Xue, F.; Hu, W.-J.; Li, L.-J. Two-dimensional materials with piezoelectric and ferroelectric functionalities. *npj 2D Mater. Appl.* **2018**, *2*, 18.
(308) Zhang, Q.; Zuo, S.; Chen, P.; Pan, C. Piezotronics in two-dimensional materials. *InfoMat* **2021**, *3*, 987−1007.
(309) Sherrell, P. C.; Fronzi, M.; Shepelin, N. A.; Corletto, A.; Winkler, D. A.; Ford, M.; Shapter, J. G.; Ellis, A. V. A bright future for engineering piezoelectric 2D crystals. *Chem. Soc. Rev.* **2022**, *51*, 650−671.
(310) Zhang, Y.; Jie, W.; Chen, P.; Liu, W.; Hao, J. Ferroelectric and piezoelectric effects on the optical process in advanced materials and devices. *Adv. Mater.* **2018**, *30*, 1707007.

(311) Zhang, D.; Schoenherr, P.; Sharma, P.; Seidel, J. Ferroelectric order in van der Waals layered materials. *Nat. Rev. Mater.* **2023**, *8*, 25−40.
(312) Sharma, P.; Xiang, F. X.; Shao, D. F.; Zhang, D.; Tsymbal, E. Y.; Hamilton, A. R.; Seidel, J. A room-temperature ferroelectric semimetal. *Sci. Adv.* **2019**, *5*, eaax5080.
(313) Yuan, S.; Luo, X.; Chan, H. L.; Xiao, C.; Dai, Y.; Xie, M.; Hao, J. Room-temperature ferroelectricity in $MoTe_2$ down to the atomic monolayer limit. *Nat. Commun.* **2019**, *10*, 1775.
(314) Wang, C.; You, L.; Cobden, D.; Wang, J. Towards two-dimensional van der Waals ferroelectrics. *Nat. Mater.* **2023**, *22*, 542−552.
(315) Li, L.; Wu, M. Binary compound bilayer and multilayer with vertical polarizations: Two-dimensional ferroelectrics, multiferroics, and nanogenerators. *ACS Nano* **2017**, *11*, 6382−6388.
(316) Yasuda, K.; Wang, X.; Watanabe, K.; Taniguchi, T.; Jarillo-Herrero, P. Stacking-engineered ferroelectricity in bilayer boron nitride. *Science* **2021**, *372*, 1458−1462.
(317) Tsymbal, E. Y. Two-dimensional ferroelectricity by design. *Science* **2021**, *372*, 1389−1390.
(318) Rogee, L.; Wang, L.; Zhang, Y.; Cai, S.; Wang, P.; Chhowalla, M.; Ji, W.; Lau, S. P. Ferroelectricity in untwisted heterobilayers of transition metal dichalcogenides. *Science* **2022**, *376*, 973−978.
(319) Weston, A.; Castanon, E. G.; Enaldiev, V.; Ferreira, F.; Bhattacharjee, S.; Xu, S.; Corte-Leon, H.; Wu, Z.; Clark, N.; Summerfield, A.; et al. Interfacial ferroelectricity in marginally twisted 2D semiconductors. *Nat. Nanotechnol.* **2022**, *17*, 390−395.
(320) Wang, X.; Yasuda, K.; Zhang, Y.; Liu, S.; Watanabe, K.; Taniguchi, T.; Hone, J.; Fu, L.; Jarillo-Herrero, P. Interfacial ferroelectricity in rhombohedral-stacked bilayer transition metal dichalcogenides. *Nat. Nanotechnol.* **2022**, *17*, 367−371.
(321) Meng, P.; Wu, Y.; Bian, R.; Pan, E.; Dong, B.; Zhao, X.; Chen, J.; Wu, L.; Sun, Y.; Fu, Q.; et al. Sliding induced multiple polarization states in two-dimensional ferroelectrics. *Nat. Commun.* **2022**, *13*, 7696.
(322) Yang, L.; Wu, M. Across-layer sliding ferroelectricity in 2D heterolayers. *Adv. Funct. Mater.* **2023**, *33*, 2301105.
(323) Klitzing, K. v.; Dorda, G.; Pepper, M. New method for high-accuracy determination of the fine-structure constant based on quantized Hall resistance. *Phys. Rev. Lett.* **1980**, *45*, 494−497.
(324) Thouless, D. J.; Kohmoto, M.; Nightingale, M. P.; den Nijs, M. Quantized Hall conductance in a two-dimensional periodic potential. *Phys. Rev. Lett.* **1982**, *49*, 405−408.
(325) Qi, X.-L.; Zhang, S.-C. Topological insulators and superconductors. *Rev. Mod. Phys.* **2011**, *83*, 1057−1110.
(326) Young, S. M.; Zaheer, S.; Teo, J. C. Y.; Kane, C. L.; Mele, E. J.; Rappe, A. M. Dirac semimetal in three dimensions. *Phys. Rev. Lett.* **2012**, *108*, 140405.
(327) Fei, Z.; Palomaki, T.; Wu, S.; Zhao, W.; Cai, X.; Sun, B.; Nguyen, P.; Finney, J.; Xu, X.; Cobden, D. H. Edge conduction in monolayer $WTe_2$. *Nat. Phys.* **2017**, *13*, 677−682.
(328) Wu, S.; Fatemi, V.; Gibson, Q. D.; Watanabe, K.; Taniguchi, T.; Cava, R. J.; Jarillo-Herrero, P. Observation of the quantum spin Hall effect up to 100 K in a monolayer crystal. *Science* **2018**, *359*, 76−79.
(329) Tang, S.; Zhang, C.; Wong, D.; Pedramrazi, Z.; Tsai, H.-Z.; Jia, C.; Moritz, B.; Claassen, M.; Ryu, H.; Kahn, S.; et al. Quantum spin Hall state in monolayer 1T'-$WTe_2$. *Nat. Phys.* **2017**, *13*, 683−687.
(330) Soluyanov, A. A.; Gresch, D.; Wang, Z.; Wu, Q.; Troyer, M.; Dai, X.; Bernevig, B. A. Type-II Weyl semimetals. *Nature* **2015**, *527*, 495−498.
(331) Sun, Y.; Wu, S.-C.; Ali, M. N.; Felser, C.; Yan, B. Prediction of Weyl semimetal in orthorhombic $MoTe_2$. *Phys. Rev. B* **2015**, *92*, 161107.
(332) Kang, K.; Li, T.; Sohn, E.; Shan, J.; Mak, K. F. Nonlinear anomalous Hall effect in few-layer $WTe_2$. *Nat. Mater.* **2019**, *18*, 324−328.
(333) Xu, S.-Y.; Ma, Q.; Shen, H.; Fatemi, V.; Wu, S.; Chang, T.-R.; Chang, G.; Valdivia, A. M. M.; Chan, C.-K.; Gibson, Q. D.; et al. Electrically switchable berry curvature dipole in the monolayer topological insulator $WTe_2$. *Nat. Phys.* **2018**, *14*, 900−906.
(334) Zhu, J.; Su, J.-J.; MacDonald, A. H. Voltage-controlled magnetic reversal in orbital chern insulators. *Phys. Rev. Lett.* **2020**, *125*, 227702.
(335) Li, T.; Jiang, S.; Shen, B.; Zhang, Y.; Li, L.; Tao, Z.; Devakul, T.; Watanabe, K.; Taniguchi, T.; Fu, L.; et al. Quantum anomalous Hall effect from intertwined moiré bands. *Nature* **2021**, *600*, 641−646.
(336) Cai, J.; Anderson, E.; Wang, C.; Zhang, X.; Liu, X.; Holtzmann, W.; Zhang, Y.; Fan, F.; Taniguchi, T.; Watanabe, K.; et al. Signatures of fractional quantum anomalous Hall states in twisted $MoTe_2$. *Nature* **2023**, *622*, 63−68.
(337) Zeng, Y.; Xia, Z.; Kang, K.; Zhu, J.; Knüppel, P.; Vaswani, C.; Watanabe, K.; Taniguchi, T.; Mak, K. F.; Shan, J. Thermodynamic evidence of fractional chern insulator in moiré $MoTe_2$. *Nature* **2023**, *622*, 69−73.
(338) Park, H.; Cai, J.; Anderson, E.; Zhang, Y.; Zhu, J.; Liu, X.; Wang, C.; Holtzmann, W.; Hu, C.; Liu, Z.; et al. Observation of fractionally quantized anomalous Hall effect. *Nature* **2023**, *622*, 74−79.
(339) Xu, F.; Sun, Z.; Jia, T.; Liu, C.; Xu, C.; Li, C.; Gu, Y.; Watanabe, K.; Taniguchi, T.; Tong, B.; et al. Observation of integer and fractional quantum anomalous Hall effects in twisted bilayer $MoTe_2$. *Phys. Rev. X* **2023**, *13*, No. 031037.
(340) Tao, J.; Chai, J.; Lu, X.; Wong, L. M.; Wong, T. I.; Pan, J.; Xiong, Q.; Chi, D.; Wang, S. Growth of wafer-scale $MoS_2$ monolayer by magnetron sputtering. *Nanoscale* **2015**, *7*, 2497−2503.
(341) He, Q.; Li, P.; Wu, Z.; Yuan, B.; Luo, Z.; Yang, W.; Liu, J.; Cao, G.; Zhang, W.; Shen, Y.; et al. Molecular beam epitaxy scalable growth of wafer-scale continuous semiconducting monolayer $MoTe_2$ on inert amorphous dielectrics. *Adv. Mater.* **2019**, *31*, 1901578.
(342) Nakano, M.; Wang, Y.; Kashiwabara, Y.; Matsuoka, H.; Iwasa, Y. Layer-by-layer epitaxial growth of scalable $WSe_2$ on sapphire by molecular beam epitaxy. *Nano Lett.* **2017**, *17*, 5595−5599.
(343) Poh, S. M.; Tan, S. J.; Zhao, X.; Chen, Z.; Abdelwahab, I.; Fu, D.; Xu, H.; Bao, Y.; Zhou, W.; Loh, K. P. Large area synthesis of 1D-$MoSe_2$ using molecular beam epitaxy. *Adv. Mater.* **2017**, *29*, 1605641.
(344) Serna, M. I.; Yoo, S. H.; Moreno, S.; Xi, Y.; Oviedo, J. P.; Choi, H.; Alshareef, H. N.; Kim, M. J.; Minary-Jolandan, M.; Quevedo-Lopez, M. A. Large-area deposition of $MoS_2$ by pulsed laser deposition with in situ thickness control. *ACS Nano* **2016**, *10*, 6054−6061.
(345) Godel, F.; Zatko, V.; Carrétéro, C.; Sander, A.; Galbiati, M.; Vecchiola, A.; Brus, P.; Bezencenet, O.; Servet, B.; Martin, M.-B.; et al. $WS_2$ 2D semiconductor down to monolayers by pulsed-laser deposition for large-scale integration in electronics and spintronics circuits. *ACS Appl. Nano Mater.* **2020**, *3*, 7908−7916.
(346) Groven, B.; Nalin Mehta, A.; Bender, H.; Meersschaut, J.; Nuytten, T.; Verdonck, P.; Conard, T.; Smets, Q.; Schram, T.; Schoenaers, B.; et al. Two-dimensional crystal grain size tuning in $WS_2$ atomic layer deposition: An insight in the nucleation mechanism. *Chem. Mater.* **2018**, *30*, 7648−7663.
(347) Kim, Y.; Woo, W. J.; Kim, D.; Lee, S.; Chung, S. M.; Park, J.; Kim, H. Atomic-layer-deposition-based 2D transition metal chalcogenides: Synthesis, modulation, and applications. *Adv. Mater.* **2021**, *33*, 2005907.
(348) Tan, L. K.; Liu, B.; Teng, J. H.; Guo, S.; Low, H. Y.; Loh, K. P. Atomic layer deposition of a $MoS_2$ film. *Nanoscale* **2014**, *6*, 10584−10588.
(349) Pyeon, J. J.; Kim, S. H.; Jeong, D. S.; Baek, S. H.; Kang, C. Y.; Kim, J. S.; Kim, S. K. Wafer-scale growth of $MoS_2$ thin films by atomic layer deposition. *Nanoscale* **2016**, *8*, 10792−10798.
(350) Jurca, T.; Moody, M. J.; Henning, A.; Emery, J. D.; Wang, B.; Tan, J. M.; Lohr, T. L.; Lauhon, L. J.; Marks, T. J. Low-temperature atomic layer deposition of $MoS_2$ films. *Angew. Chem., Int. Ed.* **2017**, *56*, 4991−4995.

(351) Jin, Z.; Shin, S.; Kwon, D. H.; Han, S. J.; Min, Y. S. Novel chemical route for atomic layer deposition of $MoS_2$ thin film on $SiO_2$/Si substrate. *Nanoscale* **2014**, *6*, 14453−14458.
(352) Jeon, W.; Cho, Y.; Jo, S.; Ahn, J. H.; Jeong, S. J. Wafer-scale synthesis of reliable high-mobility molybdenum disulfide thin films via inhibitor-utilizing atomic layer deposition. *Adv. Mater.* **2017**, *29*, 1703031.
(353) Song, J. G.; Park, J.; Lee, W.; Choi, T.; Jung, H.; Lee, C. W.; Hwang, S. H.; Myoung, J. M.; Jung, J. H.; Kim, S. H.; et al. Layer-controlled, wafer-scale, and conformal synthesis of tungsten disulfide nanosheets using atomic layer deposition. *ACS Nano* **2013**, *7*, 11333−11340.
(354) Mattinen, M.; Hatanpää, T.; Sarnet, T.; Mizohata, K.; Meinander, K.; King, P. J.; Khriachtchev, L.; Räisänen, J.; Ritala, M.; Leskelä, M. Atomic layer deposition of crystalline $MoS_2$ thin films: New molybdenum precursor for low-temperature film growth. *Adv. Mater. Interfaces* **2017**, *4*, 1700123.
(355) Sun, L.; Yuan, G.; Gao, L.; Yang, J.; Chhowalla, M.; Gharahcheshmeh, M. H.; Gleason, K. K.; Choi, Y. S.; Hong, B. H.; Liu, Z. Chemical vapour deposition. *Nat. Rev. Methods Primers* **2021**, *1*, 5.
(356) Liu, H.; Zhu, Y.; Meng, Q.; Lu, X.; Kong, S.; Huang, Z.; Jiang, P.; Bao, X. Role of the carrier gas flow rate in monolayer $MoS_2$ growth by modified chemical vapor deposition. *Nano Res.* **2017**, *10*, 643−651.
(357) van der Zande, A. M.; Huang, P. Y.; Chenet, D. A.; Berkelbach, T. C.; You, Y.; Lee, G. H.; Heinz, T. F.; Reichman, D. R.; Muller, D. A.; Hone, J. C. Grains and grain boundaries in highly crystalline monolayer molybdenum disulphide. *Nat. Mater.* **2013**, *12*, 554−561.
(358) Meyer, B. Elemental sulfur. *Chem. Rev.* **1976**, *76*, 367−388.
(359) Wu, Q.; He, L.; Wang, D.; Nong, H.; Wang, J.; Cai, Z.; Zhao, S.; Zheng, R.; Lai, S.; Zhang, R.; et al. Resolidified chalcogen-assisted growth of bilayer semiconductors with controlled stacking orders. *Small* **2024**, *20*, 2305506.
(360) Wu, Q.; Nong, H.; Zheng, R.; Zhang, R.; Wang, J.; Yang, L.; Liu, B. Resolidified chalcogen precursors for high-quality 2D semiconductor growth. *Angew. Chem.* **2023**, *135*, 202301501.
(361) Dumcenco, D.; Ovchinnikov, D.; Lopez Sanchez, O.; Gillet, P.; Alexander, D. T. L.; Lazar, S.; Radenovic, A.; Kis, A. Large-area $MoS_2$ grown using $H_2S$ as the sulphur source. *2D Mater.* **2015**, *2*, No. 044005.
(362) Tang, L.; Li, T.; Luo, Y.; Feng, S.; Cai, Z.; Zhang, H.; Liu, B.; Cheng, H. M. Vertical chemical vapor deposition growth of highly uniform 2D transition metal dichalcogenides. *ACS Nano* **2020**, *14*, 4646−4653.
(363) Feng, S.; Tan, J.; Zhao, S.; Zhang, S.; Khan, U.; Tang, L.; Zou, X.; Lin, J.; Cheng, H. M.; Liu, B. Synthesis of ultrahigh-quality monolayer molybdenum disulfide through in situ defect healing with thiol molecules. *Small* **2020**, *16*, 2003357.
(364) Jin, Y.; Cheng, M.; Liu, H.; Ouzounian, M.; Hu, T. S.; You, B.; Shao, G.; Liu, X.; Liu, Y.; Li, H.; et al. $Na_2SO_4$-regulated high-quality growth of transition metal dichalcogenides by controlling diffusion. *Chem. Mater.* **2020**, *32*, 5616−5625.
(365) Li, S.; Lin, Y.-C.; Hong, J.; Gao, B.; Lim, H. E.; Yang, X.; Liu, S.; Tateyama, Y.; Tsukagoshi, K.; Sakuma, Y.; et al. Mixed-salt enhanced chemical vapor deposition of two-dimensional transition metal dichalcogenides. *Chem. Mater.* **2021**, *33*, 7301−7308.
(366) Zuo, Y.; Liu, C.; Ding, L.; Qiao, R.; Tian, J.; Liu, C.; Wang, Q.; Xue, G.; You, Y.; Guo, Q.; et al. Robust growth of two-dimensional metal dichalcogenides and their alloys by active chalcogen monomer supply. *Nat. Commun.* **2022**, *13*, 1007.
(367) Yang, X.; Li, S.; Ikeda, N.; Sakuma, Y. Oxide scale sublimation chemical vapor deposition for controllable growth of monolayer $MoS_2$ crystals. *Small Methods* **2022**, *6*, 2101107.
(368) Zhou, J.; Lin, J.; Huang, X.; Zhou, Y.; Chen, Y.; Xia, J.; Wang, H.; Xie, Y.; Yu, H.; Lei, J.; et al. A library of atomically thin metal chalcogenides. *Nature* **2018**, *556*, 355−359.
(369) Lim, Y. F.; Priyadarshi, K.; Bussolotti, F.; Gogoi, P. K.; Cui, X.; Yang, M.; Pan, J.; Tong, S. W.; Wang, S.; Pennycook, S. J.; et al. Modification of vapor phase concentrations in $MoS_2$ growth using a NiO foam barrier. *ACS Nano* **2018**, *12*, 1339−1349.
(370) Shi, R.; He, P.; Cai, X.; Zhang, Z.; Wang, W.; Wang, J.; Feng, X.; Wu, Z.; Amini, A.; Wang, N.; et al. Oxide inhibitor-assisted growth of single-layer molybdenum dichalcogenides ($MoX_2$, X = S, Se, Te) with controllable molybdenum release. *ACS Nano* **2020**, *14*, 7593−7601.
(371) Yang, P.; Liu, F.; Li, X.; Hu, J.; Zhou, F.; Zhu, L.; Chen, Q.; Gao, P.; Zhang, Y. Highly reproducible epitaxial growth of wafer-scale single-crystal monolayer $MoS_2$ on sapphire. *Small Methods* **2023**, *7*, 2300165.
(372) Lu, Y.; Chen, T.; Ryu, G. H.; Huang, H.; Sheng, Y.; Chang, R.-J.; Warner, J. H. Self-limiting growth of high-quality 2D monolayer $MoS_2$ by direct sulfurization using precursor-soluble substrates for advanced field-effect transistors and photodetectors. *ACS Appl. Nano Mater.* **2019**, *2*, 369−378.
(373) Cai, Z.; Lai, Y.; Zhao, S.; Zhang, R.; Tan, J.; Feng, S.; Zou, J.; Tang, L.; Lin, J.; Liu, B.; Cheng, H.-M. Dissolution-precipitation growth of uniform and clean two dimensional transition metal dichalcogenides. *Natl. Sci. Rev.* **2021**, *8*, nwaa115.
(374) Wang, K.; Zhang, L.; Nguyen, G. D.; Sang, X.; Liu, C.; Yu, Y.; Ko, W.; Unocic, R. R.; Puretzky, A. A.; Rouleau, C. M.; et al. Selective antisite defect formation in $WS_2$ monolayers via reactive growth on dilute W-Au alloy substrates. *Adv. Mater.* **2022**, *34*, 2106674.
(375) Xin, X.; Chen, J.; Zhang, Y.; Chen, M. L.; Bao, Y.; Liu, W.; Liu, Y.; Xu, H.; Ren, W. Ultrafast growth of submillimeter-scale single-crystal $MoSe_2$ by pre-alloying CVD. *Nanoscale Horiz.* **2022**, *7*, 743−751.
(376) Shivayogimath, A.; Thomsen, J. D.; Mackenzie, D. M. A.; Geisler, M.; Stan, R. M.; Holt, A. J.; Bianchi, M.; Crovetto, A.; Whelan, P. R.; Carvalho, A.; et al. A universal approach for the synthesis of two-dimensional binary compounds. *Nat. Commun.* **2019**, *10*, 2957.
(377) Zhang, P.; Wang, X.; Jiang, H.; Zhang, Y.; He, Q.; Si, K.; Li, B.; Zhao, F.; Cui, A.; Wei, Y.; et al. Flux-assisted growth of atomically thin materials. *Nat. Synth.* **2022**, *1*, 864−872.
(378) Boandoh, S.; Choi, S. H.; Park, J. H.; Park, S. Y.; Bang, S.; Jeong, M. S.; Lee, J. S.; Kim, H. J.; Yang, W.; Choi, J. Y.; et al. A novel and facile route to synthesize atomic-layered $MoS_2$ film for large-area electronics. *Small* **2017**, *13*, 1701306.
(379) Li, S.; Lin, Y. C.; Liu, X. Y.; Hu, Z.; Wu, J.; Nakajima, H.; Liu, S.; Okazaki, T.; Chen, W.; Minari, T.; et al. Wafer-scale and deterministic patterned growth of monolayer $MoS_2$ via vapor-liquid-solid method. *Nanoscale* **2019**, *11*, 16122−16129.
(380) Zhao, B.; Wan, Z.; Liu, Y.; Xu, J.; Yang, X.; Shen, D.; Zhang, Z.; Guo, C.; Qian, Q.; Li, J.; et al. High-order superlattices by rolling up van der Waals heterostructures. *Nature* **2021**, *591*, 385−390.
(381) Yang, D.; Hu, X.; Zhuang, M.; Ding, Y.; Zhou, S.; Li, A.; Yu, Y.; Li, H.; Luo, Z.; Gan, L.; Zhai, T. Inversion symmetry broken 2D 3R-$MoTe_2$. *Adv. Funct. Mater.* **2018**, *28*, 1800785.
(382) Ahn, C.; Park, Y.; Shin, S.; Ahn, J. G.; Song, I.; An, Y.; Jung, J.; Kim, C. S.; Kim, J. H.; Bang, J.; et al. Growth of monolayer and multilayer $MoS_2$ films by selection of growth mode: Two pathways via chemisorption and physisorption of an inorganic molecular precursor. *ACS Appl. Mater. Interfaces* **2021**, *13*, 6805−6812.
(383) Delabie, A.; Caymax, M.; Groven, B.; Heyne, M.; Haesevoets, K.; Meersschaut, J.; Nuytten, T.; Bender, H.; Conard, T.; Verdonck, P.; et al. Low temperature deposition of 2D $WS_2$ layers from $WF_6$ and $H_2S$ precursors: Impact of reducing agents. *Chem. Commun.* **2015**, *51*, 15692−15695.
(384) Hu, D.; Xu, G.; Xing, L.; Yan, X.; Wang, J.; Zheng, J.; Lu, Z.; Wang, P.; Pan, X.; Jiao, L. Two-dimensional semiconductors grown by chemical vapor transport. *Angew. Chem., Int. Ed.* **2017**, *56*, 3611−3615.
(385) Modtland, B. J.; Navarro-Moratalla, E.; Ji, X.; Baldo, M.; Kong, J. Monolayer tungsten disulfide ($WS_2$) via chlorine-driven chemical vapor transport. *Small* **2017**, *13*, 1701232.
(386) Stoica, T.; Stoica, M.; Duchamp, M.; Tiedemann, A.; Mantl, S.; Grützmacher, D.; Buca, D.; Kardynał, B. E. Vapor transport growth

of $MoS_2$ nucleated on $SiO_2$ patterns and graphene flakes. *Nano Res.* **2016**, *9*, 3504−3514.

(387) Zhou, H.; Wang, C.; Shaw, J. C.; Cheng, R.; Chen, Y.; Huang, X.; Liu, Y.; Weiss, N. O.; Lin, Z.; Huang, Y.; et al. Large area growth and electrical properties of p-type $WSe_2$ atomic layers. *Nano Lett.* **2015**, *15*, 709−713.

(388) Zhang, Z.; Chen, P.; Yang, X.; Liu, Y.; Ma, H.; Li, J.; Zhao, B.; Luo, J.; Duan, X.; Duan, X. Ultrafast growth of large single crystals of monolayer $WS_2$ and $WSe_2$. *Natl. Sci. Rev.* **2020**, *7*, 737−744.

(389) Zhang, Z.; Chen, P.; Duan, X.; Zang, K.; Luo, J.; Duan, X. Robust epitaxial growth of two-dimensional heterostructures, multi-heterostructures, and superlattices. *Science* **2017**, *357*, 788−792.

(390) Liu, K. K.; Zhang, W.; Lee, Y. H.; Lin, Y. C.; Chang, M. T.; Su, C. Y.; Chang, C. S.; Li, H.; Shi, Y.; Zhang, H.; et al. Growth of large-area and highly crystalline $MoS_2$ thin layers on insulating substrates. *Nano Lett.* **2012**, *12*, 1538−1544.

(391) Lim, Y. R.; Han, J. K.; Kim, S. K.; Lee, Y. B.; Yoon, Y.; Kim, S. J.; Min, B. K.; Kim, Y.; Jeon, C.; Won, S.; et al. Roll-to-roll production of layer-controlled molybdenum disulfide: A platform for 2D semiconductor-based industrial applications. *Adv. Mater.* **2018**, *30*, 1705270.

(392) Zhou, S.; Liu, L.; Cui, S.; Ping, X.; Hu, D.; Jiao, L. Fast growth of large single-crystalline $WS_2$ monolayers via chemical vapor deposition. *Nano Res.* **2021**, *14*, 1659−1662.

(393) Chen, Y.; Tian, Z.; Wang, X.; Ran, N.; Wang, C.; Cui, A.; Lu, H.; Zhang, M.; Xue, Z.; Mei, Y.; et al. 2D transition metal dichalcogenide with increased entropy for piezoelectric electronics. *Adv. Mater.* **2022**, *34*, 2201630.

(394) Shang, S. L.; Lindwall, G.; Wang, Y.; Redwing, J. M.; Anderson, T.; Liu, Z. K. Lateral versus vertical growth of two-dimensional layered transition-metal dichalcogenides: Thermodynamic insight into $MoS_2$. *Nano Lett.* **2016**, *16*, 5742−5750.

(395) Najmaei, S.; Liu, Z.; Zhou, W.; Zou, X.; Shi, G.; Lei, S.; Yakobson, B. I.; Idrobo, J. C.; Ajayan, P. M.; Lou, J. Vapour phase growth and grain boundary structure of molybdenum disulphide atomic layers. *Nat. Mater.* **2013**, *12*, 754−759.

(396) Cain, J. D.; Shi, F.; Wu, J.; Dravid, V. P. Growth mechanism of transition metal dichalcogenide monolayers: The role of self-seeding fullerene nuclei. *ACS Nano* **2016**, *10*, 5440−5445.

(397) Zhou, D.; Shu, H.; Hu, C.; Jiang, L.; Liang, P.; Chen, X. Unveiling the growth mechanism of $MoS_2$ with chemical vapor deposition: From two-dimensional planar nucleation to self-seeding nucleation. *Cryst. Growth Des.* **2018**, *18*, 1012−1019.

(398) Kim, K. S.; Lee, D.; Chang, C. S.; Seo, S.; Hu, Y.; Cha, S.; Kim, H.; Shin, J.; Lee, J. H.; Lee, S.; et al. Non-epitaxial single-crystal 2D material growth by geometric confinement. *Nature* **2023**, *614*, 88−94.

(399) Li, J.; Yang, X.; Liu, Y.; Huang, B.; Wu, R.; Zhang, Z.; Zhao, B.; Ma, H.; Dang, W.; Wei, Z.; et al. General synthesis of two-dimensional van der Waals heterostructure arrays. *Nature* **2020**, *579*, 368−374.

(400) Wang, X.; Kang, K.; Chen, S.; Du, R.; Yang, E.-H. Location-specific growth and transfer of arrayed $MoS_2$ monolayers with controllable size. *2D Mater.* **2017**, *4*, No. 025093.

(401) Jiang, D.; Wang, X.; Chen, R.; Sun, J.; Kang, H.; Ji, D.; Liu, Y.; Wei, D. Self-expanding molten salt-driven growth of patterned transition-metal dichalcogenide crystals. *J. Am. Chem. Soc.* **2022**, *144*, 8746−8755.

(402) Li, M. Y.; Pu, J.; Huang, J. K.; Miyauchi, Y.; Matsuda, K.; Takenobu, T.; Li, L. J. Self-aligned and scalable growth of monolayer $WSe_2$-$MoS_2$ lateral heterojunctions. *Adv. Funct. Mater.* **2018**, *28*, 1706860.

(403) Huang, L.-Y.; Li, M.-Y.; Liew, S.-L.; Lin, S.-C.; Chou, A.-S.; Hsu, M.-C.; Hsu, C.-H.; Lin, Y.-T.; Mao, P.-S.; Hou, D.-H.; et al. Area-selective growth of two-dimensional mono- and bilayer $WS_2$ for field effect transistors. *ACS Materials Lett.* **2023**, *5*, 1760−1766.

(404) Han, G. H.; Kybert, N. J.; Naylor, C. H.; Lee, B. S.; Ping, J.; Park, J. H.; Kang, J.; Lee, S. Y.; Lee, Y. H.; Agarwal, R.; et al. Seeded growth of highly crystalline molybdenum disulphide monolayers at controlled locations. *Nat. Commun.* **2015**, *6*, 6128.

(405) Cheng, C. C.; Chung, Y. Y.; Li, M. Y.; Lin, C. T.; Li, C. F.; Chen, Y. H.; Lai, T. Y.; Li, K. S.; Shieh, J. M.; Su, S. K.; et al.. First demonstration of 40-nm channel length top-gate $WS_2$ pfet using channel area-selective CVD growth directly on $SiO_2$/Si substrate. In *39th Symposium on VLSI Technology/33rd Symposium on VLSI Circuits*, Kyoto, Japan, Jun 9−14, 2019; pp T244−T245.

(406) Liang, J.; Zhang, L.; Li, X.; Pan, B.; Luo, T.; Liu, D.; Zou, C.; Liu, N.; Hu, Y.; Yang, K.; et al. Carbon-nanoparticle-assisted growth of high quality bilayer $WS_2$ by atmospheric pressure chemical vapor deposition. *Nano Res.* **2019**, *12*, 2802−2807.

(407) Wang, J.; Cai, X.; Shi, R.; Wu, Z.; Wang, W.; Long, G.; Tang, Y.; Cai, N.; Ouyang, W.; Geng, P.; et al. Twin defect derived growth of atomically thin $MoS_2$ dendrites. *ACS Nano* **2018**, *12*, 635−643.

(408) Ling, X.; Lee, Y. H.; Lin, Y.; Fang, W.; Yu, L.; Dresselhaus, M. S.; Kong, J. Role of the seeding promoter in $MoS_2$ growth by chemical vapor deposition. *Nano Lett.* **2014**, *14*, 464−472.

(409) Guo, Y.; Shen, P. C.; Su, C.; Lu, A. Y.; Hempel, M.; Han, Y.; Ji, Q.; Lin, Y.; Shi, E.; McVay, E.; et al. Additive manufacturing of patterned 2D semiconductor through recyclable masked growth. *Proc. Natl. Acad. Sci. U. S. A.* **2019**, *116*, 3437−3442.

(410) Li, Y.; Hao, S.; DiStefano, J. G.; Murthy, A. A.; Hanson, E. D.; Xu, Y.; Wolverton, C.; Chen, X.; Dravid, V. P. Site-specific positioning and patterning of $MoS_2$ monolayers: The role of Au seeding. *ACS Nano* **2018**, *12*, 8970−8976.

(411) Patsha, A.; Sheff, V.; Ismach, A. Seeded-growth of $WS_2$ atomic layers: The effect on chemical and optical properties. *Nanoscale* **2019**, *11*, 22493−22503.

(412) Li, C.; Kameyama, T.; Takahashi, T.; Kaneko, T.; Kato, T. Nucleation dynamics of single crystal $WS_2$ from droplet precursors uncovered by in-situ monitoring. *Sci. Rep.* **2019**, *9*, 12958.

(413) Huang, M.; Ali, W.; Yang, L.; Huang, J.; Yao, C.; Xie, Y.; Sun, R.; Zhu, C.; Tan, Y.; Liu, X.; et al. Multifunctional optoelectronic synapses based on arrayed $MoS_2$ monolayers emulating human association memory. *Adv. Sci.* **2023**, *10*, 2300120.

(414) Liu, B.; Fathi, M.; Chen, L.; Abbas, A.; Ma, Y.; Zhou, C. Chemical vapor deposition growth of monolayer $WSe_2$ with tunable device characteristics and growth mechanism study. *ACS Nano* **2015**, *9*, 6119−6127.

(415) Azam, N.; Mahjouri-Samani, M. Time-resolved growth of 2D $WSe_2$ monolayer crystals. *ACS Nano* **2023**, *17*, 12519−12529.

(416) Chen, J.; Zhao, X.; Tan, S. J.; Xu, H.; Wu, B.; Liu, B.; Fu, D.; Fu, W.; Geng, D.; Liu, Y.; et al. Chemical vapor deposition of large-size monolayer $MoSe_2$ crystals on molten glass. *J. Am. Chem. Soc.* **2017**, *139*, 1073−1076.

(417) Gao, Y.; Liu, Z.; Sun, D. M.; Huang, L.; Ma, L. P.; Yin, L. C.; Ma, T.; Zhang, Z.; Ma, X. L.; Peng, L. M.; et al. Large-area synthesis of high-quality and uniform monolayer $WS_2$ on reusable Au foils. *Nat. Commun.* **2015**, *6*, 8569.

(418) Gao, Y.; Hong, Y. L.; Yin, L. C.; Wu, Z.; Yang, Z.; Chen, M. L.; Liu, Z.; Ma, T.; Sun, D. M.; Ni, Z.; et al. Ultrafast growth of high-quality monolayer $WSe_2$ on Au. *Adv. Mater.* **2017**, *29*, 1700990.

(419) Lei, J.; Xie, Y.; Yakobson, B. I. Gas-phase "prehistory" and molecular precursors in monolayer metal dichalcogenides synthesis: The case of $MoS_2$. *ACS Nano* **2021**, *15*, 10525−10531.

(420) Li, X.; Li, B.; Lei, J.; Bets, K. V.; Sang, X.; Okogbue, E.; Liu, Y.; Unocic, R. R.; Yakobson, B. I.; Hone, J.; Harutyunyan, A. R. Nickel particle-enabled width-controlled growth of bilayer molybdenum disulfide nanoribbons. *Sci. Adv.* **2021**, *7*, eabk1892.

(421) Liu, J.; Zeng, M.; Wang, L.; Chen, Y.; Xing, Z.; Zhang, T.; Liu, Z.; Zuo, J.; Nan, F.; Mendes, R. G.; et al. Ultrafast self-limited growth of strictly monolayer $WSe_2$ crystals. *Small* **2016**, *12*, 5741−5749.

(422) Yang, P.; Zou, X.; Zhang, Z.; Hong, M.; Shi, J.; Chen, S.; Shu, J.; Zhao, L.; Jiang, S.; Zhou, X.; et al. Batch production of 6-in. uniform monolayer molybdenum disulfide catalyzed by sodium in glass. *Nat. Commun.* **2018**, *9*, 979.


https://doi.org/10.1021/acs.chemrev.3c00851
*Chem. Rev.* XXXX, XXX, XXX−XXX

(423) Shi, Y.; Yang, P.; Jiang, S.; Zhang, Z.; Huan, Y.; Xie, C.; Hong, M.; Shi, J.; Zhang, Y. Na-assisted fast growth of large single-crystal $MoS_2$ on sapphire. *Nanotechnology* **2019**, *30*, No. 034002.
(424) Wang, P.; Lei, J.; Qu, J.; Cao, S.; Jiang, H.; He, M.; Shi, H.; Sun, X.; Gao, B.; Liu, W. Mechanism of alkali metal compound-promoted growth of monolayer $MoS_2$: Eutectic intermediates. *Chem. Mater.* **2019**, *31*, 873−880.
(425) Li, X.; Kahn, E.; Chen, G.; Sang, X.; Lei, J.; Passarello, D.; Oyedele, A. D.; Zakhidov, D.; Chen, K. W.; Chen, Y. X.; et al. Surfactant-mediated growth and patterning of atomically thin transition metal dichalcogenides. *ACS Nano* **2020**, *14*, 6570−6581.
(426) Huang, L.; Thi, Q. H.; Zheng, F.; Chen, X.; Chu, Y. W.; Lee, C. S.; Zhao, J.; Ly, T. H. Catalyzed kinetic growth in two-dimensional $MoS_2$. *J. Am. Chem. Soc.* **2020**, *142*, 13130−13135.
(427) Li, S.; Wang, S.; Tang, D.-M.; Zhao, W.; Xu, H.; Chu, L.; Bando, Y.; Golberg, D.; Eda, G. Halide-assisted atmospheric pressure growth of large $WSe_2$ and $WS_2$ monolayer crystals. *Appl. Mater. Today* **2015**, *1*, 60−66.
(428) Hussain, S.; Zhou, R.; Li, Y.; Qian, Z.; Urooj, Z.; Younas, M.; Zhao, Z.; Zhang, Q.; Dong, W.; Wu, Y.; et al. Liquid phase edge epitaxy of transition-metal dichalcogenide monolayers. *J. Am. Chem. Soc.* **2023**, *145*, 11348−11355.
(429) Zhang, D.; Wen, C.; McClimon, J. B.; Masih Das, P.; Zhang, Q.; Leone, G. A.; Mandyam, S. V.; Drndic, M.; Johnson, A. T. C., Jr.; Zhao, M. Q. Rapid growth of monolayer $MoSe_2$ films for large-area electronics. *Adv. Electron. Mater.* **2021**, *7*, 2001219.
(430) Zhang, Z.; Zhu, L.; Wang, D.; Tang, B.; Yang, P.; Shi, Y.; Zhou, F.; Fu, J.; Huan, Y.; Cui, F.; et al. Ultrafast growth of large-area uniform, millimeter-size $MoSe_2$ single crystals on low-cost soda-performance monolayer $MoS_2$ films lime glass. *Adv. Mater. Interfaces* **2021**, *8*, 2100415.
(431) Ji, Q.; Su, C.; Mao, N.; Tian, X.; Idrobo, J. C.; Miao, J.; Tisdale, W. A.; Zettl, A.; Li, J.; Kong, J. Revealing the bronsted-evans-polanyi relation in halide-activated fast $MoS_2$ growth toward millimeter-sized 2D crystals. *Sci. Adv.* **2021**, *7*, eabj3274.
(432) Wu, Q.; Zhang, J.; Tang, L.; Khan, U.; Nong, H.; Zhao, S.; Sun, Y.; Zheng, R.; Zhang, R.; Wang, J.; et al. Iodine-assisted ultrafast growth of high-quality monolayer $MoS_2$; with sulfur-terminated edges. *Natl. Sci. Open* **2023**, *2*, 20230009.
(433) Liu, C.; Xu, X.; Qiu, L.; Wu, M.; Qiao, R.; Wang, L.; Wang, J.; Niu, J.; Liang, J.; Zhou, X.; et al. Kinetic modulation of graphene growth by fluorine through spatially confined decomposition of metal fluorides. *Nat. Chem.* **2019**, *11*, 730−736.
(434) Huang, J. K.; Pu, J.; Hsu, C. L.; Chiu, M. H.; Juang, Z. Y.; Chang, Y. H.; Chang, W. H.; Iwasa, Y.; Takenobu, T.; Li, L. J. Large-area synthesis of highly crystalline $WSe_2$ monolayers and device applications. *ACS Nano* **2014**, *8*, 923−930.
(435) Wang, X.; Gong, Y.; Shi, G.; Chow, W. L.; Keyshar, K.; Ye, G.; Vajtai, R.; Lou, J.; Liu, Z.; Ringe, E.; et al. Chemical vapor deposition growth of crystalline monolayer $MoSe_2$. *ACS Nano* **2014**, *8*, 5125−5131.
(436) Chowdhury, S.; Roy, A.; Alam, M. H.; Pramanik, T.; Depoy, J.; Chrostowski, R.; Mangolini, F.; Akinwande, D.; Banerjee, S. K. Role of hydrogen in suppressing secondary nucleation in chemical vapor-deposited $MoS_2$. *ACS Appl. Electron. Mater.* **2022**, *4*, 6133−6141.
(437) Wan, Y.; Li, E.; Yu, Z.; Huang, J. K.; Li, M. Y.; Chou, A. S.; Lee, Y. T.; Lee, C. J.; Hsu, H. C.; Zhan, Q.; et al. Low-defect-density $WS_2$ by hydroxide vapor phase deposition. *Nat. Commun.* **2022**, *13*, 4149.
(438) Sassi, L. M.; Krishnamoorthy, A.; Hachtel, J. A.; Susarla, S.; Apte, A.; Castro-Pardo, S.; Ajnsztajn, A.; Vajtai, R.; Vashishta, P.; Tiwary, C. S.; et al. Low temperature CVD growth of $WSe_2$ enabled by moisture-assisted defects in the precursor powder. *2D Mater.* **2022**, *9*, No. 045026.
(439) Gong, Y.; Lin, Z.; Ye, G.; Shi, G.; Feng, S.; Lei, Y.; Elias, A. L.; Perea-Lopez, N.; Vajtai, R.; Terrones, H.; et al. Tellurium-assisted low-temperature synthesis of $MoS_2$ and $WS_2$ monolayers. *ACS Nano* **2015**, *9*, 11658−11666.
(440) Miakota, D. I.; Unocic, R. R.; Bertoldo, F.; Ghimire, G.; Engberg, S.; Geohegan, D.; Thygesen, K. S.; Canulescu, S. A facile strategy for the growth of high-quality tungsten disulfide crystals mediated by oxygen-deficient oxide precursors. *Nanoscale* **2022**, *14*, 9485−9497.
(441) Zhou, L.; Zubair, A.; Wang, Z.; Zhang, X.; Ouyang, F.; Xu, K.; Fang, W.; Ueno, K.; Li, J.; Palacios, T.; et al. Synthesis of high-quality large-area homogenous 1T' $MoTe_2$ from chemical vapor deposition. *Adv. Mater.* **2016**, *28*, 9526−9531.
(442) Zhan, Y.; Liu, Z.; Najmaei, S.; Ajayan, P. M.; Lou, J. Large-area vapor-phase growth and characterization of $MoS_2$ atomic layers on a $SiO_2$ substrate. *Small* **2012**, *8*, 966−971.
(443) Lin, Y. C.; Zhang, W.; Huang, J. K.; Liu, K. K.; Lee, Y. H.; Liang, C. T.; Chu, C. W.; Li, L. J. Wafer-scale $MoS_2$ thin layers prepared by $MoO_3$ sulfurization. *Nanoscale* **2012**, *4*, 6637−6641.
(444) Lee, Y.; Lee, J.; Bark, H.; Oh, I. K.; Ryu, G. H.; Lee, Z.; Kim, H.; Cho, J. H.; Ahn, J. H.; Lee, C. Synthesis of wafer-scale uniform molybdenum disulfide films with control over the layer number using a gas phase sulfur precursor. *Nanoscale* **2014**, *6*, 2821−2826.
(445) Shi, M. L.; Chen, L.; Zhang, T. B.; Xu, J.; Zhu, H.; Sun, Q. Q.; Zhang, D. W. Top-down integration of molybdenum disulfide transistors with wafer-scale uniformity and layer controllability. *Small* **2017**, *13*, 1603157.
(446) Wang, X.; Feng, H.; Wu, Y.; Jiao, L. Controlled synthesis of highly crystalline $MoS_2$ flakes by chemical vapor deposition. *J. Am. Chem. Soc.* **2013**, *135*, 5304−5307.
(447) Xue, Y.; Zhang, Y.; Liu, Y.; Liu, H.; Song, J.; Sophia, J.; Liu, J.; Xu, Z.; Xu, Q.; Wang, Z.; et al. Scalable production of a few-layer $MoS_2/WS_2$ vertical heterojunction array and its application for photodetectors. *ACS Nano* **2016**, *10*, 573−580.
(448) Park, J.; Kim, M. S.; Park, B.; Oh, S. H.; Roy, S.; Kim, J.; Choi, W. Composition-tunable synthesis of large-scale $Mo_{1-x}W_xS_2$ alloys with enhanced photoluminescence. *ACS Nano* **2018**, *12*, 6301−6309.
(449) Hynek, D. J.; Singhania, R. M.; Xu, S.; Davis, B.; Wang, L.; Yarali, M.; Pondick, J. V.; Woods, J. M.; Strandwitz, N. C.; Cha, J. J. $Cm^2$-scale synthesis of $MoTe_2$ thin films with large grains and layer control. *ACS Nano* **2021**, *15*, 410−418.
(450) Seok, H.; Megra, Y. T.; Kanade, C. K.; Cho, J.; Kanade, V. K.; Kim, M.; Lee, I.; Yoo, P. J.; Kim, H. U.; Suk, J. W.; et al. Low-temperature synthesis of wafer-scale $MoS_2$-$WS_2$ vertical hetero-structures by single-step penetrative plasma sulfurization. *ACS Nano* **2021**, *15*, 707−718.
(451) Song, I.; Park, C.; Hong, M.; Baik, J.; Shin, H. J.; Choi, H. C. Patternable large-scale molybdenium disulfide atomic layers grown by gold-assisted chemical vapor deposition. *Angew. Chem., Int. Ed.* **2014**, *53*, 1266−1269.
(452) Zhou, Z.; Hou, F.; Huang, X.; Wang, G.; Fu, Z.; Liu, W.; Yuan, G.; Xi, X.; Xu, J.; Lin, J.; et al. Stack growth of wafer-scale van der Waals superconductor heterostructures. *Nature* **2023**, *621*, 499−505.
(453) Tarasov, A.; Campbell, P. M.; Tsai, M.-Y.; Hesabi, Z. R.; Feirer, J.; Graham, S.; Ready, W. J.; Vogel, E. M. Highly uniform trilayer molybdenum disulfide for wafer-scale device fabrication. *Adv. Funct. Mater.* **2014**, *24*, 6389−6400.
(454) Xu, X.; Das, G.; He, X.; Hedhili, M. N.; Fabrizio, E. D.; Zhang, X.; Alshareef, H. N. High-performance monolayer $MoS_2$ films at the wafer scale by two-step growth. *Adv. Funct. Mater.* **2019**, *29*, 1901070.
(455) Tai, G.; Zeng, T.; Yu, J.; Zhou, J.; You, Y.; Wang, X.; Wu, H.; Sun, X.; Hu, T.; Guo, W. Fast and large-area growth of uniform $MoS_2$ monolayers on molybdenum foils. *Nanoscale* **2016**, *8*, 2234−2241.
(456) Xu, X.; Zhang, C.; Hota, M. K.; Liu, Z.; Zhang, X.; Alshareef, H. N. Enhanced quality of wafer-scale $MoS_2$ films by a capping layer annealing process. *Adv. Funct. Mater.* **2020**, *30*, 1908040.
(457) Xu, X.; Wang, Z.; Lopatin, S.; Quevedo-Lopez, M. A.; Alshareef, H. N. Wafer scale quasi single crystalline $MoS_2$ realized by epitaxial phase conversion. *2D Mater.* **2019**, *6*, No. 015030.
(458) Xu, X.; Smajic, J.; Li, K.; Min, J.-W.; Lei, Y.; Davaasuren, B.; He, X.; Zhang, X.; Ooi, B. S.; Costa, P. M. F. J.; Alshareef, H. N.


https://doi.org/10.1021/acs.chemrev.3c00851
Chem. Rev. XXXX, XXX, XXX−XXX

Lattice orientation heredity in the transformation of 2D epitaxial films. *Adv. Mater.* **2022**, *34*, 2105190.
(459) Yang, H.; Giri, A.; Moon, S.; Shin, S.; Myoung, J.-M.; Jeong, U. Highly scalable synthesis of $MoS_2$ thin films with precise thickness control via polymer-assisted deposition. *Chem. Mater.* **2017**, *29*, 5772−5776.
(460) Lim, Y. R.; Song, W.; Han, J. K.; Lee, Y. B.; Kim, S. J.; Myung, S.; Lee, S. S.; An, K. S.; Choi, C. J.; Lim, J. Wafer-scale, homogeneous $MoS_2$ layers on plastic substrates for flexible visible-light photodetectors. *Adv. Mater.* **2016**, *28*, 5025−5030.
(461) Li, W.; Xu, M.; Gao, J.; Zhang, X.; Huang, H.; Zhao, R.; Zhu, X.; Yang, Y.; Luo, L.; Chen, M.; et al. Large-scale ultra-robust $MoS_2$ patterns directly synthesized on polymer substrate for flexible sensing electronics. *Adv. Mater.* **2023**, *35*, 2207447.
(462) Baidoo, J. K.; Choi, S. H.; Agyapong-Fordjour, F. O.; Boandoh, S.; Yun, S. J.; Adofo, L. A.; Ben-Smith, A.; Kim, Y. I.; Jin, J. W.; Jung, M. H.; et al. Sequential growth of vertical transition-metal dichalcogenide heterostructures on rollable aluminum foil. *ACS Nano* **2022**, *16*, 8851−8859.
(463) Wells, R. A.; Johnson, H.; Lhermitte, C. R.; Kinge, S.; Sivula, K. Roll-to-roll deposition of semiconducting 2D nanoflake films of transition metal dichalcogenides for optoelectronic applications. *ACS Appl. Nano Mater.* **2019**, *2*, 7705−7712.
(464) Wan, X.; Miao, X.; Yao, J.; Wang, S.; Shao, F.; Xiao, S.; Zhan, R.; Chen, K.; Zeng, X.; Gu, X.; Xu, J. In situ ultrafast and patterned growth of transition metal dichalcogenides from inkjet-printed aqueous precursors. *Adv. Mater.* **2021**, *33*, 2100260.
(465) Park, S.; Lee, A.; Choi, K. H.; Hyeong, S. K.; Bae, S.; Hong, J. M.; Kim, T. W.; Hong, B. H.; Lee, S. K. Layer-selective synthesis of $MoS_2$ and $WS_2$ structures under ambient conditions for customized electronics. *ACS Nano* **2020**, *14*, 8485−8494.
(466) Cong, C.; Shang, J.; Wu, X.; Cao, B.; Peimyoo, N.; Qiu, C.; Sun, L.; Yu, T. Synthesis and optical properties of large-area single-crystalline 2D semiconductor $WS_2$ monolayer from chemical vapor deposition. *Adv. Opt. Mater.* **2014**, *2*, 131−136.
(467) Chen, K.; Chen, Z.; Wan, X.; Zheng, Z.; Xie, F.; Chen, W.; Gui, X.; Chen, H.; Xie, W.; Xu, J. A simple method for synthesis of high-quality millimeter-scale 1T' transition-metal telluride and near-field nanooptical properties. *Adv. Mater.* **2017**, *29*, 1700704.
(468) Xia, J.; Huang, X.; Liu, L. Z.; Wang, M.; Wang, L.; Huang, B.; Zhu, D. D.; Li, J. J.; Gu, C. Z.; Meng, X. M. CVD synthesis of large-area, highly crystalline $MoSe_2$ atomic layers on diverse substrates and application to photodetectors. *Nanoscale* **2014**, *6*, 8949−8955.
(469) Yu, Y.; Li, C.; Liu, Y.; Su, L.; Zhang, Y.; Cao, L. Controlled scalable synthesis of uniform, high-quality monolayer and few-layer $MoS_2$ films. *Sci. Rep.* **2013**, *3*, 1866.
(470) Lu, X.; Utama, M. I.; Lin, J.; Gong, X.; Zhang, J.; Zhao, Y.; Pantelides, S. T.; Wang, J.; Dong, Z.; Liu, Z.; et al. Large-area synthesis of monolayer and few-layer $MoSe_2$ films on $SiO_2$ substrates. *Nano Lett.* **2014**, *14*, 2419−2425.
(471) Shaw, J. C.; Zhou, H.; Chen, Y.; Weiss, N. O.; Liu, Y.; Huang, Y.; Duan, X. Chemical vapor deposition growth of monolayer $MoSe_2$ nanosheets. *Nano Res.* **2014**, *7*, 511−517.
(472) Zhou, J.; Liu, F.; Lin, J.; Huang, X.; Xia, J.; Zhang, B.; Zeng, Q.; Wang, H.; Zhu, C.; Niu, L.; et al. Large-area and high-quality 2D transition metal telluride. *Adv. Mater.* **2017**, *29*, 1603471.
(473) Zhou, J.; Kong, X.; Sekhar, M. C.; Lin, J.; Le Goualher, F.; Xu, R.; Wang, X.; Chen, Y.; Zhou, Y.; Zhu, C.; et al. Epitaxial synthesis of monolayer $PtSe_2$ single crystal on $MoSe_2$ with strong interlayer coupling. *ACS Nano* **2019**, *13*, 10929−10938.
(474) Zhang, J.; Yu, H.; Chen, W.; Tian, X.; Liu, D.; Cheng, M.; Xie, G.; Yang, W.; Yang, R.; Bai, X.; et al. Scalable growth of high-quality polycrystalline $MoS_2$ monolayers on $SiO_2$ with tunable grain sizes. *ACS Nano* **2014**, *8*, 6024−6030.
(475) Huang, J. K.; Pu, J.; Hsu, C. L.; Chiu, M. H.; Juang, Z. Y.; Chang, Y. H.; Chang, W. H.; Iwasa, Y.; Takenobu, T.; Li, L. J. Large-area synthesis of highly crystalline $WSe_2$ monolayers and device applications. *ACS Nano* **2014**, *8*, 923−930.
(476) Lan, C.; Zhou, Z.; Zhou, Z.; Li, C.; Shu, L.; Shen, L.; Li, D.; Dong, R.; Yip, S.; Ho, J. C. Wafer-scale synthesis of monolayer $WS_2$ for high-performance flexible photodetectors by enhanced chemical vapor deposition. *Nano Res.* **2018**, *11*, 3371−3384.
(477) Yu, H.; Liao, M.; Zhao, W.; Liu, G.; Zhou, X. J.; Wei, Z.; Xu, X.; Liu, K.; Hu, Z.; Deng, K.; et al. Wafer-scale growth and transfer of highly-oriented monolayer $MoS_2$ continuous films. *ACS Nano* **2017**, *11*, 12001−12007.
(478) Wang, S.; Rong, Y.; Fan, Y.; Pacios, M.; Bhaskaran, H.; He, K.; Warner, J. H. Shape evolution of monolayer $MoS_2$ crystals grown by chemical vapor deposition. *Chem. Mater.* **2014**, *26*, 6371−6379.
(479) Govind Rajan, A.; Warner, J. H.; Blankschtein, D.; Strano, M. S. Generalized mechanistic model for the chemical vapor deposition of 2D transition metal dichalcogenide monolayers. *ACS Nano* **2016**, *10*, 4330−4344.
(480) Wang, S.; Pacios, M.; Bhaskaran, H.; Warner, J. H. Substrate control for large area continuous films of monolayer $MoS_2$ by atmospheric pressure chemical vapor deposition. *Nanotechnology* **2016**, *27*, No. 085604.
(481) Feng, X.; Li, S.; Wong, S. L.; Tong, S.; Chen, L.; Zhang, P.; Wang, L.; Fong, X.; Chi, D.; Ang, K. W. Self-selective multi-terminal memtransistor crossbar array for in-memory computing. *ACS Nano* **2021**, *15*, 1764−1774.
(482) Wei, Z.; Sun, X.; Cai, Y.; Liang, Y.; Zhang, Z. Batch production of wafer-scale monolayer $MoS_2$. *Crystals* **2023**, *13*, 1275.
(483) Yu, H.; Huang, L.; Zhou, L.; Peng, Y.; Li, X.; Yin, P.; Zhao, J.; Zhu, M.; Wang, S.; Liu, J.; et al. Eight in. wafer-scale epitaxial monolayer $MoS_2$. *Adv. Mater.* **2024**, *36*, e2402855.
(484) Li, J.; Wang, S.; Li, L.; Wei, Z.; Wang, Q.; Sun, H.; Tian, J.; Guo, Y.; Liu, J.; Yu, H.; et al. Chemical vapor deposition of 4 in. wafer-scale monolayer $MoSe_2$. *Small Sci.* **2022**, *2*, 2200062.
(485) Yang, X.; Li, S.; Sakuma, Y. Highly efficient deposition of centimeter-scale $MoS_2$ monolayer film on dragontrail glass with large single-crystalline domains. *Small Methods* **2022**, *6*, 2201079.
(486) He, T.; Li, Y.; Zhou, Z.; Zeng, C.; Qiao, L.; Lan, C.; Yin, Y.; Li, C.; Liu, Y. Synthesis of large-area uniform $MoS_2$ films by substrate-moving atmospheric pressure chemical vapor deposition: From monolayer to multilayer. *2D Mater.* **2019**, *6*, No. 025030.
(487) Chiu, S.-K.; Huang, X.-Y.; Peng, C.-C.; Yang, Z.-C.; Cheng, Y.-Y.; Hu, S.-H.; Chiu, C.-L.; Chan, C.-W.; Chen, S.-H. Enhancing the photoluminescence of monolayer $MoS_2$ through gap-assisted synthesis at a wafer-scale. *J. Phys. Chem. C* **2022**, *126*, 11201−11208.
(488) Tang, P.; Shu, H.; Yang, M.; Zhang, M.; Sheng, C.; Liang, P.; Cao, D.; Chen, X. Rapid wafer-scale growth of $MoS_{2(1-x)}Se_{2x}$ alloy monolayers with tunable compositions and optical properties for high-performance photodetectors. *ACS Appl. Nano Mater.* **2021**, *4*, 12609−12618.
(489) Chen, J.; Zhao, X.; Grinblat, G.; Chen, Z.; Tan, S. J. R.; Fu, W.; Ding, Z.; Abdelwahab, I.; Li, Y.; Geng, D.; et al. Homoepitaxial growth of large-scale highly organized transition metal dichalcogenide patterns. *Adv. Mater.* **2018**, *30*, 1704674.
(490) Yang, P.; Zhang, Z.; Sun, M.; Lin, F.; Cheng, T.; Shi, J.; Xie, C.; Shi, Y.; Jiang, S.; Huan, Y.; et al. Thickness tunable wedding-cake-like $MoS_2$ flakes for high-performance optoelectronics. *ACS Nano* **2019**, *13*, 3649−3658.
(491) Alibakhshi, M. A.; Kang, X.; Clymer, D.; Zhang, Z.; Vargas, A.; Meunier, V.; Wanunu, M. Scaled-up synthesis of freestanding molybdenum disulfide membranes for nanopore sensing. *Adv. Mater.* **2023**, *35*, 2207089.
(492) Choi, H. J.; Jung, Y. S.; Lee, S. M.; Kang, S.; Seo, D.; Kim, H.; Choi, H.-J.; Lee, G.-H.; Cho, Y. S. Large-scale self-limiting synthesis of monolayer $MoS_2$ via proximity evaporation from mo films. *Cryst. Growth Des.* **2020**, *20*, 2698−2705.
(493) Withanage, S. S.; Kalita, H.; Chung, H. S.; Roy, T.; Jung, Y.; Khondaker, S. I. Uniform vapor-pressure-based chemical vapor deposition growth of $MoS_2$ using $MoO_3$ thin film as a precursor for coevaporation. *ACS Omega* **2018**, *3*, 18943−18949.
(494) Chen, J.; Shao, K.; Yang, W.; Tang, W.; Zhou, J.; He, Q.; Wu, Y.; Zhang, C.; Li, X.; Yang, X.; et al. Synthesis of wafer-scale

monolayer $WS_2$ crystals toward the application in integrated electronic devices. *ACS Appl. Mater. Interfaces* **2019**, *11*, 19381−19387.

(495) Wang, D.; Zhou, Y.; Zhang, H.; Zhang, R.; Dong, H.; Xu, R.; Cheng, Z.; He, Y.; Wang, Z. Wafer-scale growth of pristine and doped monolayer $MoS_2$ films for electronic device applications. *Inorg. Chem.* **2020**, *59*, 17356−17363.

(496) Yun, S. J.; Chae, S. H.; Kim, H.; Park, J. C.; Park, J. H.; Han, G. H.; Lee, J. S.; Kim, S. M.; Oh, H. M.; Seok, J.; et al. Synthesis of centimeter-scale monolayer tungsten disulfide film on gold foils. *ACS Nano* **2015**, *9*, 5510−5519.

(497) Lee, J.; Pak, S.; Giraud, P.; Lee, Y. W.; Cho, Y.; Hong, J.; Jang, A. R.; Chung, H. S.; Hong, W. K.; Jeong, H. Y.; et al. Thermodynamically stable synthesis of large-scale and highly crystalline transition metal dichalcogenide monolayers and their unipolar n-n heterojunction devices. *Adv. Mater.* **2017**, *29*, 1702206.

(498) Guo, J.; Peng, R.; Zhang, X.; Xin, Z.; Wang, E.; Wu, Y.; Li, C.; Fan, S.; Shi, R.; Liu, K. Perforated carbon nanotube film assisted growth of uniform monolayer $MoS_2$. *Small* **2023**, *19*, 2300766.

(499) Choudhury, T. H.; Simchi, H.; Boichot, R.; Chubarov, M.; Mohney, S. E.; Redwing, J. M. Chalcogen precursor effect on cold-wall gas-source chemical vapor deposition growth of $WS_2$. *Cryst. Growth Des.* **2018**, *18*, 4357−4364.

(500) Hofmann, W. K. Thin-films of molybdenum and tungsten disulfides by metal organic-chemical vapor-deposition. *J. Mater. Sci.* **1988**, *23*, 3981−3986.

(501) Kwon, J.; Seol, M.; Yoo, J.; Ryu, H.; Ko, D.-S.; Lee, M.-H.; Lee, E. K.; Yoo, M. S.; Lee, G.-H.; Shin, H.-J.; et al. 200-mm-wafer-scale integration of polycrystalline molybdenum disulfide transistors. *Nat. Electron.* **2024**, *7*, 356−364.

(502) Kim, T.; Mun, J.; Park, H.; Joung, D.; Diware, M.; Won, C.; Park, J.; Jeong, S. H.; Kang, S. W. Wafer-scale production of highly uniform two-dimensional $MoS_2$ by metal-organic chemical vapor deposition. *Nanotechnology* **2017**, *28*, 18LT01.

(503) Kim, T. S.; Dhakal, K. P.; Park, E.; Noh, G.; Chai, H. J.; Kim, Y.; Oh, S.; Kang, M.; Park, J.; Kim, J.; et al. Gas-phase alkali metal-assisted MOCVD growth of 2D transition metal dichalcogenides for large-scale precise nucleation control. *Small* **2022**, *18*, 2106368.

(504) Kim, H.; Ovchinnikov, D.; Deiana, D.; Unuchek, D.; Kis, A. Suppressing nucleation in metal-organic chemical vapor deposition of $MoS_2$ monolayers by alkali metal halides. *Nano Lett.* **2017**, *17*, 5056−5063.

(505) Zhang, K.; Bersch, B. M.; Zhang, F.; Briggs, N. C.; Subramanian, S.; Xu, K.; Chubarov, M.; Wang, K.; Lerach, J. O.; Redwing, J. M.; et al. Considerations for utilizing sodium chloride in epitaxial molybdenum disulfide. *ACS Appl. Mater. Interfaces* **2018**, *10*, 40831−40837.

(506) Zhang, X.; Choudhury, T. H.; Chubarov, M.; Xiang, Y.; Jariwala, B.; Zhang, F.; Alem, N.; Wang, G. C.; Robinson, J. A.; Redwing, J. M. Diffusion-controlled epitaxy of large area coalesced $WSe_2$ monolayers on sapphire. *Nano Lett.* **2018**, *18*, 1049−1056.

(507) Seol, M.; Lee, M. H.; Kim, H.; Shin, K. W.; Cho, Y.; Jeon, I.; Jeong, M.; Lee, H. I.; Park, J.; Shin, H. J. High-throughput growth of wafer-scale monolayer transition metal dichalcogenide via vertical ostwald ripening. *Adv. Mater.* **2020**, *32*, 2003542.

(508) Liu, M.; Liao, J.; Liu, Y.; Li, L.; Wen, R.; Hou, T.; Ji, R.; Wang, K.; Xing, Z.; Zheng, D.; et al. Periodical ripening for MOCVD growth of large 2D transition metal dichalcogenide domains. *Adv. Funct. Mater.* **2023**, *33*, 2212773.

(509) Cohen, A.; Patsha, A.; Mohapatra, P. K.; Kazes, M.; Ranganathan, K.; Houben, L.; Oron, D.; Ismach, A. Growth-etch metal-organic chemical vapor deposition approach of $WS_2$ atomic layers. *ACS Nano* **2021**, *15*, 526−538.

(510) Zhang, X.; Al Balushi, Z. Y.; Zhang, F.; Choudhury, T. H.; Eichfeld, S. M.; Alem, N.; Jackson, T. N.; Robinson, J. A.; Redwing, J. M. Influence of carbon in metalorganic chemical vapor deposition of few-layer $WSe_2$ thin films. *J. Electron. Mater.* **2016**, *45*, 6273−6279.

(511) Schaefer, C. M.; Caicedo Roque, J. M.; Sauthier, G.; Bousquet, J.; Hébert, C.; Sperling, J. R.; Pérez-Tomás, A.; Santiso, J.; del Corro, E.; Garrido, J. A. Carbon incorporation in MOCVD of $MoS_2$ thin films grown from an organosulfide precursor. *Chem. Mater.* **2021**, *33*, 4474−4487.

(512) Choi, S. H.; Stephen, B.; Park, J. H.; Lee, J. S.; Kim, S. M.; Yang, W.; Kim, K. K. Water-assisted synthesis of molybdenum disulfide film with single organic liquid precursor. *Sci. Rep.* **2017**, *7*, 1983.

(513) Lin, Y. C.; Jariwala, B.; Bersch, B. M.; Xu, K.; Nie, Y.; Wang, B.; Eichfeld, S. M.; Zhang, X.; Choudhury, T. H.; Pan, Y.; et al. Realizing large-scale, electronic-grade two-dimensional semiconductors. *ACS Nano* **2018**, *12*, 965−975.

(514) Mun, J.; Park, H.; Park, J.; Joung, D.; Lee, S.-K.; Leem, J.; Myoung, J.-M.; Park, J.; Jeong, S.-H.; Chegal, W.; et al. High-mobility $MoS_2$ directly grown on polymer substrate with kinetics-controlled metal-organic chemical vapor deposition. *ACS Appl. Electron. Mater.* **2019**, *1*, 608−616.

(515) Kozhakhmetov, A.; Nasr, J. R.; Zhang, F.; Xu, K.; Briggs, N. C.; Addou, R.; Wallace, R.; Fullerton-Shirey, S. K.; Terrones, M.; Das, S.; et al. Scalable BEOL compatible 2D tungsten diselenide. *2D Mater.* **2020**, *7*, No. 015029.

(516) Choi, J. H.; Ha, M. J.; Park, J. C.; Park, T. J.; Kim, W. H.; Lee, M. J.; Ahn, J. H. A strategy for wafer-scale crystalline $MoS_2$ thin films with controlled morphology using pulsed metal-organic chemical vapor deposition at low temperature. *Adv. Mater. Interfaces* **2022**, *9*, 2101785.

(517) Park, J. H.; Lu, A. Y.; Shen, P. C.; Shin, B. G.; Wang, H.; Mao, N.; Xu, R.; Jung, S. J.; Ham, D.; Kern, K.; et al. Synthesis of high-performance monolayer molybdenum disulfide at low temperature. *Small Methods* **2021**, *5*, 2000720.

(518) Hoang, A. T.; Hu, L.; Kim, B. J.; Van, T. T. N.; Park, K. D.; Jeong, Y.; Lee, K.; Ji, S.; Hong, J.; Katiyar, A. K.; et al. Low-temperature growth of $MoS_2$ on polymer and thin glass substrates for flexible electronics. *Nat. Nanotechnol.* **2023**, *18*, 1439−1447.

(519) Wu, T.; Zhang, X.; Yuan, Q.; Xue, J.; Lu, G.; Liu, Z.; Wang, H.; Wang, H.; Ding, F.; Yu, Q.; et al. Fast growth of inch-sized single-crystalline graphene from a controlled single nucleus on Cu-Ni alloys. *Nat. Mater.* **2016**, *15*, 43−47.

(520) Rong, Y.; Fan, Y.; Leen Koh, A.; Robertson, A. W.; He, K.; Wang, S.; Tan, H.; Sinclair, R.; Warner, J. H. Controlling sulphur precursor addition for large single crystal domains of $WS_2$. *Nanoscale* **2014**, *6*, 12096−12103.

(521) Chen, J.; Liu, B.; Liu, Y.; Tang, W.; Nai, C. T.; Li, L.; Zheng, J.; Gao, L.; Zheng, Y.; Shin, H. S.; et al. Chemical vapor deposition of large-sized hexagonal $WSe_2$ crystals on dielectric substrates. *Adv. Mater.* **2015**, *27*, 6722−6727.

(522) Zhang, S.; Pang, J.; Cheng, Q.; Yang, F.; Chen, Y.; Liu, Y.; Li, Y.; Gemming, T.; Liu, X.; Ibarlucea, B.; et al. High-performance electronics and optoelectronics of monolayer tungsten diselenide full film from pre-seeding strategy. *InfoMat* **2021**, *3*, 1455−1469.

(523) Chen, J.; Tang, W.; Tian, B.; Liu, B.; Zhao, X.; Liu, Y.; Ren, T.; Liu, W.; Geng, D.; Jeong, H. Y.; et al. Chemical vapor deposition of high-quality large-sized $MoS_2$ crystals on silicon dioxide substrates. *Adv. Sci.* **2016**, *3*, 1500033.

(524) Gong, Y.; Ye, G.; Lei, S.; Shi, G.; He, Y.; Lin, J.; Zhang, X.; Vajtai, R.; Pantelides, S. T.; Zhou, W.; et al. Synthesis of millimeter-scale transition metal dichalcogenides single crystals. *Adv. Funct. Mater.* **2016**, *26*, 2009−2015.

(525) Chen, W.; Zhao, J.; Zhang, J.; Gu, L.; Yang, Z.; Li, X.; Yu, H.; Zhu, X.; Yang, R.; Shi, D.; et al. Oxygen-assisted chemical vapor deposition growth of large single-crystal and high-quality monolayer $MoS_2$. *J. Am. Chem. Soc.* **2015**, *137*, 15632−15635.

(526) Xin, X.; Zhang, Y.; Chen, J.; Chen, M. L.; Xin, W.; Ding, M.; Bao, Y.; Liu, W.; Xu, H.; Liu, Y. Defect-suppressed submillimeter-scale $WS_2$ single crystals with high photoluminescence quantum yields by alternate-growth-etching CVD. *Mater. Horiz.* **2022**, *9*, 2416−2424.

(527) Chang, M. C.; Ho, P. H.; Tseng, M. F.; Lin, F. Y.; Hou, C. H.; Lin, I. K.; Wang, H.; Huang, P. P.; Chiang, C. H.; Yang, Y. C.; et al. Fast growth of large-grain and continuous $MoS_2$ films through a self-capping vapor-liquid-solid method. *Nat. Commun.* **2020**, *11*, 3682.

(528) Suzuki, H.; Hashimoto, R.; Misawa, M.; Liu, Y.; Kishibuchi, M.; Ishimura, K.; Tsuruta, K.; Miyata, Y.; Hayashi, Y. Surface diffusion-limited growth of large and high-quality monolayer transition metal dichalcogenides in confined space of microreactor. *ACS Nano* **2022**, *16*, 11360−11373.
(529) Park, J. C.; Yun, S. J.; Kim, H.; Park, J. H.; Chae, S. H.; An, S. J.; Kim, J. G.; Kim, S. M.; Kim, K. K.; Lee, Y. H. Phase-engineered synthesis of centimeter-scale 1T'- and 2H-molybdenum ditelluride thin films. *ACS Nano* **2015**, *9*, 6548−6554.
(530) Zhou, L.; Xu, K.; Zubair, A.; Liao, A. D.; Fang, W.; Ouyang, F.; Lee, Y. H.; Ueno, K.; Saito, R.; Palacios, T.; et al. Large-area synthesis of high-quality uniform few-layer $MoTe_2$. *J. Am. Chem. Soc.* **2015**, *137*, 11892−11895.
(531) Duerloo, K. A.; Li, Y.; Reed, E. J. Structural phase transitions in two-dimensional Mo- and W-dichalcogenide monolayers. *Nat. Commun.* **2014**, *5*, 4214.
(532) Xu, X.; Chen, S.; Liu, S.; Cheng, X.; Xu, W.; Li, P.; Wan, Y.; Yang, S.; Gong, W.; Yuan, K.; et al. Millimeter-scale single-crystalline semiconducting $MoTe_2$ via solid-to-solid phase transformation. *J. Am. Chem. Soc.* **2019**, *141*, 2128−2134.
(533) Xu, X.; Pan, Y.; Liu, S.; Han, B.; Gu, P.; Li, S.; Xu, W.; Peng, Y.; Han, Z.; Chen, J.; et al. Seeded 2D epitaxy of large-area single-crystal films of the van der Waals semiconductor 2H $MoTe_2$. *Science* **2021**, *372*, 195−200.
(534) Pan, Y.; Song, Y.; Wang, Q.; Wang, T.; Li, Y.; Xu, W.; Ye, Y. Direct multitier synthesis of two-dimensional semiconductor 2H-$MoTe_2$. *ACS Appl. Electron. Mater.* **2022**, *4*, 5733−5738.
(535) Xu, X.; Liu, S.; Han, B.; Han, Y.; Yuan, K.; Xu, W.; Yao, X.; Li, P.; Yang, S.; Gong, W.; et al. Scaling-up atomically thin coplanar semiconductor-metal circuitry via phase engineered chemical assembly. *Nano Lett.* **2019**, *19*, 6845−6852.
(536) Pan, Y.; Guzman, R.; Li, S.; Xu, W.; Li, Y.; Tang, N.; Yin, H.; He, J.; Wu, A.; Chen, J.; et al. Heteroepitaxy of semiconducting 2H-$MoTe_2$ thin films on arbitrary surfaces for large-scale heterogeneous integration. *Nat. Synth.* **2022**, *1*, 701−708.
(537) Su, J.; Wang, M.; Li, Y.; Wang, F.; Chen, Q.; Luo, P.; Han, J.; Wang, S.; Li, H.; Zhai, T. Sub-millimeter-scale monolayer p-type H-Phase $VS_2$. *Adv. Funct. Mater.* **2020**, *30*, 2000240.
(538) Dong, J.; Zhang, L.; Dai, X.; Ding, F. The epitaxy of 2D materials growth. *Nat. Commun.* **2020**, *11*, 5862.
(539) Koma, A.; Sunouchi, K.; Miyajima, T. Fabrication and characterization of heterostructures with subnanometer thickness. *Microelectron. Eng.* **1984**, *2*, 129−136.
(540) Koma, A. Van der Waals epitaxy for highly lattice-mismatched systems. *J. Cryst. Growth* **1999**, *201*, 236−241.
(541) Robinson, J. A. Growing vertical in the flatland. *ACS Nano* **2016**, *10*, 42−45.
(542) Wang, S.; Wang, X.; Warner, J. H. All chemical vapor deposition growth of $MoS_2$:h-BN vertical van der Waals heterostructures. *ACS Nano* **2015**, *9*, 5246−5254.
(543) Shi, Y.; Zhou, W.; Lu, A. Y.; Fang, W.; Lee, Y. H.; Hsu, A. L.; Kim, S. M.; Kim, K. K.; Yang, H. Y.; Li, L. J.; et al. Van der Waals epitaxy of $MoS_2$ layers using graphene as growth templates. *Nano Lett.* **2012**, *12*, 2784−2791.
(544) Ge, W.; Kawahara, K.; Tsuji, M.; Ago, H. Large-scale synthesis of $NbS_2$ nanosheets with controlled orientation on graphene by ambient pressure CVD. *Nanoscale* **2013**, *5*, 5773−5778.
(545) McCreary, K. M.; Hanbicki, A. T.; Robinson, J. T.; Cobas, E.; Culbertson, J. C.; Friedman, A. L.; Jernigan, G. G.; Jonker, B. T. Large-area synthesis of continuous and uniform $MoS_2$ monolayer films on graphene. *Adv. Funct. Mater.* **2014**, *24*, 6449−6454.
(546) Lin, Y. C.; Lu, N.; Perea-Lopez, N.; Li, J.; Lin, Z.; Peng, X.; Lee, C. H.; Sun, C.; Calderin, L.; Browning, P. N.; et al. Direct synthesis of van der Waals solids. *ACS Nano* **2014**, *8*, 3715−3723.
(547) Rossi, A.; Büch, H.; Di Rienzo, C.; Miseikis, V.; Convertino, D.; Al-Temimy, A.; Voliani, V.; Gemmi, M.; Piazza, V.; Coletti, C. Scalable synthesis of $WS_2$ on graphene and h-BN: An all-2D platform for light-matter transduction. *2D Mater.* **2016**, *3*, No. 031013.
(548) Piccinini, G.; Forti, S.; Martini, L.; Pezzini, S.; Miseikis, V.; Starke, U.; Fabbri, F.; Coletti, C. Deterministic direct growth of $WS_2$ on CVD graphene arrays. *2D Mater.* **2020**, *7*, No. 014002.
(549) Lin, Y. C.; Chang, C. Y.; Ghosh, R. K.; Li, J.; Zhu, H.; Addou, R.; Diaconescu, B.; Ohta, T.; Peng, X.; Lu, N.; et al. Atomically thin heterostructures based on single-layer tungsten diselenide and graphene. *Nano Lett.* **2014**, *14*, 6936−6941.
(550) Ago, H.; Endo, H.; Solis-Fernandez, P.; Takizawa, R.; Ohta, Y.; Fujita, Y.; Yamamoto, K.; Tsuji, M. Controlled van der Waals epitaxy of monolayer $MoS_2$ triangular domains on graphene. *ACS Appl. Mater. Interfaces* **2015**, *7*, 5265−5273.
(551) Forti, S.; Rossi, A.; Buch, H.; Cavallucci, T.; Bisio, F.; Sala, A.; Mentes, T. O.; Locatelli, A.; Magnozzi, M.; Canepa, M.; et al. Electronic properties of single-layer tungsten disulfide on epitaxial graphene on silicon carbide. *Nanoscale* **2017**, *9*, 16412−16419.
(552) Liu, X.; Balla, I.; Bergeron, H.; Campbell, G. P.; Bedzyk, M. J.; Hersam, M. C. Rotationally commensurate growth of $MoS_2$ on epitaxial graphene. *ACS Nano* **2016**, *10*, 1067−1075.
(553) Azizi, A.; Eichfeld, S.; Geschwind, G.; Zhang, K.; Jiang, B.; Mukherjee, D.; Hossain, L.; Piasecki, A. F.; Kabius, B.; Robinson, J. A.; et al. Freestanding van der Waals heterostructures of graphene and transition metal dichalcogenides. *ACS Nano* **2015**, *9*, 4882−4890.
(554) Bianco, G. V.; Losurdo, M.; Giangregorio, M. M.; Sacchetti, A.; Prete, P.; Lovergine, N.; Capezzuto, P.; Bruno, G. Direct epitaxial CVD synthesis of tungsten disulfide on epitaxial and CVD graphene. *RSC Adv.* **2015**, *5*, 98700−98708.
(555) Kim, J. H.; Kim, S. Y.; Cho, Y.; Park, H. J.; Shin, H. J.; Kwon, S. Y.; Lee, Z. Interface-driven partial dislocation formation in 2D heterostructures. *Adv. Mater.* **2019**, *31*, 1807486.
(556) Bachu, S.; Kowalik, M.; Huet, B.; Nayir, N.; Dwivedi, S.; Hickey, D. R.; Qian, C.; Snyder, D. W.; Rotkin, S. V.; Redwing, J. M.; et al. Role of bilayer graphene microstructure on the nucleation of $WSe_2$ overlayers. *ACS Nano* **2023**, *17*, 12140−12150.
(557) Miwa, J. A.; Dendzik, M.; Grønborg, S. S.; Bianchi, M.; Lauritsen, J. V.; Hofmann, P.; Ulstrup, Sør. Van der Waals epitaxy of two-dimensional $MoS_2$-graphene heterostructures in ultrahigh vacuum. *ACS Nano* **2015**, *9*, 6502−6510.
(558) Kobayashi, Y.; Sasaki, S.; Mori, S.; Hibino, H.; Liu, Z.; Watanabe, K.; Taniguchi, T.; Suenaga, K.; Maniwa, Y.; Miyata, Y. Growth and optical properties of high-quality monolayer $WS_2$ on graphite. *ACS Nano* **2015**, *9*, 4056−4063.
(559) Hoang, A. T.; Katiyar, A. K.; Shin, H.; Mishra, N.; Forti, S.; Coletti, C.; Ahn, J. H. Epitaxial growth of wafer-scale molybdenum disulfide/graphene heterostructures by metal-organic vapor-phase epitaxy and their application in photodetectors. *ACS Appl. Mater. Interfaces* **2020**, *12*, 44335−44344.
(560) Cui, X.; Lee, G. H.; Kim, Y. D.; Arefe, G.; Huang, P. Y.; Lee, C. H.; Chenet, D. A.; Zhang, X.; Wang, L.; Ye, F.; et al. Multi-terminal transport measurements of $MoS_2$ using a van der Waals heterostructure device platform. *Nat. Nanotechnol.* **2015**, *10*, 534−540.
(561) Pacuski, W.; Grzeszczyk, M.; Nogajewski, K.; Bogucki, A.; Oreszczuk, K.; Kucharek, J.; Polczynska, K. E.; Seredynski, B.; Rodek, A.; Bozek, R.; et al. Narrow excitonic lines and large-scale homogeneity of transition-metal dichalcogenide monolayers grown by molecular beam epitaxy on hexagonal boron nitride. *Nano Lett.* **2020**, *20*, 3058−3066.
(562) Okada, M.; Sawazaki, T.; Watanabe, K.; Taniguch, T.; Hibino, H.; Shinohara, H.; Kitaura, R. Direct chemical vapor deposition growth of $WS_2$ atomic layers on hexagonal boron nitride. *ACS Nano* **2014**, *8*, 8273−8277.
(563) Yan, A.; Velasco, J., Jr.; Kahn, S.; Watanabe, K.; Taniguchi, T.; Wang, F.; Crommie, M. F.; Zettl, A. Direct growth of single- and few-layer $MoS_2$ on h-BN with preferred relative rotation angles. *Nano Lett.* **2015**, *15*, 6324−6331.
(564) Yu, H.; Yang, Z.; Du, L.; Zhang, J.; Shi, J.; Chen, W.; Chen, P.; Liao, M.; Zhao, J.; Meng, J.; et al. Precisely aligned monolayer $MoS_2$ epitaxially grown on h-BN basal plane. *Small* **2017**, *13*, 1603005.
(565) Poh, S. M.; Zhao, X.; Tan, S. J. R.; Fu, D.; Fei, W.; Chu, L.; Jiadong, D.; Zhou, W.; Pennycook, S. J.; Castro Neto, A. H.; et al.

Molecular beam epitaxy of highly crystalline $MoSe_2$ on hexagonal boron nitride. *ACS Nano* **2018**, *12*, 7562−7570.
(566) Hotta, T.; Tokuda, T.; Zhao, S.; Watanabe, K.; Taniguchi, T.; Shinohara, H.; Kitaura, R. Molecular beam epitaxy growth of monolayer niobium diselenide flakes. *Appl. Phys. Lett.* **2016**, *109*, 133101.
(567) Zhang, X.; Zhang, F.; Wang, Y.; Schulman, D. S.; Zhang, T.; Bansal, A.; Alem, N.; Das, S.; Crespi, V. H.; Terrones, M.; et al. Defect-controlled nucleation and orientation of $WSe_2$ on hBN: A route to single-crystal epitaxial monolayers. *ACS Nano* **2019**, *13*, 3341−3352.
(568) Zhang, F.; Wang, Y.; Erb, C.; Wang, K.; Moradifar, P.; Crespi, V. H.; Alem, N. Full orientation control of epitaxial $MoS_2$ on hBN assisted by substrate defects. *Phys. Rev. B* **2019**, *99*, 155430.
(569) Fu, D.; Zhao, X.; Zhang, Y. Y.; Li, L.; Xu, H.; Jang, A. R.; Yoon, S. I.; Song, P.; Poh, S. M.; Ren, T.; et al. Molecular beam epitaxy of highly crystalline monolayer molybdenum disulfide on hexagonal boron nitride. *J. Am. Chem. Soc.* **2017**, *139*, 9392−9400.
(570) Zhang, Z.; Ji, X.; Shi, J.; Zhou, X.; Zhang, S.; Hou, Y.; Qi, Y.; Fang, Q.; Ji, Q.; Zhang, Y.; et al. Direct chemical vapor deposition growth and band-gap characterization of $MoS_2$/h-BN van der Waals heterostructures on Au foils. *ACS Nano* **2017**, *11*, 4328−4336.
(571) Fu, L.; Sun, Y.; Wu, N.; Mendes, R. G.; Chen, L.; Xu, Z.; Zhang, T.; Rummeli, M. H.; Rellinghaus, B.; Pohl, D.; et al. Direct growth of $MoS_2$/h-BN heterostructures via a sulfide-resistant alloy. *ACS Nano* **2016**, *10*, 2063−2070.
(572) Ludwiczak, K.; Da Browska, A. K.; Binder, J.; Tokarczyk, M.; Iwanski, J.; Kurowska, B.; Turczynski, J.; Kowalski, G.; Bozek, R.; Stepniewski, R.; et al. Heteroepitaxial growth of high optical quality, wafer-scale van der Waals heterostrucutres. *ACS Appl. Mater. Interfaces* **2021**, *13*, 47904−47911.
(573) Huang, J.; Chen, J.; Meng, J.; Zhang, S.; Jiang, J.; Li, J.; Zeng, L.; Yin, Z.; Wu, J.; Zhang, X. Remote heteroepitaxy of transition metal dichalcogenides through monolayer hexagonal boron nitride. *Nano Res.* **2024**, *17*, 3224.
(574) Lee, J. S.; Choi, S. H.; Yun, S. J.; Kim, Y. I.; Boandoh, S.; Park, J. H.; Shin, B. G.; Ko, H.; Lee, S. H.; Kim, Y. M.; et al. Wafer-scale single-crystal hexagonal boron nitride film via self-collimated grain formation. *Science* **2018**, *362*, 817−821.
(575) Zhang, X.; Meng, F.; Christianson, J. R.; Arroyo-Torres, C.; Lukowski, M. A.; Liang, D.; Schmidt, J. R.; Jin, S. Vertical heterostructures of layered metal chalcogenides by van der Waals epitaxy. *Nano Lett.* **2014**, *14*, 3047−3054.
(576) Yoo, Y.; Degregorio, Z. P.; Johns, J. E. Seed crystal homogeneity controls lateral and vertical heteroepitaxy of monolayer $MoS_2$ and $WS_2$. *J. Am. Chem. Soc.* **2015**, *137*, 14281−14287.
(577) Zhang, J.; Wang, J.; Chen, P.; Sun, Y.; Wu, S.; Jia, Z.; Lu, X.; Yu, H.; Chen, W.; Zhu, J.; et al. Observation of strong interlayer coupling in $MoS_2$/$WS_2$ heterostructures. *Adv. Mater.* **2016**, *28*, 1950−1956.
(578) Wu, R.; Tao, Q.; Dang, W.; Liu, Y.; Li, B.; Li, J.; Zhao, B.; Zhang, Z.; Ma, H.; Sun, G.; et al. Van der Waals epitaxial growth of atomically thin 2D metals on dangling-bond-free $WSe_2$ and $WS_2$. *Adv. Funct. Mater.* **2019**, *29*, 1806611.
(579) Ji, Q.; Zhang, Y.; Gao, T.; Zhang, Y.; Ma, D.; Liu, M.; Chen, Y.; Qiao, X.; Tan, P. H.; Kan, M.; et al. Epitaxial monolayer $MoS_2$ on mica with novel photoluminescence. *Nano Lett.* **2013**, *13*, 3870−3877.
(580) Cui, F.; Wang, C.; Li, X.; Wang, G.; Liu, K.; Yang, Z.; Feng, Q.; Liang, X.; Zhang, Z.; Liu, S.; et al. Tellurium-assisted epitaxial growth of large-area, highly crystalline $ReS_2$ atomic layers on mica substrate. *Adv. Mater.* **2016**, *28*, 5019−5024.
(581) Ueno, K.; Saiki, K.; Shimada, T.; Koma, A. Epitaxial growth of transition metal dichalcogenides on cleaved faces of mica. *Journal of Vacuum Science & Technology A: Vacuum, Surfaces, and Films* **1990**, *8*, 68−72.
(582) Wang, P.; Ge, J.; Luo, J.; Wang, H.; Song, L.; Li, Z.; Yang, J.; Wang, Y.; Du, R.; Feng, W.; et al. Interisland-distance-mediated growth of centimeter-scale two-dimensional magnetic $Fe_3O_4$ arrays with unidirectional domain orientations. *Nano Lett.* **2023**, *23*, 1758−1766.
(583) Wu, M.; Zhang, Z.; Xu, X.; Zhang, Z.; Duan, Y.; Dong, J.; Qiao, R.; You, S.; Wang, L.; Qi, J.; et al. Seeded growth of large single-crystal copper foils with high-index facets. *Nature* **2020**, *581*, 406−410.
(584) Xu, X.; Zhang, Z.; Dong, J.; Yi, D.; Niu, J.; Wu, M.; Lin, L.; Yin, R.; Li, M.; Zhou, J.; et al. Ultrafast epitaxial growth of metre-sized single-crystal graphene on industrial Cu foil. *Sci. Bull.* **2017**, *62*, 1074−1080.
(585) Wang, L.; Xu, X.; Zhang, L.; Qiao, R.; Wu, M.; Wang, Z.; Zhang, S.; Liang, J.; Zhang, Z.; Zhang, Z.; et al. Epitaxial growth of a 100-square-centimetre single-crystal hexagonal boron nitride monolayer on copper. *Nature* **2019**, *570*, 91−95.
(586) Bets, K. V.; Gupta, N.; Yakobson, B. I. How the complementarity at vicinal steps enables growth of 2D monocrystals. *Nano Lett.* **2019**, *19*, 2027−2031.
(587) Helveg, S.; Lauritsen, J. V.; Lægsgaard, E.; Stensgaard, I.; Nørskov, J. K.; Clausen, B. S.; Topsøe, H.; Besenbacher, F. Atomic-scale structure of single-layer $MoS_2$ nanoclusters. *Phys. Rev. Lett.* **2000**, *84*, 951−954.
(588) Bollinger, M. V.; Lauritsen, J. V.; Jacobsen, K. W.; Norskov, J. K.; Helveg, S.; Besenbacher, F. One-dimensional metallic edge states in $MoS_2$. *Phys. Rev. Lett.* **2001**, *87*, 196803.
(589) Shi, J.; Ma, D.; Han, G. F.; Zhang, Y.; Ji, Q.; Gao, T.; Sun, J.; Song, X.; Li, C.; Zhang, Y.; et al. Controllable growth and transfer of monolayer $MoS_2$ on Au foils and its potential application in hydrogen evolution reaction. *ACS Nano* **2014**, *8*, 10196−10204.
(590) Shi, J.; Yang, Y.; Zhang, Y.; Ma, D.; Wei, W.; Ji, Q.; Zhang, Y.; Song, X.; Gao, T.; Li, C.; et al. Monolayer $MoS_2$ growth on Au foils and on-site domain boundary imaging. *Adv. Funct. Mater.* **2015**, *25*, 842−849.
(591) Shi, J.; Zhang, X.; Ma, D.; Zhu, J.; Zhang, Y.; Guo, Z.; Yao, Y.; Ji, Q.; Song, X.; Zhang, Y.; et al. Substrate facet effect on the growth of monolayer $MoS_2$ on Au foils. *ACS Nano* **2015**, *9*, 4017−4025.
(592) Zhang, Y.; Shi, J.; Han, G.; Li, M.; Ji, Q.; Ma, D.; Zhang, Y.; Li, C.; Lang, X.; Zhang, Y.; et al. Chemical vapor deposition of monolayer $WS_2$ nanosheets on Au foils toward direct application in hydrogen evolution. *Nano Res.* **2015**, *8*, 2881−2890.
(593) Zhang, T.; Jiang, B.; Xu, Z.; Mendes, R. G.; Xiao, Y.; Chen, L.; Fang, L.; Gemming, T.; Chen, S.; Rummeli, M. H.; Fu, L. Twinned growth behaviour of two-dimensional materials. *Nat. Commun.* **2016**, *7*, 13911.
(594) Lu, J.; Bao, D. L.; Qian, K.; Zhang, S.; Chen, H.; Lin, X.; Du, S. X.; Gao, H. J. Identifying and visualizing the edge terminations of single-layer $MoSe_2$ island epitaxially grown on Au(111). *ACS Nano* **2017**, *11*, 1689−1695.
(595) Pan, S.; Yang, P.; Zhu, L.; Hong, M.; Xie, C.; Zhou, F.; Shi, Y.; Huan, Y.; Cui, F.; Zhang, Y. Effect of substrate symmetry on the orientations of $MoS_2$ monolayers. *Nanotechnology* **2021**, *32*, No. 095601.
(596) Li, J.; Wang, S.; Jiang, Q.; Qian, H.; Hu, S.; Kang, H.; Chen, C.; Zhan, X.; Yu, A.; Zhao, S.; et al. Single-crystal $MoS_2$ monolayer wafer grown on Au(111) film substrates. *Small* **2021**, *17*, 2100743.
(597) Ding, D.; Wang, S.; Xia, Y.; Li, P.; He, D.; Zhang, J.; Zhao, S.; Yu, G.; Zheng, Y.; Cheng, Y.; et al. Atomistic insight into the epitaxial growth mechanism of single-crystal two-dimensional transition-metal dichalcogenides on Au(111) substrate. *ACS Nano* **2022**, *16*, 17356−17364.
(598) Xia, Y.; Ding, D.; Xiao, K.; Zhang, J.; Xu, S.; He, D.; Yue, X.; Rao, Q.; Wang, X.; Ding, S.; et al. Wafer-scale single-crystalline $MoSe_2$ and $WSe_2$ monolayers grown by molecular-beam epitaxy at low-temperature—the role of island-substrate interaction and surface steps. *Nat. Sci.* **2023**, *3*, 20220059.
(599) Choi, S. H.; Kim, H. J.; Song, B.; Kim, Y. I.; Han, G.; Nguyen, H. T. T.; Ko, H.; Boandoh, S.; Choi, J. H.; Oh, C. S.; et al. Epitaxial single-crystal growth of transition metal dichalcogenide monolayers via the atomic sawtooth Au surface. *Adv. Mater.* **2021**, *33*, 2006601.

(600) Hu, J.; Quan, W.; Yang, P.; Cui, F.; Liu, F.; Zhu, L.; Pan, S.; Huan, Y.; Zhou, F.; Fu, J.; et al. Epitaxial growth of high-quality monolayer $MoS_2$ single crystals on low-symmetry vicinal Au(101) facets with different miller indices. *ACS Nano* **2023**, *17*, 312−321.
(601) Yang, P.; Wang, D.; Zhao, X.; Quan, W.; Jiang, Q.; Li, X.; Tang, B.; Hu, J.; Zhu, L.; Pan, S.; et al. Epitaxial growth of inch-scale single-crystal transition metal dichalcogenides through the patching of unidirectionally orientated ribbons. *Nat. Commun.* **2022**, *13*, 3238.
(602) Amano, H.; Sawaki, N.; Akasaki, I.; Toyoda, Y. Metalorganic vapor phase epitaxial growth of a high quality GaN film using an aln buffer layer. *Appl. Phys. Lett.* **1986**, *48*, 353−355.
(603) Zhang, Y.; Zhang, Y.; Ji, Q.; Ju, J.; Yuan, H.; Shi, J.; Gao, T.; Ma, D.; Liu, M.; Chen, Y.; et al. Controlled growth of high-quality monolayer $WS_2$ layers on sapphire and imaging its grain boundary. *ACS Nano* **2013**, *7*, 8963−8971.
(604) Ji, Q.; Kan, M.; Zhang, Y.; Guo, Y.; Ma, D.; Shi, J.; Sun, Q.; Chen, Q.; Zhang, Y.; Liu, Z. Unravelling orientation distribution and merging behavior of monolayer $MoS_2$ domains on sapphire. *Nano Lett.* **2015**, *15*, 198−205.
(605) Dumcenco, D.; Ovchinnikov, D.; Marinov, K.; Lazic, P.; Gibertini, M.; Marzari, N.; Lopez Sanchez, O.; Kung, Y. C.; Krasnozhon, D.; Chen, M. W.; et al. Large-area epitaxial monolayer $MoS_2$. *ACS Nano* **2015**, *9*, 4611−4620.
(606) Aljarb, A.; Cao, Z.; Tang, H. L.; Huang, J. K.; Li, M.; Hu, W.; Cavallo, L.; Li, L. J. Substrate lattice-guided seed formation controls the orientation of 2D transition-metal dichalcogenides. *ACS Nano* **2017**, *11*, 9215−9222.
(607) Suenaga, K.; Ji, H. G.; Lin, Y. C.; Vincent, T.; Maruyama, M.; Aji, A. S.; Shiratsuchi, Y.; Ding, D.; Kawahara, K.; Okada, S.; et al. Surface-mediated aligned growth of monolayer $MoS_2$ and in-plane heterostructures with graphene on sapphire. *ACS Nano* **2018**, *12*, 10032−10044.
(608) Lai, Y.-Y.; Chuang, C.-H.; Yeh, Y.-W.; Hou, C.-H.; Hsu, S.-C.; Chou, Y.; Chou, Y.-C.; Kuo, H.-C.; Wu, Y. S.; Cheng, Y.-J. Substrate lattice-guided $MoS_2$ crystal growth: Implications for van der Waals epitaxy. *ACS Appl. Nano Mater.* **2021**, *4*, 4930−4938.
(609) Ji, H. G.; Lin, Y.-C.; Nagashio, K.; Maruyama, M.; Solís-Fernández, P.; Sukma Aji, A.; Panchal, V.; Okada, S.; Suenaga, K.; Ago, H. Hydrogen-assisted epitaxial growth of monolayer tungsten disulfide and seamless grain stitching. *Chem. Mater.* **2018**, *30*, 403−411.
(610) Park, Y.; Ahn, C.; Ahn, J. G.; Kim, J. H.; Jung, J.; Oh, J.; Ryu, S.; Kim, S.; Kim, S. C.; Kim, T.; et al. Critical role of surface termination of sapphire substrates in crystallographic epitaxial growth of $MoS_2$ using inorganic molecular precursors. *ACS Nano* **2023**, *17*, 1196−1205.
(611) Koma, A.; Saiki, K.; Sato, Y. Heteroepitaxy of a two-dimensional material on a three-dimensional material. *Appl. Surf. Sci.* **1990**, *41*−*42*, 451−456.
(612) Mortelmans, W.; De Smet, K.; Meng, R.; Houssa, M.; De Gendt, S.; Heyns, M.; Merckling, C. Role of stronger interlayer van der Waals coupling in twin-free molecular beam epitaxy of 2D chalcogenides. *Adv. Mater. Interfaces* **2021**, *8*, 2100438.
(613) Cohen, A.; Mohapatra, P. K.; Hettler, S.; Patsha, A.; Narayanachari, K.; Shekhter, P.; Cavin, J.; Rondinelli, J. M.; Bedzyk, M.; Dieguez, O.; et al. Tungsten oxide mediated quasi-van der Waals epitaxy of $WS_2$ on sapphire. *ACS Nano* **2023**, *17*, 5399−5411.
(614) Ma, Z.; Wang, S.; Deng, Q.; Hou, Z.; Zhou, X.; Li, X.; Cui, F.; Si, H.; Zhai, T.; Xu, H. Epitaxial growth of rectangle shape $MoS_2$ with highly aligned orientation on twofold symmetry a-plane sapphire. *Small* **2020**, *16*, 2000596.
(615) Shi, Y.; Groven, B.; Serron, J.; Wu, X.; Nalin Mehta, A.; Minj, A.; Sergeant, S.; Han, H.; Asselberghs, I.; Lin, D.; et al. Engineering wafer-scale epitaxial two-dimensional materials through sapphire template screening for advanced high-performance nanoelectronics. *ACS Nano* **2021**, *15*, 9482−9494.
(616) Li, L.; Peng, Y.; Tian, J.; Wu, F.; Guo, X.; Li, N.; Yang, W.; Shi, D.; Du, L.; Zhang, G. Batch fabrication of $MoS_2$ devices directly on growth substrates by step engineering. *Nano Res.* **2023**, *16*, 12794−12799.
(617) Tsivion, D.; Schvartzman, M.; Popovitz-Biro, R.; von Huth, P.; Joselevich, E. Guided growth of millimeter-long horizontal nanowires with controlled orientations. *Science* **2011**, *333*, 1003−1007.
(618) Zhang, S.; Kang, L.; Wang, X.; Tong, L.; Yang, L.; Wang, Z.; Qi, K.; Deng, S.; Li, Q.; Bai, X.; et al. Arrays of horizontal carbon nanotubes of controlled chirality grown using designed catalysts. *Nature* **2017**, *543*, 234−238.
(619) Chen, L.; Liu, B.; Ge, M.; Ma, Y.; Abbas, A. N.; Zhou, C. Step-edge-guided nucleation and growth of aligned $WSe_2$ on sapphire via a layer-over-layer growth mode. *ACS Nano* **2015**, *9*, 8368−8375.
(620) Hwang, Y.; Shin, N. Hydrogen-assisted step-edge nucleation of $MoSe_2$ monolayers on sapphire substrates. *Nanoscale* **2019**, *11*, 7701−7709.
(621) Chubarov, M.; Choudhury, T. H.; Hickey, D. R.; Bachu, S.; Zhang, T.; Sebastian, A.; Bansal, A.; Zhu, H.; Trainor, N.; Das, S.; et al. Wafer-scale epitaxial growth of unidirectional $WS_2$ monolayers on sapphire. *ACS Nano* **2021**, *15*, 2532−2541.
(622) Li, H.; Cheng, M.; Wang, P.; Du, R.; Song, L.; He, J.; Shi, J. Reducing contact resistance and boosting device performance of monolayer $MoS_2$ by in situ Fe doping. *Adv. Mater.* **2022**, *34*, 2200885.
(623) Li, H.; Yang, J.; Li, X.; Luo, Q.; Cheng, M.; Feng, W.; Du, R.; Wang, Y.; Song, L.; Wen, X.; et al. Bridging synthesis and controllable doping of monolayer 4 in. length transition-metal dichalcogenides single crystals with high electron mobility. *Adv. Mater.* **2023**, *35*, 2211536.
(624) Chang, Y. M.; Yang, N.; Min, J.; Zheng, F.; Huang, C. W.; Chen, J. Y.; Zhang, Y.; Yang, P.; Li, C.; Liu, H. Y. Atomically thin decoration layers for robust orientation control of 2D transition metal dichalcogenides. *Adv. Funct. Mater.* **2024**, *34*, 11387.
(625) Li, T.; Yang, Y.; Zhou, L.; Sun, W.; Lin, W.; Liu, L.; Zou, X.; Gao, S.; Nie, Y.; Shi, Y.; et al. Halide vapor phase epitaxy of monolayer molybdenum diselenide single crystals. *Natl. Sci. Open* **2023**, *2*, 20220055.
(626) Liu, L.; Li, T.; Ma, L.; Li, W.; Gao, S.; Sun, W.; Dong, R.; Zou, X.; Fan, D.; Shao, L.; et al. Uniform nucleation and epitaxy of bilayer molybdenum disulfide on sapphire. *Nature* **2022**, *605*, 69−75.
(627) Zheng, P.; Wei, W.; Liang, Z.; Qin, B.; Tian, J.; Wang, J.; Qiao, R.; Ren, Y.; Chen, J.; Huang, C.; et al. Universal epitaxy of non-centrosymmetric two-dimensional single-crystal metal dichalcogenides. *Nat. Commun.* **2023**, *14*, 592.
(628) Xue, G.; Zhou, Z.; Guo, Q.; Zuo, Y.; Wei, W.; Yang, J.; Yin, P.; Zhang, S.; Zhong, D.; You, Y.; et al. $WS_2$ ribbon arrays with defined chirality and coherent polarity. *Science* **2024**, *384*, 1100−1104.
(629) Zhu, H.; Nayir, N.; Choudhury, T. H.; Bansal, A.; Huet, B.; Zhang, K.; Puretzky, A. A.; Bachu, S.; York, K.; Mc Knight, T. V.; et al. Step engineering for nucleation and domain orientation control in $WSe_2$ epitaxy on c-plane sapphire. *Nat. Nanotechnol.* **2023**, *18*, 1295−1302.
(630) Aljarb, A.; Min, J.; Hakami, M.; Fu, J. H.; Albaridy, R.; Wan, Y.; Lopatin, S.; Kaltsas, D.; Naphade, D.; Yengel, E.; et al. Interfacial reconstructed layer controls the orientation of monolayer transition-metal dichalcogenides. *ACS Nano* **2023**, *17*, 10010−10018.
(631) Li, L.; Wang, Q.; Wu, F.; Xu, Q.; Tian, J.; Huang, Z.; Wang, Q.; Zhao, X.; Zhang, Q.; Fan, Q.; et al. Epitaxy of wafer-scale single-crystal $MoS_2$ monolayer via buffer layer control. *Nat. Commun.* **2024**, *15*, 1825.
(632) Fu, J. H.; Min, J.; Chang, C. K.; Tseng, C. C.; Wang, Q.; Sugisaki, H.; Li, C.; Chang, Y. M.; Alnami, I.; Syong, W. R.; et al. Oriented lateral growth of two-dimensional materials on c-plane sapphire. *Nat. Nanotechnol.* **2023**, *18*, 1289−1294.
(633) Wu, L.; Yang, W.; Wang, G. Mechanism of substrate-induced anisotropic growth of monolayer $WS_2$ by kinetic monte carlo simulations. *npj 2D Mater. Appl.* **2019**, *3*, 6.
(634) Wang, J.; Luo, Y.; Cai, X.; Shi, R.; Wang, W.; Li, T.; Wu, Z.; Zhang, X.; Peng, O.; Amini, A.; et al. Multiple regulation over growth

direction, band structure, and dimension of monolayer $WS_2$ by a quartz substrate. *Chem. Mater.* **2020**, *32*, 2508−2517.
(635) Zhang, Y.; Ji, Q.; Han, G. F.; Ju, J.; Shi, J.; Ma, D.; Sun, J.; Zhang, Y.; Li, M.; Lang, X. Y.; et al. Dendritic, transferable, strictly monolayer $MoS_2$ flakes synthesized on $SrTiO_3$ single crystals for efficient electrocatalytic applications. *ACS Nano* **2014**, *8*, 8617−8624.
(636) Zhang, Y.; Ji, Q.; Wen, J.; Li, J.; Li, C.; Shi, J.; Zhou, X.; Shi, K.; Chen, H.; Li, Y.; et al. Monolayer $MoS_2$ dendrites on a symmetry-disparate $SrTiO_3(001)$ substrate: Formation mechanism and interface interaction. *Adv. Funct. Mater.* **2016**, *26*, 3299−3305.
(637) Chen, P.; Xu, W.; Gao, Y.; Warner, J. H.; Castell, M. R. Epitaxial growth of monolayer $MoS_2$ on $SrTiO_3$ single crystal substrates for applications in nanoelectronics. *ACS Appl. Nano Mater.* **2018**, *1*, 6976−6988.
(638) Huang, C.; Fu, J.; Xiang, M.; Zhang, J.; Zeng, H.; Shao, X. Single-layer $MoS_2$ grown on atomically flat $SrTiO_3$ single crystal for enhanced trionic luminescence. *ACS Nano* **2021**, *15*, 8610−8620.
(639) Li, C.; Zhang, Y.; Ji, Q.; Shi, J.; Chen, Z.; Zhou, X.; Fang, Q.; Zhang, Y. Substrate effect on the growth of monolayer dendritic $MoS_2$ on $LaAlO_3(100)$ and its electrocatalytic applications. *2D Mater.* **2016**, *3*, No. 035001.
(640) Aljarb, A.; Fu, J. H.; Hsu, C. C.; Chuu, C. P.; Wan, Y.; Hakami, M.; Naphade, D. R.; Yengel, E.; Lee, C. J.; Brems, S.; et al. Ledge-directed epitaxy of continuously self-aligned single-crystalline nanoribbons of transition metal dichalcogenides. *Nat. Mater.* **2020**, *19*, 1300−1306.
(641) Bonell, F.; Marty, A.; Vergnaud, C.; Consonni, V.; Okuno, H.; Ouerghi, A.; Boukari, H.; Jamet, M. High carrier mobility in single-crystal $PtSe_2$ grown by molecular beam epitaxy on ZnO(0001). *2D Mater.* **2022**, *9*, No. 015015.
(642) Liu, H.; Li, Y.; Xiang, M.; Zeng, H.; Shao, X. Single-layered $MoS_2$ directly grown on rutile $TiO_2(110)$ for enhanced interfacial charge transfer. *ACS Nano* **2019**, *13*, 6083−6089.
(643) Xiang, M.; Liu, H.; Huang, C.; Li, Y.; Zeng, H.; Shao, X. Mo doping assisting the CVD synthesis of size-controlled, uniformly distributed single-layer $MoS_2$ on rutile $TiO_2(110)$. *ACS Appl. Mater. Interfaces* **2020**, *12*, 34378−34387.
(644) Lan, F.; Lai, Z.; Xu, Y.; Cheng, H.; Wang, Z.; Qi, C.; Chen, J.; Zhang, S. Synthesis of vertically standing $MoS_2$ triangles on SiC. *Sci. Rep.* **2016**, *6*, 31980.
(645) Chen, Z.; Liu, H.; Chen, X.; Chu, G.; Chu, S.; Zhang, H. Wafer-size and single-crystal $MoSe_2$ atomically thin films grown on GaN substrate for light emission and harvesting. *ACS Appl. Mater. Interfaces* **2016**, *8*, 20267−20273.
(646) Ruzmetov, D.; Zhang, K.; Stan, G.; Kalanyan, B.; Bhimanapati, G. R.; Eichfeld, S. M.; Burke, R. A.; Shah, P. B.; O'Regan, T. P.; Crowne, F. J.; et al. Vertical 2D/3D semiconductor heterostructures based on epitaxial molybdenum disulfide and gallium nitride. *ACS Nano* **2016**, *10*, 3580−3588.
(647) Ohtake, A.; Sakuma, Y. Effect of substrate orientation on $MoSe_2$/GaAs heteroepitaxy. *J. Phys. Chem. C* **2020**, *124*, 5196−5203.
(648) Wang, Q. Q.; Tang, J.; Li, X. M.; Tian, J. P.; Liang, J.; Li, N.; Ji, D. P.; Xian, L. D.; Guo, Y. T.; Li, L.; et al. Layer-by-layer epitaxy of multi-layer $MoS_2$ wafers. *Natl. Sci. Rev.* **2022**, *9*, nwac077.
(649) Wu, R. X.; Tao, Q. Y.; Li, J.; Li, W.; Chen, Y.; Lu, Z. Y.; Shu, Z. W.; Zhao, B.; Ma, H. F.; Zhang, Z. W.; et al. Bilayer tungsten diselenide transistors with on-state currents exceeding 1.5 milliamperes per micrometre. *Nat. Electron.* **2022**, *5*, 497−504.
(650) Li, H.; Yin, Z. Y.; He, Q. Y.; Li, H.; Huang, X.; Lu, G.; Fam, D. W. H.; Tok, A. I. Y.; Zhang, Q.; Zhang, H. Fabrication of single- and multilayer $MoS_2$ film-based field-effect transistors for sensing NO at room temperature. *Small* **2012**, *8*, 63−67.
(651) Wang, H.; Yu, L. L.; Lee, Y. H.; Shi, Y. M.; Hsu, A.; Chin, M. L.; Li, L. J.; Dubey, M.; Kong, J.; Palacios, T. Integrated circuits based on bilayer $MoS_2$ transistors. *Nano Lett.* **2012**, *12*, 4674−4680.
(652) Zhao, Y. X.; Song, J. G.; Ryu, G. H.; Ko, K. Y.; Woo, W. J.; Kim, Y.; Kim, D.; Lim, J. H.; Lee, S.; Lee, Z.; et al. Low-temperature synthesis of 2D $MoS_2$ on a plastic substrate for a flexible gas sensor. *Nanoscale* **2018**, *10*, 9338−9345.
(653) Zhang, L.; Dong, J.; Ding, F. Strategies, status, and challenges in wafer scale single crystalline two-dimensional materials synthesis. *Chem. Rev.* **2021**, *121*, 6321−6372.
(654) Ye, H.; Zhou, J. D.; Er, D. Q.; Price, C. C.; Yu, Z. Y.; Liu, Y. M.; Lowengrub, J.; Lou, J.; Liu, Z.; Shenoy, V. B. Toward a mechanistic understanding of vertical growth of van der Waals stacked 2D materials: A multiscale model and experiments. *ACS Nano* **2017**, *11*, 12780−12788.
(655) Zheng, J.; Yan, X.; Lu, Z.; Qiu, H.; Xu, G.; Zhou, X.; Wang, P.; Pan, X.; Liu, K.; Jiao, L. High-mobility multilayered $MoS_2$ flakes with low contact resistance grown by chemical vapor deposition. *Adv. Mater.* **2017**, *29*, 1604540.
(656) Zhang, X. M.; Nan, H. Y.; Xiao, S. Q.; Wan, X.; Gu, X. F.; Du, A. J.; Ni, Z. H.; Ostrikov, K. Transition metal dichalcogenides bilayer single crystals by reverse-flow chemical vapor epitaxy. *Nat. Commun.* **2019**, *10*, 598.
(657) Peng, G.; Yang, X.; Wang, S. Y.; Zhang, J. Y.; Qi, G. J.; Zhang, S.; Liu, K.; Zhu, Z. H.; Li, Z.; Wang, G.; et al. Controllable epitaxial growth of $MoSe_2$ bilayers with different stacking orders by reverse-flow chemical vapor deposition. *ACS Appl. Mater. Interfaces* **2020**, *12*, 23347−23355.
(658) Li, X. F.; Shi, X. H.; Marian, D.; Soriano, D.; Cusati, T.; Iannaccone, G.; Fiori, G.; Guo, Q.; Zhao, W. J.; Wu, Y. Q. Rhombohedral-stacked bilayer transition metal dichalcogenides for high-performance atomically thin CMOS devices. *Sci. Adv.* **2023**, *9*, eade5706.
(659) Chang, C.; Zhang, X.; Li, W.; Guo, Q.; Feng, Z.; Huang, C.; Ren, Y.; Cai, Y.; Zhou, X.; Wang, J.; et al. Remote epitaxy of single-crystal rhombohedral $WS_2$ bilayers. *Nat. Commun.* **2024**, *15*, 4130.
(660) Qin, B.; Ma, C.; Guo, Q.; Li, X.; Wei, W.; Ma, C.; Wang, Q.; Liu, F.; Zhao, M.; Xue, G.; et al. Interfacial epitaxy of multilayer rhombohedral transition-metal dichalcogenide single crystals. *Science* **2024**, *385*, 99−104.
(661) Guo, Y. H.; Wang, Z. F.; Zhang, L. Z.; Shen, X. D.; Liu, F. Thickness dependence of surface energy and contact angle of water droplets on ultrathin $MoS_2$ films. *Phys. Chem. Chem. Phys.* **2016**, *18*, 14449−14453.
(662) Bauer, E.; Vandermerwe, J. H. Structure and growth of crystalline superlattices-from monolayer to superlattice. *Phys. Rev. B* **1986**, *33*, 3657−3671.
(663) Dong, R.; Gong, X.; Yang, J.; Sun, Y.; Ma, L.; Wang, J. The intrinsic thermodynamic difficulty and a step-guided mechanism for the epitaxial growth of uniform multilayer $MoS_2$ with controllable thickness. *Adv. Mater.* **2022**, *34*, e2201402.
(664) Kalanyan, B.; Kimes, W. A.; Beams, R.; Stranick, S. J.; Garratt, E.; Kalish, I.; Davydov, A. V.; Kanjolia, R. K.; Maslar, J. E. Rapid wafer-scale growth of polycrystalline 2H-$MoS_2$ by pulsed metal-organic chemical vapor deposition. *Chem. Mater.* **2017**, *29*, 6279−6288.
(665) Liu, H.; Chen, L.; Zhu, H.; Sun, Q. Q.; Ding, S. J.; Zhou, P.; Zhang, D. W. Atomic layer deposited 2D $MoS_2$ atomic crystals: From material to circuit. *Nano Res.* **2020**, *13*, 1644−1650.
(666) Lau, C. N.; Bockrath, M. W.; Mak, K. F.; Zhang, F. Reproducibility in the fabrication and physics of moiré materials. *Nature* **2022**, *602*, 41−50.
(667) Liu, C.; Li, Z.; Qiao, R.; Wang, Q.; Zhang, Z.; Liu, F.; Zhou, Z.; Shang, N.; Fang, H.; Wang, M.; et al. Designed growth of large bilayer graphene with arbitrary twist angles. *Nat. Mater.* **2022**, *21*, 1263−1268.
(668) Bachmatiuk, A.; Abelin, R. F.; Quang, H. T.; Trzebicka, B.; Eckert, J.; Rummeli, M. H. Chemical vapor deposition of twisted bilayer and few-layer $MoSe_2$ over $SiO_x$ substrates. *Nanotechnology* **2014**, *25*, 365603.
(669) Liu, K. H.; Zhang, L. M.; Cao, T.; Jin, C. H.; Qiu, D. A.; Zhou, Q.; Zettl, A.; Yang, P. D.; Louie, S. G.; Wang, F. Evolution of interlayer coupling in twisted molybdenum disulfide bilayers. *Nat. Commun.* **2014**, *5*, 4966.
(670) Wang, K.; Huang, B.; Tian, M.; Ceballos, F.; Lin, M. W.; Mahjouri-Samani, M.; Boulesbaa, A.; Puretzky, A. A.; Rouleau, C. M.;

Yoon, M.; et al. Interlayer coupling in twisted $WSe_2/WS_2$ bilayer heterostructures revealed by optical spectroscopy. *ACS Nano* **2016**, *10*, 6612−6622.

(671) Huang, S. X.; Ling, X.; Liang, L. B.; Kong, J.; Terrones, H.; Meunier, V.; Dresselhaus, M. S. Probing the interlayer coupling of twisted bilayer $MoS_2$ using photoluminescence spectroscopy. *Nano Lett.* **2014**, *14*, 5500−5508.

(672) Puretzky, A. A.; Liang, L. B.; Li, X. F.; Xiao, K.; Sumpter, B. G.; Meunier, V.; Geohegan, D. B. Twisted $MoSe_2$ bilayers with variable local stacking and interlayer coupling revealed by low-frequency Raman spectroscopy. *ACS Nano* **2016**, *10*, 2736−2744.

(673) Zheng, S. J.; Sun, L. F.; Zhou, X. H.; Liu, F. C.; Liu, Z.; Shen, Z. X.; Fan, H. J. Coupling and interlayer exciton in twist-stacked $WS_2$ bilayers. *Adv. Opt. Mater.* **2015**, *3*, 1600−1605.

(674) Yu, Y.; Jung, G. S.; Liu, C.; Lin, Y. C.; Rouleau, C. M.; Yoon, M.; Eres, G.; Duscher, G.; Xiao, K.; Irle, S.; et al. Strain-induced growth of twisted bilayers during the coalescence of monolayer $MoS_2$ crystals. *ACS Nano* **2021**, *15*, 4504−4517.

(675) Xu, M.; Ji, H.; Zheng, L.; Li, W.; Wang, J.; Wang, H.; Luo, L.; Lu, Q.; Gan, X.; Liu, Z.; et al. Reconfiguring nucleation for CVD growth of twisted bilayer $MoS_2$ with a wide range of twist angles. *Nat. Commun.* **2024**, *15*, 562.

(676) Xu, M.; Ji, H.; Zhang, M.; Zheng, L.; Li, W.; Luo, L.; Chen, M.; Liu, Z.; Gan, X.; Wang, X.; Huang, W.; et al. CVD synthesis of twisted bilayer $WS_2$ with tunable second harmonic generation. *Adv. Mater.* **2024**, *36*, e2313638.

(677) Shearer, M. J.; Samad, L.; Zhang, Y.; Zhao, Y.; Puretzky, A.; Eliceiri, K. W.; Wright, J. C.; Hamers, R. J.; Jin, S. Complex and noncentrosymmetric stacking of layered metal dichalcogenide materials created by screw dislocations. *J. Am. Chem. Soc.* **2017**, *139*, 3496−3504.

(678) Zhao, Y. Z.; Zhang, C. Y.; Kohler, D. D.; Scheeler, J. M.; Wright, J. C.; Voyles, P. M.; Jin, S. Supertwisted spirals of layered materials enabled by growth on non-euclidean surfaces. *Science* **2020**, *370*, 442−445.

(679) Liao, M. Z.; Wei, Z.; Du, L. J.; Wang, Q. Q.; Tang, J.; Yu, H.; Wu, F. F.; Zhao, J. J.; Xu, X. Z.; Han, B.; et al. Precise control of the interlayer twist angle in large scale $MoS_2$ homostructures. *Nat. Commun.* **2020**, *11*, 2153.

(680) Shen, D.; Zhao, B.; Zhang, Z.; Zhang, H.; Yang, X.; Huang, Z.; Li, B.; Song, R.; Jin, Y.; Wu, R.; et al. Synthesis of group VIII magnetic transition-metal-doped monolayer $MoSe_2$. *ACS Nano* **2022**, *16*, 10623−10631.

(681) Li, B.; Xing, T.; Zhong, M.; Huang, L.; Lei, N.; Zhang, J.; Li, J.; Wei, Z. A two-dimensional Fe-doped $SnS_2$ magnetic semiconductor. *Nat. Commun.* **2017**, *8*, 1958.

(682) Duan, H.; Guo, P.; Wang, C.; Tan, H.; Hu, W.; Yan, W.; Ma, C.; Cai, L.; Song, L.; Zhang, W.; et al. Beating the exclusion rule against the coexistence of robust luminescence and ferromagnetism in chalcogenide monolayers. *Nat. Commun.* **2019**, *10*, 1584.

(683) Li, Q.; Zhao, X.; Deng, L.; Shi, Z.; Liu, S.; Wei, Q.; Zhang, L.; Cheng, Y.; Zhang, L.; Lu, H.; et al. Enhanced valley zeeman splitting in Fe-doped monolayer $MoS_2$. *ACS Nano* **2020**, *14*, 4636−4645.

(684) Zhou, J.; Lin, J.; Sims, H.; Jiang, C.; Cong, C.; Brehm, J. A.; Zhang, Z.; Niu, L.; Chen, Y.; Zhou, Y.; et al. Synthesis of Co-Doped $MoS_2$ monolayers with enhanced valley splitting. *Adv. Mater.* **2020**, *32*, 1906536.

(685) Fu, S.; Kang, K.; Shayan, K.; Yoshimura, A.; Dadras, S.; Wang, X.; Zhang, L.; Chen, S.; Liu, N.; Jindal, A.; et al. Enabling room temperature ferromagnetism in monolayer $MoS_2$ via in situ iron-doping. *Nat. Commun.* **2020**, *11*, 2034.

(686) Zou, J.; Cai, Z.; Lai, Y.; Tan, J.; Zhang, R.; Feng, S.; Wang, G.; Lin, J.; Liu, B.; Cheng, H. M. Doping concentration modulation in vanadium-doped monolayer molybdenum disulfide for synaptic transistors. *ACS Nano* **2021**, *15*, 7340−7347.

(687) Zhang, K.; Feng, S.; Wang, J.; Azcatl, A.; Lu, N.; Addou, R.; Wang, N.; Zhou, C.; Lerach, J.; Bojan, V.; et al. Manganese doping of monolayer $MoS_2$: The substrate is critical. *Nano Lett.* **2015**, *15*, 6586−6591.

(688) Wang, S.; Ding, D.; Li, P.; Sui, Y.; Liu, G.; Zhao, S.; Xiao, R.; Tian, C.; Chen, Z.; Wang, H.; et al. Concentration phase separation of substitution-doped atoms in TMDCs monolayer. *Small* **2023**, *19*, 2301027.

(689) Zhang, T.; Liu, M.; Fujisawa, K.; Lucking, M.; Beach, K.; Zhang, F.; Shanmugasundaram, M.; Krayev, A.; Murray, W.; Lei, Y.; et al. Spatial control of substitutional dopants in hexagonal monolayer $WS_2$: The effect of edge termination. *Small* **2023**, *19*, 2205800.

(690) Zhang, K.; Deng, D. D.; Zheng, B.; Wang, Y.; Perkins, F. K.; Briggs, N. C.; Crespi, V. H.; Robinson, J. A. Tuning transport and chemical sensitivity via niobium doping of synthetic $MoS_2$. *Adv. Mater. Interfaces* **2020**, *7*, 2000856.

(691) Torsi, R.; Munson, K. T.; Pendurthi, R.; Marques, E.; Van Troeye, B.; Huberich, L.; Schuler, B.; Feidler, M.; Wang, K.; Pourtois, G.; et al. Dilute rhenium doping and its impact on defects in $MoS_2$. *ACS Nano* **2023**, *17*, 15629−15640.

(692) Wang, Z.; Tripathi, M.; Golsanamlou, Z.; Kumari, P.; Lovarelli, G.; Mazziotti, F.; Logoteta, D.; Fiori, G.; Sementa, L.; Marega, G. M.; et al. Substitutional p-type doping in $NbS_2$-$MoS_2$ lateral heterostructures grown by MOCVD. *Adv. Mater.* **2023**, *35*, 2209371.

(693) Gao, H.; Suh, J.; Cao, M. C.; Joe, A. Y.; Mujid, F.; Lee, K. H.; Xie, S.; Poddar, P.; Lee, J. U.; Kang, K.; et al. Tuning electrical conductance of $MoS_2$ monolayers through substitutional doping. *Nano Lett.* **2020**, *20*, 4095−4101.

(694) Kozhakhmetov, A.; Schuler, B.; Tan, A. M. Z.; Cochrane, K. A.; Nasr, J. R.; El-Sherif, H.; Bansal, A.; Vera, A.; Bojan, V.; Redwing, J. M.; et al. Scalable substitutional Re-doping and its impact on the optical and electronic properties of tungsten diselenide. *Adv. Mater.* **2020**, *32*, 2005159.

(695) Zhang, K.; Bersch, B. M.; Joshi, J.; Addou, R.; Cormier, C. R.; Zhang, C.; Xu, K.; Briggs, N. C.; Wang, K.; Subramanian, S.; et al. Tuning the electronic and photonic properties of monolayer $MoS_2$ via in situ rhenium substitutional doping. *Adv. Funct. Mater.* **2018**, *28*, 1706950.

(696) Tang, L.; Xu, R.; Tan, J.; Luo, Y.; Zou, J.; Zhang, Z.; Zhang, R.; Zhao, Y.; Lin, J.; Zou, X.; et al. Modulating electronic structure of monolayer transition metal dichalcogenides by substitutional Nb-doping. *Adv. Funct. Mater.* **2021**, *31*, 2006941.

(697) Gao, J.; Kim, Y. D.; Liang, L.; Idrobo, J. C.; Chow, P.; Tan, J.; Li, B.; Li, L.; Sumpter, B. G.; Lu, T. M.; et al. Transition-metal substitution doping in synthetic atomically thin semiconductors. *Adv. Mater.* **2016**, *28*, 9735−9743.

(698) Li, B.; Huang, L.; Zhong, M.; Huo, N.; Li, Y.; Yang, S.; Fan, C.; Yang, J.; Hu, W.; Wei, Z.; et al. Synthesis and transport properties of large-scale alloy $Co_{0.16}Mo_{0.84}S_2$ bilayer nanosheets. *ACS Nano* **2015**, *9*, 1257−1262.

(699) Xu, D.; Chen, W.; Zeng, M.; Xue, H.; Chen, Y.; Sang, X.; Xiao, Y.; Zhang, T.; Unocic, R. R.; Xiao, K.; et al. Crystal-field tuning of photoluminescence in two-dimensional materials with embedded lanthanide ions. *Angew. Chem., Int. Ed.* **2018**, *57*, 755−759.

(700) Xu, E. Z.; Liu, H. M.; Park, K.; Li, Z.; Losovyj, Y.; Starr, M.; Werbianskyj, M.; Fertig, H. A.; Zhang, S. X. P-type transition-metal doping of large-area $MoS_2$ thin films grown by chemical vapor deposition. *Nanoscale* **2017**, *9*, 3576−3584.

(701) Zhang, Q.; Ying, H.; Li, X.; Xiang, R.; Zheng, Y.; Wang, H.; Su, J.; Xu, M.; Zheng, X.; Maruyama, S.; et al. Controlled doping engineering in 2D $MoS_2$ crystals toward performance augmentation of optoelectronic devices. *ACS Appl. Mater. Interfaces* **2021**, *13*, 31861−31869.

(702) Jiang, H.; Zheng, L.; Wang, J.; Xu, M.; Gan, X.; Wang, X.; Huang, W. Inversion symmetry broken in 2H phase vanadium-doped molybdenum disulfide. *Nanoscale* **2021**, *13*, 18103−18111.

(703) Han, A.; Zhou, X.; Wang, X.; Liu, S.; Xiong, Q.; Zhang, Q.; Gu, L.; Zhuang, Z.; Zhang, W.; Li, F.; et al. One-step synthesis of single-site vanadium substitution in 1T-$WS_2$ monolayers for enhanced hydrogen evolution catalysis. *Nat. Commun.* **2021**, *12*, 709.

(704) Zhang, L.; Wang, Z.; Zhang, J.; Chen, B.; Liang, Z.; Quan, X.; Dai, Y.; Huang, J.; Wang, Y.; Liang, S. J.; et al. Quasi-continuous

tuning of carrier polarity in monolayered molybdenum dichalcogenides through substitutional vanadium doping. *Adv. Funct. Mater.* **2022**, *32*, 2204760.

(705) Cai, Z.; Shen, T.; Zhu, Q.; Feng, S.; Yu, Q.; Liu, J.; Tang, L.; Zhao, Y.; Wang, J.; Liu, B.; Cheng, H.-M. Dual-additive assisted chemical vapor deposition for the growth of Mn-doped 2D $MoS_2$ with tunable electronic properties. *Small* **2020**, *16*, 1903181.

(706) Li, W.; Huang, J.; Han, B.; Xie, C.; Huang, X.; Tian, K.; Zeng, Y.; Zhao, Z.; Gao, P.; Zhang, Y.; et al. Molten-salt-assisted chemical vapor deposition process for substitutional doping of monolayer $MoS_2$ and effectively altering the electronic structure and phononic properties. *Adv. Sci.* **2020**, *7*, 2001080.

(707) Qin, Z.; Loh, L.; Wang, J.; Xu, X.; Zhang, Q.; Haas, B.; Alvarez, C.; Okuno, H.; Yong, J. Z.; Schultz, T.; et al. Growth of Nb-doped monolayer $WS_2$ by liquid-phase precursor mixing. *ACS Nano* **2019**, *13*, 10768−10775.

(708) Zhang, T.; Fujisawa, K.; Zhang, F.; Liu, M.; Lucking, M. C.; Gontijo, R. N.; Lei, Y.; Liu, H.; Crust, K.; Granzier-Nakajima, T.; et al. Universal in situ substitutional doping of transition metal dichalcogenides by liquid-phase precursor-assisted synthesis. *ACS Nano* **2020**, *14*, 4326−4335.

(709) Zhang, F.; Zheng, B.; Sebastian, A.; Olson, D. H.; Liu, M.; Fujisawa, K.; Pham, Y. T. H.; Jimenez, V. O.; Kalappattil, V.; Miao, L.; et al. Monolayer vanadium-doped tungsten disulfide: A room-temperature dilute magnetic semiconductor. *Adv. Sci.* **2020**, *7*, 2001174.

(710) Fan, S.; Yun, S. J.; Yu, W. J.; Lee, Y. H. Tailoring quantum tunneling in a vanadium-doped $WSe_2/SnSe_2$ heterostructure. *Adv. Sci.* **2020**, *7*, 1902751.

(711) Yun, S. J.; Duong, D. L.; Ha, D. M.; Singh, K.; Phan, T. L.; Choi, W.; Kim, Y. M.; Lee, Y. H. Ferromagnetic order at room temperature in monolayer $WSe_2$ semiconductor via vanadium dopant. *Adv. Sci.* **2020**, *7*, 1903076.

(712) Li, S.; Hong, J.; Gao, B.; Lin, Y. C.; Lim, H. E.; Lu, X.; Wu, J.; Liu, S.; Tateyama, Y.; Sakuma, Y.; et al. Tunable doping of rhenium and vanadium into transition metal dichalcogenides for two-dimensional electronics. *Adv. Sci.* **2021**, *8*, 2004438.

(713) Yang, L.; Majumdar, K.; Liu, H.; Du, Y.; Wu, H.; Hatzistergos, M.; Hung, P. Y.; Tieckelmann, R.; Tsai, W.; Hobbs, C.; et al. Chloride molecular doping technique on 2D materials: $WS_2$ and $MoS_2$. *Nano Lett.* **2014**, *14*, 6275−6280.

(714) Nipane, A.; Karmakar, D.; Kaushik, N.; Karande, S.; Lodha, S. Few-layer $MoS_2$ p-type devices enabled by selective doping using low energy phosphorus implantation. *ACS Nano* **2016**, *10*, 2128−2137.

(715) Kim, E.; Ko, C.; Kim, K.; Chen, Y.; Suh, J.; Ryu, S. G.; Wu, K.; Meng, X.; Suslu, A.; Tongay, S.; et al. Site selective doping of ultrathin metal dichalcogenides by laser-assisted reaction. *Adv. Mater.* **2016**, *28*, 341−346.

(716) Chen, M.; Nam, H.; Wi, S.; Ji, L.; Ren, X.; Bian, L.; Lu, S.; Liang, X. Stable few-layer $MoS_2$ rectifying diodes formed by plasma-assisted doping. *Appl. Phys. Lett.* **2013**, *103*, 142110.

(717) Li, S.; Chen, X.; Liu, F.; Chen, Y.; Liu, B.; Deng, W.; An, B.; Chu, F.; Zhang, G.; Li, S.; et al. Enhanced performance of a CVD $MoS_2$ photodetector by chemical in situ n-type doping. *ACS Appl. Mater. Interfaces* **2019**, *11*, 11636−11644.

(718) Zhang, F.; Lu, Y.; Schulman, D. S.; Zhang, T.; Fujisawa, K.; Lin, Z.; Lei, Y.; Elias, A. L.; Das, S.; Sinnott, S. B.; Terrones, M. Carbon doping of $WS_2$ monolayers: Bandgap reduction and p-type doping transport. *Sci. Adv.* **2019**, *5*, eaav5003.

(719) Liang, T.; Habib, M. R.; Xiao, H.; Xie, S.; Kong, Y.; Yu, C.; Iwai, H.; Fujita, D.; Hanagata, N.; Chen, H.; et al. Intrinsically substitutional carbon doping in CVD-grown monolayer $MoS_2$ and the band structure modulation. *ACS Appl. Electron. Mater.* **2020**, *2*, 1055−1064.

(720) Lim, J.; Kim, T.; Byeon, J.; Park, K.-H.; Hong, J.; Pak, S.; Cha, S. Energy level modulation of $MoS_2$ monolayers by halide doping for an enhanced hydrogen evolution reaction. *J. Mater. Chem. A* **2022**, *10*, 23274−23281.

(721) Azcatl, A.; Qin, X.; Prakash, A.; Zhang, C.; Cheng, L.; Wang, Q.; Lu, N.; Kim, M. J.; Kim, J.; Cho, K.; et al. Covalent nitrogen doping and compressive strain in $MoS_2$ by remote $N_2$ plasma exposure. *Nano Lett.* **2016**, *16*, 5437−5443.

(722) Cao, Q.; Dai, Y. W.; Xu, J.; Chen, L.; Zhu, H.; Sun, Q. Q.; Zhang, D. W. Realizing stable p-type transporting in two-dimensional $WS_2$ films. *ACS Appl. Mater. Interfaces* **2017**, *9*, 18215−18221.

(723) Li, X.; Long, H.; Zhong, J.; Ding, F.; Li, W.; Zhang, Z.; Song, R.; Huang, W.; Liang, J.; Liu, J.; et al. Two-dimensional metallic alloy contacts with composition-tunable work functions. *Nat. Electron.* **2023**, *6*, 842−851.

(724) Dumcenco, D. O.; Kobayashi, H.; Liu, Z.; Huang, Y. S.; Suenaga, K. Visualization and quantification of transition metal atomic mixing in $Mo_{1-x}W_xS_2$ single layers. *Nat. Commun.* **2013**, *4*, 1351.

(725) Duan, X.; Wang, C.; Fan, Z.; Hao, G.; Kou, L.; Halim, U.; Li, H.; Wu, X.; Wang, Y.; Jiang, J.; et al. Synthesis of $WS_{2x}Se_{2-2x}$ alloy nanosheets with composition-tunable electronic properties. *Nano Lett.* **2016**, *16*, 264−269.

(726) Mann, J.; Ma, Q.; Odenthal, P. M.; Isarraraz, M.; Le, D.; Preciado, E.; Barroso, D.; Yamaguchi, K.; von Son Palacio, G.; Nguyen, A.; et al. 2-dimensional transition metal dichalcogenides with tunable direct band gaps: $MoS_{2(1-x)}Se_{2x}$ monolayers. *Adv. Mater.* **2014**, *26*, 1399−1404.

(727) Li, H.; Duan, X.; Wu, X.; Zhuang, X.; Zhou, H.; Zhang, Q.; Zhu, X.; Hu, W.; Ren, P.; Guo, P.; et al. Growth of alloy $MoS_{2x}Se_{2(1-x)}$ nanosheets with fully tunable chemical compositions and optical properties. *J. Am. Chem. Soc.* **2014**, *136*, 3756−3759.

(728) Kim, D.; Oh, G. H.; Kim, A.; Shin, C.; Park, J.; Kim, S. I.; Kim, T. Atomic layer $MoS_{2x}Te_{2(1-x)}$ ternary alloys: Two-dimensional van der Waals growth, band gap engineering, and electrical transport. *ACS Appl. Mater. Interfaces* **2020**, *12*, 40518−40524.

(729) Apte, A.; Krishnamoorthy, A.; Hachtel, J. A.; Susarla, S.; Idrobo, J. C.; Nakano, A.; Kalia, R. K.; Vashishta, P.; Tiwary, C. S.; Ajayan, P. M. Telluride-based atomically thin layers of ternary two-dimensional transition metal dichalcogenide alloys. *Chem. Mater.* **2018**, *30*, 7262−7268.

(730) Wang, X.; Pan, L.; Yang, J.; Li, B.; Liu, Y. Y.; Wei, Z. Direct synthesis and enhanced rectification of alloy-to-alloy 2D type-II $MoS_{2(1-x)}Se_{2x}/SnS_{2(1-y)}Se_{2y}$ heterostructures. *Adv. Mater.* **2021**, *33*, 2006908.

(731) Li, X.; Lin, M. W.; Basile, L.; Hus, S. M.; Puretzky, A. A.; Lee, J.; Kuo, Y. C.; Chang, L. Y.; Wang, K.; Idrobo, J. C.; et al. Isoelectronic tungsten doping in monolayer $MoSe_2$ for carrier type modulation. *Adv. Mater.* **2016**, *28*, 8240−8247.

(732) Li, X.; Puretzky, A. A.; Sang, X.; Kc, S.; Tian, M.; Ceballos, F.; Mahjouri-Samani, M.; Wang, K.; Unocic, R. R.; Zhao, H.; et al. Suppression of defects and deep levels using isoelectronic tungsten substitution in monolayer $MoSe_2$. *Adv. Funct. Mater.* **2017**, *27*, 1603850.

(733) Zhang, W.; Li, X.; Jiang, T.; Song, J.; Lin, Y.; Zhu, L.; Xu, X. CVD synthesis of $Mo_{(1-x)}W_xS_2$ and $MoS_{2(1-x)}Se_{2x}$ alloy monolayers aimed at tuning the bandgap of molybdenum disulfide. *Nanoscale* **2015**, *7*, 13554−13560.

(734) Susarla, S.; Kutana, A.; Hachtel, J. A.; Kochat, V.; Apte, A.; Vajtai, R.; Idrobo, J. C.; Yakobson, B. I.; Tiwary, C. S.; Ajayan, P. M. Quaternary 2D transition metal dichalcogenides (TMDs) with tunable bandgap. *Adv. Mater.* **2017**, *29*, 1702457.

(735) Gan, Z.; Paradisanos, I.; Estrada-Real, A.; Picker, J.; Najafidehaghani, E.; Davies, F.; Neumann, C.; Robert, C.; Wiecha, P.; Watanabe, K.; et al. Chemical vapor deposition of high-optical-quality large-area monolayer Janus transition metal dichalcogenides. *Adv. Mater.* **2022**, *34*, 2205226.

(736) Komsa, H. P.; Krasheninnikov, A. V. Two-dimensional transition metal dichalcogenide alloys: Stability and electronic properties. *J. Phys. Chem. lett.* **2012**, *3*, 3652−3656.

(737) Gong, Y.; Liu, Z.; Lupini, A. R.; Shi, G.; Lin, J.; Najmaei, S.; Lin, Z.; Elias, A. L.; Berkdemir, A.; You, G.; et al. Band gap

engineering and layer-by-layer mapping of selenium-doped molybdenum disulfide. *Nano Lett.* **2014**, *14*, 442−449.

(738) Yang, L.; Fu, Q.; Wang, W.; Huang, J.; Huang, J.; Zhang, J.; Xiang, B. Large-area synthesis of monolayered $MoS_{2(1-x)}Se_{2x}$ with a tunable band gap and its enhanced electrochemical catalytic activity. *Nanoscale* **2015**, *7*, 10490−10497.

(739) Umrao, S.; Jeon, J.; Jeon, S. M.; Choi, Y. J.; Lee, S. A homogeneous atomic layer $MoS_{2(1-x)}Se_{2x}$ alloy prepared by low-pressure chemical vapor deposition, and its properties. *Nanoscale* **2017**, *9*, 594−603.

(740) Fortin-Deschenes, M.; Watanabe, K.; Taniguchi, T.; Xia, F. Van der Waals epitaxy of tunable moirés enabled by alloying. *Nat. Mater.* **2024**, *23*, 339−346.

(741) Feng, Q.; Zhu, Y.; Hong, J.; Zhang, M.; Duan, W.; Mao, N.; Wu, J.; Xu, H.; Dong, F.; Lin, F.; et al. Growth of large-area 2D $MoS_{2(1-x)}$ $Se_{2x}$ semiconductor alloys. *Adv. Mater.* **2014**, *26*, 2648−2653.

(742) Feng, Q.; Mao, N.; Wu, J.; Xu, H.; Wang, C.; Zhang, J.; Xie, L. Growth of $MoS_{2(1-x)}Se_{2x}$ ($x$ = 0.41−1.00) monolayer alloys with controlled morphology by physical vapor deposition. *ACS Nano* **2015**, *9*, 7450−7455.

(743) Ma, Q.; Isarraraz, M.; Wang, C. S.; Preciado, E.; Klee, V.; Bobek, S.; Yamaguchi, K.; Li, E.; Odenthal, P. M.; Nguyen, A.; et al. Postgrowth tuning of the bandgap of single-layer molybdenum disulfide films by sulfur/selenium exchange. *ACS Nano* **2014**, *8*, 4672−4677.

(744) Lim, Y. R.; Han, J. K.; Yoon, Y.; Lee, J. B.; Jeon, C.; Choi, M.; Chang, H.; Park, N.; Kim, J. H.; Lee, Z.; et al. Atomic-level customization of 4 in. Transition metal dichalcogenide multilayer alloys for industrial applications. *Adv. Mater.* **2019**, *31*, 1901405.

(745) Li, H.; Wu, X.; Liu, H.; Zheng, B.; Zhang, Q.; Zhu, X.; Wei, Z.; Zhuang, X.; Zhou, H.; Tang, W.; et al. Composition-modulated two-dimensional semiconductor lateral heterostructures via layer-selected atomic substitution. *ACS Nano* **2017**, *11*, 961−967.

(746) Su, S. H.; Hsu, Y. T.; Chang, Y. H.; Chiu, M. H.; Hsu, C. L.; Hsu, W. T.; Chang, W. H.; He, J. H.; Li, L. J. Band gap-tunable molybdenum sulfide selenide monolayer alloy. *Small* **2014**, *10*, 2589−2594.

(747) Taghinejad, H.; Rehn, D. A.; Muccianti, C.; Eftekhar, A. A.; Tian, M.; Fan, T.; Zhang, X.; Meng, Y.; Chen, Y.; Nguyen, T. V.; et al. Defect-mediated alloying of monolayer transition-metal dichalcogenides. *ACS Nano* **2018**, *12*, 12795−12804.

(748) Yun, S. J.; Han, G. H.; Kim, H.; Duong, D. L.; Shin, B. G.; Zhao, J.; Vu, Q. A.; Lee, J.; Lee, S. M.; Lee, Y. H. Telluriding monolayer $MoS_2$ and $WS_2$ via alkali metal scooter. *Nat. Commun.* **2017**, *8*, 2163.

(749) Fang, Q.; Zhang, Z.; Ji, Q.; Zhu, S.; Gong, Y.; Zhang, Y.; Shi, J.; Zhou, X.; Gu, L.; Wang, Q.; et al. Transformation of monolayer $MoS_2$ into multiphasic $MoTe_2$: Chalcogen atom-exchange synthesis route. *Nano Res.* **2017**, *10*, 2761−2771.

(750) Lu, A. Y.; Zhu, H.; Xiao, J.; Chuu, C. P.; Han, Y.; Chiu, M. H.; Cheng, C. C.; Yang, C. W.; Wei, K. H.; Yang, Y.; et al. Janus monolayers of transition metal dichalcogenides. *Nat. Nanotechnol.* **2017**, *12*, 744−749.

(751) Guo, Y.; Lin, Y.; Xie, K.; Yuan, B.; Zhu, J.; Shen, P. C.; Lu, A. Y.; Su, C.; Shi, E.; Zhang, K.; et al. Designing artificial two-dimensional landscapes via atomic-layer substitution. *Proc. Natl. Acad. Sci. U. S. A.* **2021**, *118*, e2106124118.

(752) Trivedi, D. B.; Turgut, G.; Qin, Y.; Sayyad, M. Y.; Hajra, D.; Howell, M.; Liu, L.; Yang, S.; Patoary, N. H.; Li, H.; et al. Room-temperature synthesis of 2D Janus crystals and their heterostructures. *Adv. Mater.* **2020**, *32*, 2006320.

(753) Zhang, K.; Guo, Y.; Ji, Q.; Lu, A. Y.; Su, C.; Wang, H.; Puretzky, A. A.; Geohegan, D. B.; Qian, X.; Fang, S.; et al. Enhancement of van der Waals interlayer coupling through polar Janus mosse. *J. Am. Chem. Soc.* **2020**, *142*, 17499−17507.

(754) Qin, Y.; Sayyad, M.; Montblanch, A. R.; Feuer, M. S. G.; Dey, D.; Blei, M.; Sailus, R.; Kara, D. M.; Shen, Y.; Yang, S.; et al. Reaching the excitonic limit in 2D Janus monolayers by in situ deterministic growth. *Adv. Mater.* **2022**, *34*, 2106222.

(755) Shi, J.; Xu, H.; Heide, C.; HuangFu, C.; Xia, C.; de Quesada, F.; Shen, H.; Zhang, T.; Yu, L.; Johnson, A.; et al. Giant room-temperature nonlinearities in a monolayer Janus topological semiconductor. *Nat. Commun.* **2023**, *14*, 4953.

(756) Lin, Y. C.; Liu, C.; Yu, Y.; Zarkadoula, E.; Yoon, M.; Puretzky, A. A.; Liang, L.; Kong, X.; Gu, Y.; Strasser, A.; et al. Low energy implantation into transition-metal dichalcogenide monolayers to form Janus structures. *ACS Nano* **2020**, *14*, 3896−3906.

(757) Harris, S. B.; Lin, Y. C.; Puretzky, A. A.; Liang, L.; Dyck, O.; Berlijn, T.; Eres, G.; Rouleau, C. M.; Xiao, K.; Geohegan, D. B. Real-time diagnostics of 2D crystal transformations by pulsed laser deposition: Controlled synthesis of Janus wsse monolayers and alloys. *ACS Nano* **2023**, *17*, 2472−2486.

(758) Zhang, J.; Jia, S.; Kholmanov, I.; Dong, L.; Er, D.; Chen, W.; Guo, H.; Jin, Z.; Shenoy, V. B.; Shi, L.; et al. Janus monolayer transition-metal dichalcogenides. *ACS Nano* **2017**, *11*, 8192−8198.

(759) Shen, P.-C.; Lin, Y.; Su, C.; McGahan, C.; Lu, A.-Y.; Ji, X.; Wang, X.; Wang, H.; Mao, N.; Guo, Y.; et al. Healing of donor defect states in monolayer molybdenum disulfide using oxygen-incorporated chemical vapour deposition. *Nat. Electron.* **2022**, *5*, 28−36.

(760) Tang, J.; Wei, Z.; Wang, Q.; Wang, Y.; Han, B.; Li, X.; Huang, B.; Liao, M.; Liu, J.; Li, N.; et al. In situ oxygen doping of monolayer $MoS_2$ for novel electronics. *Small* **2020**, *16*, 2004276.

(761) Wei, Z.; Tang, J.; Li, X.; Chi, Z.; Wang, Y.; Wang, Q.; Han, B.; Li, N.; Huang, B.; Li, J.; et al. Wafer-scale oxygen-doped $MoS_2$ monolayer. *Small Methods* **2021**, *5*, 2100091.

(762) Peto, J.; Ollar, T.; Vancso, P.; Popov, Z. I.; Magda, G. Z.; Dobrik, G.; Hwang, C.; Sorokin, P. B.; Tapaszto, L. Spontaneous doping of the basal plane of $MoS_2$ single layers through oxygen substitution under ambient conditions. *Nat. Chem.* **2018**, *10*, 1246−1251.

(763) Kang, N.; Paudel, H. P.; Leuenberger, M. N.; Tetard, L.; Khondaker, S. I. Photoluminescence quenching in single-layer $MoS_2$ via oxygen plasma treatment. *J. Phys. Chem. C* **2014**, *118*, 21258−21263.

(764) Wu, S.; Zeng, Y.; Zeng, X.; Wang, S.; Hu, Y.; Wang, W.; Yin, S.; Zhou, G.; Jin, W.; Ren, T.; et al. High-performance p-type $MoS_2$ field-effect transistor by toroidal-magnetic-field controlled oxygen plasma doping. *2D Mater.* **2019**, *6*, No. 025007.

(765) Jadwiszczak, J.; O'Callaghan, C.; Zhou, Y.; Fox, D. S.; Weitz, E.; Keane, D.; Cullen, C. P.; O'Reilly, I.; Downing, C.; Shmeliov, A.; et al. Oxide-mediated recovery of field-effect mobility in plasma-treated $MoS_2$. *Sci. Adv.* **2018**, *4*, eaao5031.

(766) Zheng, S.; Sun, L.; Yin, T.; Dubrovkin, A. M.; Liu, F.; Liu, Z.; Shen, Z. X.; Fan, H. J. Monolayers of $W_xMo_{1-x}S_2$ alloy heterostructure with in-plane composition variations. *Appl. Phys. Lett.* **2015**, *106*, No. 063113.

(767) Susarla, S.; Kochat, V.; Kutana, A.; Hachtel, J. A.; Idrobo, J. C.; Vajtai, R.; Yakobson, B. I.; Tiwary, C. S.; Ajayan, P. M. Phase segregation behavior of two-dimensional transition metal dichalcogenide binary alloys induced by dissimilar substitution. *Chem. Mater.* **2017**, *29*, 7431−7439.

(768) Bogaert, K.; Liu, S.; Liu, T.; Guo, N.; Zhang, C.; Gradecak, S.; Garaj, S. Two-dimensional $Mo_xW_{1-x}S_2$ graded alloys: Growth and optical properties. *Sci. Rep.* **2018**, *8*, 12889.

(769) Yang, R.; Liu, L.; Feng, S.; Liu, Y.; Li, S.; Zhai, K.; Xiang, J.; Mu, C.; Nie, A.; Wen, F.; et al. One-step growth of spatially graded $Mo_{1-x}W_xS_2$ monolayers with a wide span in composition (from $x$ = 0 to 1) at a large scale. *ACS Appl. Mater. Interfaces* **2019**, *11*, 20979−20986.

(770) Susarla, S.; Hachtel, J. A.; Yang, X.; Kutana, A.; Apte, A.; Jin, Z.; Vajtai, R.; Idrobo, J. C.; Lou, J.; Yakobson, B. I.; et al. Thermally induced 2D alloy-heterostructure transformation in quaternary alloys. *Adv. Mater.* **2018**, *30*, 1804218.

(771) Wang, Z.; Liu, P.; Ito, Y.; Ning, S.; Tan, Y.; Fujita, T.; Hirata, A.; Chen, M. Chemical vapor deposition of monolayer $Mo_{1-x}W_xS_2$ crystals with tunable band gaps. *Sci. Rep.* **2016**, *6*, 21536.

(772) Lee, J.; Pak, S.; Lee, Y. W.; Park, Y.; Jang, A. R.; Hong, J.; Cho, Y.; Hou, B.; Lee, S.; Jeong, H. Y.; et al. Direct epitaxial synthesis of selective two-dimensional lateral heterostructures. *ACS Nano* **2019**, *13*, 13047−13055.

(773) Kim, J.; Seung, H.; Kang, D.; Kim, J.; Bae, H.; Park, H.; Kang, S.; Choi, C.; Choi, B. K.; Kim, J. S.; et al. Wafer-scale production of transition metal dichalcogenides and alloy monolayers by nanocrystal conversion for large-scale ultrathin flexible electronics. *Nano Lett.* **2021**, *21*, 9153−9163.

(774) Song, J. G.; Ryu, G. H.; Lee, S. J.; Sim, S.; Lee, C. W.; Choi, T.; Jung, H.; Kim, Y.; Lee, Z.; Myoung, J. M.; et al. Controllable synthesis of molybdenum tungsten disulfide alloy for vertically composition-controlled multilayer. *Nat. Commun.* **2015**, *6*, 7817.

(775) Zheng, Z.; Yao, J.; Yang, G. Centimeter-scale deposition of $Mo_{0.5}W_{0.5}Se_2$ alloy film for high-performance photodetectors on versatile substrates. *ACS Appl. Mater. Interfaces* **2017**, *9*, 14920−14928.

(776) Voiry, D.; Salehi, M.; Silva, R.; Fujita, T.; Chen, M.; Asefa, T.; Shenoy, V. B.; Eda, G.; Chhowalla, M. Conducting $MoS_2$ nanosheets as catalysts for hydrogen evolution reaction. *Nano Lett.* **2013**, *13*, 6222−6227.

(777) Voiry, D.; Yamaguchi, H.; Li, J.; Silva, R.; Alves, D. C.; Fujita, T.; Chen, M.; Asefa, T.; Shenoy, V. B.; Eda, G.; et al. Enhanced catalytic activity in strained chemically exfoliated $WS_2$ nanosheets for hydrogen evolution. *Nat. Mater.* **2013**, *12*, 850−855.

(778) Peng, J.; Liu, Y.; Luo, X.; Wu, J.; Lin, Y.; Guo, Y.; Zhao, J.; Wu, X.; Wu, C.; Xie, Y. High phase purity of large-sized 1T'-$MoS_2$ monolayers with 2D superconductivity. *Adv. Mater.* **2019**, *31*, 1900568.

(779) Yang, R.; Mei, L.; Zhang, Q.; Fan, Y.; Shin, H. S.; Voiry, D.; Zeng, Z. High-yield production of mono- or few-layer transition metal dichalcogenide nanosheets by an electrochemical lithium ion intercalation-based exfoliation method. *Nat. Protoc.* **2022**, *17*, 358−377.

(780) Eda, G.; Fujita, T.; Yamaguchi, H.; Voiry, D.; Chen, M.; Chhowalla, M. Coherent atomic and electronic heterostructures of single-layer $MoS_2$. *ACS Nano* **2012**, *6*, 7311−7317.

(781) Kang, Y.; Najmaei, S.; Liu, Z.; Bao, Y.; Wang, Y.; Zhu, X.; Halas, N. J.; Nordlander, P.; Ajayan, P. M.; Lou, J.; et al. Plasmonic hot electron induced structural phase transition in a $MoS_2$ monolayer. *Adv. Mater.* **2014**, *26*, 6467−6471.

(782) Song, S.; Keum, D. H.; Cho, S.; Perello, D.; Kim, Y.; Lee, Y. H. Room temperature semiconductor-metal transition of $MoTe_2$ thin films engineered by strain. *Nano Lett.* **2016**, *16*, 188−193.

(783) Guo, Y.; Sun, D.; Ouyang, B.; Raja, A.; Song, J.; Heinz, T. F.; Brus, L. E. Probing the dynamics of the metallic-to-semiconducting structural phase transformation in $MoS_2$ crystals. *Nano Lett.* **2015**, *15*, 5081−5088.

(784) Wang, Y.; Xiao, J.; Zhu, H.; Li, Y.; Alsaid, Y.; Fong, K. Y.; Zhou, Y.; Wang, S.; Shi, W.; Wang, Y.; et al. Structural phase transition in monolayer $MoTe_2$ driven by electrostatic doping. *Nature* **2017**, *550*, 487−491.

(785) Tan, Y.; Luo, F.; Zhu, M.; Xu, X.; Ye, Y.; Li, B.; Wang, G.; Luo, W.; Zheng, X.; Wu, N.; et al. Controllable 2H-to-1T' phase transition in few-layer $MoTe_2$. *Nanoscale* **2018**, *10*, 19964−19971.

(786) Lin, Y. C.; Dumcenco, D. O.; Huang, Y. S.; Suenaga, K. Atomic mechanism of the semiconducting-to-metallic phase transition in single-layered $MoS_2$. *Nat. Nanotechnol.* **2014**, *9*, 391−396.

(787) Cho, S.; Kim, S.; Kim, J. H.; Zhao, J.; Seok, J.; Keum, D. H.; Baik, J.; Choe, D. H.; Chang, K. J.; Suenaga, K.; et al. Phase patterning for ohmic homojunction contact in $MoTe_2$. *Science* **2015**, *349*, 625−628.

(788) Zhu, J.; Wang, Z.; Yu, H.; Li, N.; Zhang, J.; Meng, J.; Liao, M.; Zhao, J.; Lu, X.; Du, L.; et al. Argon plasma induced phase transition in monolayer $MoS_2$. *J. Am. Chem. Soc.* **2017**, *139*, 10216−10219.

(789) Cheng, Y.; Nie, A.; Zhang, Q.; Gan, L. Y.; Shahbazian-Yassar, R.; Schwingenschlogl, U. Origin of the phase transition in lithiated molybdenum disulfide. *ACS Nano* **2014**, *8*, 11447−11453.

(790) Huang, Q.; Li, X.; Sun, M.; Zhang, L.; Song, C.; Zhu, L.; Chen, P.; Xu, Z.; Wang, W.; Bai, X. The mechanistic insights into the 2H-1T phase transition of $MoS_2$ upon alkali metal intercalation: From the study of dynamic sodiation processes of $MoS_2$ nanosheets. *Adv. Mater. Interfaces* **2017**, *4*, 1700171.

(791) Gao, G.; Jiao, Y.; Ma, F.; Jiao, Y.; Waclawik, E.; Du, A. Charge mediated semiconducting-to-metallic phase transition in molybdenum disulfide monolayer and hydrogen evolution reaction in new 1T' phase. *J. Phys. Chem. C* **2015**, *119*, 13124−13128.

(792) Voiry, D.; Goswami, A.; Kappera, R.; Silva, C. C.; Kaplan, D.; Fujita, T.; Chen, M.; Asefa, T.; Chhowalla, M. Covalent functionalization of monolayered transition metal dichalcogenides by phase engineering. *Nat. Chem.* **2015**, *7*, 45−49.

(793) Kappera, R.; Voiry, D.; Yalcin, S. E.; Branch, B.; Gupta, G.; Mohite, A. D.; Chhowalla, M. Phase-engineered low-resistance contacts for ultrathin $MoS_2$ transistors. *Nat. Mater.* **2014**, *13*, 1128−1134.

(794) Sun, L.; Yan, X.; Zheng, J.; Yu, H.; Lu, Z.; Gao, S. P.; Liu, L.; Pan, X.; Wang, D.; Wang, Z.; et al. Layer-dependent chemically induced phase transition of two-dimensional $MoS_2$. *Nano Lett.* **2018**, *18*, 3435−3440.

(795) Lin, Y. C.; Yeh, C. H.; Lin, H. C.; Siao, M. D.; Liu, Z.; Nakajima, H.; Okazaki, T.; Chou, M. Y.; Suenaga, K.; Chiu, P. W. Stable 1T tungsten disulfide monolayer and its junctions: Growth and atomic structures. *ACS Nano* **2018**, *12*, 12080−12088.

(796) Zhang, Q.; Xiao, Y.; Zhang, T.; Weng, Z.; Zeng, M.; Yue, S.; Mendes, R. G.; Wang, L.; Chen, S.; Rümmeli, M. H.; et al. Iodine-mediated chemical vapor deposition growth of metastable transition metal dichalcogenides. *Chem. Mater.* **2017**, *29*, 4641−4644.

(797) Kim, T.; Park, H.; Joung, D.; Kim, D.; Lee, R.; Shin, C. H.; Diware, M.; Chegal, W.; Jeong, S. H.; Shin, J. C.; et al. Wafer-scale epitaxial 1T', 1T'-2H mixed, and 2H phases $MoTe_2$ thin films grown by metal-organic chemical vapor deposition. *Adv. Mater. Interfaces* **2018**, *5*, 1800439.

(798) Li, P.; Cui, J.; Zhou, J.; Guo, D.; Zhao, Z.; Yi, J.; Fan, J.; Ji, Z.; Jing, X.; Qu, F.; et al. Phase transition and superconductivity enhancement in Se-substituted $MoTe_2$ thin films. *Adv. Mater.* **2019**, *31*, 1904641.

(799) Fraser, J. P.; Masaityte, L.; Zhang, J.; Laing, S.; Moreno-López, J. C.; McKenzie, A. F.; McGlynn, J. C.; Panchal, V.; Graham, D.; Kazakova, O.; et al. Selective phase growth and precise-layer control in $MoTe_2$. *Commun. Mater.* **2020**, *1*, 48.

(800) Thakur, D.; Kumar, P.; Balakrishnan, V. Phase selective CVD growth and photoinduced 1T → 1H phase transition in a $WS_2$ monolayer. *J. Mater. Chem. C* **2020**, *8*, 10438−10447.

(801) Wang, X.; Shang, J.; Zhu, M.; Zhou, X.; Hao, R.; Sun, L.; Xu, H.; Zheng, J.; Lei, X.; Li, C.; et al. Controlled growth of large-scale uniform 1T' $MoTe_2$ crystals with tunable thickness and their photodetector applications. *Nanoscale Horiz.* **2020**, *5*, 954−959.

(802) Okada, M.; Pu, J.; Lin, Y. C.; Endo, T.; Okada, N.; Chang, W. H.; Lu, A. K. A.; Nakanishi, T.; Shimizu, T.; Kubo, T.; et al. Large-scale 1T'-phase tungsten disulfide atomic layers grown by gas-source chemical vapor deposition. *ACS Nano* **2022**, *16*, 13069−13081.

(803) Lai, Z.; Yao, Y.; Li, S.; Ma, L.; Zhang, Q.; Ge, Y.; Zhai, W.; Chi, B.; Chen, B.; Li, L.; et al. Salt-assisted 2H-to-1T' phase transformation of transition metal dichalcogenides. *Adv. Mater.* **2022**, *34*, 2201194.

(804) Zhou, J.; Zhu, C.; Zhou, Y.; Dong, J.; Li, P.; Zhang, Z.; Wang, Z.; Lin, Y. C.; Shi, J.; Zhang, R.; et al. Composition and phase engineering of metal chalcogenides and phosphorous chalcogenides. *Nat. Mater.* **2023**, *22*, 450−458.

(805) Zhang, C.; Kc, S.; Nie, Y.; Liang, C.; Vandenberghe, W. G.; Longo, R. C.; Zheng, Y.; Kong, F.; Hong, S.; Wallace, R. M.; et al. Charge mediated reversible metal-insulator transition in monolayer $MoTe_2$ and $W_xMo_{1-x}Te_2$ alloy. *ACS Nano* **2016**, *10*, 7370−7375.

(806) Yu, P.; Lin, J.; Sun, L.; Le, Q. L.; Yu, X.; Gao, G.; Hsu, C. H.; Wu, D.; Chang, T. R.; Zeng, Q.; et al. Metal-semiconductor phase-transition in $WSe_{2(1-x)}Te_{2x}$ monolayer. *Adv. Mater.* **2017**, *29*, 1603991.

(807) Wang, Z.; Shen, Y.; Ito, Y.; Zhang, Y.; Du, J.; Fujita, T.; Hirata, A.; Tang, Z.; Chen, M. Synthesizing 1T-1H two-phase $Mo_{1-x}W_xS_2$ monolayers by chemical vapor deposition. *ACS Nano* **2018**, *12*, 1571−1579.
(808) Tang, B.; Zhou, J.; Sun, P.; Wang, X.; Bai, L.; Dan, J.; Yang, J.; Zhou, K.; Zhao, X.; Pennycook, S. J.; Liu, Z. Phase-controlled synthesis of monolayer ternary telluride with a random local displacement of tellurium atoms. *Adv. Mater.* **2019**, *31*, 1900862.
(809) Cheng, F.; Hu, Z.; Xu, H.; Shao, Y.; Su, J.; Chen, Z.; Ji, W.; Loh, K. P. Interface engineering of Au(111) for the growth of 1T'-$MoSe_2$. *ACS Nano* **2019**, *13*, 2316−2323.
(810) Chen, W.; Hu, M.; Zong, J.; Xie, X.; Meng, Q.; Yu, F.; Wang, L.; Ren, W.; Chen, A.; Liu, G.; et al. Epitaxial growth of single-phase 1T'-$WSe_2$ monolayer with assistance of enhanced interface interaction. *Adv. Mater.* **2021**, *33*, 2004930.
(811) Liu, L.; Wu, J.; Wu, L.; Ye, M.; Liu, X.; Wang, Q.; Hou, S.; Lu, P.; Sun, L.; Zheng, J.; et al. Phase-selective synthesis of 1T' $MoS_2$ monolayers and heterophase bilayers. *Nat. Mater.* **2018**, *17*, 1108−1114.
(812) Yu, Y.; Nam, G. H.; He, Q.; Wu, X. J.; Zhang, K.; Yang, Z.; Chen, J.; Ma, Q.; Zhao, M.; Liu, Z.; et al. High phase-purity 1T'-$MoS_2$- and 1T'-$MoSe_2$-layered crystals. *Nat. Chem.* **2018**, *10*, 638−643.
(813) Lai, Z.; He, Q.; Tran, T. H.; Repaka, D. V. M.; Zhou, D. D.; Sun, Y.; Xi, S.; Li, Y.; Chaturvedi, A.; Tan, C.; et al. Metastable 1T'-phase group VIB transition metal dichalcogenide crystals. *Nat. Mater.* **2021**, *20*, 1113−1120.
(814) Tosun, M.; Chan, L.; Amani, M.; Roy, T.; Ahn, G. H.; Taheri, P.; Carraro, C.; Ager, J. W.; Maboudian, R.; Javey, A. Air-stable n-doping of $WSe_2$ by anion vacancy formation with mild plasma treatment. *ACS Nano* **2016**, *10*, 6853−6860.
(815) Man, P.; Jiang, S.; Leung, K. H.; Lai, K. H.; Guang, Z. Q.; Chen, H. L.; Huang, L. L.; Chen, T. R.; Gao, S.; Peng, Y. K.; et al. Salt-induced high-density vacancy-rich 2D $MoS_2$ for efficient hydrogen evolution. *Adv. Mater.* **2024**, *36*, 2304808.
(816) Zhou, W.; Zou, X.; Najmaei, S.; Liu, Z.; Shi, Y.; Kong, J.; Lou, J.; Ajayan, P. M.; Yakobson, B. I.; Idrobo, J. C. Intrinsic structural defects in monolayer molybdenum disulfide. *Nano Lett.* **2013**, *13*, 2615−2622.
(817) Hong, J. H.; Hu, Z. X.; Probert, M.; Li, K.; Lv, D. H.; Yang, X. N.; Gu, L.; Mao, N. N.; Feng, Q. L.; Xie, L. M.; et al. Exploring atomic defects in molybdenum disulphide monolayers. *Nat. Commun.* **2015**, *6*, 6293.
(818) Cheng, J.; Jiang, T.; Ji, Q.; Zhang, Y.; Li, Z.; Shan, Y.; Zhang, Y.; Gong, X.; Liu, W.; Wu, S. Kinetic nature of grain boundary formation in as-grown $MoS_2$ monolayers. *Adv. Mater.* **2015**, *27*, 4069−4074.
(819) Ge, J.; Luo, T. C.; Lin, Z. Z.; Shi, J. P.; Liu, Y. Z.; Wang, P. Y.; Zhang, Y. F.; Duan, W. H.; Wang, J. Magnetic moments induced by atomic vacancies in transition metal dichalcogenide flakes. *Adv. Mater.* **2021**, *33*, 2005465.
(820) Zhu, Y. R.; Lim, J.; Zhang, Z. P.; Wang, Y.; Sarkar, S.; Ramsden, H.; Li, Y.; Yan, H.; Phuyal, D.; Gauriot, N.; et al. Room-temperature photoluminescence mediated by sulfur vacancies in 2D molybdenum disulfide. *ACS Nano* **2023**, *17*, 13545−13553.
(821) Nan, H. Y.; Wang, Z. L.; Wang, W. H.; Liang, Z.; Lu, Y.; Chen, Q.; He, D. W.; Tan, P. H.; Miao, F.; Wang, X. R.; et al. Strong photoluminescence enhancement of $MoS_2$ through defect engineering and oxygen bonding. *ACS Nano* **2014**, *8*, 5738−5745.
(822) Pandey, M.; Rasmussen, F. A.; Kuhar, K.; Olsen, T.; Jacobsen, K. W.; Thygesen, K. S. Defect-tolerant monolayer transition metal dichalcogenides. *Nano Lett.* **2016**, *16*, 2234−2239.
(823) Ly, T. H.; Perello, D. J.; Zhao, J.; Deng, Q.; Kim, H.; Han, G. H.; Chae, S. H.; Jeong, H. Y.; Lee, Y. H. Misorientation-angle-dependent electrical transport across molybdenum disulfide grain boundaries. *Nat. Commun.* **2016**, *7*, 10426.
(824) Pak, S.; Jang, S.; Kim, T.; Lim, J.; Hwang, J. S.; Cho, Y.; Chang, H.; Jang, A.-R.; Park, K.-H.; Hong, J.; Cha, S. Electrode-induced self-healed monolayer $MoS_2$ for high performance transistors and phototransistors. *Adv. Mater.* **2021**, *33*, 2102091.
(825) Zhao, X. X.; Ji, Y. J.; Chen, J. Y.; Fu, W.; Dan, J. D.; Liu, Y. Y.; Pennycook, S. J.; Zhou, W.; Loh, K. P. Healing of planar defects in 2D materials via grain boundary sliding. *Adv. Mater.* **2019**, *31*, 1900237.
(826) Zhang, X. K.; Liao, Q. L.; Liu, S.; Kang, Z.; Zhang, Z.; Du, J. L.; Li, F.; Zhang, S. H.; Xiao, J. K.; Liu, B. S.; et al. Poly(4-styrenesulfonate)-induced sulfur vacancy self-healing strategy for monolayer $MoS_2$ homojunction photodiode. *Nat. Commun.* **2017**, *8*, 15881.
(827) Liu, S.; Liu, Y.; Holtzman, L.; Li, B.; Holbrook, M.; Pack, J.; Taniguchi, T.; Watanabe, K.; Dean, C. R.; Pasupathy, A. N.; et al. Two-step flux synthesis of ultrapure transition-metal dichalcogenides. *ACS Nano* **2023**, *17*, 16587−16596.
(828) Zhang, X.; Liao, Q.; Kang, Z.; Liu, B.; Liu, X.; Ou, Y.; Xiao, J.; Du, J.; Liu, Y.; Gao, L.; et al. Hidden vacancy benefit in monolayer 2D semiconductors. *Adv. Mater.* **2021**, *33*, e2007051.
(829) Xiao, J. K.; Chen, K. L.; Zhang, X. K.; Liu, X. Z.; Yu, H. H.; Gao, L.; Hong, M. Y.; Gu, L.; Zhang, Z.; Zhang, Y. Approaching ohmic contacts for ideal monolayer $MoS_2$ transistors through sulfur-vacancy engineering. *Small Methods* **2023**, *7*, 2300611.
(830) Deng, J.; Li, H. B.; Xiao, J. P.; Tu, Y. C.; Deng, D. H.; Yang, H. X.; Tian, H. F.; Li, J. Q.; Ren, P. J.; Bao, X. H. Triggering the electrocatalytic hydrogen evolution activity of the inert two-dimensional $MoS_2$ surface single-atom metal doping. *Energy Environl. Sci.* **2015**, *8*, 1594−1601.
(831) Gao, C.; Rao, D. W.; Yang, H.; Yang, S. K.; Ye, J. J.; Yang, S. S.; Zhang, C. N.; Zhou, X. C.; Jing, T. Y.; Yan, X. H. Dual transition-metal atoms doping: An effective route to promote the ORR and OER activity on $MoTe_2$. *New J. Chem.* **2021**, *45*, 5589−5595.
(832) Jiang, K.; Luo, M.; Liu, Z. X.; Peng, M.; Chen, D. C.; Lu, Y. R.; Chan, T. S.; de Groot, F. M. F.; Tan, Y. W. Rational strain engineering of single-atom ruthenium on nanoporous $MoS_2$ for highly efficient hydrogen evolution. *Nat. Commun.* **2021**, *12*, 1687.
(833) Xuan, N. N.; Chen, J. H.; Shi, J. J.; Yue, Y. W.; Zhuang, P. Y.; Ba, K.; Sun, Y. Y.; Shen, J. F.; Liu, Y. Y.; Ge, B. H.; et al. Single-atom electroplating on two dimensional materials. *Chem. Mater.* **2019**, *31*, 429−435.
(834) Zhang, J. M.; Xu, X. P.; Yang, L.; Cheng, D. J.; Cao, D. P. Single-atom Ru doping induced phase transition of $MoS_2$ and s vacancy for hydrogen evolution reaction. *Small Methods* **2019**, *3*, 1900653.
(835) Li, H.; Tsai, C.; Koh, A. L.; Cai, L. L.; Contryman, A. W.; Fragapane, A. H.; Zhao, J. H.; Han, H. S.; Manoharan, H. C.; Abild-Pedersen, F.; et al. Activating and optimizing $MoS_2$ basal planes for hydrogen evolution through the formation of strained sulphur vacancies. *Nat. Mater.* **2016**, *15*, 48−53.
(836) Xu, J.; Shao, G.; Tang, X.; Lv, F.; Xiang, H.; Jing, C.; Liu, S.; Dai, S.; Li, Y.; Luo, J.; Zhou, Z. Frenkel-defected monolayer $MoS_2$ catalysts for efficient hydrogen evolution. *Nat. Commun.* **2022**, *13*, 2193.
(837) Ma, X. L.; Zhang, J. X.; Sun, Y.; Wu, C.; Geng, G. Y.; Zhang, J.; Wu, E. X.; Xu, L. Y.; Wu, S.; Hu, X. D.; et al. Engineering of oxidized line defects on CVD-grown $MoS_2$ flakes. *ACS Appl. Mater. Interfaces* **2022**, *14*, 47288−47299.
(838) He, Y. M.; Liu, L. R.; Zhu, C.; Guo, S. S.; Golani, P.; Koo, B.; Tang, P. Y.; Zhao, Z. Q.; Xu, M. Z.; Yu, P.; et al. Amorphizing noble metal chalcogenide catalysts at the single-layer limit towards hydrogen production. *Nat. Catal.* **2022**, *5*, 212−221.
(839) He, Y. M.; Tang, P. Y.; Hu, Z. L.; He, Q. Y.; Zhu, C.; Wang, L. Q.; Zeng, Q. S.; Golani, P.; Gao, G. H.; Fu, W.; et al. Engineering grain boundaries at the 2D limit for the hydrogen evolution reaction. *Nat. Commun.* **2020**, *11*, 57.
(840) Hus, S. M.; Ge, R. J.; Chen, P. A.; Liang, L. B.; Donnelly, G. E.; Ko, W.; Huang, F. M.; Chiang, M. H.; Li, A. P.; Akinwande, D. Observation of single-defect memristor in an $MoS_2$ atomic sheet. *Nat. Nanotechnol.* **2021**, *16*, 58−62.

(841) Choi, W. B.; Kim, J. Y.; Lee, E. H.; Mehta, G.; Prasad, V. Asymmetric 2D $MoS_2$ for scalable and high-performance piezoelectric sensors. *ACS Appl. Mater. Interfaces* **2021**, *13*, 13596−13603.
(842) Huang, C.; Wu, S.; Sanchez, A. M.; Peters, J. J.; Beanland, R.; Ross, J. S.; Rivera, P.; Yao, W.; Cobden, D. H.; Xu, X. Lateral heterojunctions within monolayer $MoSe_2$-$WSe_2$ semiconductors. *Nat. Mater.* **2014**, *13*, 1096−1101.
(843) Gong, Y.; Lin, J.; Wang, X.; Shi, G.; Lei, S.; Lin, Z.; Zou, X.; Ye, G.; Vajtai, R.; Yakobson, B. I.; et al. Vertical and in-plane heterostructures from $WS_2/MoS_2$ monolayers. *Nat. Mater.* **2014**, *13*, 1135−1142.
(844) Heo, H.; Sung, J. H.; Jin, G.; Ahn, J. H.; Kim, K.; Lee, M. J.; Cha, S.; Choi, H.; Jo, M. H. Rotation-misfit-free heteroepitaxial stacking and stitching growth of hexagonal transition-metal dichalcogenide monolayers by nucleation kinetics controls. *Adv. Mater.* **2015**, *27*, 3803−3810.
(845) Duan, X.; Wang, C.; Shaw, J. C.; Cheng, R.; Chen, Y.; Li, H.; Wu, X.; Tang, Y.; Zhang, Q.; Pan, A.; et al. Lateral epitaxial growth of two-dimensional layered semiconductor heterojunctions. *Nat. Nanotechnol.* **2014**, *9*, 1024−1030.
(846) Choudhary, N.; Park, J.; Hwang, J. Y.; Chung, H. S.; Dumas, K. H.; Khondaker, S. I.; Choi, W.; Jung, Y. Centimeter scale patterned growth of vertically stacked few layer only 2D $MoS_2/WS_2$ van der Waals heterostructure. *Sci. Rep* **2016**, *6*, 25456.
(847) Islam, M. A.; Kim, J. H.; Schropp, A.; Kalita, H.; Choudhary, N.; Weitzman, D.; Khondaker, S. I.; Oh, K. H.; Roy, T.; Chung, H. S.; et al. Centimeter-scale 2D van der Waals vertical heterostructures integrated on deformable substrates enabled by gold sacrificial layer-assisted growth. *Nano Lett.* **2017**, *17*, 6157−6165.
(848) Li, M. Y.; Shi, Y.; Cheng, C. C.; Lu, L. S.; Lin, Y. C.; Tang, H. L.; Tsai, M. L.; Chu, C. W.; Wei, K. H.; He, J. H.; et al. Epitaxial growth of a monolayer $WSe_2$-$MoS_2$ lateral p−n junction with an atomically sharp interface. *Science* **2015**, *349*, 524−528.
(849) Gong, Y.; Lei, S.; Ye, G.; Li, B.; He, Y.; Keyshar, K.; Zhang, X.; Wang, Q.; Lou, J.; Liu, Z.; et al. Two-step growth of two-dimensional $WSe_2/MoSe_2$ heterostructures. *Nano Lett.* **2015**, *15*, 6135−6141.
(850) Zhou, W.; Zhang, Y. Y.; Chen, J.; Li, D.; Zhou, J.; Liu, Z.; Chisholm, M. F.; Pantelides, S. T.; Loh, K. P. Dislocation-driven growth of two-dimensional lateral quantum-well superlattices. *Sci. Adv.* **2018**, *4*, eaap9096.
(851) Liu, D.; Hong, J.; Li, X.; Zhou, X.; Jin, B.; Cui, Q.; Chen, J.; Feng, Q.; Xu, C.; Zhai, T.; et al. Synthesis of 2H-1T′ $WS_2$-$ReS_2$ heterophase structures with atomically sharp interface via hydrogen-triggered one-pot growth. *Adv. Funct. Mater.* **2020**, *30*, 1910169.
(852) Xie, S.; Tu, L.; Han, Y.; Huang, L.; Kang, K.; Lao, K. U.; Poddar, P.; Park, C.; Muller, D. A.; DiStasio, R. A., Jr.; et al. Coherent, atomically thin transition-metal dichalcogenide superlattices with engineered strain. *Science* **2018**, *359*, 1131−1136.
(853) Sahoo, P. K.; Memaran, S.; Xin, Y.; Balicas, L.; Gutierrez, H. R. One-pot growth of two-dimensional lateral heterostructures via sequential edge-epitaxy. *Nature* **2018**, *553*, 63−67.
(854) Huang, Z.; Deng, W.; Zhang, Z.; Zhao, B.; Zhang, H.; Wang, D.; Li, B.; Liu, M.; Huangfu, Y.; Duan, X. Terminal atom-controlled etching of 2D-TMDs. *Adv. Mater.* **2023**, *35*, e2211252.
(855) Zhang, Z.; Huang, Z.; Li, J.; Wang, D.; Lin, Y.; Yang, X.; Liu, H.; Liu, S.; Wang, Y.; Li, B.; et al. Endoepitaxial growth of monolayer mosaic heterostructures. *Nat. Nanotechnol.* **2022**, *17*, 493−499.
(856) Park, S.; Yun, S. J.; Kim, Y. I.; Kim, J. H.; Kim, Y. M.; Kim, K. K.; Lee, Y. H. Tailoring domain morphology in monolayer $NbSe_2$ and $W_xNb_{1-x}Se_2$ heterostructure. *ACS Nano* **2020**, *14*, 8784−8792.
(857) Fu, Q.; Wang, X.; Zhou, J.; Xia, J.; Zeng, Q.; Lv, D.; Zhu, C.; Wang, X.; Shen, Y.; Li, X.; et al. One-step synthesis of metal/semiconductor heterostructure $NbS_2/MoS_2$. *Chem. Mater.* **2018**, *30*, 4001−4007.
(858) Zhang, K.; Ding, C.; Pan, B.; Wu, Z.; Marga, A.; Zhang, L.; Zeng, H.; Huang, S. Visualizing Van der Waals epitaxial growth of 2D heterostructures. *Adv. Mater.* **2021**, *33*, e2105079.
(859) Liu, L.; Zhai, T. Wafer-scale vertical van der Waals heterostructures. *InfoMat* **2021**, *3*, 3−21.
(860) Shi, J.; Tong, R.; Zhou, X.; Gong, Y.; Zhang, Z.; Ji, Q.; Zhang, Y.; Fang, Q.; Gu, L.; Wang, X.; et al. Temperature-mediated selective growth of $MoS_2$ /$WS_2$ and $WS_2$ /$MoS_2$ vertical stacks on Au foils for direct photocatalytic applications. *Adv. Mater.* **2016**, *28*, 10664−10672.
(861) Jin, G.; Lee, C. S.; Okello, O. F. N.; Lee, S. H.; Park, M. Y.; Cha, S.; Seo, S. Y.; Moon, G.; Min, S. Y.; Yang, D. H.; et al. Heteroepitaxial van der Waals semiconductor superlattices. *Nat. Nanotechnol.* **2021**, *16*, 1092−1098.
(862) Fivaz, R.; Mooser, E. Mobility of charge carriers in semiconducting layer structures. *Phys. Rev.* **1967**, *163*, 743−755.
(863) Palummo, M.; Bernardi, M.; Grossman, J. C. Exciton radiative lifetimes in two-dimensional transition metal dichalcogenides. *Nano Lett.* **2015**, *15*, 2794−2800.
(864) Luo, R.; Gao, M.; Wang, C.; Zhu, J.; Guzman, R.; Zhou, W. Probing functional structures, defects, and interfaces of 2D transition metal dichalcogenides by electron microscopy. *Adv. Funct. Mater.* **2024**, *34*, 07625.
(865) Binnig, G.; Rohrer, H.; Gerber, C.; Weibel, E. Tunneling through a controllable vacuum gap. *Appl. Phys. Lett.* **1982**, *40*, 178−180.
(866) Zhao, X. X.; Loh, K. P.; Pennycook, S. J. Electron beam triggered single-atom dynamics in two-dimensional materials. *J. Phys.: Condens. Matter* **2021**, *33*, No. 063001.
(867) Eigler, D. M.; Schweizer, E. K. Positioning single atoms with a scanning tunneling microscope. *Nature* **1990**, *344*, 524−526.
(868) Lee, J. U.; Woo, S.; Park, J.; Park, H. C.; Son, Y. W.; Cheong, H. Strain-shear coupling in bilayer $MoS_2$. *Nat. Commun.* **2017**, *8*, 1370.
(869) Vu, V.; Vu, T. T. H.; Phan, T. L.; Kang, W. T.; Kim, Y. R.; Tran, M. D.; Nguyen, H. T. T.; Lee, Y. H.; Yu, W. J. One-step synthesis of $NbSe_2$/Nb-doped-$WSe_2$ metal/doped-semiconductor van der Waals heterostructures for doping controlled ohmic contact. *ACS Nano* **2021**, *15*, 13031−13040.
(870) Taghizadeh, A.; Leffers, U.; Pedersen, T. G.; Thygesen, K. S. A library of ab initio Raman spectra for automated identification of 2D materials. *Nat. Commun.* **2020**, *11*, 3011.
(871) Jadczak, J.; Dumcenco, D. O.; Huang, Y. S.; Lin, Y. C.; Suenaga, K.; Wu, P. H.; Hsu, H. P.; Tiong, K. K. Composition dependent lattice dynamics in $MoS_xSe_{(2-x)}$ alloys. *J. Appl. Phys.* **2014**, *116*, 193505.
(872) Parkin, W. M.; Balan, A.; Liang, L. B.; Das, P. M.; Lamparski, M.; Naylor, C. H.; Rodríguez-Manzo, J. A.; Johnson, A. T. C.; Meunier, V.; Drndic, M. Raman shifts in electron-irradiated monolayer $MoS_2$. *ACS Nano* **2016**, *10*, 4134−4142.
(873) Mignuzzi, S.; Pollard, A. J.; Bonini, N.; Brennan, B.; Gilmore, I. S.; Pimenta, M. A.; Richards, D.; Roy, D. Effect of disorder on Raman scattering of single-layer $MoS_2$. *Phys. Rev. B* **2015**, *91*, 195411.
(874) Jiang, Y.; Wang, X.; Pan, A. L. Properties of excitons and photogenerated charge carriers in metal halide perovskites. *Adv. Mater.* **2019**, *31*, 1806671.
(875) Kaupmees, R.; Komsa, H.-P.; Krustok, J. Photoluminescence study of B-Trions in $MoS_2$ monolayers with high density of defects. *Phys. Status Solidi B* **2019**, *256*, 1800384.
(876) Lorchat, E.; López, L. E. P.; Robert, C.; Lagarde, D.; Froehlicher, G.; Taniguchi, T.; Watanabe, K.; Marie, X.; Berciaud, S. Filtering the photoluminescence spectra of atomically thin semiconductors with graphene. *Nat. Nanotechnol.* **2020**, *15*, 283−288.
(877) Tongay, S.; Suh, J.; Ataca, C.; Fan, W.; Luce, A.; Kang, J. S.; Liu, J.; Ko, C.; Raghunathanan, R.; Zhou, J.; et al. Defects activated photoluminescence in two-dimensional semiconductors: Interplay between bound, charged, and free excitons. *Sci. Rep.* **2013**, *3*, 2657.
(878) Ly, T. H.; Chiu, M.-H.; Li, M.-Y.; Zhao, J.; Perello, D. J.; Cichocka, M. O.; Oh, H. M.; Chae, S. H.; Jeong, H. Y.; Yao, F.; et al. Observing grain boundaries in CVD-grown monolayer transition metal dichalcogenides. *ACS Nano* **2014**, *8*, 11401−11408.
(879) Jeong, H. Y.; Lee, S. Y.; Ly, T. H.; Han, G. H.; Kim, H.; Nam, H.; Jiong, Z.; Shin, B. G.; Yun, S. J.; Kim, J.; et al. Visualizing point

defects in transition-metal dichalcogenides using optical microscopy. *ACS Nano* **2016**, *10*, 770−777.
(880) Wang, J.; Xu, X.; Qiao, R.; Liang, J.; Liu, C.; Zheng, B.; Liu, L.; Gao, P.; Jiao, Q.; Yu, D.; et al. Visualizing grain boundaries in monolayer $MoSe_2$ using mild $H_2O$ vapor etching. *Nano Res.* **2018**, *11*, 4082−4089.
(881) Xu, C. Y.; Qin, J. K.; Yan, H.; Li, Y.; Shao, W. Z.; Zhen, L. Homogeneous surface oxidation and triangle patterning of monolayer $MoS_2$ by hydrogen peroxide. *Appl. Surf. Sci.* **2018**, *452*, 451−456.
(882) Guo, Y. T.; Wang, Q. Q.; Li, X. M.; Wei, Z.; Li, L.; Peng, Y. L.; Yang, W.; Yang, R.; Shi, D. X.; Bai, X. D.; et al. Direct visualization of structural defects in 2D semiconductors. *Chin. Phys. B* **2022**, *31*, No. 076105.
(883) Wang, J. H.; Huang, C.; You, Y. L.; Guo, Q. L.; Xue, G. D.; Hong, H.; Jiao, Q. Z.; Yu, D. P.; Du, L. N.; Zhao, Y.; et al. Monitoring the material quality of two-dimensional transition metal dichalcogenides. *J. Phys. Chem. C* **2022**, *126*, 3797−3810.
(884) Ho, Y. T.; Ma, C. H.; Luong, T. T.; Wei, L. L.; Yen, T. C.; Hsu, W. T.; Chang, W. H.; Chu, Y. C.; Tu, Y. Y.; Pande, K. P.; et al. Layered $MoS_2$ grown on c-sapphire by pulsed laser deposition. *Phys. Status Solidi RRL* **2015**, *9*, 187−191.
(885) Xenogiannopoulou, E.; Tsipas, P.; Aretouli, K. E.; Tsoutsou, D.; Giamini, S. A.; Bazioti, C.; Dimitrakopulos, G. P.; Komninou, P.; Brems, S.; Huyghebaert, C.; et al. High-quality, large-area $MoSe_2$ and $MoSe_2/Bi_2Se_3$ heterostructures on AlN(0001)/Si(111) substrates by molecular beam epitaxy. *Nanoscale* **2015**, *7*, 7896−7905.
(886) Liu, Z.; Amani, M.; Najmaei, S.; Xu, Q.; Zou, X.; Zhou, W.; Yu, T.; Qiu, C.; Birdwell, A. G.; Crowne, F. J.; et al. Strain and structure heterogeneity in $MoS_2$ atomic layers grown by chemical vapour deposition. *Nat. Commun.* **2014**, *5*, 5246.
(887) Cheng, J.; Jiang, T.; Ji, Q.; Zhang, Y.; Li, Z.; Shan, Y.; Zhang, Y.; Gong, X.; Liu, W.; Wu, S. Kinetic nature of grain boundary formation in as-grown $MoS_2$ monolayers. *Adv. Mater.* **2015**, *27*, 4069−4074.
(888) Karvonen, L.; Säynätjoki, A.; Huttunen, M. J.; Autere, A.; Amirsolaimani, B.; Li, S.; Norwood, R. A.; Peyghambarian, N.; Lipsanen, H.; Eda, G.; et al. Rapid visualization of grain boundaries in monolayer $MoS_2$ by multiphoton microscopy. *Nat. Commun.* **2017**, *8*, 15714.
(889) Chubarov, M.; Choudhury, T. H.; Zhang, X.; Redwing, J. M. In-plane X-ray diffraction for characterization of monolayer and few-layer transition metal dichalcogenide films. *Nanotechnology* **2018**, *29*, No. 055706.
(890) Bana, H.; Travaglia, E.; Bignardi, L.; Lacovig, P.; Sanders, C. E.; Dendzik, M.; Michiardi, M.; Bianchi, M.; Lizzit, D.; Presel, F.; et al. Epitaxial growth of single-orientation high-quality $MoS_2$ monolayers. *2D Mater.* **2018**, *5*, No. 035012.
(891) Gaur, A. P.; Sahoo, S.; Ahmadi, M.; Dash, S. P.; Guinel, M. J.; Katiyar, R. S. Surface energy engineering for tunable wettability through controlled synthesis of $MoS_2$. *Nano Lett.* **2014**, *14*, 4314−4321.
(892) Annamalai, M.; Gopinadhan, K.; Han, S. A.; Saha, S.; Park, H. J.; Cho, E. B.; Kumar, B.; Patra, A.; Kim, S. W.; Venkatesan, T. Surface energy and wettability of van der Waals structures. *Nanoscale* **2016**, *8*, 5764−5770.
(893) Bertolazzi, S.; Brivio, J.; Kis, A. Stretching and breaking of ultrathin $MoS_2$. *ACS Nano* **2011**, *5*, 9703−9709.
(894) Meitl, M. A.; Zhu, Z.-T.; Kumar, V.; Lee, K. J.; Feng, X.; Huang, Y. Y.; Adesida, I.; Nuzzo, R. G.; Rogers, J. A. Transfer printing by kinetic control of adhesion to an elastomeric stamp. *Nat. Mater.* **2006**, *5*, 33−38.
(895) Ponomarenko, L. A.; Geim, A. K.; Zhukov, A. A.; Jalil, R.; Morozov, S. V.; Novoselov, K. S.; Grigorieva, I. V.; Hill, E. H.; Cheianov, V. V.; Fal'ko, V. I.; et al. Tunable metal-insulator transition in double-layer graphene heterostructures. *Nat. Phys.* **2011**, *7*, 958−961.
(896) Wang, X.; Chen, X.; Ma, J.; Gou, S.; Guo, X.; Tong, L.; Zhu, J.; Xia, Y.; Wang, D.; Sheng, C.; et al. Pass-transistor logic circuits based on wafer-scale 2D semiconductors. *Adv. Mater.* **2022**, *34*, 2202472.
(897) Polyushkin, D. K.; Wachter, S.; Mennel, L.; Paur, M.; Paliy, M.; Iannaccone, G.; Fiori, G.; Neumaier, D.; Canto, B.; Mueller, T. Analogue two-dimensional semiconductor electronics. *Nat. Electron.* **2020**, *3*, 486−491.
(898) Lopez-Sanchez, O.; Lembke, D.; Kayci, M.; Radenovic, A.; Kis, A. Ultrasensitive photodetectors based on monolayer $MoS_2$. *Nat. Nanotechnol.* **2013**, *8*, 497−501.
(899) Wu, D.; Guo, C.; Zeng, L.; Ren, X.; Shi, Z.; Wen, L.; Chen, Q.; Zhang, M.; Li, X. J.; Shan, C.-X.; Jie, J. Phase-controlled van der Waals growth of wafer-scale 2D $MoTe_2$ layers for integrated high-sensitivity broadband infrared photodetection. *Light Sci. Appl.* **2023**, *12*, 5.
(900) Reina, A.; Son, H.; Jiao, L.; Fan, B.; Dresselhaus, M. S.; Liu, Z.; Kong, J. Transferring and identification of single-and few-layer graphene on arbitrary substrates. *J. Phys. Chem. C* **2008**, *112*, 17741−17744.
(901) Zhang, S.; Xu, H.; Liao, F.; Sun, Y.; Ba, K.; Sun, Z.; Qiu, Z. J.; Xu, Z.; Zhu, H.; Chen, L.; et al. Wafer-scale transferred multilayer $MoS_2$ for high performance field effect transistors. *Nanotechnology* **2019**, *30*, 174002.
(902) Zhang, D.; Du, J.; Hong, Y. L.; Zhang, W.; Wang, X.; Jin, H.; Burn, P. L.; Yu, J.; Chen, M.; Sun, D. M.; et al. A double support layer for facile clean transfer of two-dimensional materials for high-performance electronic and optoelectronic devices. *ACS Nano* **2019**, *13*, 5513−5522.
(903) Mondal, A.; Biswas, C.; Park, S.; Cha, W.; Kang, S. H.; Yoon, M.; Choi, S. H.; Kim, K. K.; Lee, Y. H. Low ohmic contact resistance and high on/off ratio in transition metal dichalcogenides field-effect transistors via residue-free transfer. *Nat. Nanotechnol.* **2024**, *19*, 34−43.
(904) Chen, Y.-J.; Cain, J. D.; Stanev, T. K.; Dravid, V. P.; Stern, N. P. Valley-polarized exciton-polaritons in a monolayer semiconductor. *Nat. Photonics* **2017**, *11*, 431−435.
(905) Wood, J. D.; Doidge, G. P.; Carrion, E. A.; Koepke, J. C.; Kaitz, J. A.; Datye, I.; Behnam, A.; Hewaparakrama, J.; Aruin, B.; Chen, Y.; et al. Annealing free, clean graphene transfer using alternative polymer scaffolds. *Nanotechnology* **2015**, *26*, No. 055302.
(906) Whelan, P. R.; Jessen, B. S.; Wang, R.; Luo, B.; Stoot, A. C.; Mackenzie, D. M. A.; Braeuninger-Weimer, P.; Jouvray, A.; Prager, L.; Camilli, L.; et al. Raman spectral indicators of catalyst decoupling for transfer of CVD grown 2D materials. *Carbon* **2017**, *117*, 75−81.
(907) Quellmalz, A.; Wang, X.; Sawallich, S.; Uzlu, B.; Otto, M.; Wagner, S.; Wang, Z.; Prechtl, M.; Hartwig, O.; Luo, S.; et al. Large-area integration of two-dimensional materials and their heterostructures by wafer bonding. *Nat. Commun.* **2021**, *12*, 917.
(908) Gao, L.; Ren, W.; Xu, H.; Jin, L.; Wang, Z.; Ma, T.; Ma, L. P.; Zhang, Z.; Fu, Q.; Peng, L. M.; et al. Repeated growth and bubbling transfer of graphene with millimetre-size single-crystal grains using platinum. *Nat. Commun.* **2012**, *3*, 699.
(909) Ma, D.; Shi, J.; Ji, Q.; Chen, K.; Yin, J.; Lin, Y.; Zhang, Y.; Liu, M.; Feng, Q.; Song, X.; et al. A universal etching-free transfer of $MoS_2$ films for applications in photodetectors. *Nano Res.* **2015**, *8*, 3662−3672.
(910) Castellanos-Gomez, A.; Buscema, M.; Molenaar, R.; Singh, V.; Janssen, L.; van der Zant, H. S. J.; Steele, G. A. Deterministic transfer of two-dimensional materials by all-dry viscoelastic stamping. *2D Mater.* **2014**, *1*, No. 011002.
(911) Kim, K.; Yankowitz, M.; Fallahazad, B.; Kang, S.; Movva, H. C.; Huang, S.; Larentis, S.; Corbet, C. M.; Taniguchi, T.; Watanabe, K.; et al. Van der Waals heterostructures with high accuracy rotational alignment. *Nano Lett.* **2016**, *16*, 1989−1995.
(912) Lee, Y. H.; Yu, L.; Wang, H.; Fang, W.; Ling, X.; Shi, Y.; Lin, C. T.; Huang, J. K.; Chang, M. T.; Chang, C. S.; et al. Synthesis and transfer of single-layer transition metal disulfides on diverse surfaces. *Nano Lett.* **2013**, *13*, 1852−1857.
(913) Gurarslan, A.; Yu, Y.; Su, L.; Yu, Y.; Suarez, F.; Yao, S.; Zhu, Y.; Ozturk, M.; Zhang, Y.; Cao, L. Surface-energy-assisted perfect

transfer of centimeter-scale monolayer and few-layer $MoS_2$ films onto arbitrary substrates. *ACS Nano* **2014**, *8*, 11522−11528.
(914) Phan, H. D.; Kim, Y.; Lee, J.; Liu, R.; Choi, Y.; Cho, J. H.; Lee, C. Ultraclean and direct transfer of a wafer-scale $MoS_2$ thin film onto a plastic substrate. *Adv. Mater.* **2017**, *29*, 1603928.
(915) Cai, J.; Chen, H.; Ke, Y.; Deng, S. A capillary-force-assisted transfer for monolayer transition-metal-dichalcogenide crystals with high utilization. *ACS Nano* **2022**, *16*, 15016−15025.
(916) Xu, Z. Q.; Zhang, Y.; Lin, S.; Zheng, C.; Zhong, Y. L.; Xia, X.; Li, Z.; Sophia, P. J.; Fuhrer, M. S.; Cheng, Y. B.; et al. Synthesis and transfer of large-area monolayer $WS_2$ crystals: Moving toward the recyclable use of sapphire substrates. *ACS Nano* **2015**, *9*, 6178−6187.
(917) Hong, M.; Yang, P.; Zhou, X.; Zhao, S.; Xie, C.; Shi, J.; Zhang, Z.; Fu, Q.; Zhang, Y. Decoupling the interaction between wet-transferred $MoS_2$ and graphite substrate by an interfacial water layer. *Adv. Mater. Interfaces* **2018**, *5*, 1800641.
(918) Liu, H.; Thi, Q. H.; Man, P.; Chen, X.; Chen, T.; Wong, L. W.; Jiang, S.; Huang, L.; Yang, T.; Leung, K. H.; et al. Controlled adhesion of ice-toward ultraclean 2D materials. *Adv. Mater.* **2023**, *35*, 2210503.
(919) Lin, Z.; Zhao, Y.; Zhou, C.; Zhong, R.; Wang, X.; Tsang, Y. H.; Chai, Y. Controllable growth of large-size crystalline $MoS_2$ and resist-free transfer assisted with a Cu thin film. *Sci. Rep.* **2016**, *5*, 18596.
(920) Shim, J.; Bae, S. H.; Kong, W.; Lee, D.; Qiao, K.; Nezich, D.; Park, Y. J.; Zhao, R.; Sundaram, S.; Li, X.; et al. Controlled crack propagation for atomic precision handling of wafer-scale two-dimensional materials. *Science* **2018**, *362*, 665−670.
(921) Huang, Y.; Pan, Y. H.; Yang, R.; Bao, L. H.; Meng, L.; Luo, H. L.; Cai, Y. Q.; Liu, G. D.; Zhao, W. J.; Zhou, Z.; et al. Universal mechanical exfoliation of large-area 2D crystals. *Nat. Commun.* **2020**, *11*, 2453.
(922) Liu, F.; Wu, W.; Bai, Y.; Chae, S. H.; Li, Q.; Wang, J.; Hone, J.; Zhu, X. Y. Disassembling 2D van der Waals crystals into macroscopic monolayers and reassembling into artificial lattices. *Science* **2020**, *367*, 903−906.
(923) Jung, Y.; Choi, M. S.; Nipane, A.; Borah, A.; Kim, B.; Zangiabadi, A.; Taniguchi, T.; Watanabe, K.; Yoo, W. J.; Hone, J.; et al. Transferred via contacts as a platform for ideal two-dimensional transistors. *Nat. Electron.* **2019**, *2*, 187−194.
(924) Satterthwaite, P. F.; Zhu, W.; Jastrzebska-Perfect, P.; Tang, M.; Spector, S. O.; Gao, H.; Kitadai, H.; Lu, A.-Y.; Tan, Q.; Tang, S.-Y.; et al. Van der Waals device integration beyond the limits of van der Waals forces using adhesive matrix transfer. *Nat. Electron.* **2024**, *7*, 17−28.
(925) Kang, K.; Lee, K. H.; Han, Y.; Gao, H.; Xie, S.; Muller, D. A.; Park, J. Layer-by-layer assembly of two-dimensional materials into wafer-scale heterostructures. *Nature* **2017**, *550*, 229−233.
(926) Kim, S. E.; Mujid, F.; Rai, A.; Eriksson, F.; Suh, J.; Poddar, P.; Ray, A.; Park, C.; Fransson, E.; Zhong, Y.; et al. Extremely anisotropic van der Waals thermal conductors. *Nature* **2021**, *597*, 660−665.
(927) Mannix, A. J.; Ye, A.; Sung, S. H.; Ray, A.; Mujid, F.; Park, C.; Lee, M.; Kang, J. H.; Shreiner, R.; High, A. A.; et al. Robotic four-dimensional pixel assembly of van der Waals solids. *Nat. Nanotechnol.* **2022**, *17*, 361−366.
(928) Camellini, A.; Mennucci, C.; Cinquanta, E.; Martella, C.; Mazzanti, A.; Lamperti, A.; Molle, A.; de Mongeot, F. B.; Della Valle, G.; Zavelani-Rossi, M. Ultrafast anisotropic exciton dynamics in nanopatterned $MoS_2$ sheets. *ACS Photonics* **2018**, *5*, 3363−3371.
(929) Martella, C.; Mennucci, C.; Lamperti, A.; Cappelluti, E.; de Mongeot, F. B.; Molle, A. Designer shape anisotropy on transition-metal-dichalcogenide nanosheets. *Adv. Mater.* **2018**, *30*, 1705615.
(930) Liu, X.; Howell, S. T.; Conde-Rubio, A.; Boero, G.; Brugger, J. Thermomechanical nanocutting of 2D materials. *Adv. Mater.* **2020**, *32*, 2001232.
(931) Conti, S.; Pimpolari, L.; Calabrese, G.; Worsley, R.; Majee, S.; Polyushkin, D. K.; Paur, M.; Pace, S.; Keum, D. H.; Fabbri, F.; et al. Low-voltage 2D materials-based printed field-effect transistors for integrated digital and analog electronics on paper. *Nat. Commun.* **2020**, *11*, 3566.
(932) Meng, W.; Xu, F.; Yu, Z.; Tao, T.; Shao, L.; Liu, L.; Li, T.; Wen, K.; Wang, J.; He, L.; et al. Three-dimensional monolithic micro-LED display driven by atomically thin transistor matrix. *Nat. Nanotechnol.* **2021**, *16*, 1231−1236.
(933) Munkhbat, B.; Yankovich, A. B.; Baranov, D. G.; Verre, R.; Olsson, E.; Shegai, T. O. Transition metal dichalcogenide metamaterials with atomic precision. *Nat. Commun.* **2020**, *11*, 4604.
(934) Liu, M.; Huang, Z.; Guo, Y.; Zhang, Z.; Zhang, L.; Zhang, H.; Zhong, J.; Li, S.; Deng, W.; Wang, D.; et al. Patterning two-dimensional semiconductors with thermal etching. *InfoMat* **2023**, *5*, e12474.
(935) Tong, L.; Wan, J.; Xiao, K.; Liu, J.; Ma, J.; Guo, X.; Zhou, L.; Chen, X.; Xia, Y.; Dai, S.; et al. Heterogeneous complementary field-effect transistors based on silicon and molybdenum disulfide. *Nat. Electron.* **2022**, *6*, 37−44.
(936) Huang, Z.; Geyer, N.; Werner, P.; de Boor, J.; Gosele, U. Metal-assisted chemical etching of silicon: A review. *Adv. Mater.* **2011**, *23*, 285−308.
(937) Choi, A.; Hoang, A. T.; Ngoc Van, T. T.; Shong, B.; Hu, L.; You Thai, K.; Ahn, J.-H. Residue-free photolithographic patterning of graphene. *Chem. Eng. J.* **2022**, *429*, 132504.
(938) Xie, Y.; Çakıroğlu, O.; Hu, W.; He, K.; Puebla, S.; Pucher, T.; Zhao, Q.; Ma, X.; Munuera, C.; Castellanos-Gomez, A. Laser trimming for lithography-free fabrications of $MoS_2$ devices. *Nano Res.* **2023**, *16*, 5042−5046.
(939) Wei, Z.; Liao, M.; Guo, Y.; Tang, J.; Cai, Y.; Chen, H.; Wang, Q.; Jia, Q.; Lu, Y.; Zhao, Y.; et al. Scratching lithography for wafer-scale $MoS_2$ monolayers. *2D Mater.* **2020**, *7*, No. 045028.
(940) Zhao, P.; Wang, R.; Lien, D. H.; Zhao, Y.; Kim, H.; Cho, J.; Ahn, G. H.; Javey, A. Scanning probe lithography patterning of monolayer semiconductors and application in quantifying edge recombination. *Adv. Mater.* **2019**, *31*, 1900136.
(941) Hu, D.; Li, H.; Zhu, Y.; Lei, Y.; Han, J.; Xian, S.; Zheng, J.; Guan, B.-O.; Cao, Y.; Bi, L.; Li, X. Ultra-sensitive nanometric flat laser prints for binocular stereoscopic image. *Nat. Commun.* **2021**, *12*, 1154.
(942) Lin, H.; Xu, Z. Q.; Cao, G.; Zhang, Y.; Zhou, J.; Wang, Z.; Wan, Z.; Liu, Z.; Loh, K. P.; Qiu, C. W.; et al. Diffraction-limited imaging with monolayer 2D material-based ultrathin flat lenses. *Light Sci. Appl.* **2020**, *9*, 137.
(943) Lin, L.; Li, J.; Li, W.; Yogeesh, M. N.; Shi, J.; Peng, X.; Liu, Y.; Rajeeva, B. B.; Becker, M. F.; Liu, Y.; et al. Optothermoplasmonic nanolithography for on-demand patterning of 2D materials. *Adv. Funct. Mater.* **2018**, *28*, 1803990.
(944) Poddar, P. K.; Zhong, Y.; Mannix, A. J.; Mujid, F.; Yu, J.; Liang, C.; Kang, J. H.; Lee, M.; Xie, S.; Park, J. Resist-free lithography for monolayer transition metal dichalcogenides. *Nano Lett.* **2022**, *22*, 726−732.
(945) Derby, B. Inkjet printing of functional and structural materials: Fluid property requirements, feature stability, and resolution. *Annu. Rev. Mater. Res.* **2010**, *40*, 395−414.
(946) Shao, Y.; Fu, J. H.; Cao, Z.; Song, K.; Sun, R.; Wan, Y.; Shamim, A.; Cavallo, L.; Han, Y.; Kaner, R. B.; et al. 3D crumpled ultrathin 1T $MoS_2$ for inkjet printing of Mg-ion asymmetric micro-supercapacitors. *ACS Nano* **2020**, *14*, 7308−7318.
(947) Zeng, Z.; Yin, Z.; Huang, X.; Li, H.; He, Q.; Lu, G.; Boey, F.; Zhang, H. Single-layer semiconducting nanosheets: High-yield preparation and device fabrication. *Angew. Chem., Int. Ed.* **2011**, *50*, 11093−11097.
(948) Coleman, J. N.; Lotya, M.; O'Neill, A.; Bergin, S. D.; King, P. J.; Khan, U.; Young, K.; Gaucher, A.; De, S.; Smith, R. J.; et al. Two-dimensional nanosheets produced by liquid exfoliation of layered materials. *Science* **2011**, *331*, 568−571.
(949) Tang, B.; Veluri, H.; Li, Y.; Yu, Z. G.; Waqar, M.; Leong, J. F.; Sivan, M.; Zamburg, E.; Zhang, Y.-W.; Wang, J.; Thean, A. V-Y. Wafer-scale solution-processed 2D material analog resistive memory array for memory-based computing. *Nat. Commun.* **2022**, *13*, 3037.


https://doi.org/10.1021/acs.chemrev.3c00851
*Chem. Rev.* XXXX, XXX, XXX−XXX

(950) Li, J.; Song, P.; Zhao, J.; Vaklinova, K.; Zhao, X.; Li, Z.; Qiu, Z.; Wang, Z.; Lin, L.; Zhao, M.; et al. Printable two-dimensional superconducting monolayers. *Nat. Mater.* **2021**, *20*, 181−187.
(951) Kwon, Y. A.; Kim, J.; Jo, S. B.; Roe, D. G.; Rhee, D.; Song, Y.; Kang, B.; Kim, D.; Kim, J.; Kim, D. W.; et al. Wafer-scale transistor arrays fabricated using slot-die printing of molybdenum disulfide and sodium-embedded alumina. *Nat. Electron.* **2023**, *6*, 443−450.
(952) Lanza, M.; Radu, I. Electronic circuits made of 2D materials. *Adv. Mater.* **2022**, *34*, e2207843.
(953) Li, M. Y.; Su, S. K.; Wong, H. S. P.; Li, L. J. How 2D semiconductors could extend Moore's law. *Nature* **2019**, *567*, 169−170.
(954) Xie, L.; Liao, M.; Wang, S.; Yu, H.; Du, L.; Tang, J.; Zhao, J.; Zhang, J.; Chen, P.; Lu, X.; et al. Graphene-contacted ultrashort channel monolayer $MoS_2$ transistors. *Adv. Mater.* **2017**, *29*, 1702522.
(955) Wu, F.; Tian, H.; Shen, Y.; Hou, Z.; Ren, J.; Gou, G.; Sun, Y.; Yang, Y.; Ren, T. L. Vertical $MoS_2$ transistors with sub-1-nm gate lengths. *Nature* **2022**, *603*, 259−264.
(956) Chen, M. L.; Sun, X.; Liu, H.; Wang, H.; Zhu, Q.; Wang, S.; Du, H.; Dong, B.; Zhang, J.; Sun, Y.; et al. A FinFET with one atomic layer channel. *Nat. Commun.* **2020**, *11*, 1205.
(957) Huang, X.; Liu, C.; Zeng, S.; Tang, Z.; Wang, S.; Chen, X.; Zhang, D. W.; Zhou, P. Ultrathin multibridge channel transistor enabled by van der Waals assembly. *Adv. Mater.* **2021**, *33*, e2102201.
(958) Liu, M.; Niu, J.; Yang, G.; Chen, K.; Lu, W.; Liao, F.; Lu, C.; Lu, N.; Li, L. Large-scale ultrathin channel nanosheet-stacked CFET based on CVD 1L $MoS_2/WSe_2$. *Adv. Electron. Mater.* **2023**, *9*, 2200722.
(959) Guo, Y.; Li, J.; Zhan, X.; Wang, C.; Li, M.; Zhang, B.; Wang, Z.; Liu, Y.; Yang, K.; Wang, H.; et al. Van der Waals polarity-engineered 3D integration of 2D complementary logic. *Nature* **2024**, *630*, 346−352.
(960) Xiong, X.; Tong, A.; Wang, X.; Liu, S.; Li, X.; Huang, R.; Wu, Y. Demonstration of vertically-stacked CVD monolayer channels: $MoS_2$ nanosheets GAA-FET with $I_{on}$ > 700 $\mu$A/$\mu$m and $MoS_2/WSe_2$ CFET. In *2021 IEEE International Electron Devices Meeting (IEDM)*, 2021.
(961) Lu, D.; Chen, Y.; Lu, Z.; Ma, L.; Tao, Q.; Li, Z.; Kong, L.; Liu, L.; Yang, X.; Ding, S.; et al. Monolithic three-dimensional tier-by-tier integration via van der Waals lamination. *Nature* **2024**, *630*, 340−345.
(962) Wang, Y.; Chhowalla, M. Making clean electrical contacts on 2D transition metal dichalcogenides. *Nat. Rev. Phys.* **2022**, *4*, 101−112.
(963) Shen, P.-C.; Su, C.; Lin, Y.; Chou, A.-S.; Cheng, C.-C.; Park, J.-H.; Chiu, M.-H.; Lu, A.-Y.; Tang, H.-L.; Tavakoli, M. M.; et al. Ultralow contact resistance between semimetal and monolayer semiconductors. *Nature* **2021**, *593*, 211−217.
(964) Jiang, J.; Xu, L.; Du, L.; Li, L.; Zhang, G.; Qiu, C.; Peng, L.-M. Yttrium-doping-induced metallization of molybdenum disulfide for ohmic contacts in two-dimensional transistors. *Nat. Electron.* **2024**, DOI: 10.1038/s41928-024-01176-2.
(965) Wang, Y.; Kim, J. C.; Li, Y.; Ma, K. Y.; Hong, S.; Kim, M.; Shin, H. S.; Jeong, H. Y.; Chhowalla, M. P-type electrical contacts for 2D transition-metal dichalcogenides. *Nature* **2022**, *610*, 61−66.
(966) Gong, C.; Huang, C.; Miller, J.; Cheng, L.; Hao, Y.; Cobden, D.; Kim, J.; Ruoff, R. S.; Wallace, R. M.; Cho, K.; et al. Metal contacts on physical vapor deposited monolayer $MoS_2$. *ACS Nano* **2013**, *7*, 11350−11357.
(967) Wang, Y.; Kim, J. C.; Wu, R. J.; Martinez, J.; Song, X.; Yang, J.; Zhao, F.; Mkhoyan, A.; Jeong, H. Y.; Chhowalla, M. Van der Waals contacts between three-dimensional metals and two-dimensional semiconductors. *Nature* **2019**, *568*, 70−74.
(968) Liu, W.; Kang, J.; Sarkar, D.; Khatami, Y.; Jena, D.; Banerjee, K. Role of metal contacts in designing high-performance monolayer n-type $WSe_2$ field effect transistors. *Nano Lett.* **2013**, *13*, 1983−1990.
(969) Li, W.; Gong, X.; Yu, Z.; Ma, L.; Sun, W.; Gao, S.; Koroglu, C.; Wang, W.; Liu, L.; Li, T.; et al. Approaching the quantum limit in two-dimensional semiconductor contacts. *Nature* **2023**, *613*, 274−279.
(970) Cui, X.; Shih, E. M.; Jauregui, L. A.; Chae, S. H.; Kim, Y. D.; Li, B.; Seo, D.; Pistunova, K.; Yin, J.; Park, J. H.; et al. Low-temperature ohmic contact to monolayer $MoS_2$ by van der Waals bonded Co/h-BN electrodes. *Nano Lett.* **2017**, *17*, 4781−4786.
(971) Liu, Y.; Liu, S.; Wang, Z.; Li, B.; Watanabe, K.; Taniguchi, T.; Yoo, W. J.; Hone, J. Low-resistance metal contacts to encapsulated semiconductor monolayers with long transfer length. *Nat. Electron.* **2022**, *5*, 579−585.
(972) Yang, X.; Li, J.; Song, R.; Zhao, B.; Tang, J.; Kong, L.; Huang, H.; Zhang, Z.; Liao, L.; Liu, Y.; et al. Highly reproducible van der Waals integration of two-dimensional electronics on the wafer scale. *Nat. Nanotechnol.* **2023**, *18*, 471−478.
(973) Zhang, X.; Huang, C.; Li, Z.; Fu, J.; Tian, J.; Ouyang, Z.; Yang, Y.; Shao, X.; Han, Y.; Qiao, Z.; Zeng, H. Reliable wafer-scale integration of two-dimensional materials and metal electrodes with van der Waals contacts. *Nat. Commun.* **2024**, *15*, 4619.
(974) Liu, Y.; Guo, J.; Zhu, E.; Liao, L.; Lee, S. J.; Ding, M.; Shakir, I.; Gambin, V.; Huang, Y.; Duan, X. Approaching the Schottky-mott limit in van der Waals metal-semiconductor junctions. *Nature* **2018**, *557*, 696−700.
(975) Xu, Y.; Liu, T.; Liu, K.; Zhao, Y.; Liu, L.; Li, P.; Nie, A.; Liu, L.; Yu, J.; Feng, X.; et al. Scalable integration of hybrid high-$\kappa$ dielectric materials on two-dimensional semiconductors. *Nat. Mater.* **2023**, *22*, 1078−1084.
(976) Luo, P.; Liu, C.; Lin, J.; Duan, X.; Zhang, W.; Ma, C.; Lv, Y.; Zou, X.; Liu, Y.; Schwierz, F.; et al. Molybdenum disulfide transistors with enlarged van der Waals gaps at their dielectric interface via oxygen accumulation. *Nat. Electron.* **2022**, *5*, 849−858.
(977) Pu, J.; Yomogida, Y.; Liu, K. K.; Li, L. J.; Iwasa, Y.; Takenobu, T. Highly flexible $MoS_2$ thin-film transistors with ion gel dielectrics. *Nano Lett.* **2012**, *12*, 4013−4017.
(978) Pu, J.; Funahashi, K.; Chen, C. H.; Li, M. Y.; Li, L. J.; Takenobu, T. Highly flexible and high-performance complementary inverters of large-area transition metal dichalcogenide monolayers. *Adv. Mater.* **2016**, *28*, 4111−4119.
(979) Zan, W.; Zhang, Q.; Xu, H.; Liao, F.; Guo, Z.; Deng, J.; Wan, J.; Zhu, H.; Chen, L.; Sun, Q.; et al. Large capacitance and fast polarization response of thin electrolyte dielectrics by spin coating for two-dimensional $MoS_2$ devices. *Nano Res.* **2018**, *11*, 3739−3745.
(980) Sangwan, V. K.; Lee, H. S.; Bergeron, H.; Balla, I.; Beck, M. E.; Chen, K. S.; Hersam, M. C. Multi-terminal memtransistors from polycrystalline monolayer molybdenum disulfide. *Nature* **2018**, *554*, 500−504.
(981) Li, N.; Zhang, S.; Peng, Y.; Li, X.; Zhang, Y.; He, C.; Zhang, G. 2D semiconductor-based optoelectronics for artificial vision. *Adv. Funct. Mater.* **2023**, *33*, 230558.
(982) Kumar, D.; Joharji, L.; Li, H.; Rezk, A.; Nayfeh, A.; El-Atab, N. Artificial visual perception neural system using a solution-processable $MoS_2$-based in-memory light sensor. *Light Sci. Appl.* **2023**, *12*, 109.
(983) Ham, D.; Park, H.; Hwang, S.; Kim, K. Neuromorphic electronics based on copying and pasting the brain. *Nat. Electron.* **2021**, *4*, 635−644.
(984) Li, N.; Wang, Q.; Shen, C.; Wei, Z.; Yu, H.; Zhao, J.; Lu, X.; Wang, G.; He, C.; Xie, L.; et al. Large-scale flexible and transparent electronics based on monolayer molybdenum disulfide field-effect transistors. *Nat. Electron.* **2020**, *3*, 711−717.
(985) Choi, J. M.; Jang, H. Y.; Kim, A. R.; Kwon, J. D.; Cho, B.; Park, M. H.; Kim, Y. Ultra-flexible and rollable 2D-$MoS_2$/Si heterojunction-based near-infrared photodetector via direct synthesis. *Nanoscale* **2021**, *13*, 672−680.
(986) Daus, A.; Vaziri, S.; Chen, V.; Köroğlu, Ç.; Grady, R. W.; Bailey, C. S.; Lee, H. R.; Schauble, K.; Brenner, K.; Pop, E. High-performance flexible nanoscale transistors based on transition metal dichalcogenides. *Nat. Electron.* **2021**, *4*, 495−501.
(987) Tang, J.; Wang, Q.; Tian, J.; Li, X.; Li, N.; Peng, Y.; Li, X.; Zhao, Y.; He, C.; Wu, S.; et al. Low power flexible monolayer $MoS_2$ integrated circuits. *Nat. Commun.* **2023**, *14*, 3633.
(988) Kim, H.; Lien, D. H.; Amani, M.; Ager, J. W.; Javey, A. Highly stable near-unity photoluminescence yield in monolayer $MoS_2$ by

fluoropolymer encapsulation and superacid treatment. *ACS Nano* **2017**, *11*, 5179−5185.
(989) Woo, Y.; Hong, W.; Yang, S. Y.; Kang, T.; Choi, S.-Y. High-performance $MoS_2$ thin-film transistors for flexible OLED display. *SID Symposium Digest of Technical Papers* **2018**, *49*, 797−799.
(990) Park, M.; Park, Y. J.; Chen, X.; Park, Y. K.; Kim, M. S.; Ahn, J. H. $MoS_2$-based tactile sensor for electronic skin applications. *Adv. Mater.* **2016**, *28*, 2556−2562.
(991) Yoo, G.; Park, H.; Kim, M.; Song, W. G.; Jeong, S.; Kim, M. H.; Lee, H.; Lee, S. W.; Hong, Y. K.; Lee, M. G.; et al. Real-time electrical detection of epidermal skin $MoS_2$ biosensor for point-of-care diagnostics. *Nano Res.* **2017**, *10*, 767−775.
(992) Migliato Marega, G.; Zhao, Y.; Avsar, A.; Wang, Z.; Tripathi, M.; Radenovic, A.; Kis, A. Logic-in-memory based on an atomically thin semiconductor. *Nature* **2020**, *587*, 72−77.
(993) Wang, Y.; Tang, H.; Xie, Y.; Chen, X.; Ma, S.; Sun, Z.; Sun, Q.; Chen, L.; Zhu, H.; Wan, J.; et al. An in-memory computing architecture based on two-dimensional semiconductors for multiply-accumulate operations. *Nat. Commun.* **2021**, *12*, 3347.
(994) Ning, H.; Yu, Z.; Zhang, Q.; Wen, H.; Gao, B.; Mao, Y.; Li, Y.; Zhou, Y.; Zhou, Y.; Chen, J.; et al. An in-memory computing architecture based on a duplex two-dimensional material structure for in situ machine learning. *Nat. Nanotechnol.* **2023**, *18*, 493−500.
(995) Migliato Marega, G.; Ji, H. G.; Wang, Z.; Pasquale, G.; Tripathi, M.; Radenovic, A.; Kis, A. A large-scale integrated vector-matrix multiplication processor based on monolayer molybdenum disulfide memories. *Nat. Electron.* **2023**, *6*, 991−998.
(996) Radisavljevic, B.; Whitwick, M. B.; Kis, A. Integrated circuits and logic operations based on single-layer $MoS_2$. *ACS Nano* **2011**, *5*, 9934−9938.
(997) Xu, H.; Zhang, H.; Guo, Z.; Shan, Y.; Wu, S.; Wang, J.; Hu, W.; Liu, H.; Sun, Z.; Luo, C.; et al. High-performance wafer-scale $MoS_2$ transistors toward practical application. *Small* **2018**, *14*, 1803465.
(998) Zhu, K.; Wen, C.; Aljarb, A. A.; Xue, F.; Xu, X.; Tung, V.; Zhang, X.; Alshareef, H. N.; Lanza, M. The development of integrated circuits based on two-dimensional materials. *Nat. Electron.* **2021**, *4*, 775−785.
(999) Wachter, S.; Polyushkin, D. K.; Bethge, O.; Mueller, T. A microprocessor based on a two-dimensional semiconductor. *Nat. Commun.* **2017**, *8*, 14948.
(1000) Huo, N.; Konstantatos, G. Ultrasensitive all-2D $MoS_2$ phototransistors enabled by an out-of-plane $MoS_2$ PN homojunction. *Nat. Commun.* **2017**, *8*, 572.
(1001) Graphene is not alone. *Nat. Nanotechnol.* **2012**, *7*, 683.
(1002) Chang, Y. H.; Zhang, W.; Zhu, Y.; Han, Y.; Pu, J.; Chang, J. K.; Hsu, W. T.; Huang, J. K.; Hsu, C. L.; Chiu, M. H.; et al. Monolayer $MoSe_2$ grown by chemical vapor deposition for fast photodetection. *ACS Nano* **2014**, *8*, 8582−8590.
(1003) Zhang, Y.; Chang, T. R.; Zhou, B.; Cui, Y. T.; Yan, H.; Liu, Z.; Schmitt, F.; Lee, J.; Moore, R.; Chen, Y.; et al. Direct observation of the transition from indirect to direct bandgap in atomically thin epitaxial $MoSe_2$. *Nat. Nanotechnol.* **2014**, *9*, 111−115.
(1004) Li, Q.; Alfrey, A.; Hu, J.; Lydick, N.; Paik, E.; Liu, B.; Sun, H.; Lu, Y.; Wang, R.; Forrest, S.; Deng, H. Macroscopic transition metal dichalcogenides monolayers with uniformly high optical quality. *Nat. Commun.* **2023**, *14*, 1837.
(1005) Lohof, F.; Steinhoff, A.; Florian, M.; Lorke, M.; Erben, D.; Jahnke, F.; Gies, C. Prospects and limitations of transition metal dichalcogenide laser gain materials. *Nano Lett.* **2019**, *19*, 210−217.
(1006) Wen, W.; Wu, L.; Yu, T. Excitonic lasers in atomically thin 2D semiconductors. *ACS Materials Lett.* **2020**, *2*, 1328−1342.
(1007) Du, W.; Li, C.; Sun, J.; Xu, H.; Yu, P.; Ren, A.; Wu, J.; Wang, Z. Nanolasers based on 2D materials. *Laser Photonics Rev.* **2020**, *14*, 2000271.
(1008) Wu, S.; Buckley, S.; Schaibley, J. R.; Feng, L.; Yan, J.; Mandrus, D. G.; Hatami, F.; Yao, W.; Vuckovic, J.; Majumdar, A.; et al. Monolayer semiconductor nanocavity lasers with ultralow thresholds. *Nature* **2015**, *520*, 69−72.
(1009) Ye, Y.; Wong, Z. J.; Lu, X.; Ni, X.; Zhu, H.; Chen, X.; Wang, Y.; Zhang, X. Monolayer excitonic laser. *Nat. Photonics* **2015**, *9*, 733−737.
(1010) Salehzadeh, O.; Djavid, M.; Tran, N. H.; Shih, I.; Mi, Z. Optically pumped two-dimensional $MoS_2$ lasers operating at room-temperature. *Nano Lett.* **2015**, *15*, 5302−5306.
(1011) Shang, J.; Cong, C.; Wang, Z.; Peimyoo, N.; Wu, L.; Zou, C.; Chen, Y.; Chin, X. Y.; Wang, J.; Soci, C.; et al. Room-temperature 2D semiconductor activated vertical-cavity surface-emitting lasers. *Nat. Commun.* **2017**, *8*, 543.
(1012) Li, Y.; Zhang, J.; Huang, D.; Sun, H.; Fan, F.; Feng, J.; Wang, Z.; Ning, C. Z. Room-temperature continuous-wave lasing from monolayer molybdenum ditelluride integrated with a silicon nanobeam cavity. *Nat. Nanotechnol.* **2017**, *12*, 987−992.
(1013) Liu, Y.; Fang, H.; Rasmita, A.; Zhou, Y.; Li, J.; Yu, T.; Xiong, Q.; Zheludev, N.; Liu, J.; Gao, W. Room temperature nanocavity laser with interlayer excitons in 2D heterostructures. *Sci. Adv.* **2019**, *5*, eaav4506.
(1014) Yu, J. X.; Xing, S.; Dai, G. Y.; Ling-Hu, S. Y.; Gu, F. X. Direct-bandgap bilayer $WSe_2$ /microsphere monolithic cavity for low-threshold lasing. *Adv. Mater.* **2022**, *34*, 2106502.
(1015) Paik, E. Y.; Zhang, L.; Burg, G. W.; Gogna, R.; Tutuc, E.; Deng, H. Interlayer exciton laser of extended spatial coherence in atomically thin heterostructures. *Nature* **2019**, *576*, 80−84.
(1016) Rong, K.; Duan, X.; Wang, B.; Reichenberg, D.; Cohen, A.; Liu, C. L.; Mohapatra, P. K.; Patsha, A.; Gorovoy, V.; Mukherjee, S.; et al. Spin-valley rashba monolayer laser. *Nat. Mater.* **2023**, *22*, 1085−1093.
(1017) Zhao, L.; Shang, Q.; Li, M.; Liang, Y.; Li, C.; Zhang, Q. Strong exciton-photon interaction and lasing of two-dimensional transition metal dichalcogenide semiconductors. *Nano Res.* **2021**, *14*, 1937−1954.
(1018) Zhao, L.; Shang, Q.; Gao, Y.; Shi, J.; Liu, Z.; Chen, J.; Mi, Y.; Yang, P.; Zhang, Z.; Du, W.; et al. High-temperature continuous-wave pumped lasing from large-area monolayer semiconductors grown by chemical vapor deposition. *ACS Nano* **2018**, *12*, 9390−9396.
(1019) Liu, N.; Yang, X.; Zhang, J.; Zhu, Z.; Liu, K. Room-temperature excitonic nanolaser array with directly grown monolayer $WS_2$. *ACS Photonics* **2023**, *10*, 283−289.
(1020) Yang, J.; Wang, Z.; Wang, F.; Xu, R.; Tao, J.; Zhang, S.; Qin, Q.; Luther-Davies, B.; Jagadish, C.; Yu, Z.; et al. Atomically thin optical lenses and gratings. *Light Sci. Appl.* **2016**, *5*, e16046.
(1021) Wang, Z.; Yuan, G.; Yang, M.; Chai, J.; Steve Wu, Q. Y.; Wang, T.; Sebek, M.; Wang, D.; Wang, L.; Wang, S.; et al. Exciton-enabled meta-optics in two-dimensional transition metal dichalcogenides. *Nano Lett.* **2020**, *20*, 7964−7972.
(1022) Qin, F.; Liu, B.; Zhu, L.; Lei, J.; Fang, W.; Hu, D.; Zhu, Y.; Ma, W.; Wang, B.; Shi, T.; et al. Π-phase modulated monolayer supercritical lens. *Nat. Commun.* **2021**, *12*, 32.
(1023) van de Groep, J.; Song, J.-H.; Celano, U.; Li, Q.; Kik, P. G.; Brongersma, M. L. Exciton resonance tuning of an atomically thin lens. *Nat. Photonics* **2020**, *14*, 426−430.
(1024) Lynch, J.; Guarneri, L.; Jariwala, D.; van de Groep, J. Exciton resonances for atomically-thin optics. *J. Appl. Phys.* **2022**, *132*, No. 091102.
(1025) Lee, M.; Hong, H.; Yu, J.; Mujid, F.; Ye, A.; Liang, C.; Park, J. Wafer-scale delta waveguides for integrated two-dimensional photonics. *Science* **2023**, *381*, 648−653.
(1026) Liao, F.; Yu, J.; Gu, Z.; Yang, Z.; Hasan, T.; Linghu, S.; Peng, J.; Fang, W.; Zhuang, S.; Gu, M.; Gu, F. Enhancing monolayer photoluminescence on optical micro/nanofibers for low-threshold lasing. *Sci. Adv.* **2019**, *5*, eaax7398.
(1027) Ngo, G. Q.; Najafidehaghani, E.; Gan, Z.; Khazaee, S.; Siems, M. P.; George, A.; Schartner, E. P.; Nolte, S.; Ebendorff-Heidepriem, H.; Pertsch, T.; et al. In-fibre second-harmonic generation with embedded two-dimensional materials. *Nat. Photonics* **2022**, *16*, 769−776.

(1028) Dai, C. H.; Liu, Y. Q.; Wei, D. C. Two-dimensional field-effect transistor sensors: The road toward commercialization. *Chem. Rev.* **2022**, *122*, 10319−10392.
(1029) Huang, Y. C.; Liu, Y.; Ma, C.; Cheng, H. C.; He, Q. Y.; Wu, H.; Wang, C.; Lin, C. Y.; Huang, Y.; Duan, X. F. Sensitive pressure sensors based on conductive microstructured air-gap gates and two-dimensional semiconductor transistors. *Nat. Electron.* **2020**, *3*, 59−69.
(1030) Luo, Y. F.; Abidian, M. R.; Ahn, J. H.; Akinwande, D.; Andrews, A. M.; Antonietti, M.; Bao, Z. N.; Berggren, M.; Berkey, C. A.; Bettinger, C. J.; et al. Technology roadmap for flexible sensors. *ACS Nano* **2023**, *17*, 5211−5295.
(1031) Ma, C.; Xu, D.; Wang, P. Q.; Lin, Z. Y.; Zhou, J. Y.; Jia, C. C.; Huang, J.; Li, S. T.; Huang, Y.; Duan, X. F. Two-dimensional van der Waals thin film transistors as active matrix for spatially resolved pressure sensing. *Nano Res.* **2021**, *14*, 3395−3401.
(1032) Park, Y. J.; Sharma, B. K.; Shinde, S. M.; Kim, M. S.; Jang, B.; Kim, J. H.; Ahn, J. H. All $MoS_2$-based large area, skin-attachable active-matrix tactile sensor. *ACS Nano* **2019**, *13*, 3023−3030.
(1033) Daus, A.; Jaikissoon, M.; Khan, A. I.; Kumar, A.; Grady, R. W.; Saraswat, K. C.; Pop, E. Fast-response flexible temperature sensors with atomically thin molybdenum disulfide. *Nano Lett.* **2022**, *22*, 6135−6140.
(1034) Liu, B.; Chen, L.; Liu, G.; Abbas, A. N.; Fathi, M.; Zhou, C. High-performance chemical sensing using Schottky-contacted chemical vapor deposition grown monolayer $MoS_2$ transistors. *ACS Nano* **2014**, *8*, 5304−5314.
(1035) Cho, B.; Hahm, M. G.; Choi, M.; Yoon, J.; Kim, A. R.; Lee, Y. J.; Park, S. G.; Kwon, J. D.; Kim, C. S.; Song, M.; et al. Charge-transfer-based gas sensing using atomic-layer $MoS_2$. *Sci. Rep.* **2015**, *5*, 8052.
(1036) Pawbake, A. S.; Waykar, R. G.; Late, D. J.; Jadkar, S. R. Highly transparent wafer-scale synthesis of crystalline $WS_2$ nanoparticle thin film for photodetector and humidity-sensing applications. *ACS Appl. Mater. Interfaces* **2016**, *8*, 3359−3365.
(1037) Kim, Y.; Kang, S. K.; Oh, N. C.; Lee, H. D.; Lee, S. M.; Park, J.; Kim, H. Improved sensitivity in Schottky contacted two-dimensional $MoS_2$ gas sensor. *ACS Appl. Mater. Interfaces* **2019**, *11*, 38902−38909.
(1038) Zulkefli, A.; Mukherjee, B.; Sahara, R.; Hayakawa, R.; Iwasaki, T.; Wakayama, Y.; Nakaharai, S. Enhanced selectivity in volatile organic compound gas sensors based on $ReS_2$-FETs under light-assisted and gate-bias tunable operation. *ACS Appl. Mater. Interfaces* **2021**, *13*, 43030−43038.
(1039) Liu, L. X.; Ye, K.; Lin, C. Q.; Jia, Z. Y.; Xue, T. Y.; Nie, A. M.; Cheng, Y. C.; Xiang, J. Y.; Mu, C. P.; Wang, B. C.; et al. Grain-boundary-rich polycrystalline monolayer $WS_2$ film for attomolar-level $Hg^{2+}$ sensors. *Nat. Commun.* **2021**, *12*, 3870.
(1040) Liao, W. G.; Wei, W.; Tong, Y.; Chim, W. K.; Zhu, C. X. Low-frequency noise in layered $ReS_2$ field effect transistors on $HfO_2$ and its application for ph sensing. *ACS Appl. Mater. Interfaces* **2018**, *10*, 7248−7255.
(1041) Mia, A. K.; Meyyappan, M.; Giri, P. K. Two-dimensional transition metal dichalcogenide based biosensors: From fundamentals to healthcare applications. *Biosensors-Basel* **2023**, *13*, 169.
(1042) Bahri, M.; Shi, B.; Elaguech, M. A.; Djebbi, K.; Zhou, D. M.; Liang, L. Y.; Tlili, C.; Wang, D. Q. Tungsten disulfide nanosheet-based field-effect transistor biosensor for DNA hybridization detection. *ACS Appl. Nano Mater.* **2022**, *5*, 5035−5044.
(1043) Fathi-Hafshejani, P.; Azam, N.; Wang, L.; Kuroda, M. A.; Hamilton, M. C.; Hasim, S.; Mahjouri-Samani, M. Two-dimensional-material-based field-effect transistor biosensor for detecting COVID-19 virus (SARS-CoV-2). *ACS Nano* **2021**, *15*, 11461−11469.
(1044) Majd, S. M.; Salimi, A.; Ghasemi, F. An ultrasensitive detection of mirna-155 in breast cancer via direct hybridization assay using two-dimensional molybdenum disulfide field-effect transistor biosensor. *Biosens. Bioelectron.* **2018**, *105*, 6−13.
(1045) Wang, L.; Wang, Y.; Wong, J. I.; Palacios, T.; Kong, J.; Yang, H. Y. Functionalized $MoS_2$ nanosheet-based field-effect biosensor for label-free sensitive detection of cancer marker proteins in solution. *Small* **2014**, *10*, 1101−1105.
(1046) Park, H.; Baek, S.; Sen, A.; Jung, B. J.; Shim, J.; Park, Y. C.; Lee, L. P.; Kim, Y. J.; Kim, S. Ultrasensitive and selective field-effect transistor-based biosensor created by rings of $MoS_2$ nanopores. *ACS Nano* **2022**, *16*, 1826−1835.
(1047) Zhu, D.; Liu, W.; Zhao, D. X.; Hao, Q.; Li, J.; Huang, J. X.; Shi, J. Y.; Chao, J.; Su, S.; Wang, L. H. Label-free electrochemical sensing platform for microrna-21 detection using thionine and gold nanoparticles co-functionalized $MoS_2$ nanosheet. *ACS Appl. Mater. Interfaces* **2017**, *9*, 35597−35603.
(1048) Kong, R. M.; Ding, L.; Wang, Z. J.; You, J. M.; Qu, F. L. A novel aptamer-functionalized $MoS_2$ nanosheet fluorescent biosensor for sensitive detection of prostate specific antigen. *Anal. Bioanal. Chem.* **2015**, *407*, 369−377.
(1049) Dhenadhayalan, N.; Yadav, K.; Sriram, M. I.; Lee, H. L.; Lin, K. C. Ultra-sensitive DNA sensing of a prostate-specific antigen based on 2D nanosheets in live cells. *Nanoscale* **2017**, *9*, 12087−12095.
(1050) Wang, W. B.; Qi, J. L.; Wu, Z. X.; Zhai, W.; Pan, Y. H.; Bao, K.; Zhai, L.; Wu, J. K.; Ke, C. X.; Wang, L. Z.; et al. On-chip electrocatalytic microdevices. *Nat. Protoc.* **2023**, *18*, 2891−2926.
(1051) Tsai, C.; Chan, K.; Abild-Pedersen, F.; Nørskov, J. K. Active edge sites in $MoSe_2$ and $WSe_2$ catalysts for the hydrogen evolution reaction: A density functional study. *Phys. Chem. Chem. Phys.* **2014**, *16*, 13156−13164.
(1052) Gao, M. R.; Liang, J. X.; Zheng, Y. R.; Xu, Y. F.; Jiang, J.; Gao, Q.; Li, J.; Yu, S. H. An efficient molybdenum disulfide/cobalt diselenide hybrid catalyst for electrochemical hydrogen generation. *Nat. Commun.* **2015**, *6*, 5982.
(1053) Lukowski, M. A.; Daniel, A. S.; English, C. R.; Meng, F.; Forticaux, A.; Hamers, R. J.; Jin, S. Highly active hydrogen evolution catalysis from metallic $WS_2$ nanosheets. *Energy Environl. Sci.* **2014**, *7*, 2608−2613.
(1054) Yang, J.; Mohmad, A. R.; Wang, Y.; Fullon, R.; Song, X. J.; Zhao, F.; Bozkurt, I.; Augustin, M.; Santos, E. J. G.; Shin, H. S.; et al. Ultrahigh-current-density niobium disulfide catalysts for hydrogen evolution. *Nat. Mater.* **2019**, *18*, 1309−1314.
(1055) Fu, Q.; Han, J. C.; Wang, X. J.; Xu, P.; Yao, T.; Zhong, J.; Zhong, W. W.; Liu, S. W.; Gao, T. L.; Zhang, Z. H.; et al. 2D transition metal dichalcogenides: Design, modulation, and challenges in electrocatalysis. *Adv. Mater.* **2021**, *33*, 1907818.
(1056) Jin, H. Y.; Guo, C. X.; Liu, X.; Liu, J. L.; Vasileff, A.; Jiao, Y.; Zheng, Y.; Qiao, S. Z. Emerging two-dimensional nanomaterials for electrocatalysis. *Chem. Rev.* **2018**, *118*, 6337−6408.
(1057) Jaramillo, T. F.; Jorgensen, K. P.; Bonde, J.; Nielsen, J. H.; Horch, S.; Chorkendorff, I. Identification of active edge sites for electrochemical $H_2$ evolution from $MoS_2$ nanocatalysts. *Science* **2007**, *317*, 100−102.
(1058) Xiong, Q.; Zhang, X.; Wang, H. J.; Liu, G. Q.; Wang, G. Z.; Zhang, H. M.; Zhao, H. J. One-step synthesis of cobalt-doped $MoS_2$ nanosheets as bifunctional electrocatalysts for overall water splitting under both acidic and alkaline conditions. *Chem. Commun.* **2018**, *54*, 3859−3862.
(1059) Shi, Z.; Zhang, X.; Lin, X.; Liu, G.; Ling, C.; Xi, S.; Chen, B.; Ge, Y.; Tan, C.; Lai, Z.; et al. Phase-dependent growth of Pt on $MoS_2$ for highly efficient $H_2$ evolution. *Nature* **2023**, *621*, 300−305.
(1060) Zhang, J.; Wang, T.; Pohl, D.; Rellinghaus, B.; Dong, R. H.; Liu, S. H.; Zhuang, X. D.; Feng, X. L. Interface engineering of $MoS_2$/$NiS_2$ heterostructures for highly enhanced electrochemical overall-water-splitting activity. *Angew. Chem.* **2016**, *55*, 6702−6707.
(1061) Hu, J.; Zhang, C. X.; Jiang, L.; Lin, H.; An, Y. M.; Zhou, D.; Leung, M. K. H.; Yang, S. H. Nanohybridization of $MoS_2$ with layered double hydroxides efficiently synergizes the hydrogen evolution in alkaline media. *Joule* **2017**, *1*, 383−393.
(1062) Chia, X. Y.; Pumera, M. Characteristics and performance of two-dimensional materials for electrocatalysis. *Nat. Catal.* **2018**, *1*, 909−921.


https://doi.org/10.1021/acs.chemrev.3c00851
*Chem. Rev.* XXXX, XXX, XXX−XXX

(1063) Sun, Z. Y.; Ma, T.; Tao, H. C.; Fan, Q.; Han, B. X. Fundamentals and challenges of electrochemical $CO_2$ reduction using two-dimensional materials. *Chem.* **2017**, *3*, 560−587.
(1064) Tong, X.; Zhan, X. X.; Rawach, D.; Chen, Z. S.; Zhang, G. X.; Sun, S. H. Low-dimensional catalysts for oxygen reduction reaction. *Prog. Nat. Sci.: Mater. Int.* **2020**, *30*, 787−795.
(1065) Asadi, M.; Kim, K.; Liu, C.; Addepalli, A. V.; Abbasi, P.; Yasaei, P.; Phillips, P.; Behranginia, A.; Cerrato, J. M.; Haasch, R.; et al. Nanostructured transition metal dichalcogenide electrocatalysts for $CO_2$ reduction in ionic liquid. *Science* **2016**, *353*, 467−470.
(1066) Asadi, M.; Kumar, B.; Behranginia, A.; Rosen, B. A.; Baskin, A.; Repnin, N.; Pisasale, D.; Phillips, P.; Zhu, W.; Haasch, R.; et al. Robust carbon dioxide reduction on molybdenum disulphide edges. *Nat. Commun.* **2014**, *5*, 4470.
(1067) Acerce, M.; Voiry, D.; Chhowalla, M. Metallic 1T phase $MoS_2$ nanosheets as supercapacitor electrode materials. *Nat. Nanotechnol.* **2015**, *10*, 313−318.
(1068) Yun, Q.; Li, L.; Hu, Z.; Lu, Q.; Chen, B.; Zhang, H. Layered transition metal dichalcogenide-based nanomaterials for electrochemical energy storage. *Adv. Mater.* **2020**, *32*, 1903826.
(1069) Wan, C.; Gu, X.; Dang, F.; Itoh, T.; Wang, Y.; Sasaki, H.; Kondo, M.; Koga, K.; Yabuki, K.; Snyder, G. J.; et al. Flexible n-type thermoelectric materials by organic intercalation of layered transition metal dichalcogenide $TiS_2$. *Nat. Mater.* **2015**, *14*, 622−627.
(1070) Huang, H.; Cui, Y.; Li, Q.; Dun, C.; Zhou, W.; Huang, W.; Chen, L.; Hewitt, C. A.; Carroll, D. L. Metallic 1T phase $MoS_2$ nanosheets for high-performance thermoelectric energy harvesting. *Nano Energy* **2016**, *26*, 172−179.
(1071) Jiang, P.; Qian, X.; Gu, X.; Yang, R. Probing anisotropic thermal conductivity of transition metal dichalcogenides $MX_2$ (M = Mo, W and X = S, Se) using time-domain thermoreflectance. *Adv. Mater.* **2017**, *29*, 1701068.
(1072) Qian, X.; Shen, S.; Liu, T.; Cheng, L.; Liu, Z. Two-dimensional $TiS_2$ nanosheets for in vivo photoacoustic imaging and photothermal cancer therapy. *Nanoscale* **2015**, *7*, 6380−6387.
(1073) Sweet, C.; Pramanik, A.; Jones, S.; Ray, P. C. Two-photon fluorescent molybdenum disulfide dots for targeted prostate cancer imaging in the biological II window. *ACS Omega* **2017**, *2*, 1826−1835.
(1074) Chen, H.; Liu, T.; Su, Z.; Shang, L.; Wei, G. 2D transition metal dichalcogenide nanosheets for photo/thermo-based tumor imaging and therapy. *Nanoscale Horiz.* **2018**, *3*, 74−89.
(1075) Verhalen, B.; Ernst, S.; Börsch, M.; Wilkens, S. Dynamic ligand-induced conformational rearrangements in p-glycoprotein as probed by fluorescence resonance energy transfer spectroscopy. *J. Biol. Chem.* **2012**, *287*, 1112−1127.
(1076) Wan, Z.; Liu, H.; Zheng, Y.; Ma, Y.; Liu, K.; Zhou, X.; Liu, C.; Liu, K.; Wang, E. A review of acoustic devices based on suspended 2D materials and their composites. *Adv. Funct. Mater.* **2024**, *34*, 2303519.
(1077) Maxey, K.; Naylor, C. H.; O'Brien, K. P.; Penumatcha, A.; Oni, A.; Mokhtarzadeh, C.; Dorow, C. J.; Rogan, C.; Holybee, B.; Tronic, T.; et al.. 300 mm MOCVD 2D CMOS materials for more (than) moore scaling. In *2022 IEEE Symposium on VLSI Technology and Circuits (VLSI Technology and Circuits)*, 2022.
(1078) Schram, T.; Smets, Q.; Groven, B.; Heyne, M. H.; Kunnen, E.; Thiam, A.; Devriendt, K.; Delabie, A.; Lin, D.; Lux, M.; et al.. $WS_2$ transistors on 300 mm wafers with BEOL compatibility. In *47th European Solid-State Device Research Conference (ESSDERC)*, Leuven, BELGIUM, Sep 11−14, 2017; pp 212−215.
(1079) Hu, J.; Zhou, F.; Wang, J.; Cui, F.; Quan, W.; Zhang, Y. Chemical vapor deposition syntheses of wafer-scale 2D transition metal dichalcogenide films toward next-generation integrated circuits related applications. *Adv. Funct. Mater.* **2023**, *33*, 2303520.
(1080) Ning, H.; Yu, Z.; Li, T.; Shen, H.; Long, G.; Shi, Y.; Wang, X. From lab to fab: Path forward for 2D material electronics. *Sci. China Inform. Sci.* **2023**, *66*, 160411.
(1081) Schram, T.; Sutar, S.; Radu, I.; Asselberghs, I. Challenges of wafer-scale integration of 2D semiconductors for high-performance transistor circuits. *Adv. Mater.* **2022**, *34*, 2109796.
(1082) Thomas, S. An industry view on two-dimensional materials in electronics. *Nat. Electron.* **2021**, *4*, 856−857.
(1083) O'Brien, K. P.; Naylor, C. H.; Dorow, C.; Maxey, K.; Penumatcha, A. V.; Vyatskikh, A.; Zhong, T.; Kitamura, A.; Lee, S.; Rogan, C.; et al. Process integration and future outlook of 2D transistors. *Nat. Commun.* **2023**, *14*, 6400.
(1084) Chung, Y.-Y.; Shieh, J.-M.; Su, S.-K.; Chiang, H.-L.; Chen, T.-C.; Li, L.-J.; Wong, H. S. P.; Jian, W.-B.; Chien, C.-H.; Lu, K.-C.; et al. Demonstration of 40-nm channel length top-gate p-mosfet of $WS_2$ channel directly grown on $SiO_2$/Si substrates using area-selective CVD technology. *IEEE Trans. Electron Devices* **2019**, *66*, 5381−5386.
(1085) Liu, C.; Liu, K. Monolayer mosaic heterostructures. *Nat. Nanotechnol.* **2022**, *17*, 439−440.
(1086) Zhang, K.; She, Y.; Cai, X.; Zhao, M.; Liu, Z.; Ding, C.; Zhang, L.; Zhou, W.; Ma, J.; Liu, H.; et al. Epitaxial substitution of metal iodides for low-temperature growth of two-dimensional metal chalcogenides. *Nat. Nanotechnol.* **2023**, *18*, 448−455.
(1087) Jin, Z.; Li, X.; Mullen, J. T.; Kim, K. W. Intrinsic transport properties of electrons and holes in monolayer transition-metal dichalcogenides. *Phys. Rev. B* **2014**, *90*, No. 045422.
(1088) Xiong, Y.; Xu, D.; Feng, Y.; Zhang, G.; Lin, P.; Chen, X. P-type 2D semiconductors for future electronics. *Adv. Mater.* **2023**, *35*, 2206939.
(1089) Zhao, B.; Shen, D.; Zhang, Z.; Lu, P.; Hossain, M.; Li, J.; Li, B.; Duan, X. 2D metallic transition-metal dichalcogenides: Structures, synthesis, properties, and applications. *Adv. Funct. Mater.* **2021**, *31*, 2105132.
(1090) Lin, L.; Peng, H.; Liu, Z. Synthesis challenges for graphene industry. *Nat. Mater.* **2019**, *18*, 520−524.
(1091) Cheng, Z.; Pang, C.-S.; Wang, P.; Le, S. T.; Wu, Y.; Shahrjerdi, D.; Radu, I.; Lemme, M. C.; Peng, L.-M.; Duan, X.; et al. How to report and benchmark emerging field-effect transistors. *Nat. Electron.* **2022**, *5*, 416−423.
(1092) *International roadmap for devices and systems*. IEEE, 2020. https://irds.ieee.org/images/files/pdf/2020/2020IRDS_MM.pdf (accessed 2024-04-01).